830-H-10

NAS1.55:3064

NASA Conference Publication 3064

APR 2 0 1990

Research in Structures, Structural Dynamics and Materials 1990

Work-in-Progress papers from a conference held in Long Beach, California April 2-4, 1990

NASA

NASA Conference Publication 3064

Research in Structures, Structural Dynamics and Materials 1990

Compiled by
Jean-François M. Barthelemy
NASA Langley Research Center
Hampton, Virginia

Ahmed K. Noor
The George Washington University
Joint Institute for Advancement of Flight Sciences
NASA Langley Research Center
Hampton, Virginia

Work-in-Progress papers
presented at the AIAA/ASME/ASCE/AHS/ASC
31st Structures, Structural Dynamics and
Materials Conference held in
Long Beach, California
April 2–4, 1990

NASA
National Aeronautics and
Space Administration
Office of Management
Scientific and Technical
Information Division
1990

I

PREFACE

This document contains a collection of 21 papers presented at the AIAA/ASME/ ASCE/AHS/ASC/ 31st Structures, Structural Dynamics and Materials Conference held in Long Beach, California, April 2-4, 1990. The conference had a total of 284 papers, including 263 full-length papers and 21 short presentations in the work-in-progress sessions. All of the papers appearing in this document were presented in the two work-in-progress sessions. Most of the full-length papers are contained in the conference proceedings published by AIAA.

The fields covered by the conference are rapidly changing, and if new results and anticipated future directions are to have maximum impact and use, it is imperative that they reach workers in the field as soon as possible. This consideration led to the decision to publish these proceedings prior to the conference. Special thanks go to the members of the Research Information and Applications Division at NASA Langley Research Center for their cooperation in publishing this volume.

The use of trademarks or manufacturers' names does not constitute endorsement, either expressed or implied, by the National Aeronautics and Space Administration.

Jean-François M. Barthelemy
Ahmed K. Noor

Compilers

CONTENTS

PREFACE iii

SESSION 39 (W1) - WORK-IN-PROGRESS I

TEST/SEMI-EMPIRICAL ANALYSIS OF A CARBON/EPOXY FABRIC STIFFENED PANEL 3
E. E. Spier and J. A. Anderson

REPEATED BUCKLING OF COMPOSITE SHEAR PANELS 37
Josef Singer and Tanchum Weller

COMPRESSIVE FAILURE OF THICK-SECTION COMPOSITE LAMINATES WITH AND WITHOUT CUTOUTS SUBJECTED TO BIAXIAL LOADING 43
L. Rouxel and S. S. Wang

AN ANALYTICAL SOLUTION FOR THE ELASTOPLASTIC RESPONSE OF A CONTINUOUS FIBER COMPOSITE UNDER UNIAXIAL LOADING 55
Jong-Won Lee and David H. Allen

THE LOOPED ADHESIVE STRIP: AN EXAMPLE OF COPLANAR DELAMINATION INTERACTION 67
W. J. Bottega

A NEW BEAM THEORY USING FIRST-ORDER WARPING FUNCTIONS 85
C. A. Ie and J. B. Kosmatka

PROBABILISTIC STRUCTURAL ANALYSIS BY EXTREMUM METHODS 103
Avinash M. Nafday

PROBABILISTIC FAILURE ASSESSMENT WITH APPLICATION TO SOLID ROCKET MOTORS 115
Darrell L. Jan, Barry D. Davidson and Nicholas R. Moore

GLOBAL OPTIMIZATION METHODS FOR ENGINEERING DESIGN 123
Jasbir S. Arora

EXPONENTIAL APPROXIMATIONS IN OPTIMAL DESIGN 137
A. D. Belegundu, S. D. Rajan and J. Rajgopal

CONSERVATIVE BUFFERING OF APPROXIMATE NONLINEAR CONSTRAINTS 151
H. L. Thomas and L. A. Schmit

EVALUATION OF ALTERNATIVES FOR BEST-FIT PARABOLOID FOR DEFORMED ANTENNA SURFACES 159
Menahem Baruch and Raphael T. Haftka

SESSION 43 (W2) - WORK-IN-PROGRESS II

COMBINED DESIGN OF STRUCTURES AND CONTROLLERS FOR OPTIMAL MANEUVERABILITY 179
Jer Ling, Pierre Kabamba and John Taylor

GROUND TEST PROGRAM FOR NEW ATLAS PAYLOAD FAIRINGS 193
Michael J. Robbins

DIRECT USE OF LINEAR TIME-DOMAIN AERODYNAMICS IN AEROSERVO-ELASTIC ANALYSIS: AERODYNAMIC MODEL 207
J. A. Woods and M. G. Gilbert

COMPUTATION OF MAXIMUM GUST LOADS IN NONLINEAR AIRCRAFT USING A NEW METHOD BASED ON THE MATCHED FILTER APPROACH AND NUMERICAL OPTIMIZATION 221
Anthony S. Pototzky, Jennifer Heeg and Boyd Perry III

PIEZOELECTRICALLY FORCED VIBRATIONS OF ELECTRODED DOUBLY ROTATED QUARTZ PLATES BY STATE SPACE METHOD 231
R. Chander

ANALYSIS OF ELASTICALLY TAILORED VISCOELASTIC DAMPING MEMBER 239
G -S. Chen and B. P Dolgin

STATIC AND DYNAMIC AEROELASTIC CHARACTERIZATION OF AN AERO-DYNAMICALLY HEATED GENERIC HYPERSONIC AIRCRAFT CONFIGURATION 249
Jennifer Heeg, Michael G. Gilbert and Anthony S. Pototzky

STRUCTURAL RISK ASSESSMENT AND AIRCRAFT FLEET MAINTENANCE 263
Herb Smith, Jr., C. R. Saff and Tom F. Christian

DEVELOPING A FRAMEWORK FOR QUALITATIVE ENGINEERING - RESEARCH IN DESIGN AND ANALYSIS OF COMPLEX STRUCTURAL SYSTEMS 275
Bruno M. Franck

SESSION 39 (W1)
WORK-IN-PROGRESS I

TEST/SEMI-EMPIRICAL ANALYSIS OF A CARBON/EPOXY FABRIC STIFFENED PANEL

E.E. Spier and J.A. Anderson
Rohr Industries, Inc.
San Diego, California

Test/Semi-Empirical Analysis

Since 1975, extensive testing of carbon/epoxy tape plates and stiffened panels has been performed (Reference 1 through 6). Attempts were made to predict the crippling failure of stiffened panels, fabricated from C/Ep tape, using the non-linear option in the STAGS computer code (Reference 7). However, no meaningful results were acquired. Therefore, a semi-empirical crippling method was developed.

To date, a semi-empirical analysis method has not been developed for plates and stiffened panels manufactured from C/Ep fabric. The purpose of this work-in-progress is to present a semi-empirical analysis method developed to predict the buckling and crippling loads of carbon/epoxy fabric blade stiffened panels in compression. This is a hand analysis method comprised of well known, accepted techniques, logical engineering judgements, and experimental data that results in conservative solutions. In order to verify this method, a stiffened panel was fabricated and tested. Both the test and analysis results are presented.

Buckling/Crippling Test Specimen

This figure shows the test panel configuration. It consists of a skin with three blade stiffeners. The blade stiffeners contain flanges which were cocured to the skin. The entire panel was made from Hercules AS4/3501-5A carbon/epoxy fabric except for the C/Ep tow used at the flange/blade intersection. This C/Ep tow provides structural integrity at the joint, including significant torsional stiffness provided at the blades.

The blade stiffened panel was completely A and C-scanned and no defects were found. Prior to test, the panel was machined and assembled with potted aluminum end channels. The end surfaces were then ground parallel within .001 inch.

The unloaded edges of the outer skin elements were supported by split rigid steel tubes to simulate simple support boundary conditions. This isolates the three stiffeners as though they were in a much wider stiffened panel. Thus, it was sufficient to analyze just the middle stiffener and apply this result to all three. The load carried by the skin adjacent to each split tube was justifiably neglected because it is such a small percentage of the total panel load.

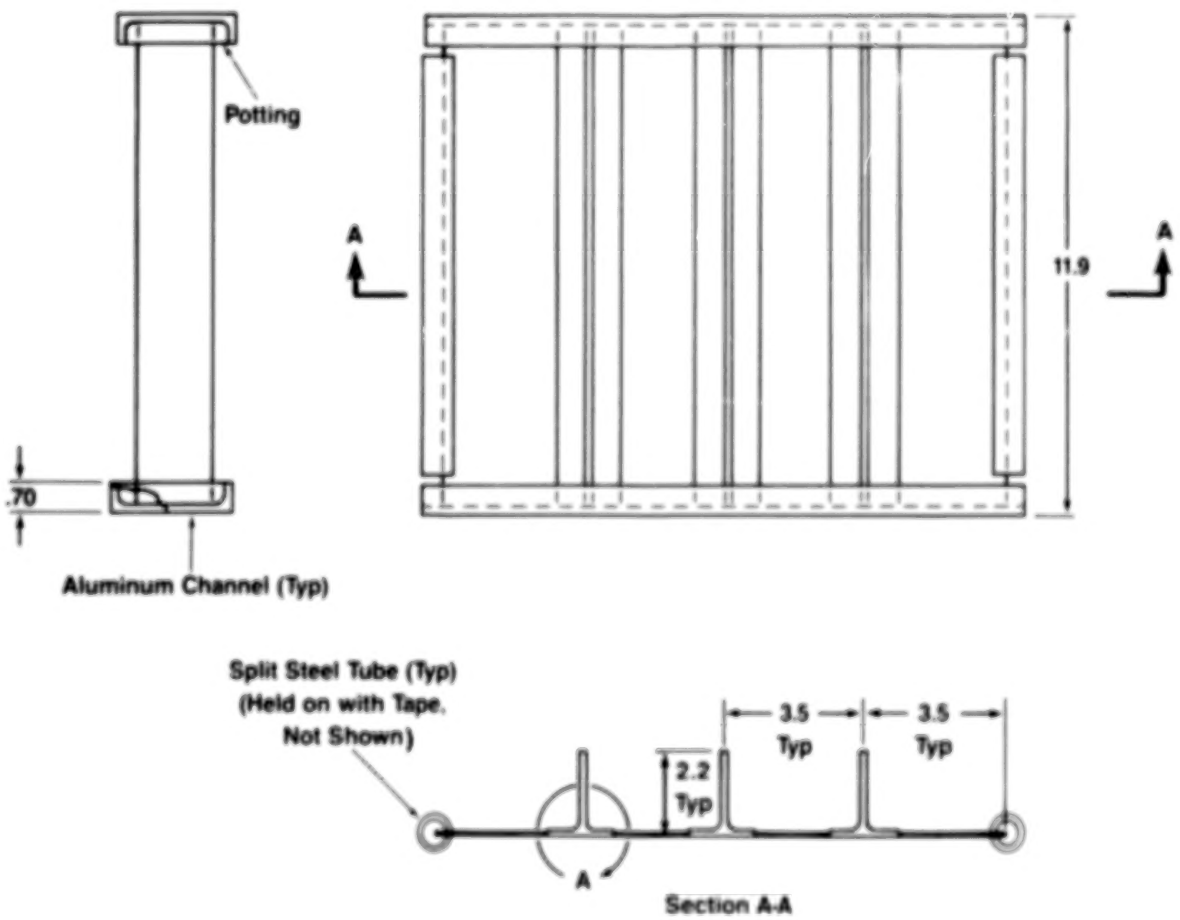

Detail A - Cross Section

This is the cross section of the stiffener/skin intersection. As mentioned above, the region adjacent to the blade, between the flange & skin, was filled with longitudinal carbon/epoxy tow. This juncture provides substantial support to the skin and the blades. However, the load carrying capability of the tow is neglected in the analysis.

The panel elements were configured so that the skin buckled first and the blades buckled second. Thus, the flanges, which buckle last, support both the skin and the blades.

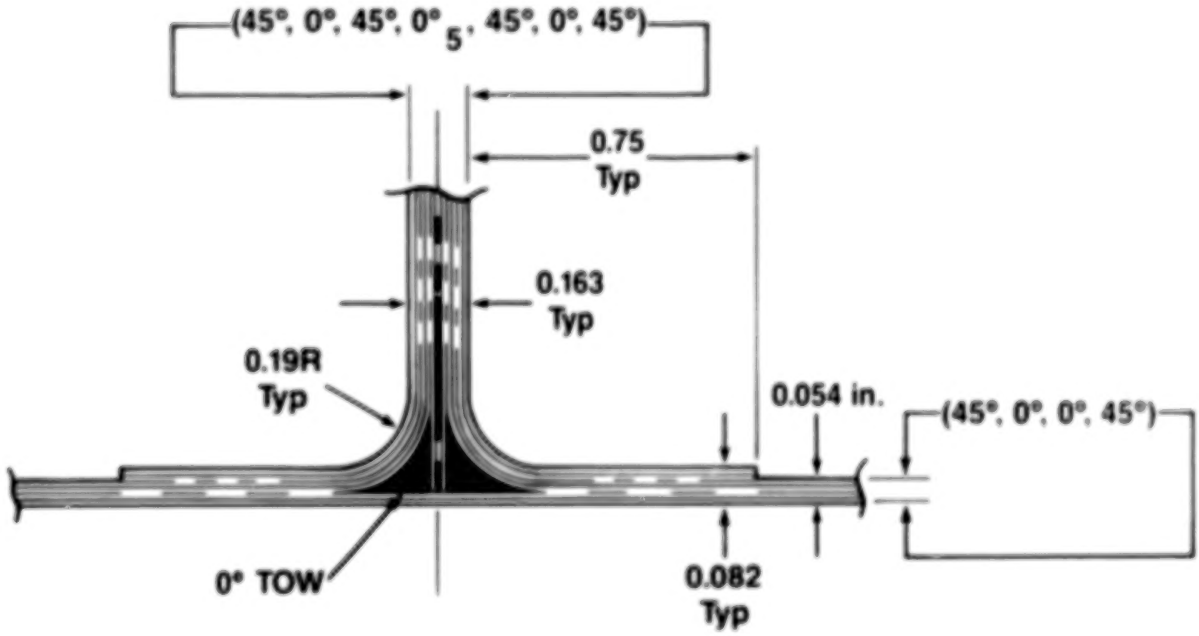

Typical Blade/Skin Intersection

This is a photomicrograph of the manufactured stiffener/skin intersection. Good consolidation was achieved and structural integrity of this joint was expected. The curvature of the blade middle plies was inadvertent, but no reduction of boundary constraint was predicted.

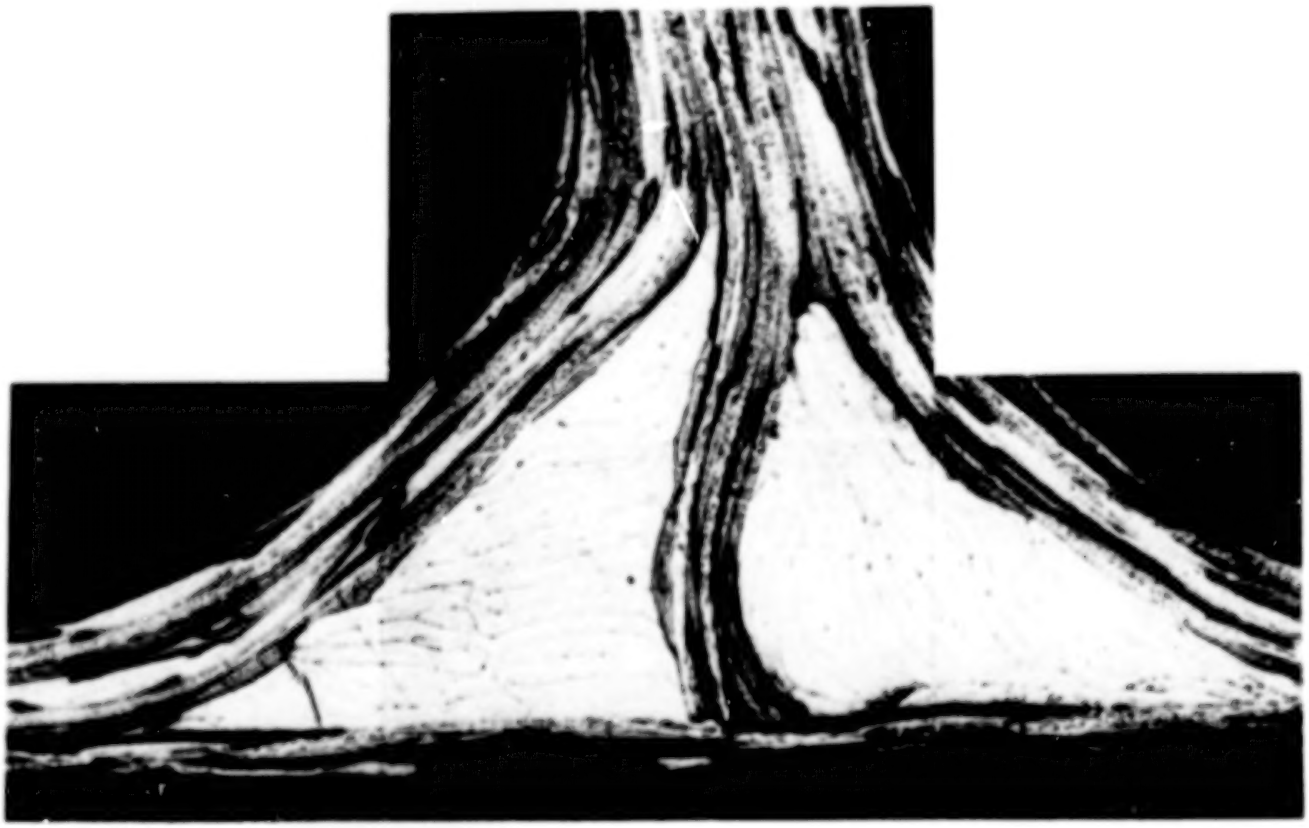

No-Edge-Free Postbuckling Test

In order to develop a semi-empirical stability analysis for carbon/epoxy fabric stiffened panels, empirical buckling and crippling curves for plates were generated. The plates tested were symmetric and balanced C/Ep fabric laminates. Each test plate was rectangular with clamped boundary conditions on the loaded edges (i.e., the short sides). Various b/t ratios were examined.

Two unloaded edge boundary conditions were tested. The first, designated "no-edge-free", was simply supported on both unloaded edges. The second, designated "one-edge-free", was simply supported on one edge and free on the other.

This is a typical no-edge-free plate test in compression. The unloaded edges are supported by steel v-blocks, simulating simple-support boundary conditions. The test specimen is in a postbuckled state. A full longitudinal wave can be seen.

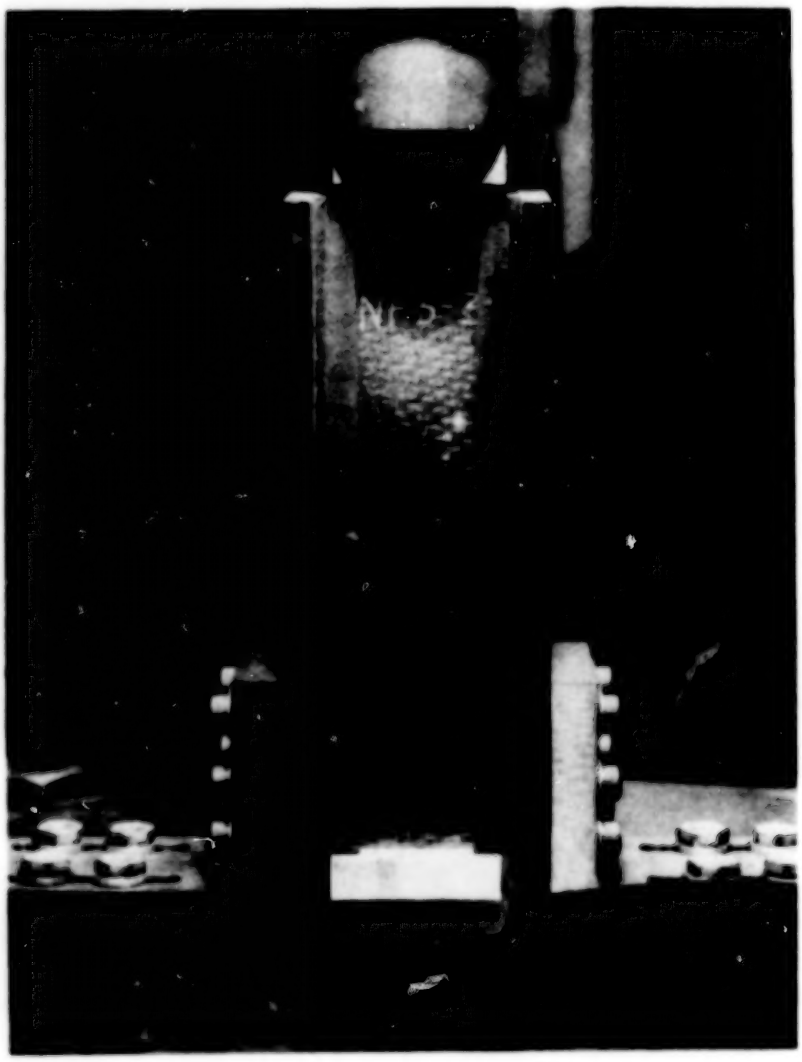

No-Edge-Free Crippling Test

Postbuckling failure of the no-edge-free compression test specimen is shown. This failure is referred to as "crippling". The type of failure shown is typical for carbon/epoxy fabric plates.

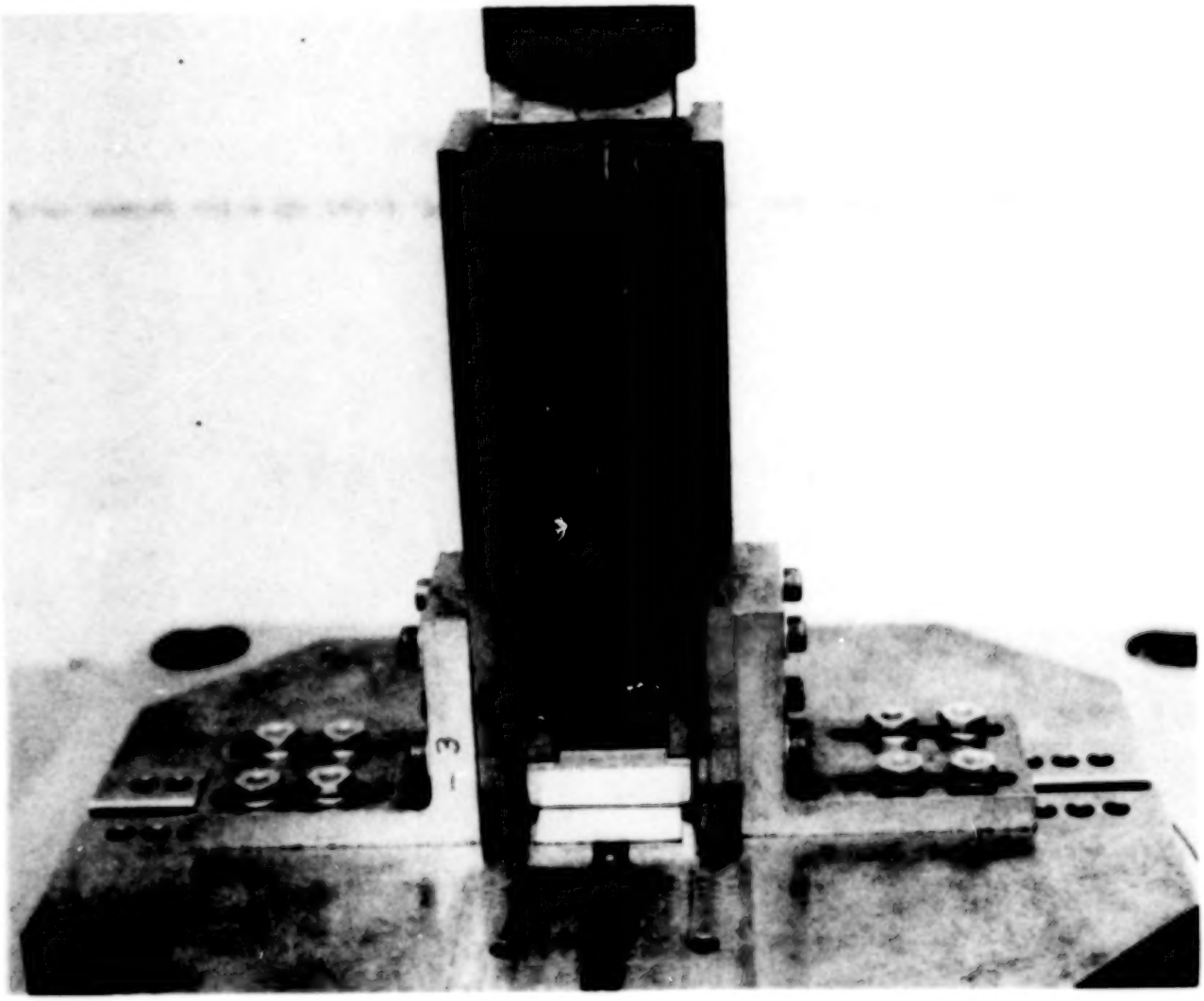

One-Edge-Free Postbuckling Test

This is a typical one-edge-free plate test in compression. One unloaded edge is supported by a steel v-block, simulating a simple-support boundary condition while the other unloaded edge is free. The test specimen is in a postbuckled state. One longitudinal half-wave can be seen.

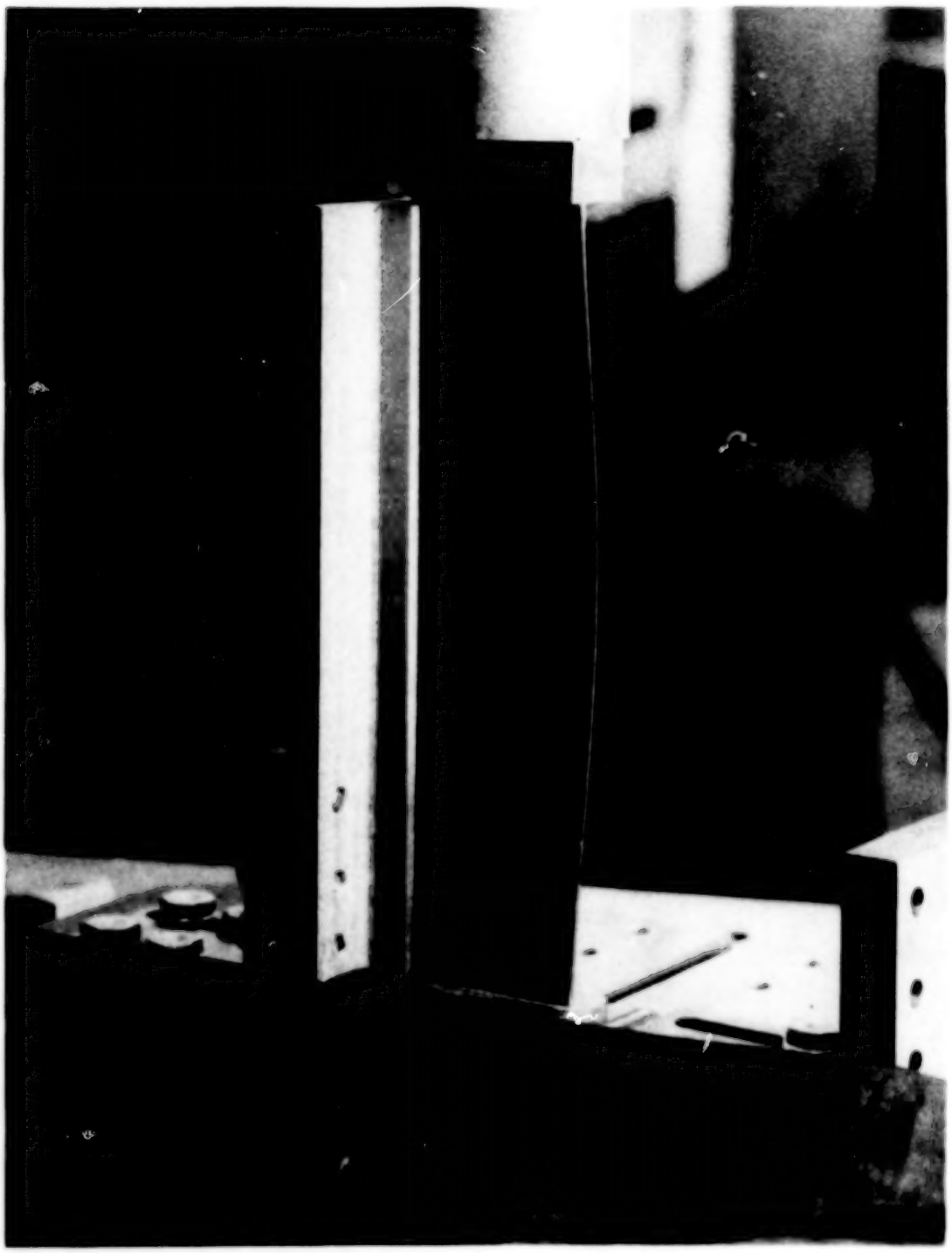

One-Edge-Free Crippling Test

Postbuckling failure (or crippling) of the one-edge-free compression test specimen is shown. This type of failure is typical for carbon/epoxy fabric plates.

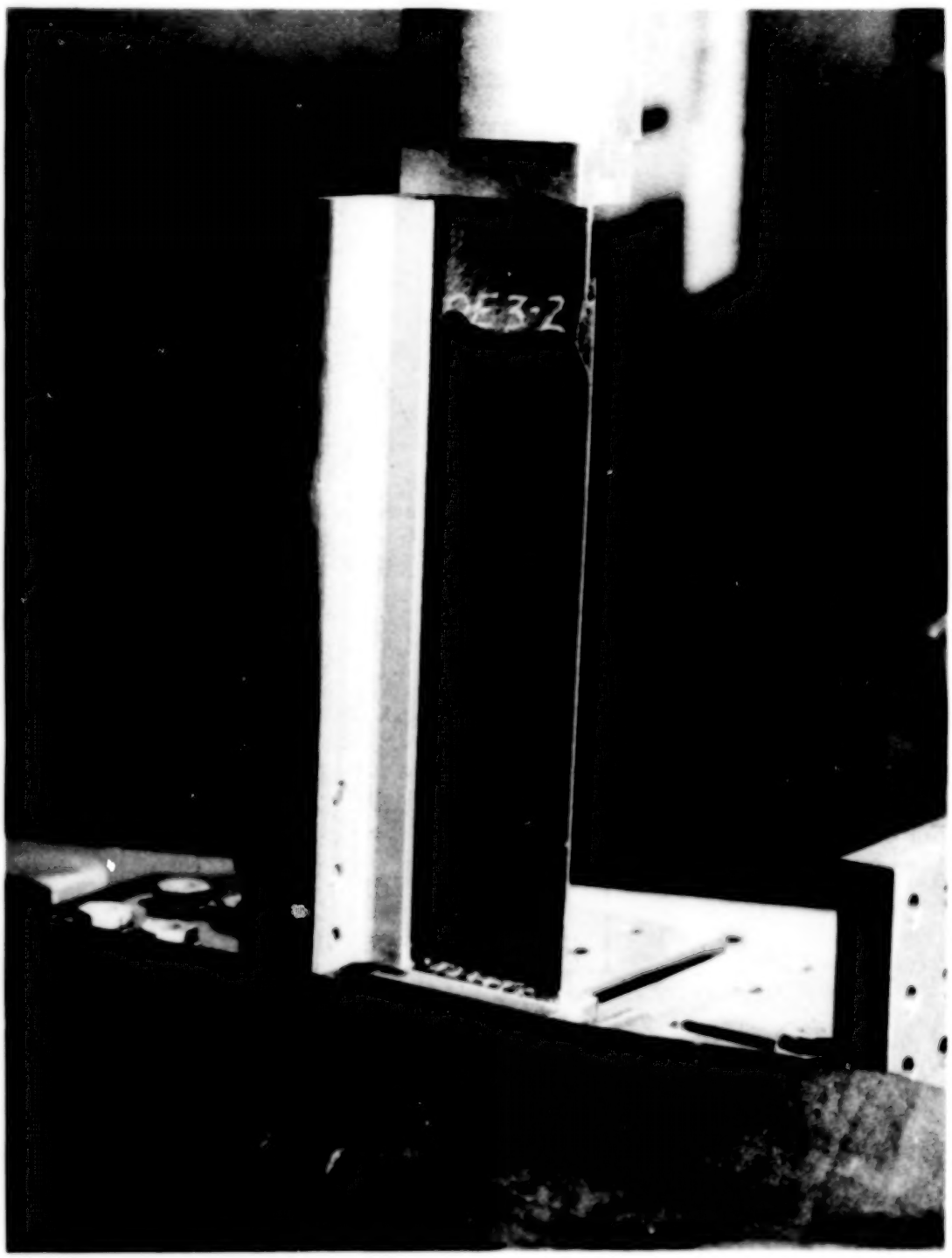

Typical load-Displacement Curve from Cripoling Test

This is a typical load-displacement curve for a plate compression test, either no-edge-free or one-edge-free. Displacement refers to the end-shortening of the test specimen. Buckling (P^{cr}) occurs at the bifurcation point of the linear curve. Crippling (P^{cc}) is the maximum postbuckling load that is reached prior to failure.

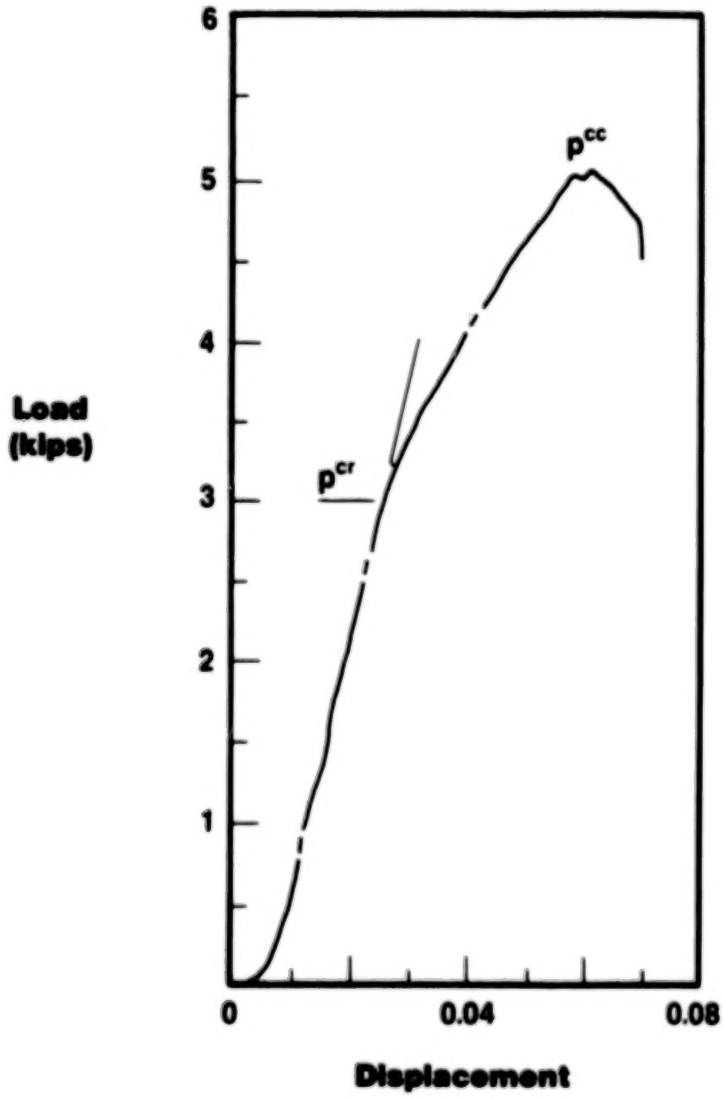

No-Edge-Free Buckling Graph

The no-edge-free buckling test data shown defines an empirical buckling curve for composites with similar layups. The ordinate is the ratio of the test buckling stress divided by the calculated classical buckling stress (F^{cr}/F^{cr}_{cl}). The abscissa is the width-to-thickness (b/t) ratio. The value for the classical buckling strength (F^{cr}_{cl}) can be obtained by using one of the following equations.

* Simply Supported Unloaded Edges

$$F^{cr,u,\phi E}_{cl,i,ss} = \frac{2\pi^2}{tb^2}\left[(D_{11}D_{22})^{\frac{1}{2}} + D_{12} + 2D_{66}\right]$$

* Fixed Unloaded Edges

$$F^{cr,u,\phi E}_{cl,i,fx} = \frac{\pi^2}{tb^2}\left[4.6(D_{11}D_{22}) + 2.67(D_{12}) + 5.33(D_{66})\right]$$

The classical buckling stress can be quite unconservative at low b/t ratios. However, the classical theory is accurate at b/t ratios greater than 50.

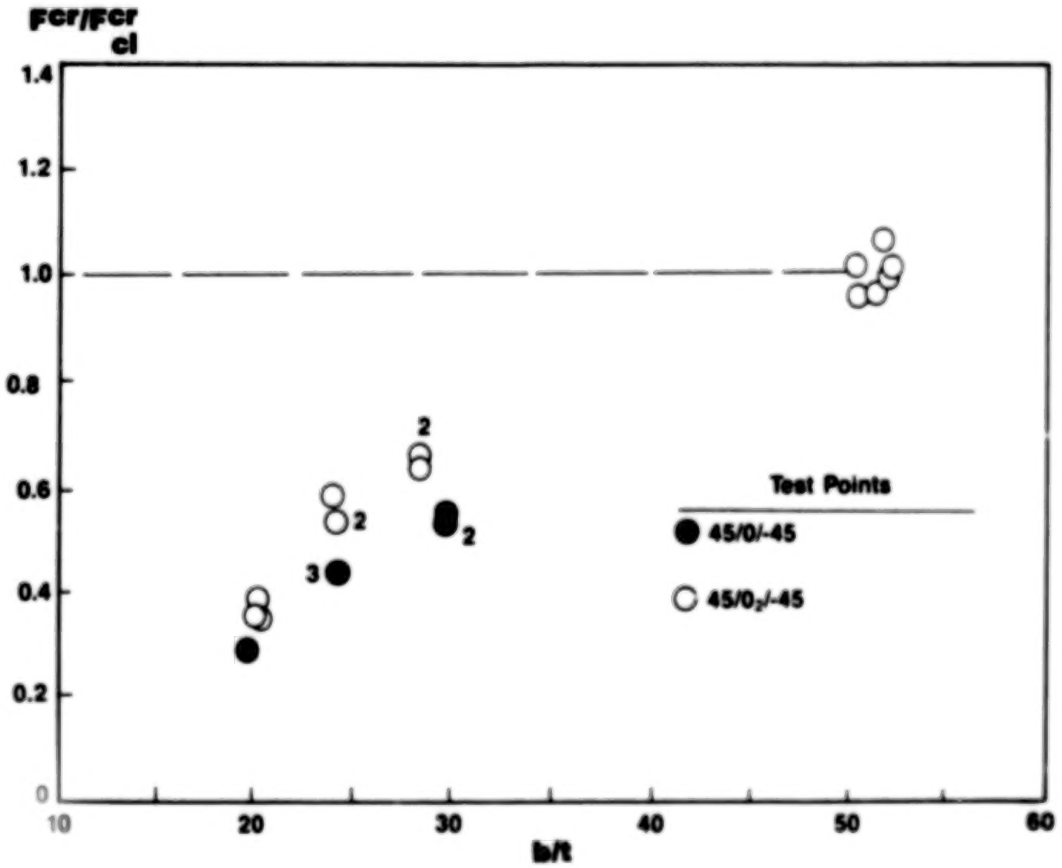

One-Edge-Free Buckling Graph

The one-edge-free buckling test data shown defines an empirical buckling curve for similar composite layups. The value for the one-edge-free classical buckling strength can be obtained by using the following equation.

$$F^{cr,u,1E}_{cl,i,ss} = \frac{12D_{66}}{tb^2} + \frac{\pi^2 D_{11}}{t(L')^2} \quad \text{where } L' = \frac{L}{(\sqrt{C})}$$

C is the end-fixity coefficient of columns and is approximately equal to 3.6 for potted end columns in a test machine.

This graph and its use is similar to that for no-edge-free composite plates. The discrepancy between classical and experimental buckling at low b/t ratios is the result of low transverse shear stiffness (Reference 8). This effect is insignificant at large b/t ratios.

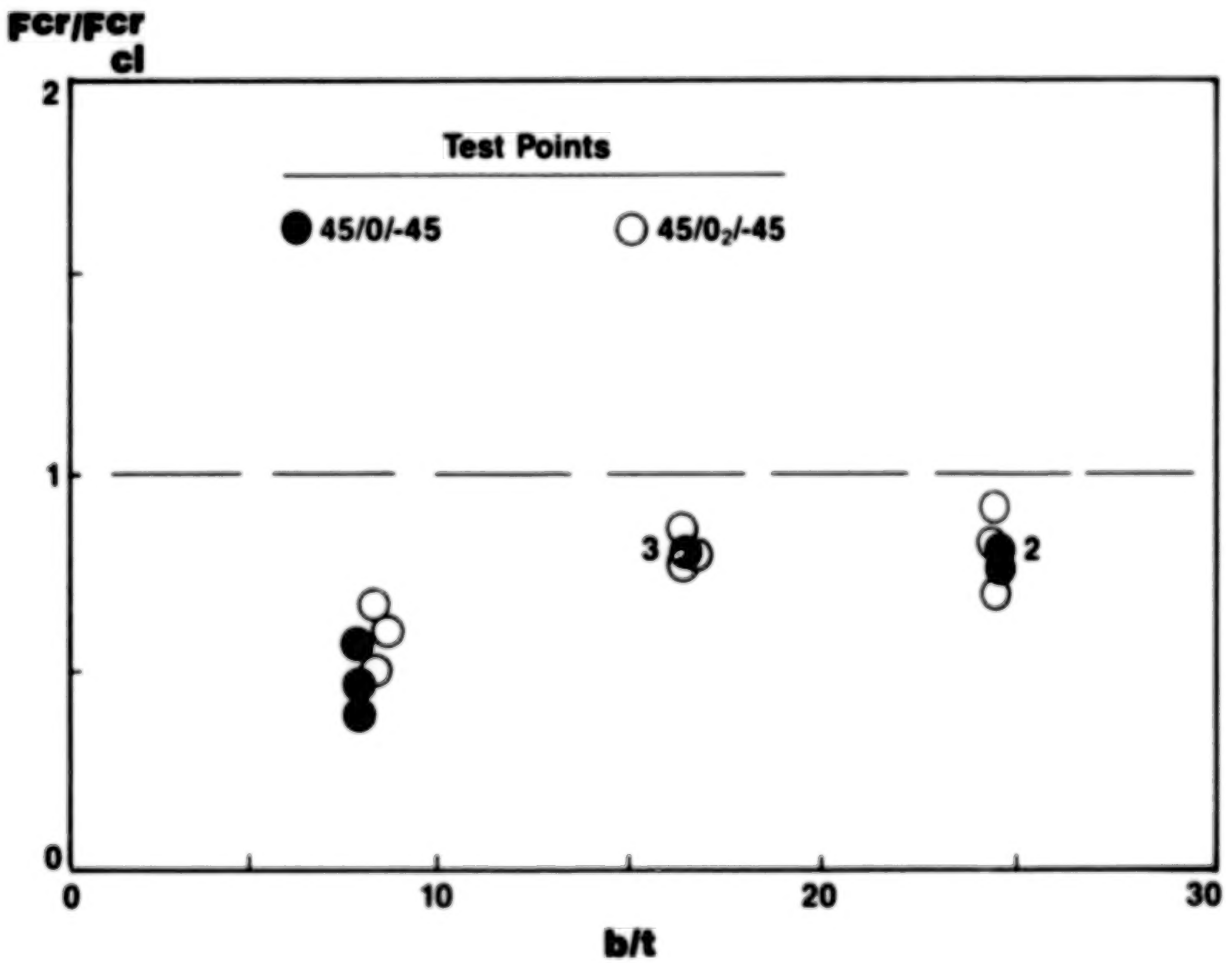

Laminate Ultimate Compressive Strength

This figure shows the ultimate compressive strength (F^{cu}) for AS4/3501-5A fabric 0°, 45° composite laminates. This data was generated because F^{cu} is required for the nondimensional empirical crippling curves which follow.

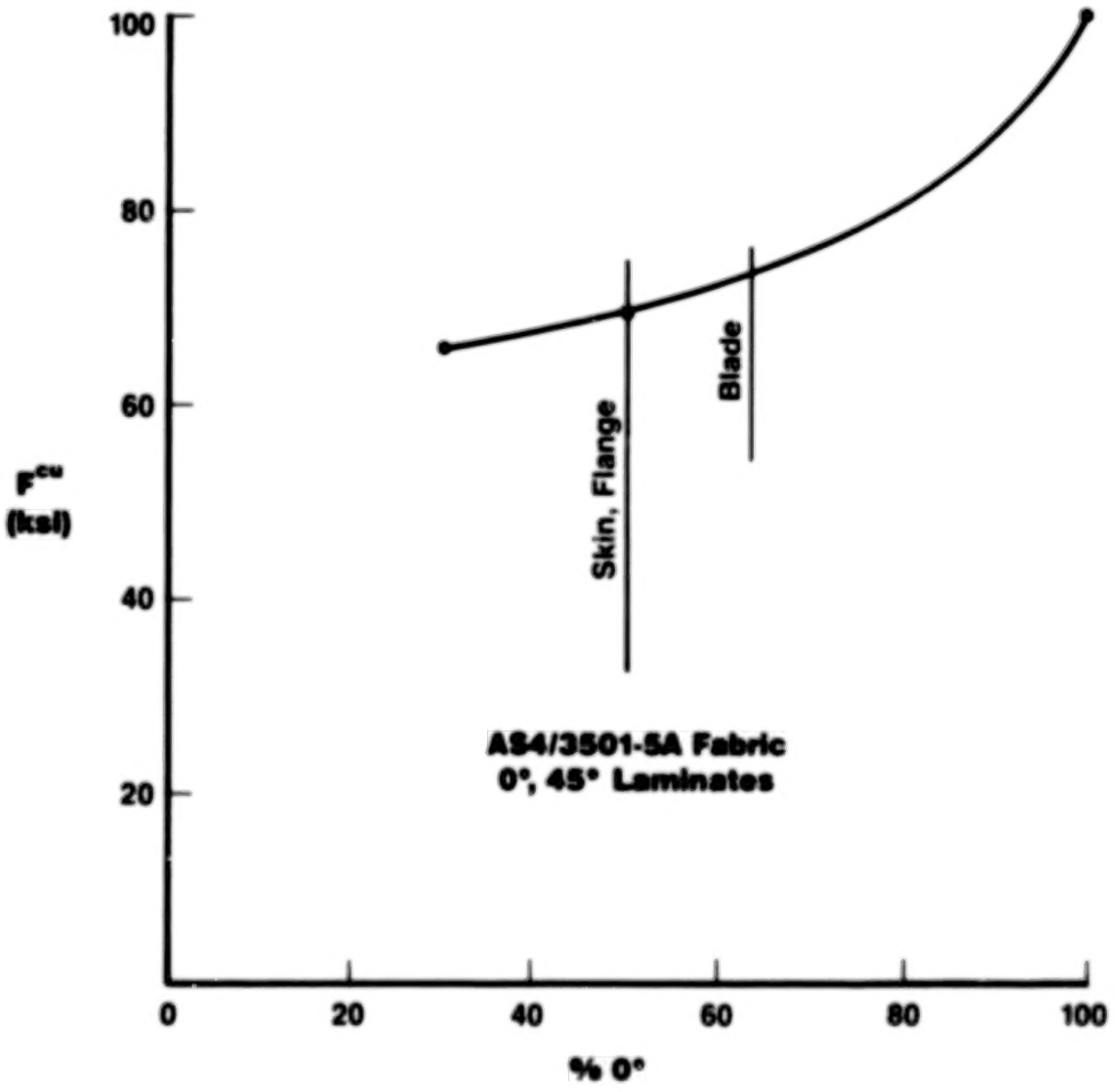

No-Edge-Free Crippling Graph

The no-edge-crippling test data shown was used to define the approximate mean crippling graph. The ordinate is the crippling stress (F^{cc}) divided by the classical buckling stress (F^{cr}_{cl}), while the abscissa is the ultimate compressive stress (F^{cu}) divided by F^{cr}_{cl}. Thus, for plates with similar layups, where the value for F^{cu} is known and F^{cr}_{cl} can be calculated, the predicted crippling stress may be obtained.

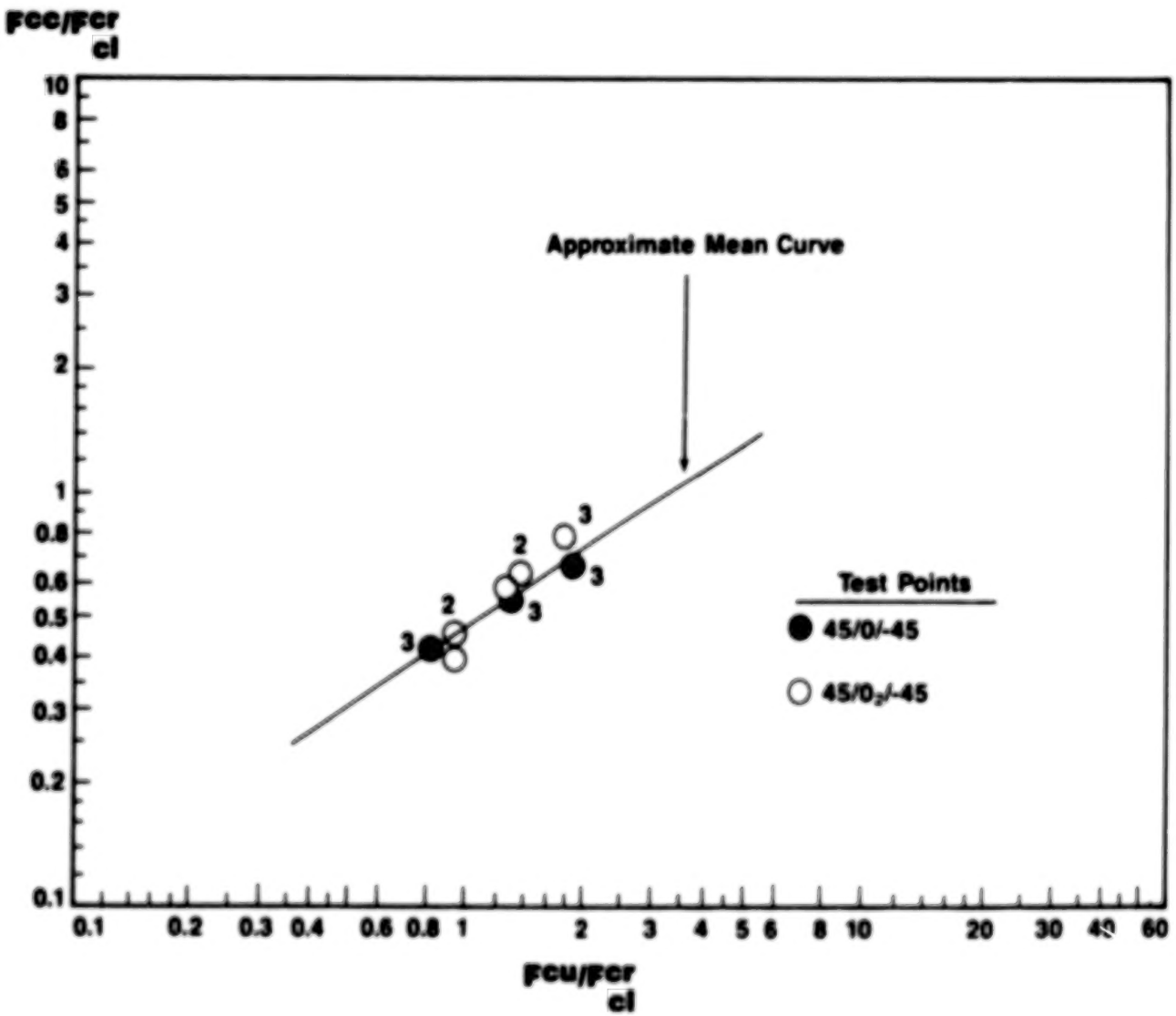

One-Edge-Free Crippling Graph

The one-edge-crippling graph shown is defined and utilized in a similar fashion to that for the no-edge-free graph.

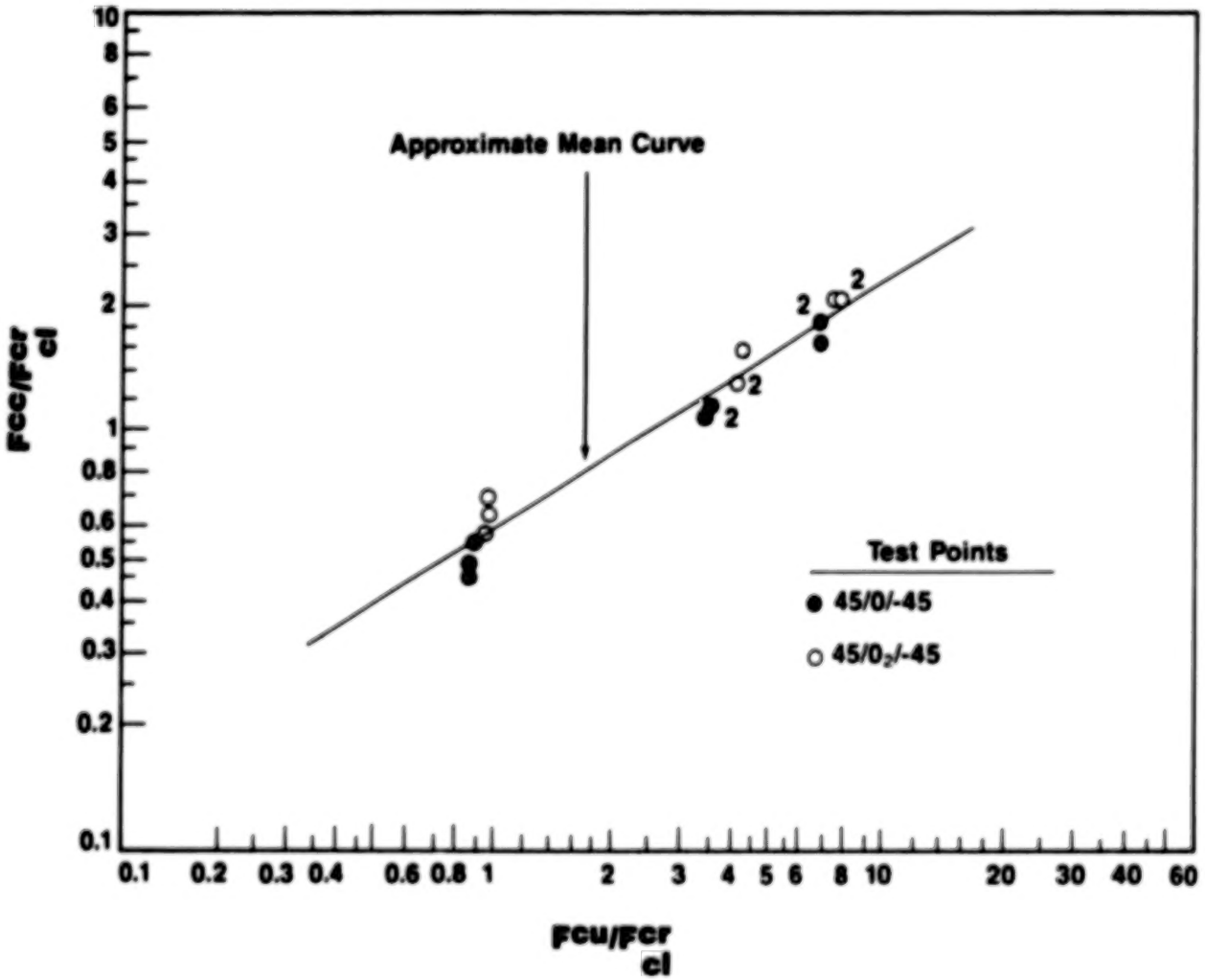

Crippling Strength Predictions

Armed with the empirical buckling and crippling curves, a step by step process can be used to calculate the crippling strength of the middle stiffener's blade and flanges. The classical buckling strains ($\epsilon_{\star}^{cr,st}$) for the blade and flange elements are .00309 in/in and .00582 in/in, respectively. In this case, the blade buckles first and causes the flange element to buckle prematurely. Therefore, the minimum classical buckling strain is equal to .00309 in/in.

The classical buckling strain is theoretical, not actual, and is referred to as a pseudo-strain. Using this strain (.00309 in/in) and the elastic modulus ($E_{Th,i}^{c,u}$), the pseudo-buckling stresses ($F_{\star,i}^{cr,u}$) are calculated. The compression strengths ($F_{n,u}^{cu,i}$) are found from lamination theory or test results. The resulting pseudo-crippling stresses ($F_{\star,i}^{cc,u}$) are then obtained from the one-edge-free empirical crippling curve.

However, the empirical crippling curve was developed from testing plates with simply supported boundary conditions. The actual blade has a boundary condition better than simply supported but certainly not fixed. Consequently, the boundary condition was assumed to be equal to one-half the increase in fixity from simply supported to fully fixed. This correction factor (Ca) is only applied to the blade because the flange supports the blade until it buckles, but at that point, the blade cannot provide greater than simple-support to the flange. The crippling load of the middle stiffener is obtained by summing the stiffener element pseudo-crippling loads ($C_a P_{\star,i}^{cc,b} + 2P_{\star,i}^{cc,f}$).

1	2	3	4	5	6	7	8	9	10	11	12
ELEMENT	A_i^u ($in.^2$)	$E_{Th,i}^{c,u}$ (psi)	$\epsilon_{\star}^{cr,st}$	$F_{\star,i}^{cr,u} = 3 * 4$ (psi)	$F_{n,i}^{cu,u}$ (psi)	$F_{n,i}^{cu,u} / F_{\star,i}^{cr,u} = 6 / 5$	$F^{cc} / F_{\star,i}^{cr,u}$	$F_{\star,i}^{cc,u} = 5 * 8$ (psi)	$P_{\star,i}^{cc,u} = 2.9$	C_a	$C_a P_{\star,i}^{cc,u} = 10 * 11$ (lb)
BLADE	0.326	7.60×10^6	0.00309	23,457	73,000	3.11	1.19	29,913	9,100	1.5	13,650
FLANGE	0.062	7.47×10^6	0.00309	23,08	,000	2.99	1.18	27,237	1,689	1.0	1,689

Effective-Width from Compressive Stress Distribution in a Buckled Flat Plate

In order to calculate the crippling strength of the panel, the skin, which buckles first, must also be considered. This requires an effective-width concept which was originally developed for metal structures by T. von Karman (Reference 9). In this method, a uniform compressive stress ($\sigma^{c,es}_{,i}$), at the same average strain as the stiffener at crippling, acts on a width of plate w_i^{es} directly adjacent to the supported edges. The value of w_i^{es} is adjusted so the $(\sigma^{c,es}_{,i})*(w_i^{es})*(t_i^{sk})$ is equal to the total load carried by the skin on one side of the stiffener. Thus, for a skin having the postbuckled distribution shown, the effective-width can be found using von Karman's equation. The value of $(\sigma^{c,es}_{,i})$ depends upon the magnitude of the applied design load or, in the case of analyzing a tested panel, the failure load.

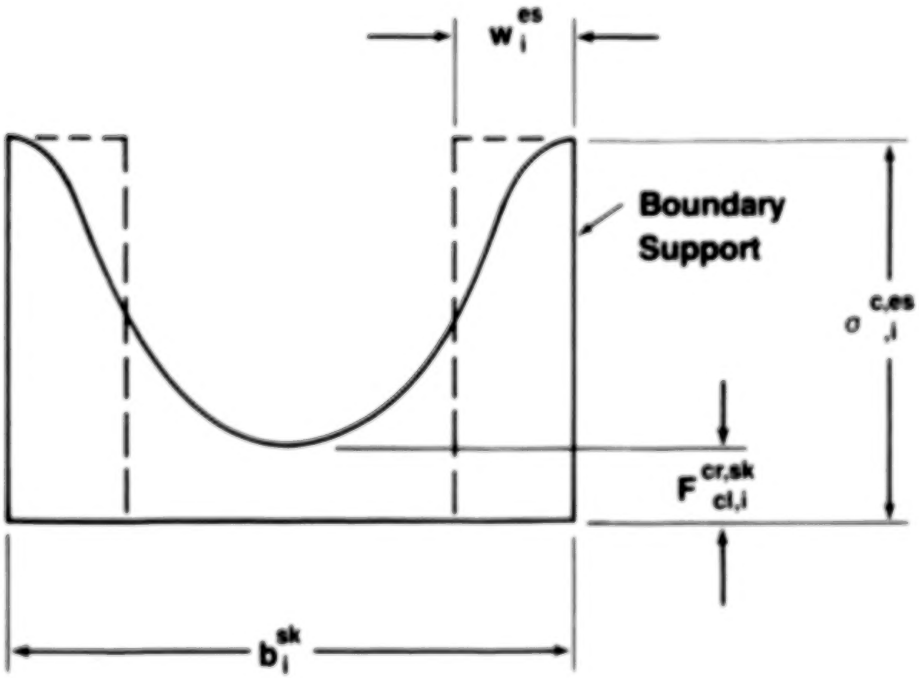

Effective-Width Equation (von Karman):

$$w_i^{es} = (b_i^{sk}/4)\left[1 + \left(F^{cr,sk,\Phi E}_{cl,i,f_\chi} / \sigma^{c,es}_{,i}\right)\right]$$

Middle Stiffener with Skin Effective-Widths

The detail buckling and crippling analysis is directed at this cross section. The calculations focus on only the middle stiffener which carries one-third of the total load up to crippling. The predicted crippling load of the middle stiffener and skin is equal to the summation of the stiffener element pseudo-crippling loads and the effective-width skin load.

$$P^{cc,ses}_{*,i} = [\, Ca(P^{cc,b}_{*,i}) + 2(P^{cc,f}_{*,i} + P^{c,es}_{,i})]$$

$$P^{c,es}_{,i} = (\sigma^{c,es}_{,i})*(\dot{w}^{es}_i)*(t^{sk}_i), \quad \text{where} \quad \dot{w}^{es}_i = (w^{es}_i - b^{f}_i)$$

Pertinent dimensions and effective-widths are shown.

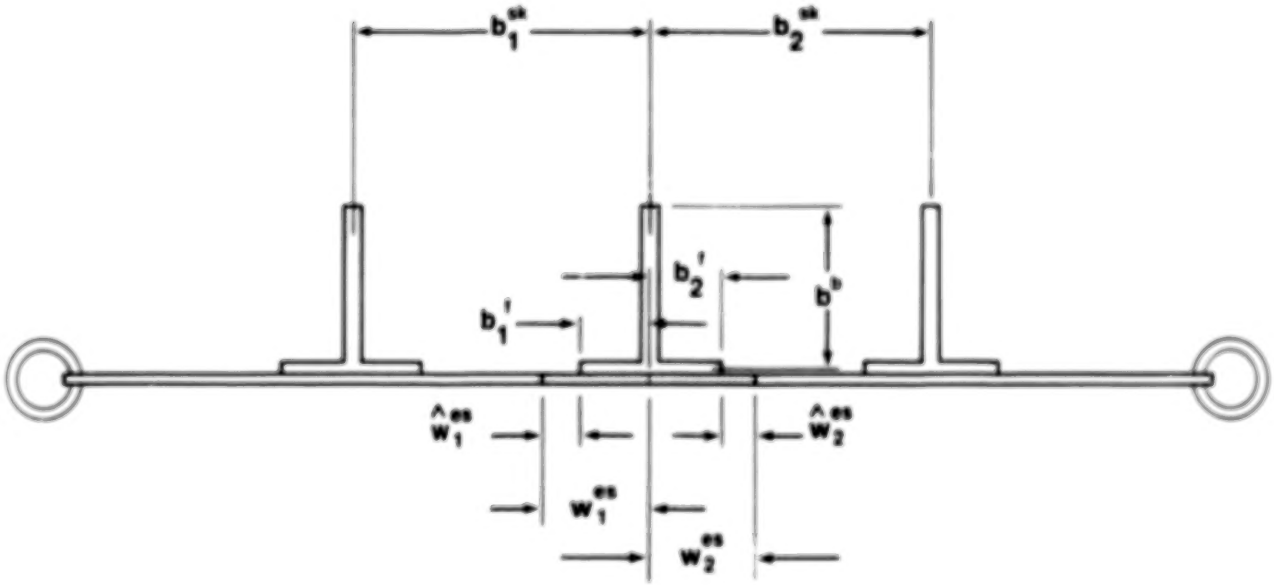

Strain Gage Locations on stiffened Panel

Before the analytical results are presented, an examination of the test data is required. This examination includes a review of strain gauge locations, an investigation of strain results, and finally, photographs of the test panel at different stages of postbuckling.

Twenty-four strain gauges were mounted on the test panel. Only those gauges that were actually used in the evaluation are shown. Test results indicate that compressive strain was uniform up to skin buckling. In addition, buckling of stiffener elements (i.e., blade and flanges) was also detected.

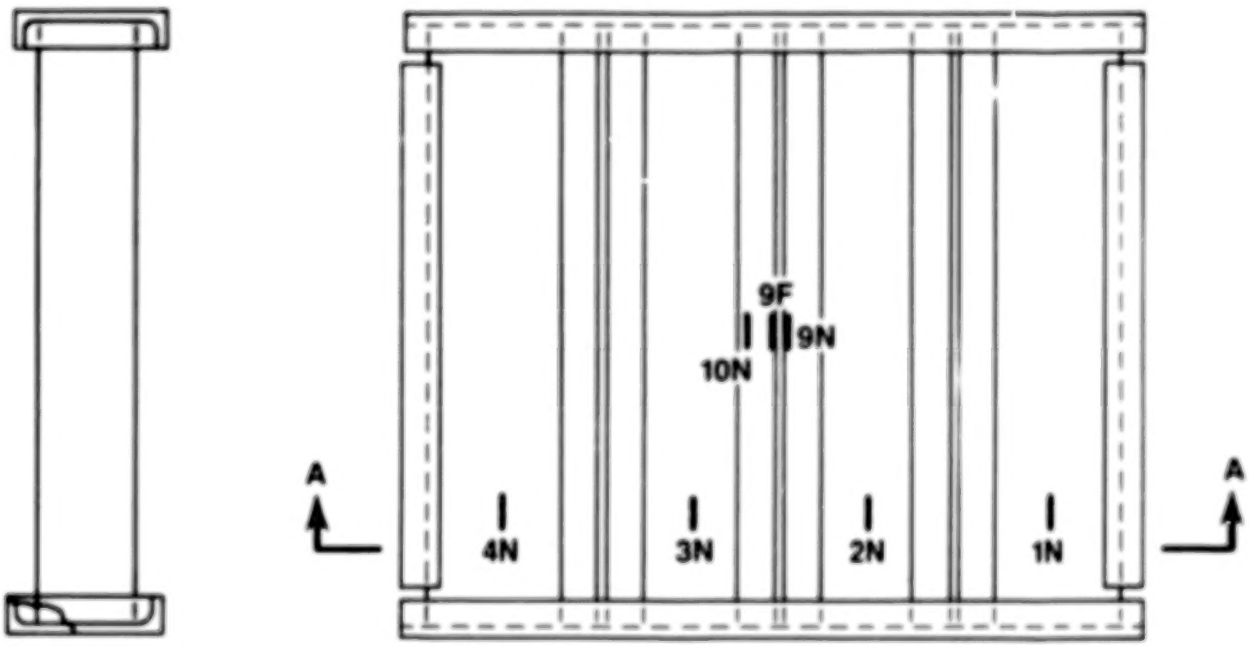

Section A-A

Load/Strain Curves Across Panel

Uniform strain was found in the central panels up to skin buckling as shown by gauges 1N through 4N. Although one of the outer panel gauges (1N) is displaced from the others, it has the same slope. These gauges indicate that the applied compression load was uniform.

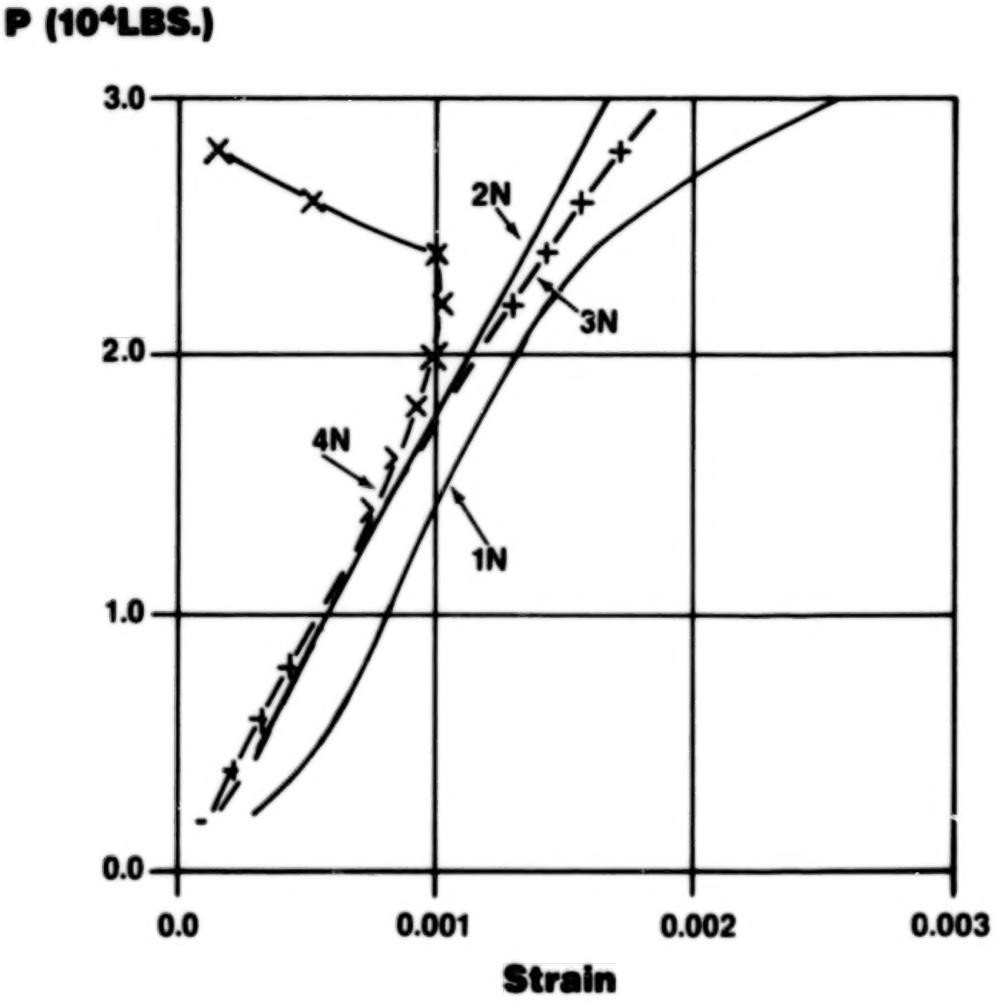

Back-To-Back Load/Strain Plots in Inner Skin Panel

The postbuckling behavior of the inner panels, based upon gauges 3N & 3F, was moderately nonlinear. This plot indicates that buckling occurred between 20,000 Lbs and 25,000 Lbs.

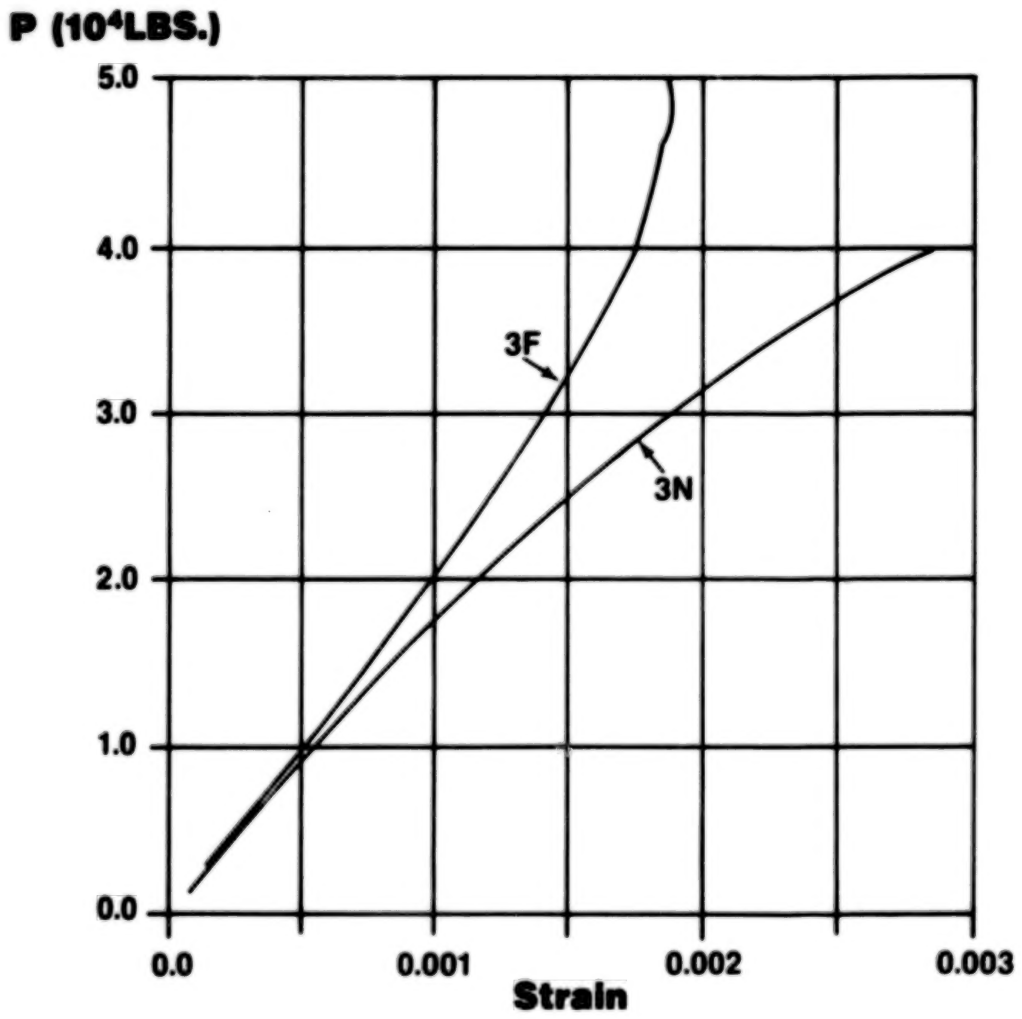

Back-To-Back Load/Strain Plots in Outer Skin Panels

The postbuckling behavior of the outer panels, based upon gauges 1N & 1F, was quite nonlinear. This plot indicates that buckling occurred between 22,000 Lbs and 24,000 Lbs.

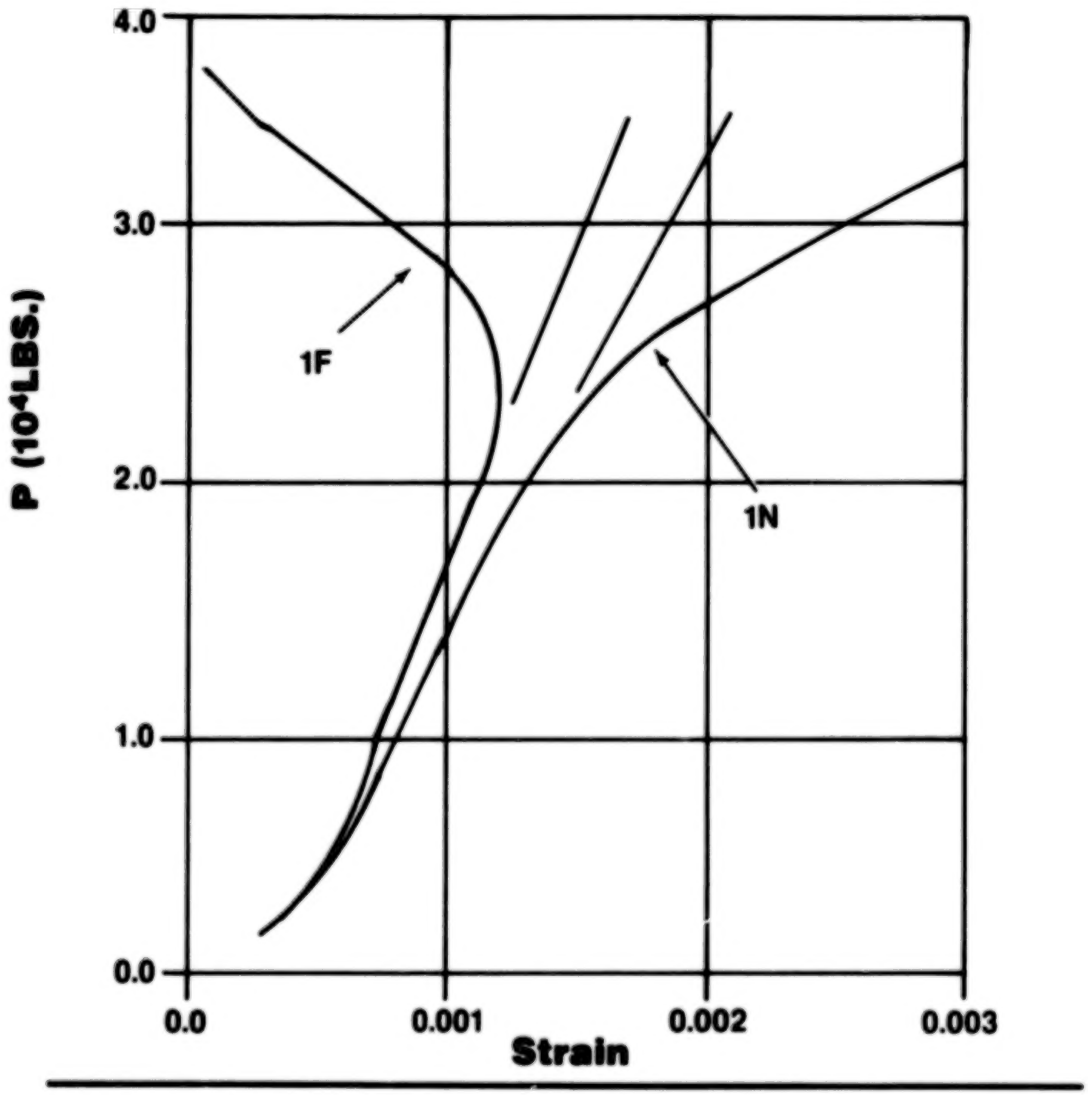

Back-to-Back Load/Strain Plots at Tip of Middle Blade

The lateral buckling of the middle stiffener's blade is indicated by the plot of back-to-back gauges 9N and 9F. Initial buckling appears to occur at a panel load of about 32,000 lbs, where the postbuckling behavior is slight up to a load of about 42,000 lbs. Beyond this load level, significant buckling deformation begins.

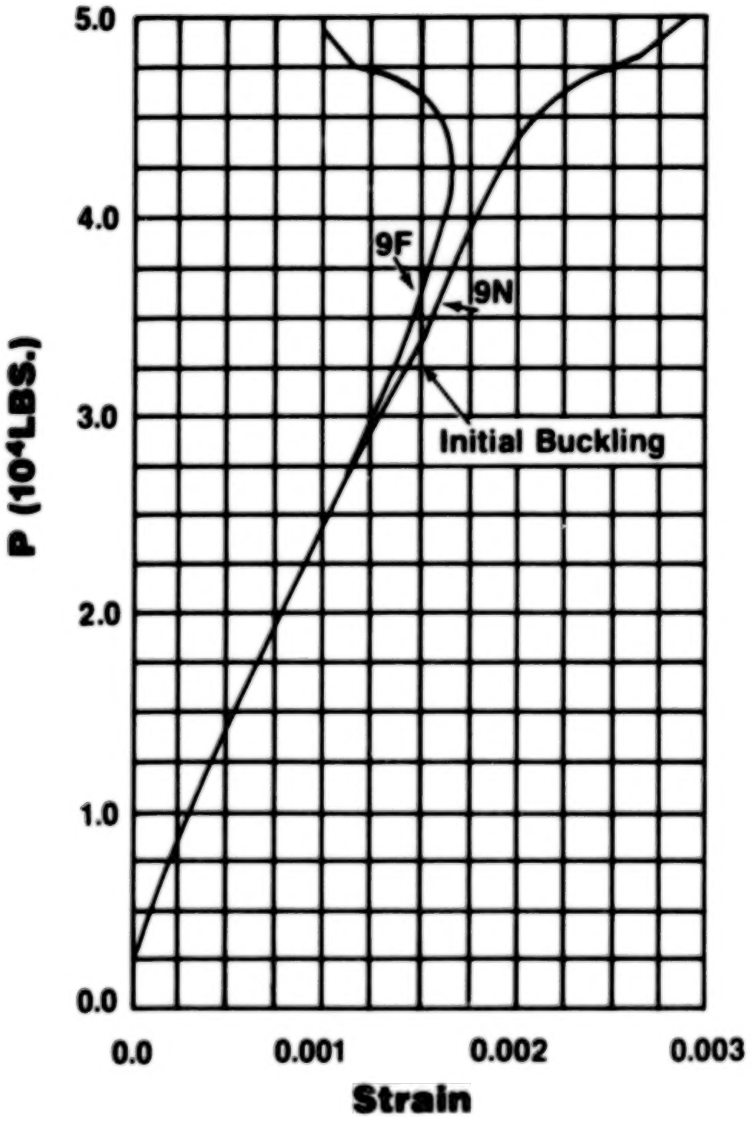

Back-To-Back Load/Strain Plots on Flange of Middle Stiffener

The behavior of one of the stiffener flanges is shown by the back-to-back gauges 10N and 10F. The load-strain plots are nearly linear up to a panel load of approximately 40,000 lbs. Buckling becomes quite evident at a panel load of about 45,000 lbs, which is slightly greater than that previously shown for the blade.

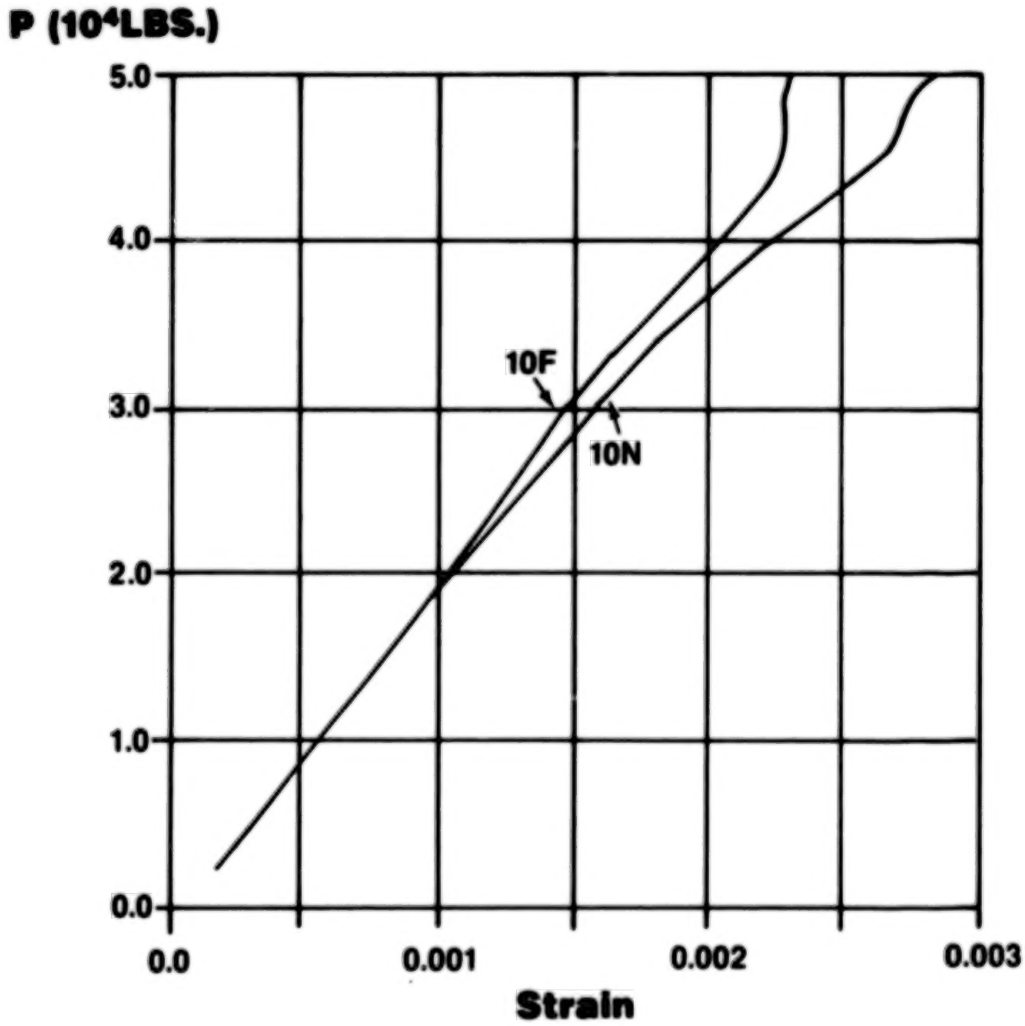

Postbuckling Behavior of Blade-Stiffened Panel at 48,000 Lbs

The compressive load on the stiffened panel is 48,000 lbs. At this load, strain gauges indicate that both the skin and blades have buckled. Note that the split steel tubes have been mounted on the outer unloaded edges.

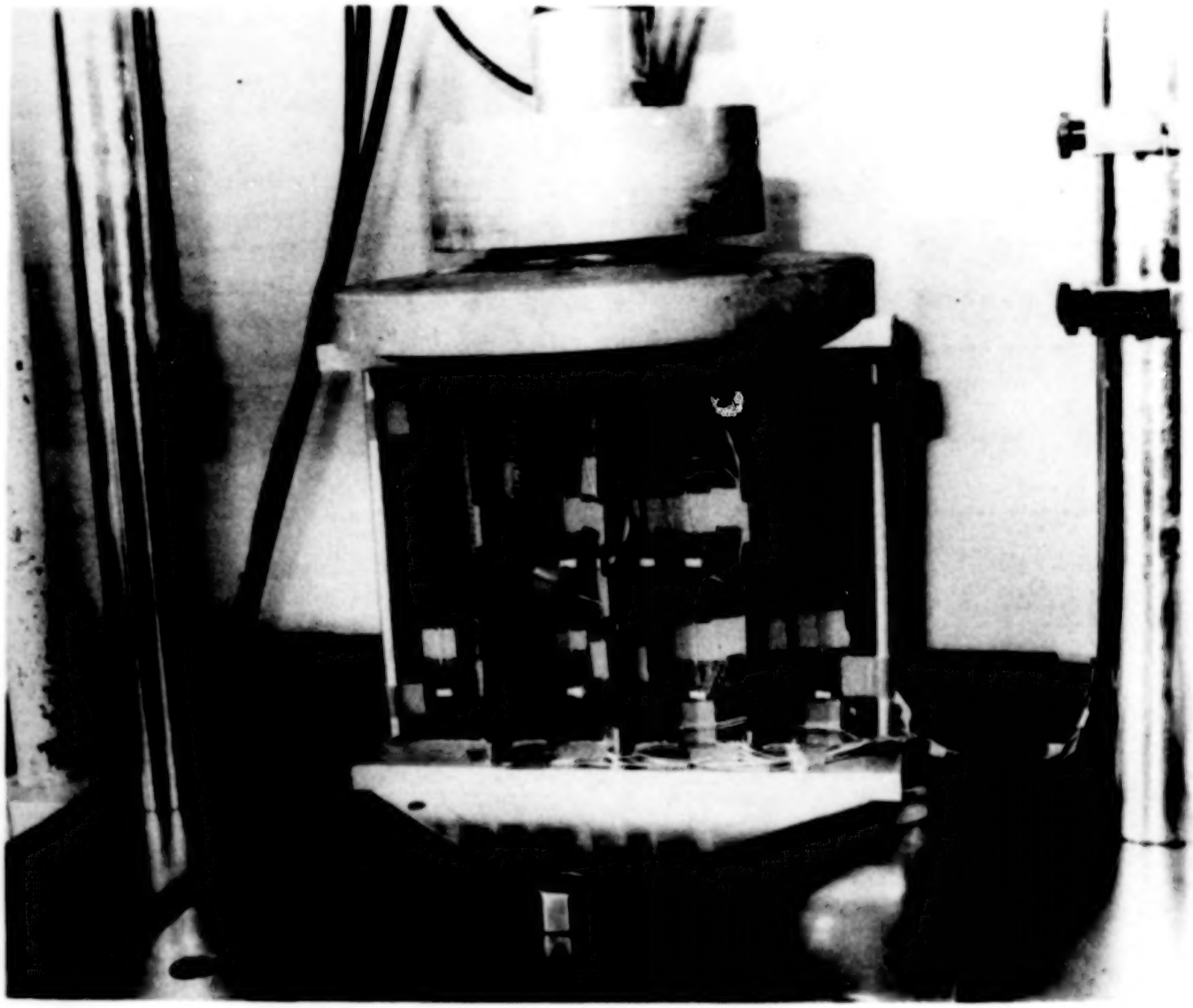

Postbuckling Behavior of Blade-Stiffened Panel at 55,600 Lbs

At 55,600 lbs., the buckling of the skin, and particularly the blades, has become quite severe. However, out of plane deformation will become much greater before crippling occurs.

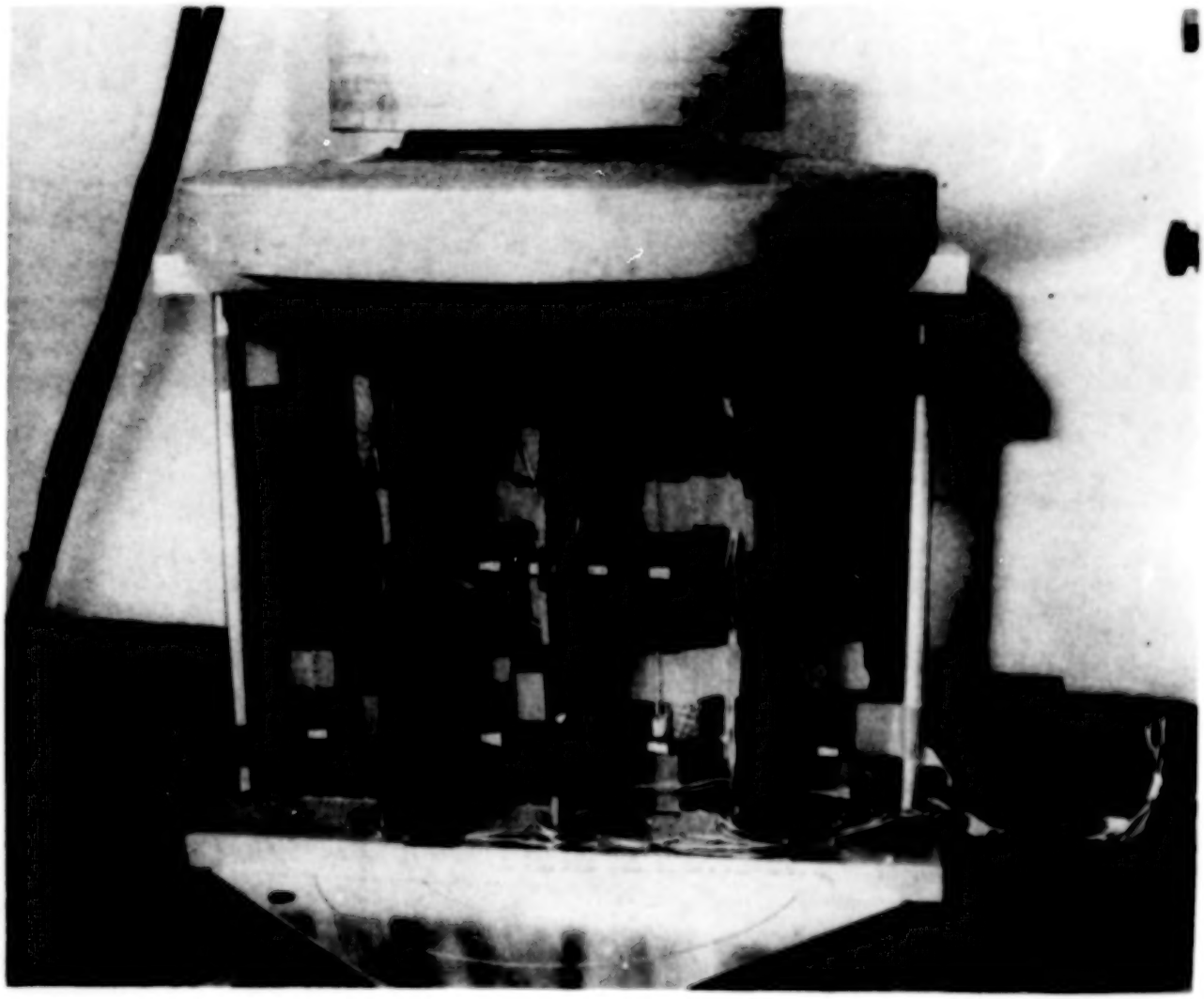

Postbuckling Behavior of Blade-Stiffened Panel at 67,750 Lbs

The crippling load of the stiffened panel was 67,750 pounds. The failed specimen is shown after being removed from the test rig. Note the severe crimping of the skin and the extensive delamination of the left blade. The postbuckling forces of the outer skin panels also severely bent the steel split tubes.

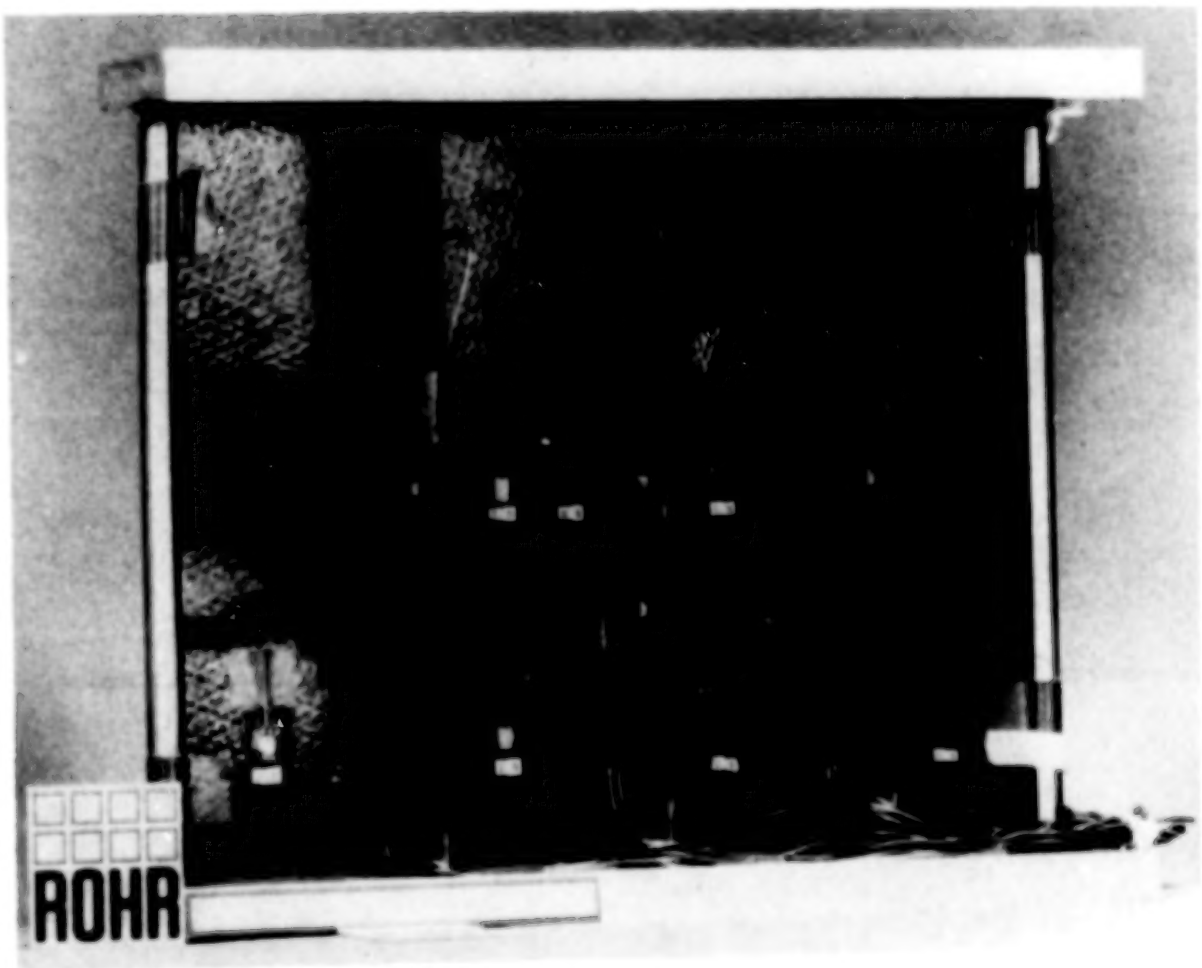

Stability Analysis Boundary Conditions

For completeness, buckling and crippling predictions were obtained for two boundary condition configurations. Configuration A represents simply supported boundary conditions. Configuration B represents boundary restraint between simply supported and fully fixed. The results are presented in the following table.

Configuration A		Configuration B	
Skin	Both Edges Simply Supported	Skin	Both Edges Fixed
Blade	One Edge Simply Supported One Edge Free	Blade	One Edge Simply Supported/Fixed One Edge Free
Flange	One Edge Simply Supported One Edge Free	Flange	One Edge Simply Supported One Edge Free

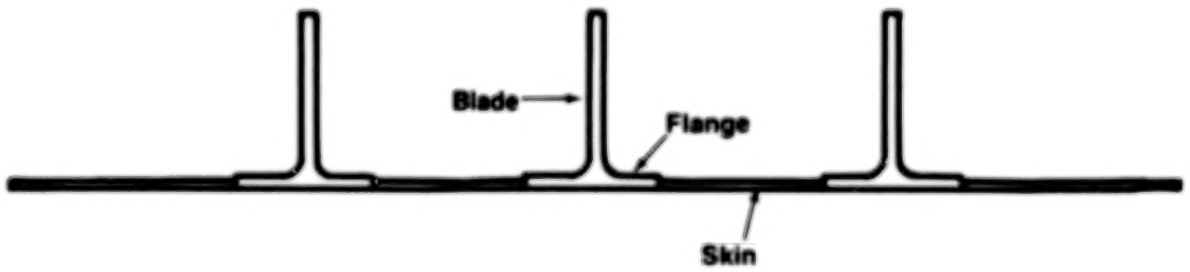

A Comparison of Test and Analysis Results

This table shows the comparisons between test and analysis for the configurations just defined. The analysis is conservative for both configurations. However, Configuration B provides much closer agreement between test and analysis for both buckling and crippling. The predicted buckling strength is about 12% conservative and the predicted crippling load is about 17% conservative.

In conclusion, a test to failure of a blade-stiffened carbon/epoxy stiffened panel has been presented. Axial strain gauges were employed to verify uniformity of axial strain prior to any local buckling. In addition, back-to-back axial strain gauges were used for detection of initial buckling and postbuckling behavior of the skins, blades, and flanges. The stiffened panel behaved as designed. The skins buckled first, the blades second, and the flanges last. In the analysis, it was assumed that crippling of a blade occurred first, where initial failure would be at the supported edge, the location of maximum compressive stress. A videotape of the test was made, and it appeared that failure did indeed start at one of the blade/skin intersections.

	Test Result	Analysis			
		Configuration A		Configuration B	
Stability Mode	Load (Lb.)	Load (Lb.)	Difference (%)	Load (Lb.)	Difference (%)
Buckling	≈23,000	12,600	45	20,200	12
Crippling	67,750	41,000	39	56,300	17

Symbols and Abbreviations

A_i^u	area of element "i", type "u"
b	blade
b/t	width over thickness ratio
b_i^b	Height of blade element "i"
b_i^f	width of flange element "i"
b_i^{sk}	width of skin element "i"
C	end-fixity coefficient of column: approximately equal to 3.6 for potted end columns in a test machine
Ca	correction factor for edge support of blade and stiffener
D_{ij}	flexural/twisting stiffness terms of laminated plate
$E_{Th,i}^{c,u}$	in-plane compression modulus of element "i", type "u"
F^{cc}	crippling stress (psi)
$F_{*,i}^{cc,u}$	expected crippling stress of element "i", type "u"
F^{cr}	buckling stress (psi)
F_{cl}^{cr}	classical buckling stress (psi)
$F_{cl,i}^{cr,sk}$	classical buckling stress of skin element "i"
$F_{*,i}^{cr,u}$	expected buckling stress of element "i", type "u"
$F_{cl,i,ss}^{cr,u,\phi E}$	classical buckling strength of a long plate type "u", element "i" with simply supported unloaded edges

Symbols and Abbreviations

$F_{cl,i,fx}^{cr,u,\phi E}$	classical buckling strength of a long plate type "u", element "i" with fixed unloaded edges
$F_{cl,i,ss}^{cr,u,1E}$	classical buckling strength of a long plate type "u", element "i" with one simply suppported unloaded edge
F^{cu}	ultimate compression strength (psi)
$F_{n\ ,i}^{cu,u}$	ultimate compression strength of element "i", type "u", and data type "n"
i	element number (i.e., each stiffener has 1 blade, 2 flanges and 2 skins)
L	column length
L'	effective column length ($L' = L \div \sqrt{C}$)
n	data type (i.e., empirical "Em", classical "cl", or theoretical)
$P_{\ ,i}^{c,es}$	compression load in effective skin element "i"
P^{cc}	crippling load (lbs)
$P_{\bullet\ ,i}^{cc,b}$	expected crippling load of blade element "i"
$P_{\bullet\ ,i}^{cc,f}$	expected crippling load of flange element "i"
$P_{\bullet,i}^{cc,ses}$	expected crippling load of stiffener/effective skin element "i"
P^{cr}	buckling load (lbs)
t	thickness (inch)
t_i^{sk}	thickness of skin element "i"
u	element type (i.e., blade "b", flange "f", stringer "st", skin "sk", effective skin "es", stiffener/skin "sts", stiffener/effective skin "ses", panel "p")

Symbols and Abbreviations

w_i^{es}	effective width of skin element "i"
$\hat{w}_i^{es}$	effective width of skin element "i" excluding the width of the adjacent stiffener flange
$\epsilon_*^{cr,st}$	expected buckling strain of stiffener element "i"
$\sigma_{,i}^{c,es}$	compression stress of effective skin element "i"

REFERENCES

1. Spier, E.E., "Stability of graphite/epoxy Structures with Arbitrary Symmetrical Laminates", "Experimental Mechanics", Vol. 18, No. 11, November 1978, pp 255-271.

2. Spier, E.E., and Klouman, F.L., "Empirical Crippling Analysis of graphite/epoxy Laminated Plates", Composite Materials: Testing and Design (4th Conference), ASTM STP 617, 1977, pp 255-271.

3. Spier, E.E., "On Experimental Versus Theoretical Incipient Buckling of Narrow graphite/epoxy Plates in Compression", AIAA-80-0686-paper, published in "Proceedings of AIAA/ASME/AHS 21st Structures, Structural Dynamics and Materials Conference, May 12-14, 1980, pp 187-193.

4. Spier, E.E., and Klouman, F.L., "Ultimate Compressive Strength and Nonlinear Stress-Strain Curves of graphite/epoxy laminates", Proceedings 8th National SAMPE Conference, "Bicentennial of Materials Progress - Part II", Seattle, Washington, October 1976, pp 213-223.

5. Spier, E.E., and Klouman, F.L., "Postbuckling Behavior of graphite/epoxy Laminated Plates and Channels", Army Symposium on Solid Mechanics, Composite Materials: The Influence of Mechanics of Failure on Design, Cape Cod, Mass., September 1976, pp 62-78.

6. Spier, E.E., "Local Buckling, Postbuckling, and Crippling Behavior of graphite/epoxy Short Thin Walled Compression Member", NASC-N100019-80-c-0174, July 1981.

7. Almroth, B.O., et al, Structural Analysis of Generals Shells, User Instructions for STAGSC, Vol. III, Report No. LMSC D502277, Lockheed Structural Mechanics Laboratory, Lockheed Palo Alto Research Laboratory, Palo Alto, California, December 1975.

8. Arnold, R.R., and Mayers, J., "Buckling, Postbuckling, and Crippling of Materially Nonlinear Laminated Composite Plates", International Journal of Solids and Structures, Vol. 20, No. 9/10, 1984, pp 863-880.

9. von Karman, Th., Sechler, E., and Donnell, L., "The Strength of Thin Plates in Compression", Trans. ASME, Volume 54, Number 2, June 30, 1932.

REPEATED BUCKLING OF COMPOSITE SHEAR PANELS

Josef Singer* and Tanchum Weller**
Faculty of Aerospace Engineering
Technion - Israel Institute of Technology
Haifa 32000, Israel.

---

*L. Shirley Tark Professor of Aircraft Structures, Fellow AIAA
**Associate Professor, Member AIAA

REPEATED BUCKLING OF COMPOSITE SHEAR PANELS

SUMMARY

Failures in service of aerospace structures and research at the Technion Aircraft Structures Laboratory have revealed that repeatedly buckled stiffened shear panels might be susceptible to premature fatigue failures. Extensive experimental and analytical studies have been performed at Technion on repeated buckling, far in excess of initial buckling, for both metal and composite shear panels with focus on the influence of the surrounding structure (see for example Refs. 1 and 2).

The core of the experimental investigation consisted of repeated buckling and postbuckling tests on "Wagner beams" in a three-point loading system under realistic test conditions. The effects of varying sizes of stiffeners, of the magnitude of initial buckling loads, of the panel aspect ratio and of the cyclic shearing force, V_{cyc}, were studied. The cyclic to critical shear buckling ratios, (V_{cyc}/V_{cr}) were on the high side, as needed for efficient panel design, yet all within possible flight envelopes. The experiments were supplemented by analytical and numerical analyses.

For the metal shear panels the test and numerical results were synthesized in Ref. 2 into prediction formulas, which relate the life of the metal shear panels to two cyclic load parameters: the (working/buckling) load ratio, (V_{cyc}/V_{cr}), and the (ultimate/working) load ratio, (V_{ult}/V_{cyc}), which reflects the working load level in the flight envelope, and one geometrical parameter: the (plate/stiffener) stiffness ratio, (b^3t/I_f). It was also found there that the level of shear load, at which local yielding first takes place, V_y dominates the endurance of the panel, and hence the life predictions could be expressed in a simpler manner, in terms of a single load ratio (V_{cyc}/V_y).

The composite shear panels studied were hybrid beams with Graphite/Epoxy webs bonded to aluminum alloy frames (see Fig. 1). The test results (see Refs. 3 and 4)* demonstrated that composite panels were less fatigue sensitive than comparable metal ones, and that repeated buckling, even when causing extensive damage, did not reduce the residual strength by more than 20 percent. All the composite panels sustained the specified fatigue life of 250,000 cycles. The extent of damage depended on the working load level V_{cyc}, but no matter how pronounced it was it did not affect the fatigue life and did not result in immediate catastrophic failure (see Fig. 2 for damages in a typical test).

*See reference list.

The effect of local unstiffened holes on the durability of repeatedly buckled shear panels was studied for one series of the metal panels (see Ref. 5). Tests on 2024 T3 aluminum panels with relatively small unstiffened holes in the center of the panels demonstrated premature fatigue failure, compared to panels without holes. Even very small holes (of 3 mm diameter and less) caused very significant reductions in fatigue life, already at a relatively low load level, for which no fatigue failure is predicted in the case of similar unperforated panels. The holes caused a shift in the mode of the fatigue failure, initiating now instead of in the corners of the shear web in its center (see Fig. 3). Holes with initially introduced cracks were compared with smooth ones, the former exhibiting more pronounced life degradation, especially for the smaller holes.

Preliminary tests on two graphite epoxy shear panels with small holes in the center showed no similar fatigue life degradation and no shift in failure mode (see Fig. 4). Further tests on the effect of holes are in progress.

REFERENCES

1. Ari-Gur, J., Singer, J. and Libai, A., "Repeated Buckling Tests of Stiffened Thin Shear Panels", Israel Journal of Technology, Vol. 20, 1982, pp. 220-231.
2. Weller, T., Kollet, M., Libai, A. and Singer, J., "Durability Under Repeated Buckling of Stiffened Shear Panels", *ICAS 1984, Proceedings of the 14th Congress of the International Council of the Aeronautical Sciences*, Laschka, B. and Staufenbiel, R., Eds., International Council of the Aeronautical Sciences, Toulouse, France, Sept. 1984, pp. 932-942; Synoptic in J. of Aircraft, Vol. 24, No. 1, 1987, pp. 6-7.
3. Weller, T., Messer, G. and Libai, A., "Repeated Buckling of Graphite Epoxy Shear Panels With Bonded Metal Stiffeners", TAE Report No. 546, Department of Aeronautical Engineering, Technion - Israel Institute of Technology, Haifa, Israel, 1984.
*4. Weller, T. and Singer, J., "Durability of Stiffened Composite Panels Under Repeated Buckling", (to be published in International Journal of Solids and Structures - Babcock Memorial Issue).
5. Weller, T., "Effect of Local Unstiffened Holes on the Durability of Shear Panels Subjected to Repeated Buckling", *Fatigue Life Analysis and Prediction*, Goel, V.S., Ed., American Society of Metals, 1985.

*Not available at time of publication.

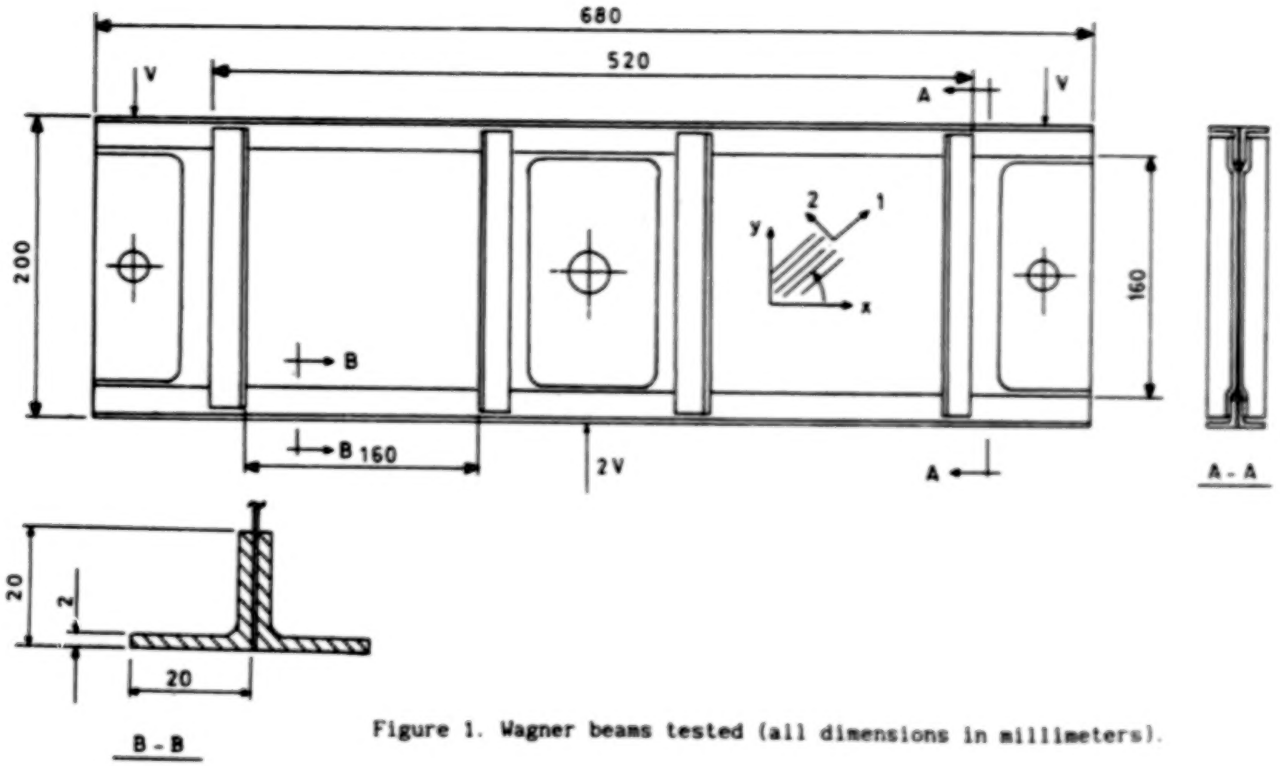

B - B

Figure 1. Wagner beams tested (all dimensions in millimeters).

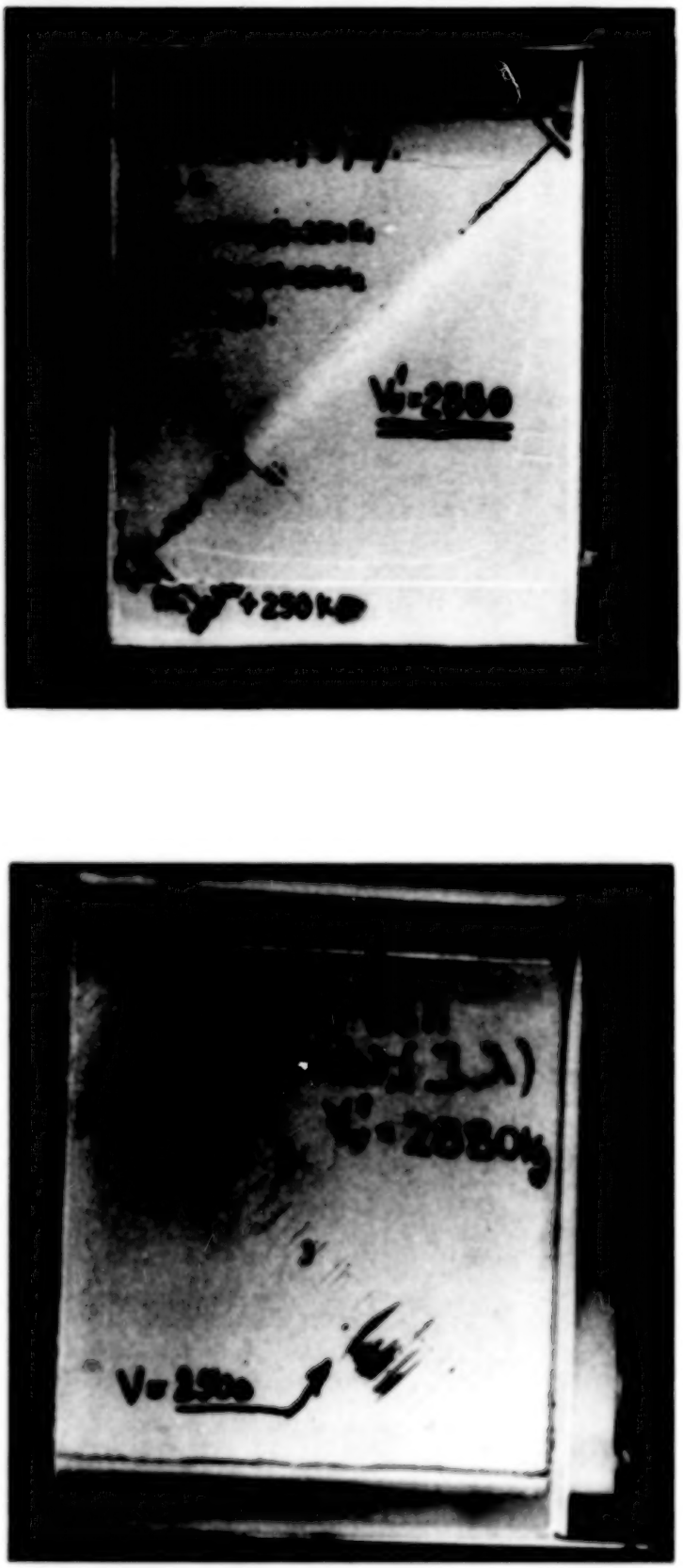

Figure 2. Typical failure mode of a graphite/epoxy panel (HWB 6A), dynamically loaded through two complete "fatigue lives" of 250,000 cycles each, and then tested statically from (Weller & Singer, 1990).

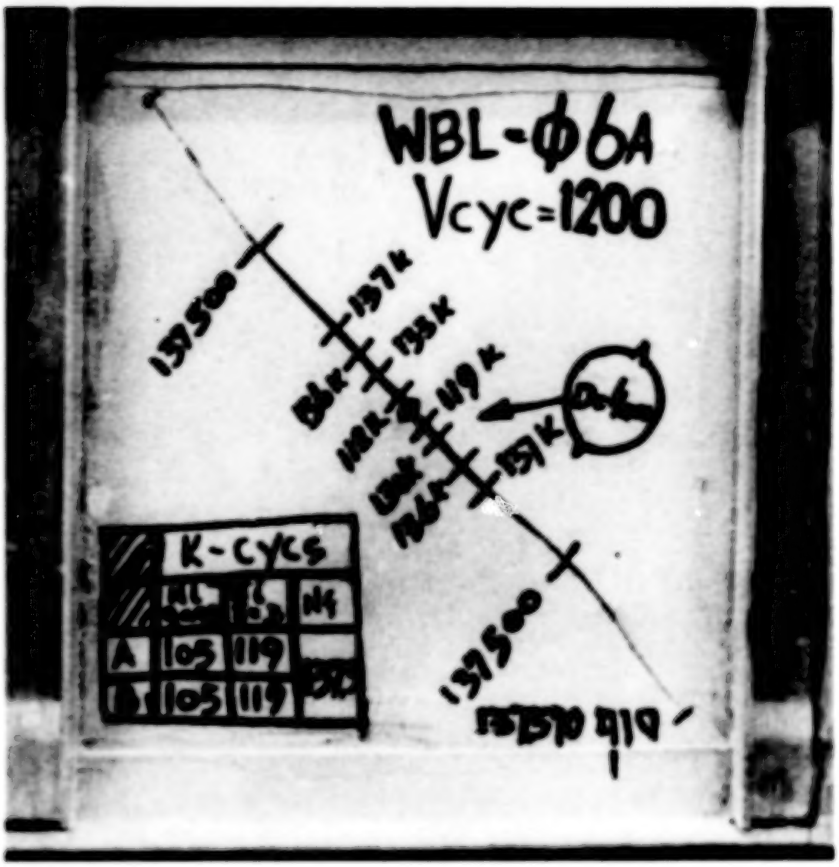

Figure 3. Fatigue failure of 2024 T3 aluminum alloy shear panel, with a central hole of 4 mm diameter (WBL 6A), after 137500 cycles at V_{cyc}=1200 kg. The failure occurs as a crack perpendicular to the tension diagonal initiating at the hole (two initial cracks made matters worse here).

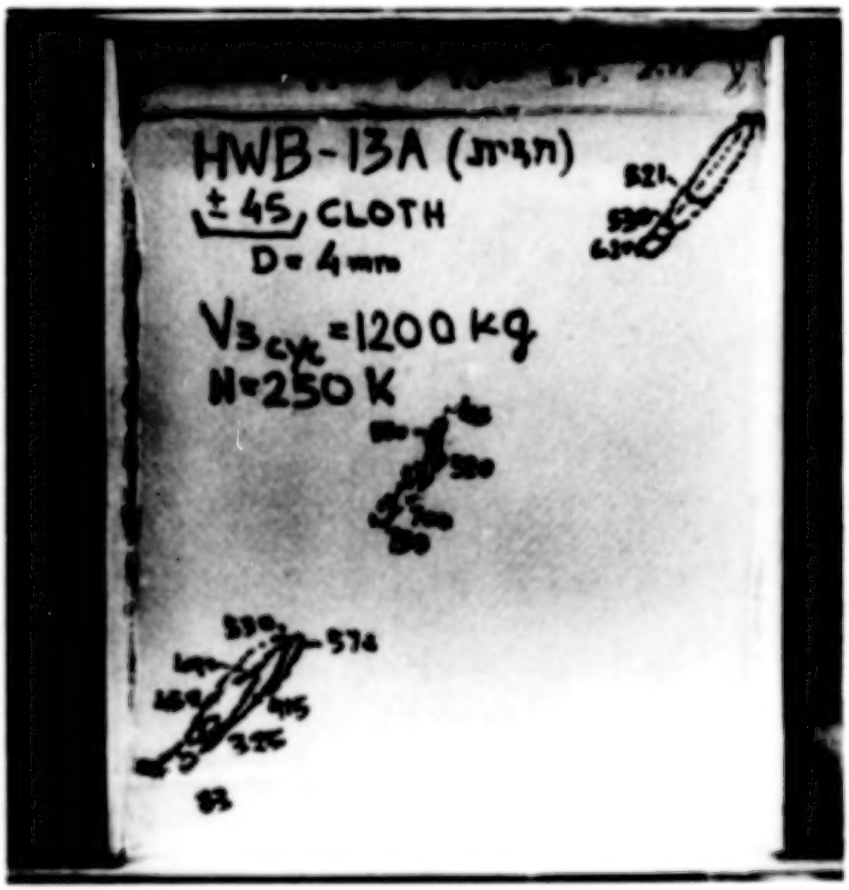

Figure 4. Fatigue failure of a graphite/epoxy shear panel (HWB 13A), with a central hole of 4 mm diameter, after 250,000 cycles at V_{cyc}=1200 kg. The failure occurs as cracks along the tension diagonal, emanating from the stress concentrations at the corners, as in unperforated shear panels.

COMPRESSIVE FAILURE OF THICK-SECTION COMPOSITE LAMINATES WITH AND WITHOUT CUTOUTS SUBJECTED TO BIAXIAL LOADING

L. Rouxel* and S. S. Wang**
National Center for Composite Materials Research
College of Engineering
University of Illinois at Urbana-Champaign
Urbana, Illinois 61801

---

* Graduate Research Assistant
** Professor and Director

Coordinates and geometry of a composite laminate with a central circular cutout under compressive loading

The composites studied are fiber-composite laminate plates made of carbon fibers and a thermoplastic-matrix material. The elastic properties of the lamina are: E_{11} = 15.6 x 10^6 (psi), E_{22} = 0.9 x 10^6 (psi), ν_{12} = 0.313, G_{12} = G_{13} = 0.77 x 10^6 (psi), and G_{23} = 0.31 x 10^6 (psi). The plates have a square geometry with a length of 12 (in), a cutout diameter of 2 (in) and a constant lamina thickness of 0.005 (in). A $[0/90/\pm45]_{ns}$ layup is considered. Biaxial loading is applied in the form of uniform displacements along the edges of the laminates.

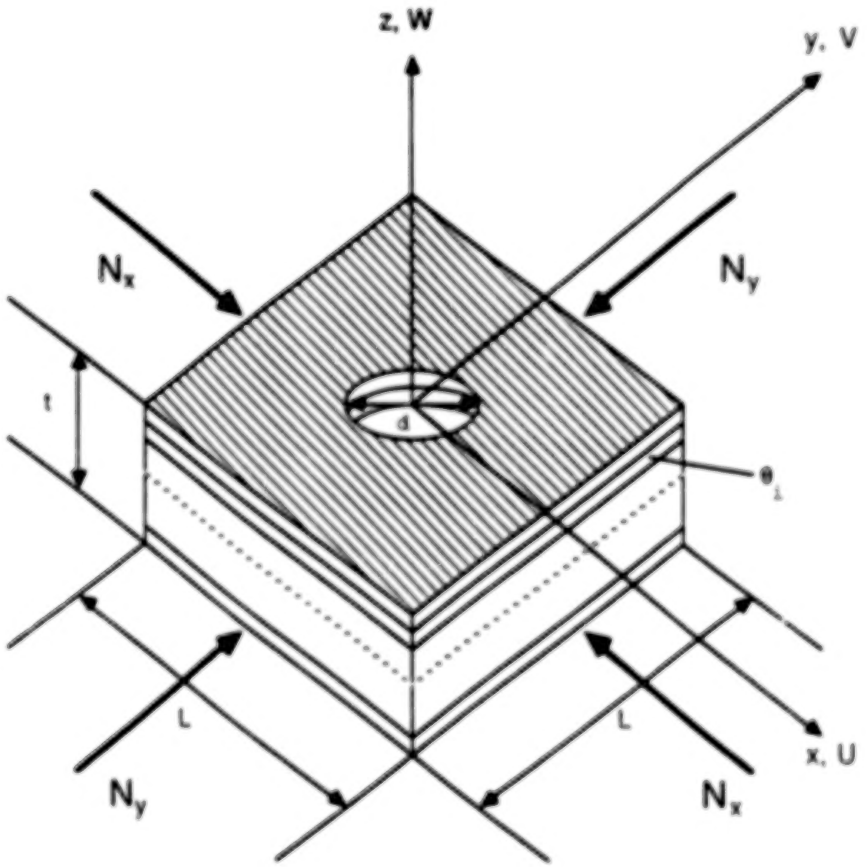

Solution convergence for transverse shear Q_x at (-3.,-3.) (in) in a clamped $[0/90/\pm45]_{12s}$ plate without cutout under biaxial compression (N_x/N_y = 2, t/L = 0.04)

The transverse shear force Q_x is the resultant of τ_{xz} integrated over the laminate thickness. Q_x is interpolated at (-3.,-3.) (in) from the values at the four Gaussian points of the element containing this location (using a bilinear interpolation). Three finite-element meshes are considered.

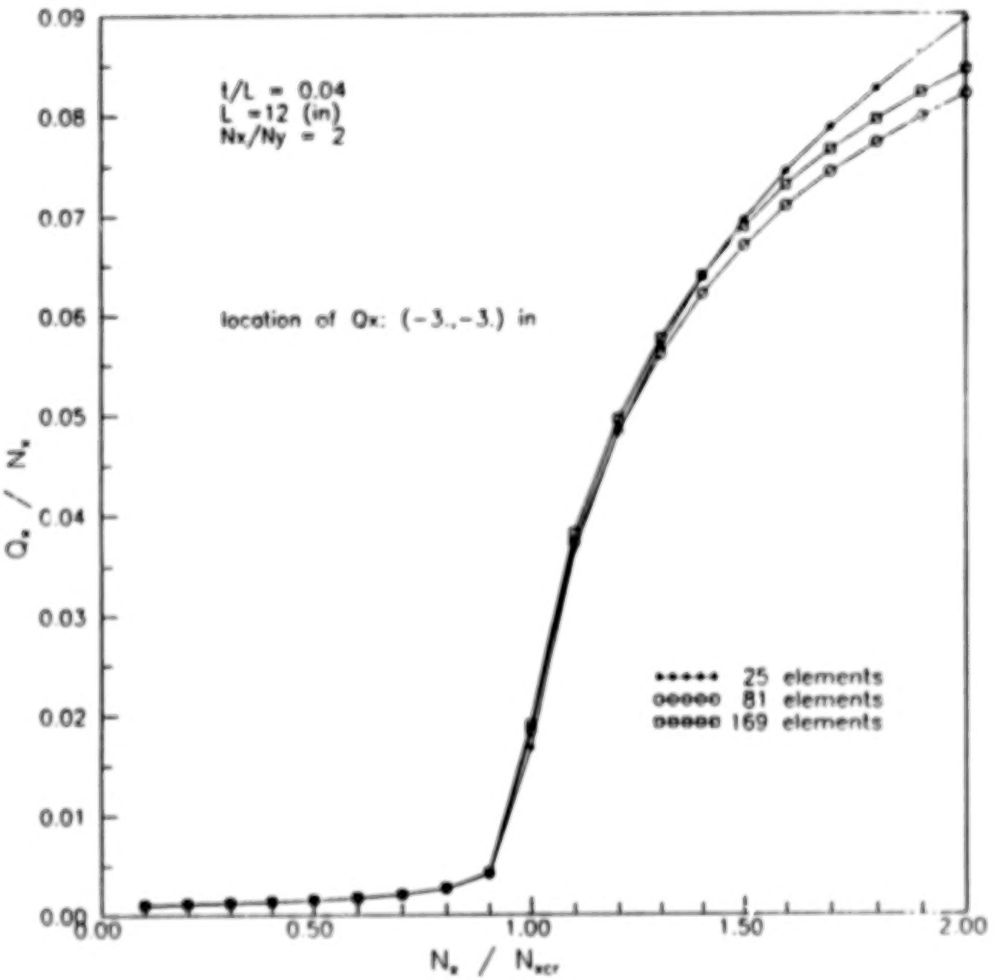

Effects of cutout and laminate thickness on maximum shear Q_x in buckling and postbuckling response of a clamped $[0/90/\pm45]_{ns}$ plate under biaxial compression

Without cutout, $|Q_{x\ max}|$ is located at (±3.3,0.) for t/L = 0.02 and t/L = 0.04, and also for t/L = 0.06 and t/L = 0.08 before activation of higher (i.e., second and third lowest) modes takes place for these two thickness/length ratios (beyond $N_x = 1.7\ N_{xcr}$ and $N_x = 1.5\ N_{xcr}$, respectively). After activation of higher modes, the location is at (±6.,±4.7) for t/L = 0.06 and t/L =0.08.

With cutout, $|Q_{x\ max}|$ is located at (±3.5,±1.8) for t/L = 0.02 and t/L = 0.04, and for t/L = 0.06 before activation of higher modes ($N_x < 1.7\ N_{xcr}$). However, for t/L = 0.08, $|Q_{x\ max}|$ is located at the hole free edge at (0.38,±0.92) before activation of higher modes. After activation of higher modes for t/L = 0.06 and t/L =0.08, the location is at (±6.,±4.7).

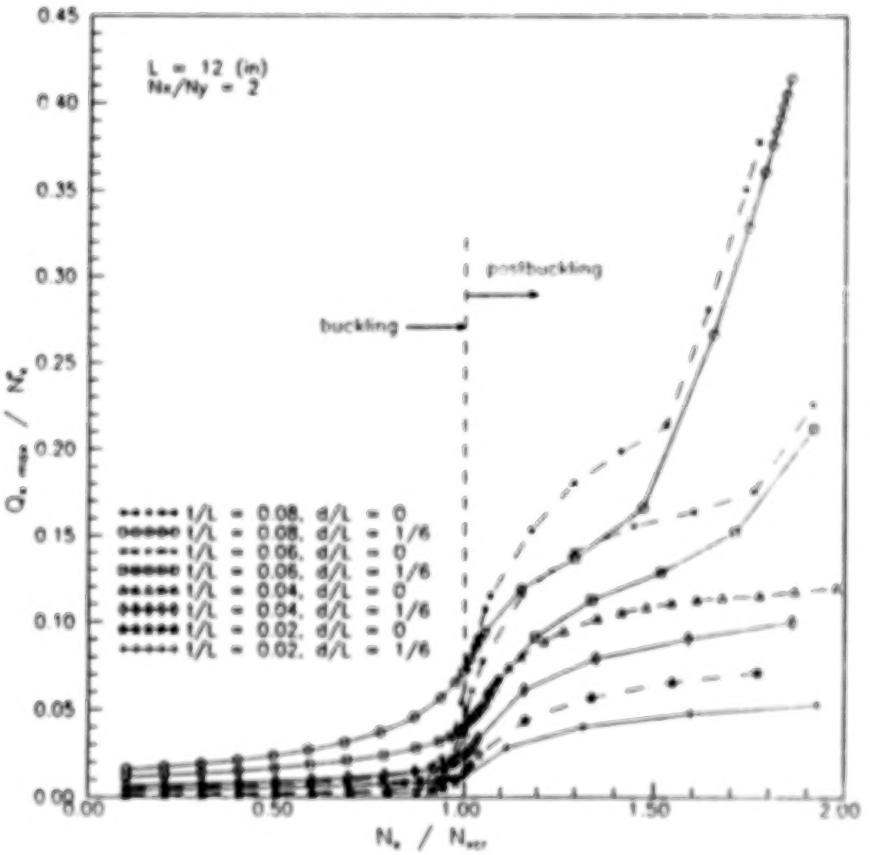

Effects of cutout and laminate thickness on maximum shear Q_y in buckling and postbuckling response of a clamped $[0/90/\pm45]_{ns}$ plate under biaxial compression

Without cutout, $|Q_{y\ max}|$ is located at (0.,±6.) for t/L = 0.02 and t/L = 0.04, and also for t/L = 0.06 and t/L = 0.08 before activation of higher modes takes place (beyond $N_x = 1.7\ N_{xcr}$ and $N_x = 1.5\ N_{xcr}$, respectively). After activation of higher modes, the location is at (0.,±4.7) for t/L = 0.06 and t/L =0.08.

With cutout, $|Q_{y\ max}|$ is located at (0.,±6.) for all four thickness/length ratios considered. Activation of higher modes for t/L = 0.06 and t/L = 0.08 does not change the location of $|Q_{y\ max}|$.

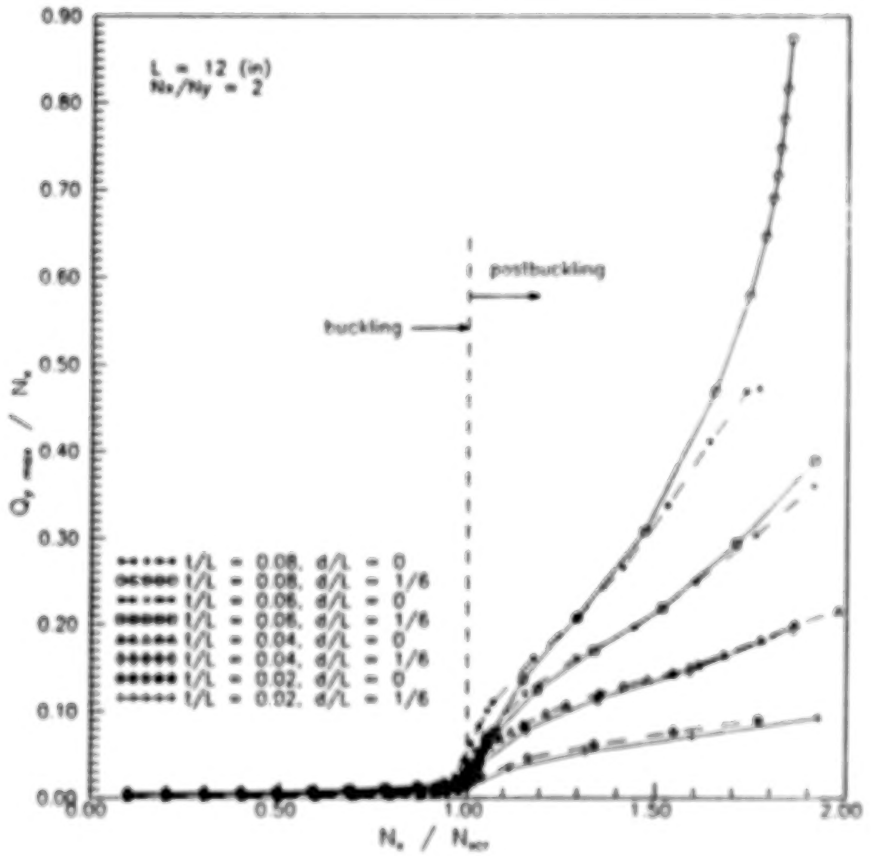

Effect of mesh refinement on buckling and postbuckling solution convergence for a clamped plate $[0/90/\pm45]_{24s}$ without cutout under biaxial compression (N_x/N_y = 2, t/L = 0.08)

For this thick laminate, activation of second and third lowest eigenmodes takes place beyond $N_x = 1.5\ N_{xcr}$ but no change in buckling mode occurs as the structure gradually loses its stiffness and becomes unstable.

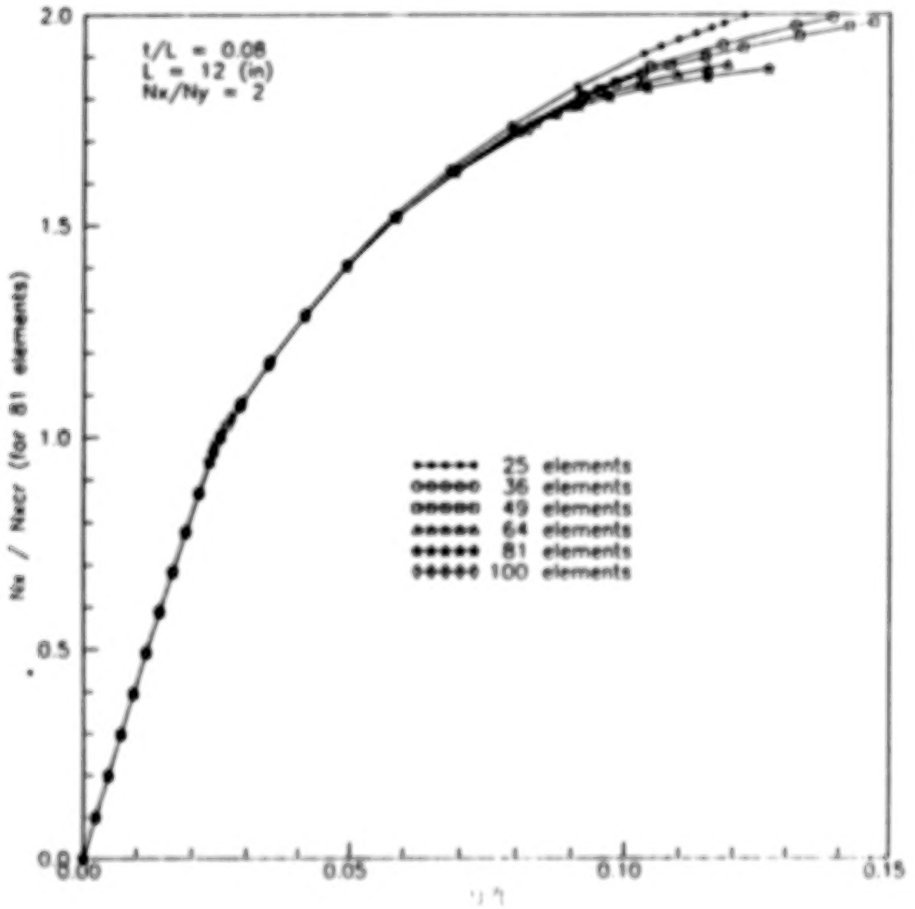

Effects of cutout and laminate thickness of lowest three eigenvalues of a clamped $[0/90/\pm45]_{ns}$ plate under biaxial compression ($N_x/N_y = 2$)

The eigenvalue parameter ($\lambda N_{x_0} L_2 / D_{22}$) is defined in such form that the lowest eigenvalue would have the same value for all thickness/length ratios if transverse shear was not present. This parameter is plotted with respect to the thickness/length ratio.

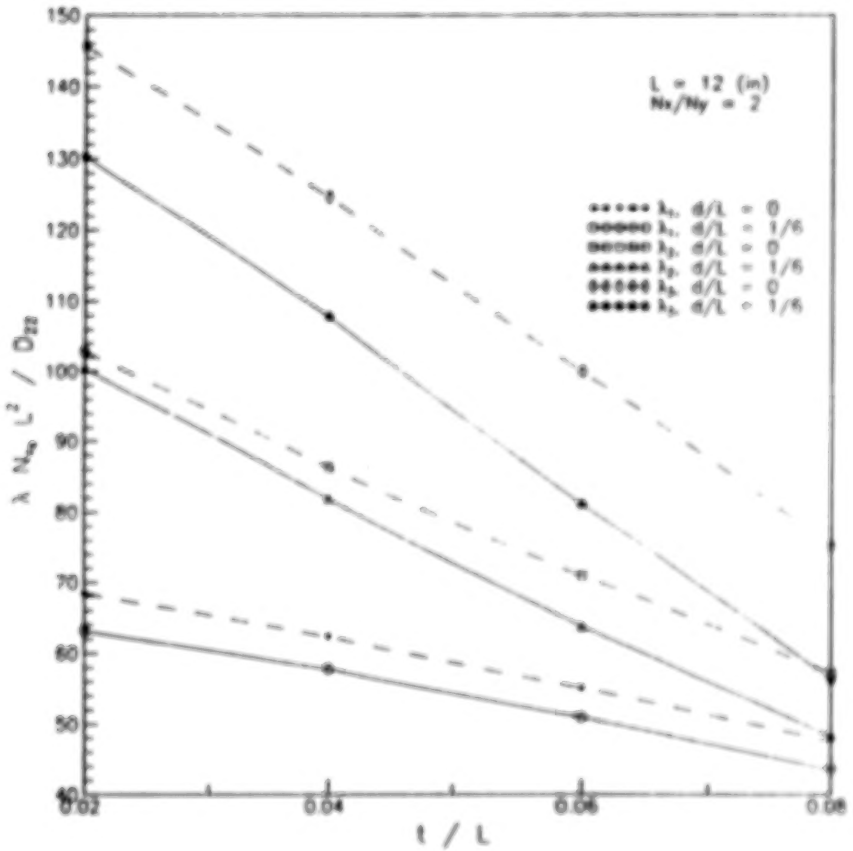

Effects of cutout and laminate thickness on buckling and postbuckling response of a clamped $[0/90/\pm45]_{ns}$ plate under biaxial compression ($N_x/N_y = 2$)

The load parameter ($N_x L^2 / D_{22}$) is defined in such form that buckling would occur at the same value for all thickness/length ratios if transverse shear was not present. Likewise, the strain parameter $U L / t^2$ is such that all load/end-shortening curves for the cases with cutout and for the cases without cutout are identical prior to buckling, respectively.

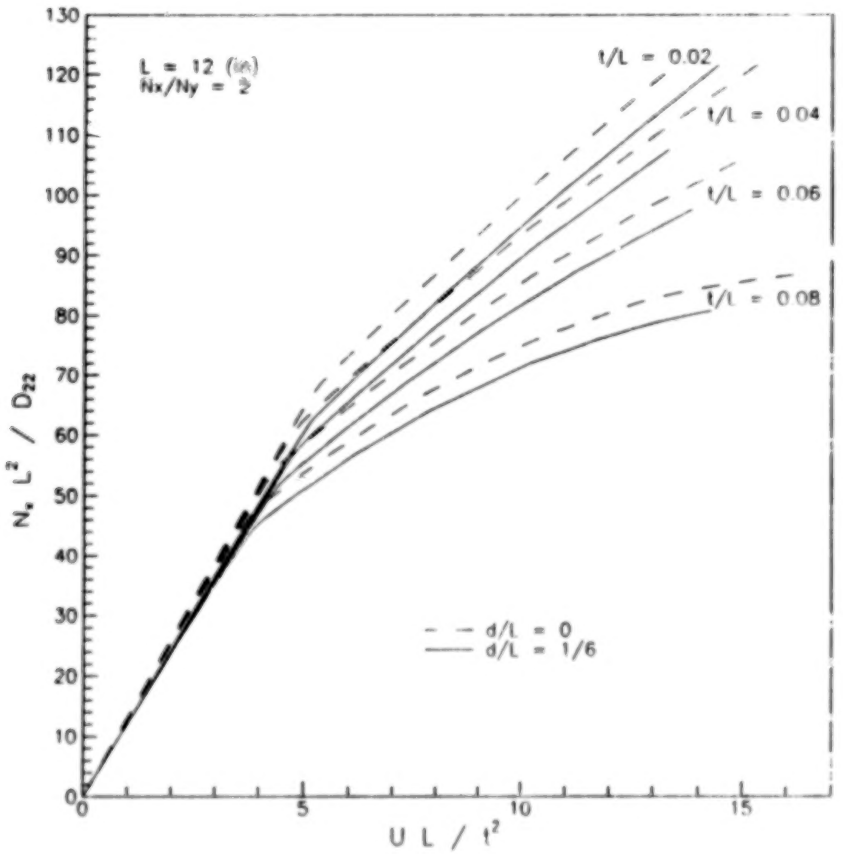

Effect of imperfection sensitivity on transverse shear Q_x at (-3.,-3.) (in) in a clamped $[0/90/\pm45]_{12s}$ plate without cutout under biaxial compression (N_x/N_y = 2, t/L = 0.04)

Three imperfection magnitudes (with respect to the laminate thickness) are considered: 0.1%, 1% and 10%. The imperfections are made of a linear combination of the normalized three lowest eigenmodes. The resulting imperfection geometry is close to the first eigenmode (buckling mode).

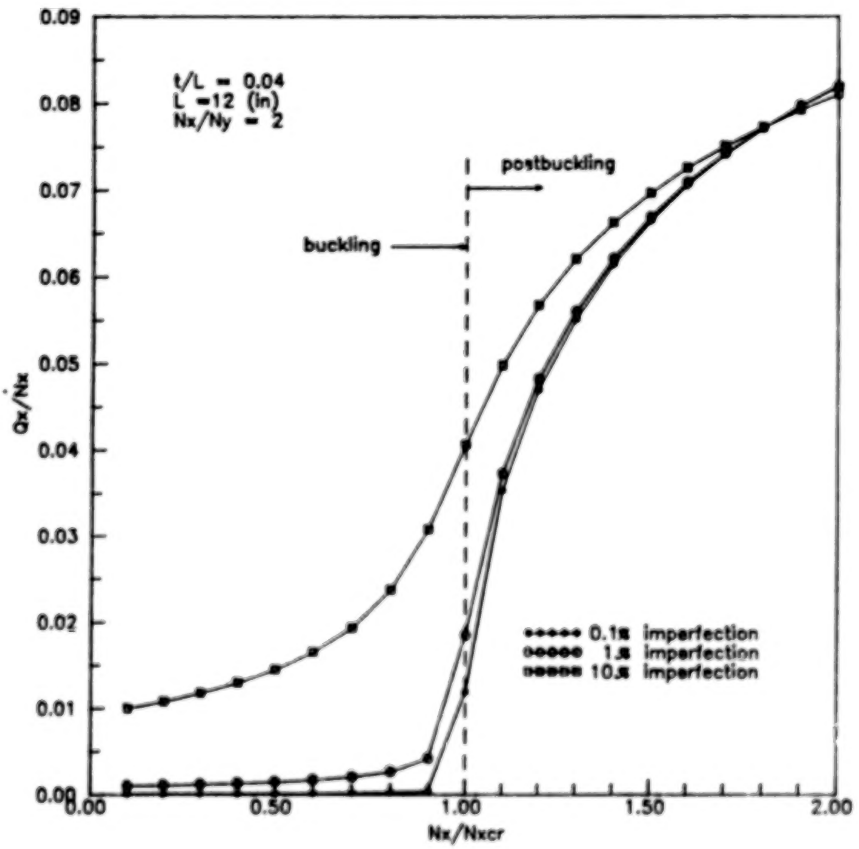

Effect of imperfection sensitivity on buckling and postbuckling response (with a change in buckling mode) of a clamped $[0/90/\pm45]_{12s}$ plate without cutout under uniaxial compression ($N_y = 0$, $t/L = 0.04$)

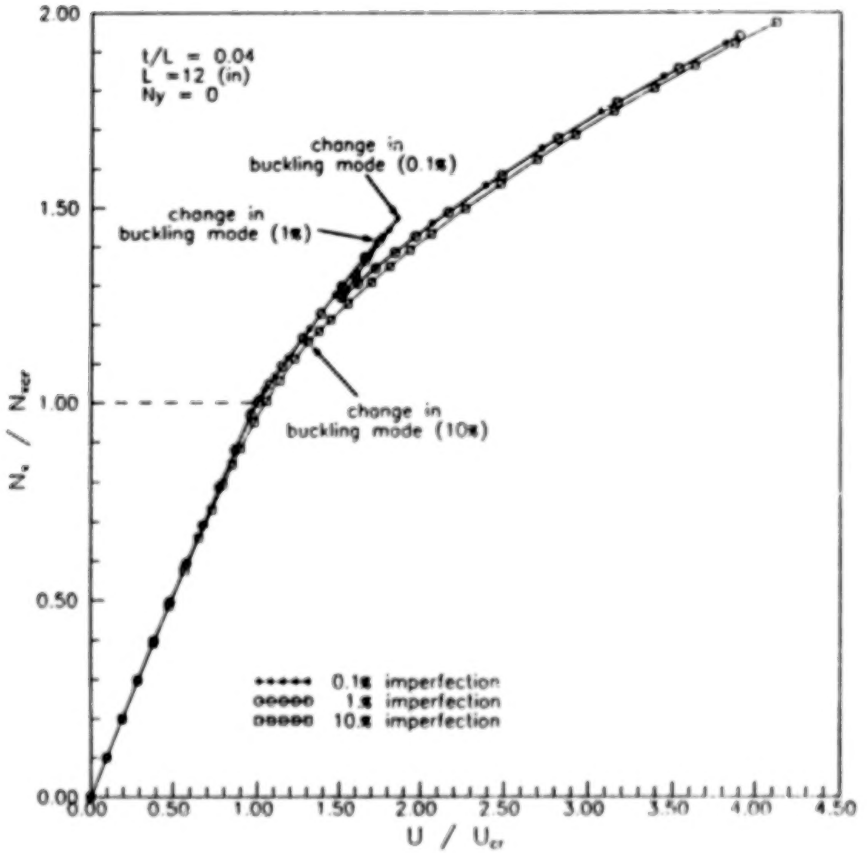

Effects of boundary conditions and stress-biaxiality ratio on maximum transverse shear Q_x in a clamped $[0/90/\pm45]_{12s}$ laminate without cutout (t/L = 0.04)

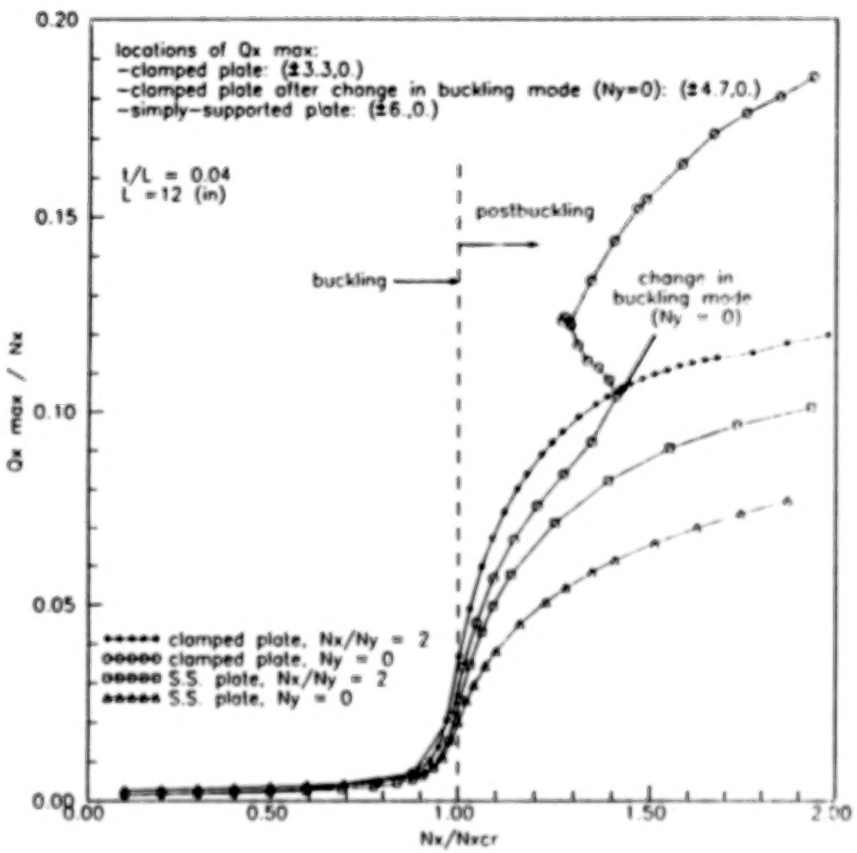

Effects of boundary conditions and stress-biaxiality ratio on maximum transverse shear Q_y in a clamped $[0/90/\pm45]_{12s}$ laminate without cutout (t/L = 0.04)

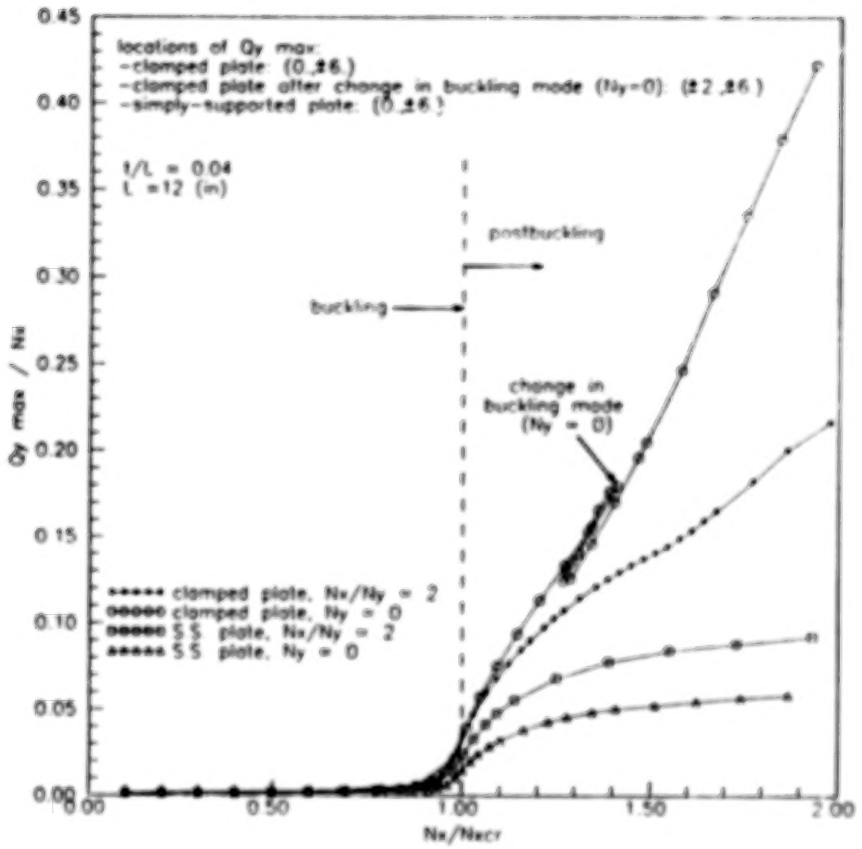

AN ANALYTICAL SOLUTION FOR THE ELASTOPLASTIC RESPONSE OF A CONTINUOUS FIBER COMPOSITE UNDER UNIAXIAL LOADING

Jong-Won Lee, Research Assistant
David H. Allen, Professor

Aerospace Engineering Department
Texas A&M University
College Station, Texas 77843

ABSTRACT

A continuous fiber composite is modelled by a two-element composite cylinder in order to predict the elastoplastic response of the composite under a monotonically increasing tensile loading parallel to fibers. The fibers and matrix are assumed to be elastic-perfectly plastic materials obeying Hill's and Tresca's yield criteria, respectively. The present paper investigates the composite behavior when the fibers yield prior to the matrix.

INTRODUCTION

The elastoplastic response of fibrous composites has been the subject of a number of theoretical studies[1-4]. When a composite is subjected to uniaxial tension loading parallel to the fibers, a two-element composite cylinder(Figure 1-a) has been frequently utilized to model the composite response. The loading direction together with the axisymmetric geometry of the representative volume element simplify the mathematical difficulties associated with the equilibrium equations. By implementing a traction-free boundary condition to the outermost surface of the representative volume element, it becomes possible to construct a well-posed boundary value problem when the fibers and the matrix are assumed to obey Hill's and Tresca's yield criteria, respectively. A closed form analytical solution requires further simplifications such as elastic-perfectly plastic constituents, perfect interfacial bonding, etc. When the composite constituents are assumed to obey the modified yield criterion proposed by Hill[1], the hardening effect of the matrix can be taken into account without mathematical difficulties. However, the present study focuses on a composite with non-hardening constituents.

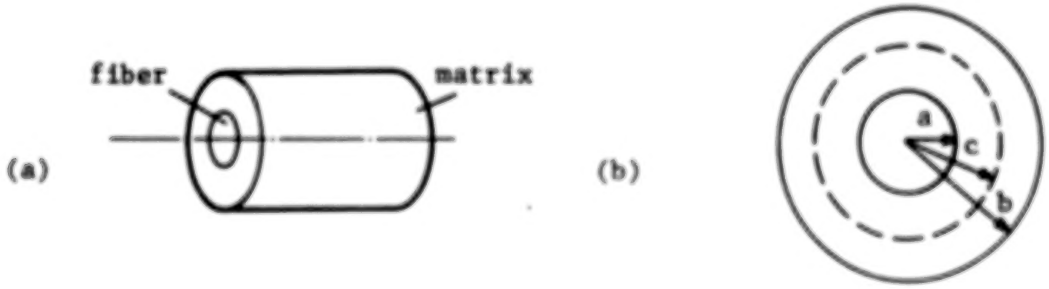

Figure 1. Continuous Fiber Composite

(a) Representative Volume Element
(b) Cross section

Hill proposed a relatively simple yield criterion which assumes the difference between the axial stress and the arithmetic mean value of the radial and circumferential stresses to be equal to the yield stress[1]. When this yield condition is implemented to a composite with elastic fibers surrounded by an elastic-perfectly plastic matrix, the entire matrix yields simultaneously, resulting in a discontinuity in the slope of the effective stress-strain curve.

Mulhern, Roger, and Spencer[2] proposed a rigorous analytical solution for a two-element composite cylinder under cyclic loading. Their study models an elastic core fiber surrounded by an elastic-perfectly plastic matrix tube obeying Tresca's yield criterion. The resulting composite behavior is almost as bilinear as Hill's solution. However, the slope of the effective stress-strain curve is continuous because the plastically deformed matrix zone propagates from the fiber -matrix interface to the outer surface of the matrix.

Ebert and Gadd[3] studied a similar problem for an elastic-perfectly plastic core fiber surrounded by elastic matrix. Ebert, et al.[4] extended this to an elastic-perfectly plastic matrix. However, the application of their numerical solution is restricted to a composite in which the Poisson's ratios of the fiber and the matrix are equivalent.

The present paper extends the study of Ebert and other authors[3,4] to a two-element composite cylinder representing a transversely isotropic fiber surrounded by an isotropic matrix in which the Poisson's ratios of the core fiber and the matrix need not be identical.

MODEL FORMULATION

Consider a metal matrix composite reinforced by continuous fibers under uniaxial tension loading parallel to the fibers. The globally averaged stress state of the representative volume element is assumed to be one dimensional. The elastic-plastic response of the bar can be analytically predicted by solving an equivalent boundary value problem of a single core fiber which is perfectly bonded to the surrounding matrix tube. The volume element representing the equivalent boundary value problem is illustrated in Figure 1. The uniaxial tension loading in the fiber direction produces a three dimensional stress state in both the core fiber and the surrounding matrix. When the tension loading increases monotonically, either the fiber or matrix yields at a certain magnitude of the applied tension loading. Further increment of the tension loading induces the yielding everywhere in the composite. The possible yield sequences for the composite constituents of the representative volume element can be categorized into three cases as shown in Figure 2. The present study provides analytical solutions to the first case under monotonically increasing tension loading.

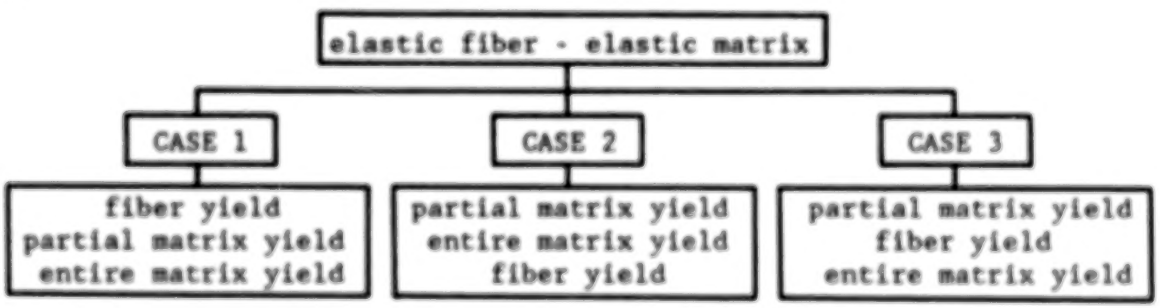

Figure 2. Possible Composite Yield Sequences

The entire mathematical formulation of the present study is based on the following key assumptions:

1. The core is assumed to be a transversely isotropic fiber surrounded by an isotropic matrix.
2. Both constituents are assumed to be elastic-perfectly plastic.
3. The interfacial bonding between the core fiber and the matrix is assumed to be perfect throughout deformation.
4. The core fiber is assumed to obey Hill's yield criterion.
5. The matrix tube is assumed to obey Tresca's yield criterion.
6. The axial strain is assumed to be spatially homogeneous.

Since the geometry of the representative volume element is axisymmetric and the loading direction is parallel to the core fiber, the only non-trivial equilibrium equation is

$$\frac{\partial \sigma_r}{\partial r} + \frac{\sigma_r - \sigma_\theta}{r} = 0 \tag{1}$$

The constitutive equations for the transversely isotropic core fiber and the isotropic matrix are

$$\begin{Bmatrix} \epsilon_r^f - \epsilon_r^p \\ \epsilon_\theta^f - \epsilon_\theta^p \\ \epsilon_z^f - \epsilon_z^p \end{Bmatrix} = \begin{bmatrix} 1/E_T & -\nu_{TT}/E_T & -\nu_{LT}/E_L \\ -\nu_{TT}/E_T & 1/E_T & -\nu_{LT}/E_L \\ -\nu_{LT}/E_L & -\nu_{LT}/E_L & 1/E_L \end{bmatrix} \begin{Bmatrix} \sigma_r^f \\ \sigma_\theta^f \\ \sigma_z^f \end{Bmatrix} \tag{2-a}$$

and

$$\begin{Bmatrix} \sigma_r^m \\ \sigma_\theta^m \\ \sigma_z^m \end{Bmatrix} = \frac{E_m}{(1+\nu_m)(1-2\nu_m)} \begin{bmatrix} 1-\nu_m & \nu_m & \nu_m \\ \nu_m & 1-\nu_m & \nu_m \\ \nu_m & \nu_m & 1-\nu_m \end{bmatrix} \begin{Bmatrix} \epsilon_r^m - \epsilon_r^p \\ \epsilon_\theta^m - \epsilon_\theta^p \\ \epsilon_z^m - \epsilon_z^p \end{Bmatrix} \tag{2-b}$$

respectively.
Since the plastic strain is incompressible,

$$\epsilon_r^p + \epsilon_\theta^p + \epsilon_z^p = 0 \tag{3}$$

It can be shown that Hill's yield criterion becomes the following yield condition for the transversely isotropic core fiber under a transversely isotropic loading:

$$| \sigma_z^f - \sigma_r^f | = | \sigma_z^f - \sigma_\theta^f | = Y_L \tag{4-a}$$

This mathematical expression is identical to Tresca's yield criterion.

The surrounding matrix will yield according to one of the following conditions.

$$| \sigma_z^m - \sigma_r^m | = Y_m \tag{4-b}$$

$$| \sigma_z^m - \sigma_\theta^m | = Y_m \tag{4-c}$$

$$| \sigma_z^m - \sigma_r^m | = | \sigma_z^m - \sigma_\theta^m | = Y_m \tag{4-d}$$

The external boundary conditions and interior compatibility are

$$\sigma_r = 0 \text{ at } r = b \tag{5-a}$$

$$\sigma_r = \text{unique at } r = a \text{ or } r = a, c \tag{5-b}$$

$$u_r = 0 \text{ at } r = 0 \tag{5-c}$$

$$u_r = \text{unique at } r = a \text{ or } r = a, c \tag{5-d}$$

When both fiber and matrix responses are elastic, the stress state and the displacement field in the representative volume element are determined by matching the radial stress and displacement at the fiber-matrix interface. The problem solving procedure for this elastic deformation is simple and straightforward as discussed below.

Since the stress state in the fiber is always transversely isotropic,

$$\sigma_r^f = \sigma_\theta^f = -P \tag{6-a}$$

$$\sigma_z^f = -2\nu_{LT}P + E_L\epsilon_z \tag{6-b}$$

where P is an unknown constant to be determined. The radial displacement in the fiber is given by

$$u_r = C_1 r \tag{7-a}$$

The strain components become

$$\epsilon_r^f = \epsilon_\theta^f = C_1 \tag{7-b}$$

From (2-a),(6), and (7-b),

$$C_1 = -[(1-\nu_{TT}-2\nu_{LT}\nu_{TL})P/E_T + \nu_{LT}\epsilon_z]r \tag{8-c}$$

Within the matrix,

$$\sigma_r^m = \frac{Pa^2}{b^2-a^2}\left[1 - \frac{b^2}{r^2}\right] \tag{9-a}$$

$$\sigma_\theta^m = \frac{Pa^2}{b^2-a^2}\left[1 + \frac{b^2}{r^2}\right] \tag{9-b}$$

$$\sigma_z^m = \frac{2P\nu_m a^2}{b^2-a^2} + E_m\epsilon_z \tag{9-c}$$

$$u_r^m = C_2 r + C_3/r \tag{10-a}$$

The strain components become

$$\epsilon_r^m = u_{r,r} = C_2 - C_3/r^2 \tag{10-b}$$

$$\epsilon_\theta^m = u_r/r = C_2 + C_3/r^2 \tag{10-c}$$

From (5-a) and (5-b), C_2 and C_3 are determined as functions of P.

$$C_2 = \frac{Pa^2(1+\nu_m)(1-2\nu_m)}{E_m(b^2-a^2)} - \nu_m\epsilon_z \tag{11-a}$$

$$C_3 = \frac{Pa^2b^2(1+\nu_m)}{E_m(b^2-a^2)} \tag{11-b}$$

Then the radial displacement in the matrix becomes

$$u_r = \frac{Pa^2(1+\nu_m)}{E_m(b^2-a^2)}[(1-2\nu_m)r+b^2/r] - \nu_m\epsilon_z \tag{12}$$

The interfacial stress in the radial direction, -P, is determined from the displacement compatibility given by (5-d).

$$-P = -\frac{(\nu_m-\nu_{LT})\epsilon_z}{A_1} \tag{13-a}$$

where

$$A_1 = \left[\frac{1-\nu_{TT}-\nu_{LT}\nu_{TL}}{E_T}\right] + \left[\frac{1+\nu_m}{E_m}\right]\left[\frac{a^2(1-2\nu_m+b^2/a^2)}{b^2-a^2}\right] \tag{13-b}$$

It can be shown that the effective axial Young's modulus of the volume element is given by

$$E_c = E_L(a/b)^2 + E_m(b^2-a^2)/b^2 + 2(a/b)^2(\nu_m-\nu_{LT})^2/A_1 \tag{14}$$

Under monotonically increasing axial strain, ϵ_z , either the core fiber or the surrounding matrix yields first. The yield strains, strengths, and the Poisson's ratios of the constituents govern the composite yield sequence. When the applied axial strain reaches a certain value, ϵ_{zY}, the core fiber yields first if the

longitudinal yield strength of the fiber is much smaller than the yield strength of the matrix. The initial yield strain, ϵ_{zY}, at which the entire fiber yields is given by

$$\epsilon_{zY} = \frac{Y_L}{E_L}\left[1 - \frac{(\nu_m-\nu_{LT})(1-2\nu_{LT})}{E_L A_1 + (\nu_m-\nu_{LT})(1-2\nu_{LT})} \right] \tag{15}$$

After the core fiber yields, the surrounding matrix behaves elastically until matrix yield at the interface occurs. Since the plastic strain is incompressible and the stress state is transversely isotropic in the core fiber, stresses, total strains and plastic strains in the fiber become

$$\overset{f}{\sigma_r} = \overset{f}{\sigma_\theta} = -P, \quad \overset{f}{\sigma_z} = -P + Y_L \tag{16-a}$$

$$\overset{p}{\epsilon_r} = \overset{p}{\epsilon_\theta} = -\overset{p}{\epsilon_z}/2 \tag{16-b}$$

$$\overset{f}{\epsilon_r} = \overset{f}{\epsilon_\theta} = \overset{f}{u_{r,r}} = \overset{f}{u_r}/r \tag{16-c}$$

where -P is the unknown interfacial stress to be determined.

The first strain invariant, $\overset{f}{\epsilon_r}+\overset{f}{\epsilon_\theta}+\overset{f}{\epsilon_z}$, together with the uniqueness of the radial displacement at the material interface determine the magnitudes of the fiber stress components as functions of the applied axial strain. During this strain increment where the matrix still deforms elastically, the stress components and the radial displacement in the matrix given by equations (9-a), (9-b), and (9-c) are still valid if the interfacial stress in the radial direction is redefined as

$$P = \frac{-\eta_1\eta_2}{\eta_1+2\eta_2}\left[(1-2\nu_m)\epsilon_z-(1-2\nu_{LT})\frac{Y_L}{E_L}\right] \tag{17-a}$$

where

$$\eta_1 = \frac{E_m}{1+\nu_m}\left[\frac{(b^2-a^2)/a^2}{1-2\nu_m+(b/a)^2}\right] \tag{17-b}$$

$$\eta_2 = \frac{E_T}{2-2\nu_{TT}-4\nu_{TL}+\nu_{TL}/\nu_{LT}} \tag{17-c}$$

The radial displacement in the fiber becomes

$$\overset{f}{u_r} = -\left[\frac{\nu_m\eta_1+\eta_2}{\eta_1+2\eta_2}\right]\epsilon_z\, r + \left[\frac{(1-2\nu_{LT})\eta_2}{\eta_1+2\eta_2}\right]\frac{Y_L}{E_L}\, r \tag{18}$$

Further increase of the applied axial strain causes yielding of the matrix material. The plastically deformed region then propagates toward the outer surface of the matrix. During this strain increment, the elastically deformed mat-

rix and the plastically deformed matrix exist together as shown in Figure 1-b. Outside the interface between the plastic matrix and elastic matrix, the stress state and deformation are given by the elasticity solution with an unknown internal pressure, P^*, acting on the interfacial surface between the plastic matrix and elastic matrix. Therefore, within the elastically deformed matrix,

$$\sigma_r^m = \frac{P^* c^2}{b^2 - c^2}\left[1 - \frac{b^2}{r^2}\right] \tag{19-a}$$

$$\sigma_\theta^m = \frac{P^* c^2}{b^2 - c^2}\left[1 + \frac{b^2}{r^2}\right] \tag{19-b}$$

$$\sigma_z^m = \frac{2P^* \nu_m c^2}{b^2 - c^2} + E_m \epsilon_z \tag{19-c}$$

$$u_r^m = \frac{P^* c^2 (1+\nu_m)}{E_m (b^2 - c^2)}[(1-2\nu_m) r + b^2/r] - \nu_m \epsilon_z r \tag{20}$$

where P^* is determined from Tresca's yield criterion given below.

$$\text{At } r = c, \quad \begin{cases} |\sigma_z^m - \sigma_r^m| = Y_m \ , & \text{for } \nu_m > \nu_{LT} \quad (21\text{-a}) \\ |\sigma_z^m - \sigma_\theta^m| = Y_m \ , & \text{for } \nu_m < \nu_{LT} \quad (21\text{-b}) \end{cases}$$

Then,

$$P^* = \frac{(Y_m - E_m \epsilon_z)(b^2 - c^2)/c^2}{2\nu_m - (b^2 + c^2)/c^2} \tag{22}$$

where c is an unknown function of the applied axial strain, ϵ_z.

Within the plastically deformed matrix, Tresca's yield criterion given by eqs. (21-a) and (21-b) determines the stress state and displacement field. If the Poisson's ratio of the matrix is smaller than that of the fiber, the fiber-matrix interfacial stress in the radial direction is always tensile. On the other hand, when the Poisson's ratio of the matrix is greater than that of the fiber, the fiber-matrix interfacial stress may be either compressive or tensile. After the core fiber deforms plastically, the apparent Poisson's ratio of the fiber approaches 0.5 as the applied axial strain increases. The interfacial stress in the radial direction may be changed from compressive to tensile before the initiation of matrix yield. If the matrix yield strain is far greater than that of the core fiber, the interfacial stress in the radial direction at the onset of matrix yield becomes tensile. Then, from eq. (3) and (4-c),

$$\epsilon_r^p = 0, \quad \epsilon_\theta^p = -\epsilon_z^p \tag{23}$$

$$\sigma_\theta^m + \sigma_z^m = 2\sigma_\theta^m + Y_m = \frac{E_m}{(1+\nu_m)(1-2\nu_m)}(2\nu_m \epsilon_r^m + \epsilon_\theta^m + \epsilon_z^m) \tag{24}$$

From eq. (24) and the strain-displacement relationships, the radial and circumferential stresses are expressed in terms of the radial displacement and its gradient with respect to r.

$$\sigma_r^m = \frac{E_m}{(1+\nu_m)(1-2\nu_m)} [(1-\nu_m)u_{r,r}^m + \nu_m u_r^m/r + \nu_m \epsilon_z] \tag{25-a}$$

$$\sigma_\theta^m = \frac{E_m/2}{(1+\nu_m)(1-2\nu_m)} (2\nu_m u_{r,r}^m + u_r^m/r + \epsilon_z) - Y_m/2 \tag{25-b}$$

The equilibrium equation thus becomes

$$2(1-\nu_m)r^2 u_{r,rr}^m + 2(1-\nu_m)r u_{r,r}^m - u_r^m = -r(1-2\nu_m)[(1+\nu_m)Y_m/E_m - \epsilon_z] \tag{26}$$

The solution to the above differential equation is given by

$$u_r^m = -[(1+\nu_m)Y_m/E_m - \epsilon_z]r + C_2 r^k + C_3 r^{-k} \tag{27}$$

where

$$k = [2(1-\nu_m)]^{-1/2}$$

Since the radial stress and displacement must be single-valued at r=c and r=a, the unknown constants are determined as

$$C_2 = \frac{-(1+\nu_m)(E_m\epsilon_z - Y_m)b^2 c^{-(k+1)}}{kE_m(1-2\nu_m+b^2/c^2)} \tag{28-a}$$

$$C_3 = \frac{(1+\nu_m)(E_m\epsilon_z - Y_m)b^2 c^{(k-1)}}{kE_m(1-2\nu_m+b^2/c^2)} \tag{28-b}$$

The radius of the matrix yield front, c, can also be determined as a function of the applied axial strain, ϵ_z, and material properties. However, it is more convenient to express the applied axial strain as a function of the radius of the matrix yield front by satisfying the uniqueness of the radial displacement at the fiber-matrix interface. Until the yield front reaches the outermost surface of the matrix tube, the axial strain is given as

$$\epsilon_z = \frac{Y_m}{E_m} - \frac{(1-2\nu_m)\frac{Y_m}{E_m} - (1-2\nu_{LT})\frac{Y_L}{E_L}}{1-2\nu_m+2\phi_2(1+\nu_m)\cdot\frac{E_m\phi 1}{\eta_2(1-2\nu_m)}} \tag{29-a}$$

where

$$\phi_1 = 1 - \frac{(b/c)^2[(1-\nu_m+\nu_m/k)(a/c)^{(k-1)}+(1-\nu_m-\nu_m/k)(a/c)^{-(k+1)}]}{1 - 2\nu_m + (b/c)^2} \tag{29-b}$$

$$\phi_2 = 1 - \frac{(b/c)^2[(a/c)^{(k-1)}-(a/c)^{-(k+1)}]/k}{1 - 2\nu_m + (b/c)^2} \tag{29-c}$$

After the entire matrix yields, it can be shown that eqns. (28-a) and (28-b) should be corrected for further axial strain increment as

$$C_2 = \frac{\left[\frac{1-(1-2\eta_2/\alpha_2)(a/b)^{-(k+1)}}{1-2\nu_m} - \frac{3\eta_2}{E_m}\right](E_m\epsilon_z - Y_m) - \alpha_3}{\alpha_1 a^{(k-1)}[(1-2\eta_2/\alpha_2)(a/b)^{-2k} - (1-2\eta_2/\alpha_1)]} \tag{30-a}$$

$$C_3 = \frac{\left[\frac{1-(1-2\eta_2/\alpha_1)(a/b)^{(k-1)}}{1-2\nu_m} - \frac{3\eta_2}{E_m}\right](E_m\epsilon_z - Y_m) - \alpha_3}{\alpha_2 a^{-(k+1)}[(1-2\eta_2/\alpha_1)(a/b)^{2k} - (1-2\eta_2/\alpha_2)]} \tag{30-b}$$

$$\alpha_1 = \frac{E_m[\nu_m+(1-\nu_m)k]}{(1+\nu_m)(1-2\nu_m)} \tag{30-c}$$

$$\alpha_2 = \frac{E_m[\nu_m-(1-\nu_m)k]}{(1+\nu_m)(1-2\nu_m)} \tag{30-d}$$

$$\alpha_3 = \frac{Y_m\eta_2}{E_m}\left[1-2\nu_m-(1-2\nu_{LT})\frac{Y_L E_m}{E_L Y_m}\right] \tag{30-e}$$

Then the stress components in the matrix become:

$$\sigma_r^m = \frac{E_m\epsilon_z - Y_m}{1-2\nu_m} + \alpha_1 C_2 r^{(k-1)} + \alpha_2 C_3 r^{-(k+1)} \tag{31-a}$$

$$\sigma_\theta^m = \frac{E_m\epsilon_z - Y_m}{1-2\nu_m} + \frac{E_m[(\nu_m k+1/2)C_2 r^{(k-1)}-(\nu_m k-1/2)C_3 r^{-(k+1)}]}{(1+\nu_m)(1-2\nu_m)} \tag{31-b}$$

$$\sigma_z^m = \sigma_\theta^m + Y_m \tag{31-c}$$

Further increase of the axial strain, as mentioned in ref. [2], may cause another type of plastically deformed matrix region in which the radial and circumferential stresses are identical. The present paper, however, does not consider this case because the infinitesimal strain assumption may not be valid for further increase of the applied axial strain.

RESULTS AND DISCUSSION

The effective stress-strain curve for a composite cylinder can be predicted by calculating the average value of the axial stress, σ_z, as a function of the applied axial strain, ϵ_z, and the mechanical properties of the composite constituents. As an example, the effective stress-strain curve of the composite studied by Ebert, et al.[4] is demonstrated in Figure 3. The mechanical properties of the composite constituents appear in Table 1. In Figure 3, the solid lines represent the present analysis. Within the straight line segment(OA), both the core fiber and the surrounding matrix tube are within their elastic limits. When the applied axial strain reaches ϵ_{zY}, the entire core fiber yields. The next line segment(AB) represents the hardening behavior of the composite with plastically deformed core surrounded by an elastic tube. When the applied axial strain reaches ϵ_{z1} in the same figure, the surrounding matrix starts yielding from the fiber-matrix interface. This strain can be calculated from eq. (29-a) by setting c=a. Then the plastically deformed matrix region propagates outward until the entire matrix tube yields. This smooth transient region is represented by the line segment BC. The applied axial strain, ϵ_{z2}, where this transient phenomenon terminates can be calculated from the same equation by setting c=b. The composite response to further axial strain increase then follows the remaining line segment. Within the transient region and for the higher value of the applied axial strain, the matrix tube material is assumed to be nonhardening even though the material hardens significantly(Figure 3 in ref. 4). The experimental results of Ebert, et al.[4] are also plotted in the same figure.

Table 1. Constituent Properties the Composite[4]

Material	Ultimate Strength (Ksi)	0.05% Offset Yield (Ksi)	Elastic Modulus (Msi)	Poisson's ratio
SAE 4140 (Core)	93	54.9	28.7	0.29
Maraging Steel (Matrix Tube)	318	288	25.5	0.29

In Figure 4, the radial variations of the radial, circumferential and axial stresses in the composite cylinder of which the core volume fraction is 0.5 are plotted for two distinctive axial strain values, ϵ_{z1} and ϵ_{z2}. The stresses in the core material decrease slightly as the axial strain increases from ϵ_{z1}. At the onset of the initiation of the matrix yield, the axial stress in the matrix tube is constant. As the applied axial strain increases beyond ϵ_{z1}, the axial stress in the matrix has its maximum value at the free surface.

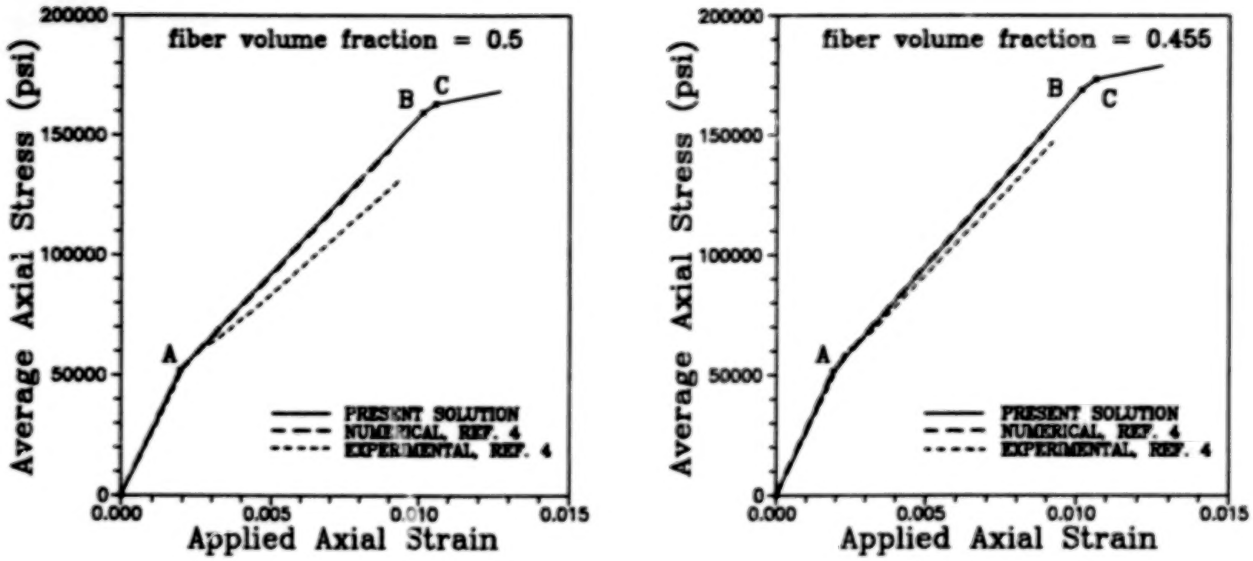

Figure 3. Composite stress-strain curve

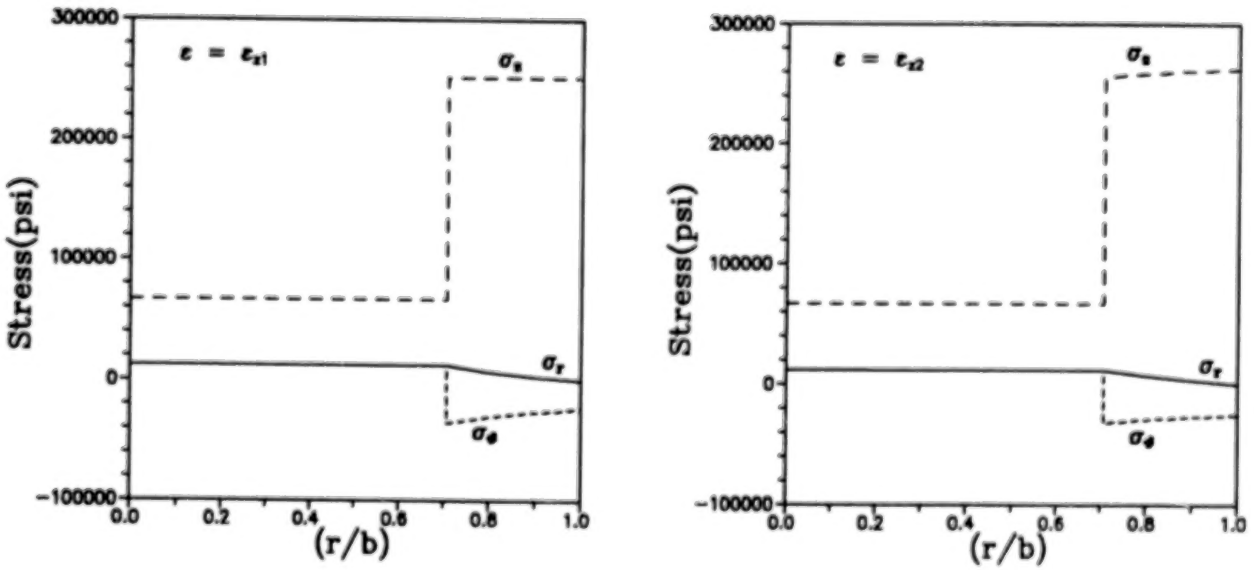

Figure 4. Stresses in the composite

CONCLUSIONS

The present study provides an analytical prediction of the elastoplastic response of continuous fiber composites with weaker fibers. The incremental form proposed by Ebert, et al.[4] must be replaced by the second order ordinary differential equation given by eq. (26). Furthermore, the present analysis can handle the mismatch of the Poisson's ratios as well as transversely isotropic fibers. The present analysis will be generalized for the same type of composites under cyclic loading for providing a comparison to the study of Mulhern, et al.[2]

REFERENCES

1. Hill, R., "Theory of Mechanical Properties of Fibre-Strengthened Materials: II. Inelastic Behavior," J. Mech. Phys. Solids, Pergamon Press Ltd., Vol. 12, pp. 213-218, 1964.
2. Mulhern, J. F., Rogers, T. G., and Spencer A. J. M., "Cyclic Extension of an Elastic Fiber with an Elastic-Plastic Coating," J. Inst. Maths Applics, Vol. 3, pp. 21-40, 1967.
3. Ebert, L. J. and Gadd, J. D., "A Mathematical Model for Mechanical Behavior of Interfaces in Composite Materials," Fiber Composite Materials, Papers Presented at a Seminar of the ASTM, October 17-18, 1964, pp. 89-113.
4. Ebert, L. J., Hecker, S. S., and Hamilton, C. H., "The Stress-Strain Behavior of Concentric Composite Cylinders," J. Composite Materials, Vol. 2, No. 4, pp. 458-476, Oct. 1968.

THE LOOPED ADHESIVE STRIP:
An Example of Coplanar Delamination Interaction

W. J. Bottega
Dept. of Mechanics and Materials Science
Rutgers University
Piscataway, N.J.

Introduction

The phenomenon of peeling and debonding of thin layers is a subject of interest to those concerned with adhesives, thin films, and layered materials. In recent years much attention has been focused on such problems as a result of increased interest and application of advanced composites and thin film coatings. (See for example ref. 1. An extensive list of references pertaining to the subject can be found therein.) A related problem which is of interest for its own sake but also represents a simple example of a tangled adhesive strip and of coplanar delamination interaction, is the problem of a looped adhesive strip. This is the subject of the present study.

We consider here the problem of an elastic strip which possesses an adherend on (at least) one of its surfaces. If the strip is deformed so that two portions of such a surface are brought into contact, a portion of the strip becomes bonded and a loop is formed (Figure 1). We shall be interested in determining the equilibrium configuration of such a strip and investigating the behavior of the strip when its edges are pulled apart.

The problem shall be approached as a moving interior boundary problem in the calculus of variations with the strip modeled as an inextensible elastica and the bond strength characterized by its surface energy.* A Griffith type energy criterion shall be employed for debonding, and solutions corresponding to the problem of interest obtained. The solution obtained will be seen to predict the interesting phenomenon of "bond point propagation", as well as the more standard peeling type behavior. Numerical results demonstrating the phenomena of interest are presented as well and will be seen to reveal both stable and unstable propagation of the boundaries of the bonded portion of the strip, depending upon the loading conditions.

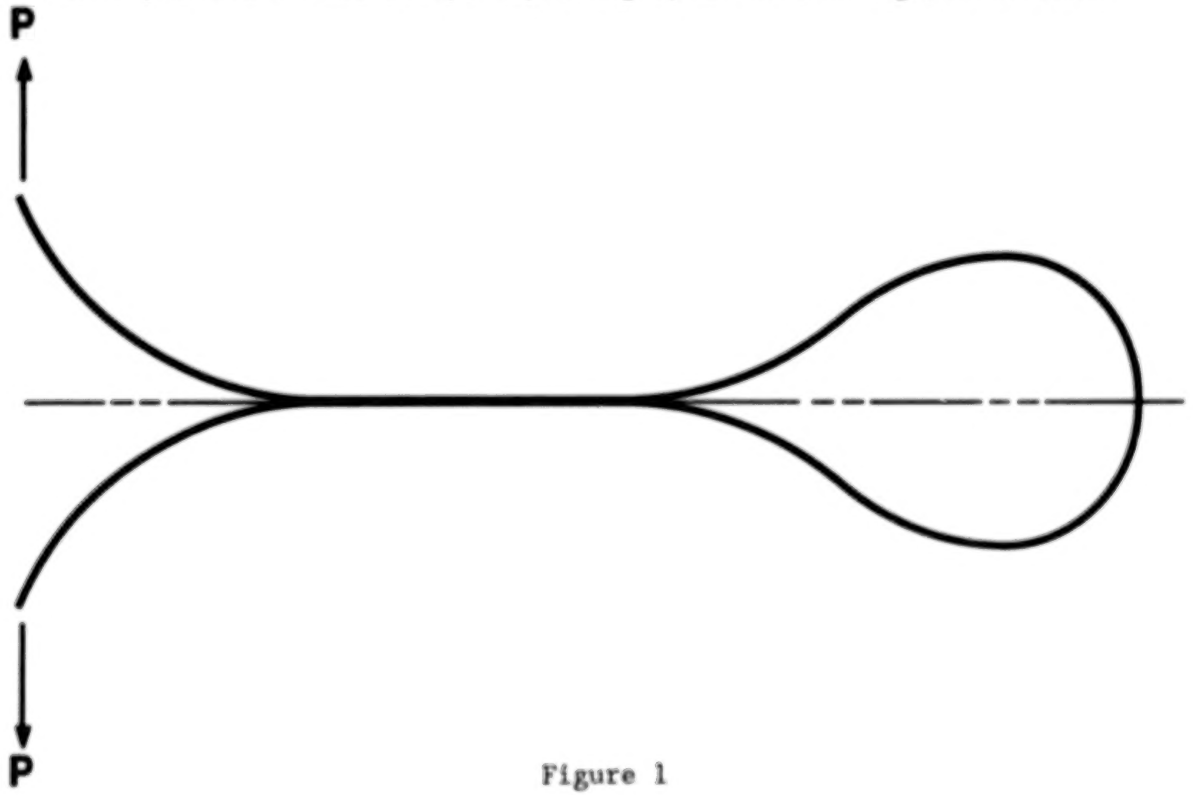

Figure 1

*Bottega, W.J.: Peeling and Bond Point Propagation in a Self-Adhered Elastica. To appear in Quart. J. Mech. and Appl. Math.

Formulation of the Problem

Consider a thin elastic strip which possesses an adherend on one of its surfaces, and let the strip be closed on itself in a symmetric manner such that there exists a region in the plane of symmetry where the strip is bonded to itself (Figure 1). Additionally, let the edges of the strip be subjected to equal and opposite forces as shown. As a result of the inherent symmetry of the problem, only half of the strip need be considered in the ensuing analysis (Figure 2). The strip thus consists of a lifted segment, a bonded segment, and a looped segment. In what follows, all length scales have been normalized with respect to the half length, L, of the entire strip.

We shall identify each point on the centerline of the strip by its normalized arc length, s, measured from the edge at which the external force is applied. In so doing, the half strip will be divided into four regions; corresponding to the lifted segment defined on $0 \le s \le a$, $a \le s \le b$ corresponding to the bonded segment , with the looped segment of the strip divided into two regions, defined by $b \le s \le s^*$ preceding the associated inflection point, s^*, and $s^* \le s \le 1$ following the inflection point. We shall be interested in assessing the behavior of the above system as a function of the magnitude of the applied load or the corresponding edge displacement.

Let us first define the right handed cartesian coordinate system (x,y) as shown in the figure. In addition, let us define the angle $\theta(s)$ which measures the angle that the tangent of the strip at point "s" makes with the x-axis as s increases (see Figure 2). One then may easily find the relations

$$x(s_2)-x(s_1) = \int_{s_1}^{s_2} \cos\theta \, ds \qquad \text{and} \qquad y(s_2)-y(s_1) = \int_{s_1}^{s_2} \sin\theta \, ds \, . \qquad \text{(i-a,b)}$$

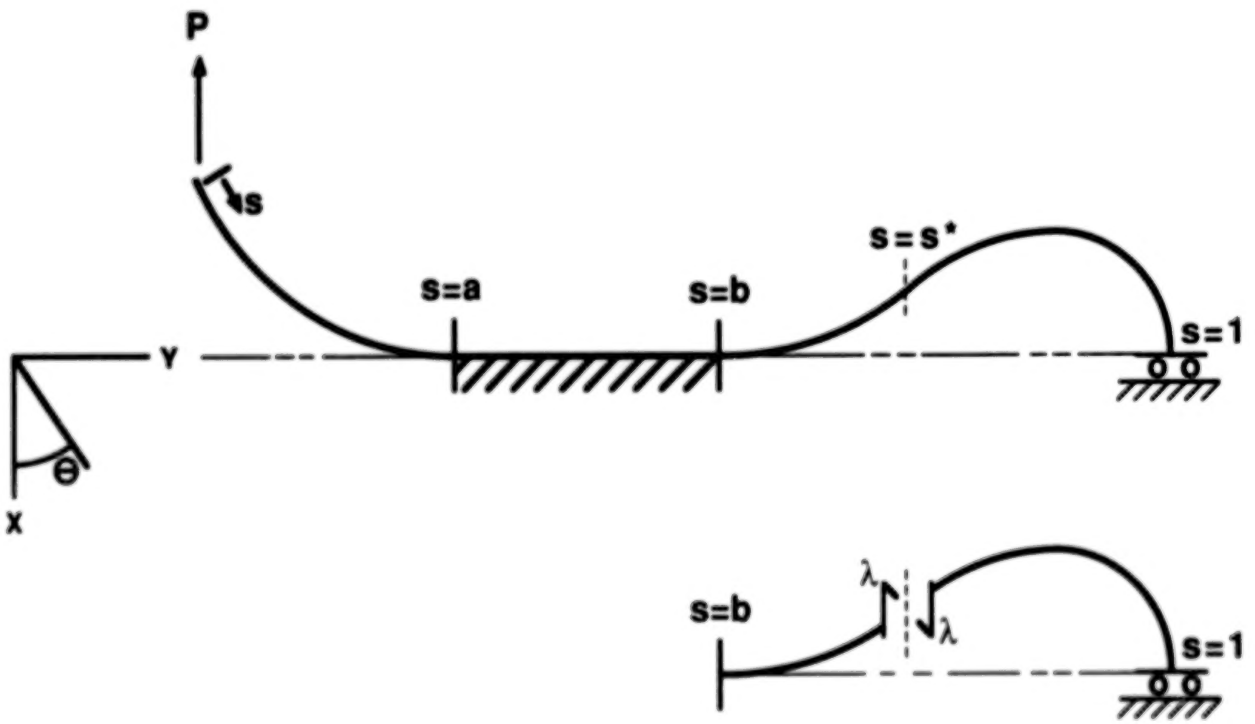

Figure 2

Energy Functional

As we shall approach the problem as a moving interior boundary value problem in the calculus of variations, we next define the energy functional $\prod$ given in Table 1 where $U^{(i)}$ corresponds to the normalized strain energy of the segment of the strip defined on the domain D_i, and is seen to be comprised solely of bending energy as the elastica is assumed to be inextensible. The strain energy of the (perfectly) bonded segment of the strip, i.e., the portion of the strip on [a,b], is thus seen to vanish identically. The functional W corresponds to the normalized work done by the applied load. In that expression, $P = \tilde{P}L^2/\tilde{D}$ corresponds to the normalized counterpart of the magnitude of the applied load, $\tilde{P}$, and $\tilde{D}$ represents the bending stiffness of the strip. The functional Γ corresponds to the "delamination energy" where $\gamma = \tilde{\gamma}L^2/\tilde{D}$ represents the normalized counterpart of the surface energy of the bond, γ, while a_0 and b_0 correspond to the initial values of a and b respectively.

Finally, we introduce the constraint functional Λ, with Lagrange multiplier λ, which constrains the deflections of the segments of the strip on D_3 and D_4 to be continuous at $s = s^*$. The functions $x_3(s^*)$ and $x_4(s^*)$ may be expressed in terms of θ by eq. (i-a). Thus,

$$\Lambda = \lambda \int_b^{s^*} \cos\theta \, ds + \lambda \int_{s^*}^1 \cos\theta \, ds \quad . \tag{2e'}$$

We note that the inclusion of Λ is equivalent to treating the segments on D_3 and D_4 as separate structures and including the work done by the internal force λ, at $s = s^*$. It may be seen that the line of action of this force must be parallel to the x-axis as a result of the support condition at $s = 1$ (see Figure 2).

Table 1

$$\prod = \sum_{i=1}^{4} U^{(i)} - W + \Gamma - \Lambda \tag{1}$$

where:

$$U^{(i)} = \int_{D_i} \frac{1}{2}(d\theta/ds)^2 \, ds \tag{2a}$$

$$U^{(2)} \equiv 0 \tag{2b}$$

$$W = -P\,x(o) = P \int_o^a \cos\theta \, ds \tag{2c}$$

$$\Gamma = 2\gamma(a-a_o) - 2\gamma(b-b_o) \tag{2d}$$

$$\Lambda = \lambda[x_3(s^*) - x_4(s^*)] \tag{2e}$$

The Governing Equations

The governing differential equations, boundary conditions, matching conditions and transversality conditions for the problem of interest are found by invoking the principle of stationary potential energy as shown in Table 2 below. In equation (3), the parameter δ represents the variational operator.

The transversality conditions (7a,b,c) result from the moving boundaries during peeling or bonding of the strip and thus are associated with equilibrium configurations of the system during these processes.

The intermediate boundaries a, b and s*, as well as the inflection point angles α and α^* are found as part of the solution to the problem.

Table 2

Principle of Stationary P.E.: $\delta\Pi = 0$ (3)

(1) into (3):

$$\frac{1}{2}\left(\frac{d\theta_i}{ds}\right)^2 + P_i(\cos\alpha_i - \cos\theta_i) = 0\,, \qquad (i = 1,3,4) \tag{4}$$

$$\theta_2 = \pi/2$$

where: $\theta_1 = \theta \equiv \pi - \theta$, $\alpha_1 = \alpha \equiv \theta(0)$, $P_1 = P$,

$$\theta_{2,3,4} = \theta \ , \quad \alpha_{3,4} = \alpha^* \equiv \theta(s^*) \ , \quad P_{3,4} = \lambda \tag{5}$$

with B.C.s and M.C.s: and T.C.s:

$\theta_1(a) = \theta_3(b) = \pi/2$, (6a,b) $G(a^-) \equiv \frac{1}{2}\left(\frac{d\theta_1}{ds}\right)^2\Big|_{s=a^-} = 2\gamma$ (7a)

$\theta_4(1) = 0$ (6c)

$\theta_3(s^*) = \theta_4(s^*) = \alpha^*$ (6d) $G(b^+) = \frac{1}{2}\left(\frac{d\theta_3}{ds}\right)^2\Big|_{s=b^+} = 2\gamma$ (7b)

$\int_b^{s^*} \cos\theta\, ds = -\int_{s^*}^1 \cos\theta\, ds$ (6e) $\frac{d\theta_3}{ds}\Big|_{s=s^*} = \frac{d\theta_4}{ds}\Big|_{s=s^*} = 0$ (7c)

Criteria for Propagation of the "Bond Zone" Boundaries

The conditions (7a) and (7b) establish the bond zone boundaries during their propagation and state that the values of a and b corresponding to equilibrium configurations of the system during propagation of each interior boundary are those for which the bending energy densities at the point $s = a^-$ and $s = b^+$ are just balanced by the energy of the bond. In this context the quantities $G(a^-)$ and $G(b^+)$ may be identified as the "energy release rates" at the bond zone boundaries. The above suggests the criteria for propagation of the boundaries of the bonded region of the elastica, as listed in Tables 3a and 3b.

Peeling

If, for some initial $a = a_o$, eqn. (8a) is satisfied, no peeling will occur and a will remain at its initial value a_o with the lifted segment bending away from the plane of symmetry. If, for some initial $a = a_o$, eqn. (8b) is satisfied, the lifted segment of the strip peels away from the plane of symmetry such that the value of a increases until the corresponding equality (7a) is satisfied.

Following the above reasoning, we conclude that for the loop to maintain its initial configuration, conditions must be such that eqn. (9a) is satisfied. If eqn. (9b) holds, the loop would open as a result of excess bending energy at its edge, with b taking on smaller values until the energy of deformation is just balanced by the energy of the bond.

Table 3a

Criteria for Propagation of Bond Zone Boundaries:

Peeling:

If $G\{a^-_o\} < 2\gamma$	No Peeling	(8a)
If $G\{a^-_o\} > 2\gamma$	Peeling until a satisfies equality (7a)	(8b)

Similarly,

If $G\{b^+_o\} < 2\gamma$	Loop maintains initial configuration	(9a)
If $G\{b^+_o\} > 2\gamma$	Loop grows (b decreases until b satisfies equality (7b)	(9b)

Bond Point Propagation

If conditions are such that the bending energy $G(a^-)$ is sufficiently large while $G(b_o^+)$ is sufficiently small, the bond zone boundary "a" will increase while b remains at its initial value until $a \to b^-$. At this stage, as the resultant bending moment m_{ba} acting at the bond point satisfies eqn (10) (Table-3b), and hence acts in a clockwise sense, tending to rotate the strip in this sense, while simultaneously there exists a sufficient surplus of bond energy to counter the bending energy of the loop and induce bonding at the loop edge, the strip behaves locally as if rolling over its counterpart and the "bond point" $s \to a \to b$ will propagate such that the loop closes and shrinks until the corresponding equality (7b) is satisfied. At this point the surplus bond energy is depleted and bonding at $s \to b^+$ can no longer occur. Equivalently, the growth condition (9b) as well as (8b) will become satisfied and conditions will then be such that propagation can occur in both directions simultaneously. Under such conditions, the loop will expire and the strip will separate completely.

Table 3b

"BOND POINT PROPAGATION":

If (9a) and (8b) satisfied, $a \to b_o^-$.

Resultant Bending Moment:

$$m_{ba} = [[d\theta/ds]]_{s=b} = [d\theta/ds]_{s=b^+} - [d\theta/ds]_{s=b^-} < 0 \qquad (10)$$

(thus, m_{ba} is clockwise)

Thus, "bond point" propagates until equality (7b) satisfied and loop expires.

Basic Integrals

The nonlinear differential equations (4) governing the local rotations on each segment of the strip are seen to be of standard form, which upon solving for ds, integrating over the corresponding domain, and using the transformation given by (11), results in expressions for the segment arc lengths ℓ_i (i=1,3,4) in terms of the inflection point angles and corresponding external or internal loads as given in Table 4. We note that these lengths will vary as a result of bonding and debonding. The functionals $F(q,\Phi)$ and $F_k(q)$ in eqns. (12) correspond to elliptic integrals of the first kind and complete elliptic integrals of the first kind, respectively, defined by

$$F(q_i,\Phi) = \int_0^{\Phi} \frac{d\phi_i}{\sqrt{1-q_i^2\sin^2\phi_i}} \quad \text{and} \quad F_k(q_i) = F(q_i,\pi/2) \quad . \qquad \text{(ii-a,b)}$$

We shall first consider equilibrium configurations of the lifted segment ($\theta\in D_1$) and of the looped segment ($\theta\in D_3+D_4$) separately, and then examine their interaction.

Table 4

BASIC INTEGRALS

Transformation:

$$\sin(\epsilon_i/2) = q_i \sin\phi_i \qquad \text{(11a)}$$

$$q_i = \sin(\alpha_i/2) \quad (i = 1,3,4) \qquad \text{(11b)}$$

(11) into (4), solving for ds and integrating -

segment arc lengths ℓ_i :

$$\ell_1 = a = [F_k(q_1) - F(q_1,\hat{\phi}_1)]/\sqrt{P} \qquad \text{(12a)}$$

$$\ell_3 = s^* - b = [F_k(q^*) - F(q^*,\hat{\phi}_3)]/\sqrt{\lambda} \qquad \text{(12b)}$$

$$\ell_4 = 1-s^* = F_k(q^*)/\sqrt{\lambda} \qquad \text{(12c)}$$

where $q_3 = q_4 = q^*$ (13a)

$$\hat{\phi}_i = \sin^{-1}\{1/(q_i\sqrt{2})\} \qquad \text{(13b)}$$

$F(q,\phi)$ - Elliptic Integral of 1st Kind

$F_k(q_i)$ - Complete E.I. of 1st Kind

Behavior of the Lifted Region

The deflection of the edge of the strip at which the load is applied is found by solving equation (4a) for $d\theta_1/ds$ and substituting the resulting expression into equation (i-a), with appropriate limits of integration. Then, upon incorporating the transformation (13), we obtain the load edge deflection, Δ_o, as given in Table 5, where

$$E(q_i,\Phi) = \int_o^{\Phi} \sqrt{1-q_i^2\sin^2\phi_i}\; d\phi_i \qquad \text{and} \qquad E_k(q_i) = E(q_i,\pi/2) \quad , \quad \text{(iii-a,b)}$$

correspond to elliptic integrals of the second kind, and complete elliptic integrals of the second kind, respectively. The explicit form of the transversality condition at the "trailing edge" of the bonded region (i.e., at $s = a$) may be found by solving equation (4a) for $[d\theta_1/ds]_{s=a}$ and substituting the resulting expression into (7a). We then have the condition which (implicitly) defines the location of the trailing edge of the "bond zone", during peeling, given by eqn. (15).

Substitution of equation (15) into equation (12), with $i = 1$, and equation (14) gives explicit relations for the magnitude of the applied load as a function of "a" and the normalized load point deflection as a function of "a" respectively, with the load point rotation $\dot{\alpha}$ a parameter. Specific results corresponding to selected values of γ will be presented in a later section.

Table 5

BEHAVIOR OF LIFTED REGION

LOAD POINT DEFLECTION:

$$\Delta_o \equiv -x|_{s=o} = \frac{1}{\sqrt{P}}\left([2E(q_1,\hat{\theta}_1) - F(q_1,\hat{\theta}_1)]\right.$$

$$\left. - [2\Xi_k(q_1) - F_k(q_1)]\right) \qquad (14)$$

where $E(q,\theta)$ = Elliptical Integral of 2nd Kind

$E_k(q_i)$ = Complete E.I. of 2nd Kind

T.C. @ $s = a^-$ (7a) becomes

$$P = -2\gamma/\cos\dot{\alpha} \qquad (\pi/2 < \dot{\alpha} \le \pi) \qquad (15)$$

Equilibrium Configurations of the Loop

The angle which measures the rotation of the tangent of the loop at its inflection point $s = s^*$ is found by imposing the condition (6e). Thus, solving equations (4b) and (4c) for $d\phi/ds$, substituting the resulting expressions into the left and right hand sides of (6e) respectively, noting (6d) and incorporating the transformation (11) for $i = 3,4$ we obtain the condition given by (16) below where as defined earlier, $\alpha^* = \alpha_3 = \alpha_4$ and $q^* = q_3 = q_4$. It may be seen from equation (16) that α^* is independent of the size of the loop, of the material and geometric properties of the strip and bond, and of the magnitude of the applied load, and thus is a "characteristic angle" of the problem. Equation (16) may be solved numerically to yield the value of α^* as given below.

The total (half) arc length of the loop, ℓ, is simply comprised of the sum of the lengths of its constituent segments. Thus, adding equations (12b) and (12c) yields the relation for ℓ, given by (18). The relative portions of the loop corresponding to its constituent segments are then found by dividing eqns.(12b) and (12c) by (18). We thus have

$$\ell_3/\ell = [F_k(q^*) - F(q^*,\Phi^*)]/[2F_k(q^*) - F(q^*,\Phi^*)] \qquad (19a')$$

and

$$\ell_4/\ell = F_k(q^*)/[2F_k(q^*) - F(q^*,\Phi^*)] \ , \qquad (19b')$$

which are seen to correspond to "characteristic length ratios" of the problem. The above ratios may be evaluated, using the computed value of α^*, to yield the values given at the bottom of Table 6.

Table 6

EQUILIBRIUM CONFIGURATIONS OF THE LOOP

Imposing (6e):

$$2[2E_k(q^*) - F_k(q^*)] = 2E(q^*, \theta^*) - F(q^*, \theta^*) \qquad (16)$$

(where $\theta^* = \hat{\theta}_3 = \hat{\theta}_4$).

Solving (16) yields "characteristic angle" of inflection point

$$\alpha^* = 117.54^\circ \quad \text{(for any loop size and mat'l./geom. props.)} \qquad (17)$$

(12b) + (12c) = loop (half) arc length ℓ:

$$\ell = \ell_3 + \ell_4 = [2F_k(q^*) - F(q^*, \theta^*)]/\sqrt{\lambda} \qquad (18)$$

(12b,c)/(18) = "Characteristic Arc Length Ratios":

$$\ell_3/\ell = 0.3254 \text{ and } \ell_4/\ell = 0.6746 \qquad (19a,b)$$

(for any loop size and mat'l./geom. props.)

Debonding of the Looped Segment

We may next consider equilibrium configurations of the looped segment of the strip as it opens (debonds) by evaluating the explicit form of the transversality condition at $s = b^*$ in a manner analogous to that done earlier for the lifted segment. Doing so we find that during opening of the loop, the condition (7b) takes the form given by eq'n.(20) where α^* is given by (17). Since, as discussed earlier, α^* is a "characteristic angle" (i.e., it maintains a fixed value for any equilibrium configuration of the loop,) it is seen from the above expression that the internal force λ maintains a constant value during debonding of the loop.

Substitution of (20) into equation (18) yields a critical value of the loop length given by equation (21) below, with the inequalities (9a,b) now interpreted in terms of the arc length of the loop; e.g. - (22a,b).

It may be noted that a minimum value of the normalized bond energy is required for the elastica to remain adhered to itself. This value $\gamma = \gamma_{min}$ corresponds to the limiting case where the loop traverses the entire strip and is in self-contact only at the loading edge $s = 0$ (i.e., it corresponds to the limiting case when $\ell_{cr} = 1$). Upon employing the result (19) we find the desired value given below. Adherends whose normalized bond energies possess magnitudes which are below this value are thus not "strong enough" to maintain a self-adhered configuration.

Table 7

T.C. @ $s = b^+$ (7b) becomes:

$$\lambda = -2\gamma/\cos\alpha^* \quad (= \text{constant for given } \gamma) \qquad (20)$$

(20) into (18):

$$\ell = [2F_E(q^*) - F(q^*, \theta^*)]/\sqrt{(-\cos\alpha^*)/2\gamma} \qquad (21)$$

If $\ell > \ell_{cr}$ No debonding of loop occurs (22a)

If $\ell < \ell_{cr}$ Debonding of loop occurs

ℓ increases (b decreases) until $\ell = \ell_{cr}$ (22b)

$$\ell_{cr} = 1 = \gamma = \gamma_{min} = 2.292 \qquad (23)$$

Effective Bond Strength and Propagation Behavior

A plot of ℓ_{cr} versus γ is displayed in Figure 3. It may be observed from the figure that the amount of "effective bond strength" gained, as measured by the relative decrease in ℓ_{cr}, significantly decreases as γ is increased beyond 200.

Peeling and Bond Point Propagation

The above solution offers the following scenario for a looped adhesive strip with given $\gamma > \gamma_{min}$ existing in an initial configuration such that $\ell_o = 1-b_o > \ell_{cr}$ (or equivalently $b_o < b_{cr} = 1-\ell_{cr}$), with an initial lift zone size of $\ell_1 = a_o$. As P is increased the corresponding value of $\alpha_1 = \bar{\alpha}$ is increased according to equation (12a), with the associated deflection Δ_o varied according to equation (14). This process is continued until equation (15) is satisfied at which point peeling begins with the "trailing edge" of the "bond zone" s = a propagating (and ℓ_1 increasing). As the initial loop length ℓ_o is larger than the critical length, the loop edge boundary of the bond zone remains at its initial value until $a = b_o$. At this point if conditions are such (equation (15) satisfied) that peeling continues, the bond point a = b propagates with ℓ decreasing (b increasing). During this phase the values of α^*, ℓ_3/ℓ, and ℓ_4/ℓ maintain the values given by (17) and (19a,b) respectively. The loop thus shrinks in size during this phase, with its geometry evolving through successive self-similar shapes (as if the strip were being pulled through a rigid clamp at s = b). This process continues until $\ell = \ell_{cr}$, at which point conditions are such that peeling may occur at both $s = b^-$ and $s = b^+$ (i.e., in both directions) simultaneously. At this instant the loop is terminated and the surfaces on each side of the plane of symmetry separate. Results corresponding to specific values of γ are presented next.

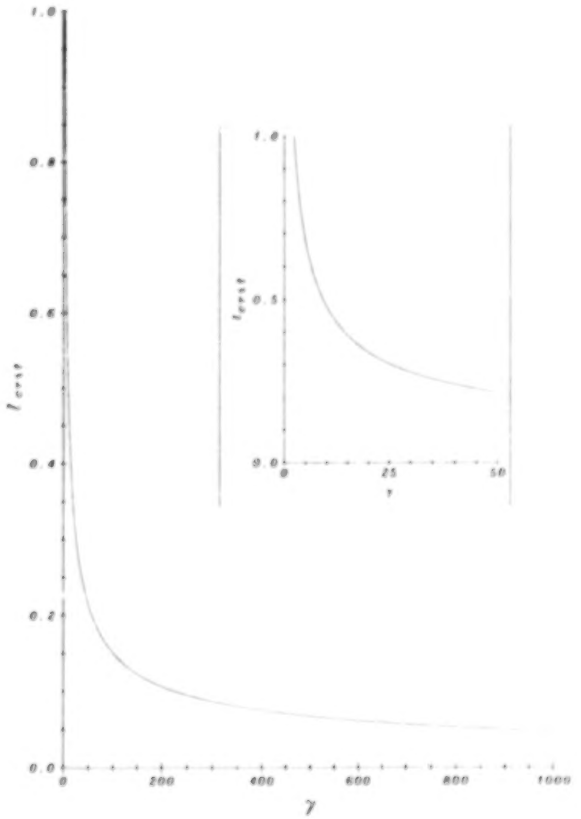

Fig. 3. Variation of Critical Loop (Half) Length with Normalized Bond Energy

Numerical Results

Results are presented corresponding to selected values of the normalized bond energy. Specifically, we consider the strip/adherend systems whose material and geometric properties are characterized by the values γ = 5, 10, 50, 100, and 1000 respectively.

The projections of the associated lift zone/bond point "propagation paths" in the Δ_o-a, P-a and P-Δ_o spaces are calculated and are displayed in Figures 4-7. Each curve is terminated at the critical values $a = b_{cr} = 1-\ell_{cr}$, which are given by the values b_{cr} = .3230, .5213, .7859, .8486, and .9522 for the respective values of γ considered. The prepropagation load-deflection behavior of lift zone segments corresponding to initial lengths of a_o = 0.25 and a_o - 0.50 are also displayed in Figure 6. Finally, the variation of the magnitude of the internal force λ, as a function of the loop length ℓ, is displayed in Figure 8.

It may be seen from the figures that propagation of the lift zone boundary or bond point occurs in a stable manner for a deflection controlled test, and in an unstable and "catastrophic" manner for a force controlled test. The following example illustrates the general behavior of the self-adhered elastica.

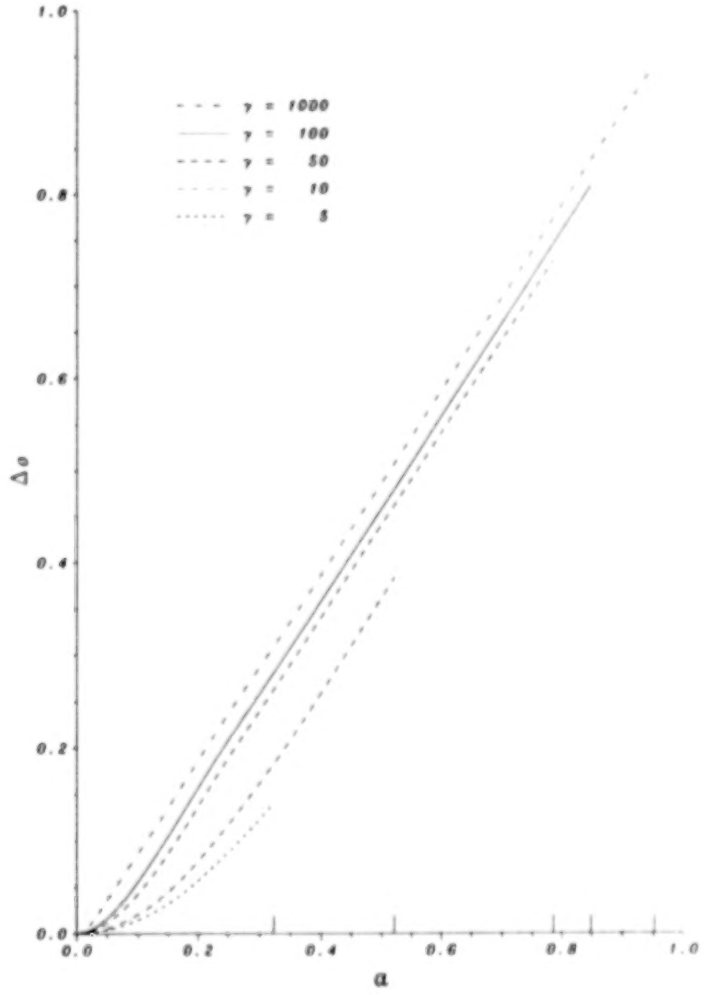

Fig. 4. Lift Zone/Bond Point Propagation Paths (γ = 5, 10, 50, 100, 1000): Load Edge Deflection vs. Bond Zone Boundary

Let us consider a strip/adherend combination with $\gamma = 50$ which is initially configured such that $a_o = 0.25$ and $b_o = 0.60$. It may be observed that a system characterized by one of the smaller values of γ considered could not maintain a loop size this small (b_o this large) and that for such a system the loop edge boundary, b, would immediately decrease to its corresponding critical value. Returning to the previously defined case ($\gamma = 50$), the system initially follows the prepropagation path for $a_o = 0.25$ in Figure 6, as P and Δ_o increase from the origin. During this phase, the system simultaneously follows a purely vertical path, corresponding to $a = 0.25$, in the Δ_o-a and P-a spaces (Figures 4 and 5). The system continues to behave in this fashion until the propagation path corresponding to $\gamma = 50$ is intercepted. At this point the lifted segment of the strip has accumulated enough bending energy at the bond zone boundary $s = a^-$, for the lift zone to propagate. We note that as $\ell_o > \ell_{cr}$ ($b_o < b_{cr}$) the bending energy of the looped segment at $s = b^+$ is insufficient for propagation so b remains at its initial value. Let us first consider the case where the load edge deflection, Δ_o, is controlled. For this case, as Δ_o is incrementally increased, a increases incrementally following the corresponding path in Figure 4. The corresponding values of P may be observed, from Figs. 5 and 6, to decrease accordingly. This process continues, with the strip peeling from its symmetric counterpart in a stable manner, until $a = b_o$. At this point the bending energy of the loop at $s = b^+$ is still sufficiently low as to maintain the bond, while that at $s = b^-$ is large enough to permit debonding. As Δ_o is increased further, the bond point $s = a = b$ then propagates in a stable manner, with the loop shrinking through a series of self-similar shapes until $\ell = \ell_{cr}$, at which point sufficient bending energy exists on both sides of the bond point and the strip separates. For the case where P rather than Δ_o is controlled, the system behaves

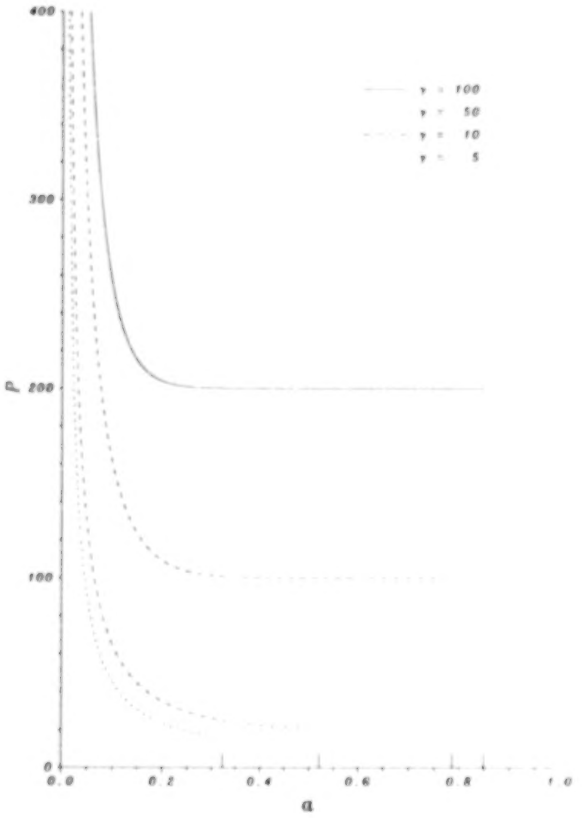

Fig. 5. Lift Zone/Bond Point Propagation Paths ($\gamma = 5$, 10, 50, 100): Applied Load vs. Bond Zone Boundary

in an analogous manner except that all behavior during the propagation phases occur in an unstable manner. Thus, for this case the process of complete separation of the elastica is initiated as soon as P reaches a critical value.

The phenomena described above may be observed by simply closing a piece of adhesive tape on itself, thus forming a loop, and then peeling the edges apart. Such an "experiment" would correspond to a deflection controlled test, with the normalized bond energy characterizing the tape observed to be at the upper end of the range of values considered in the numerical simulations presented herein.

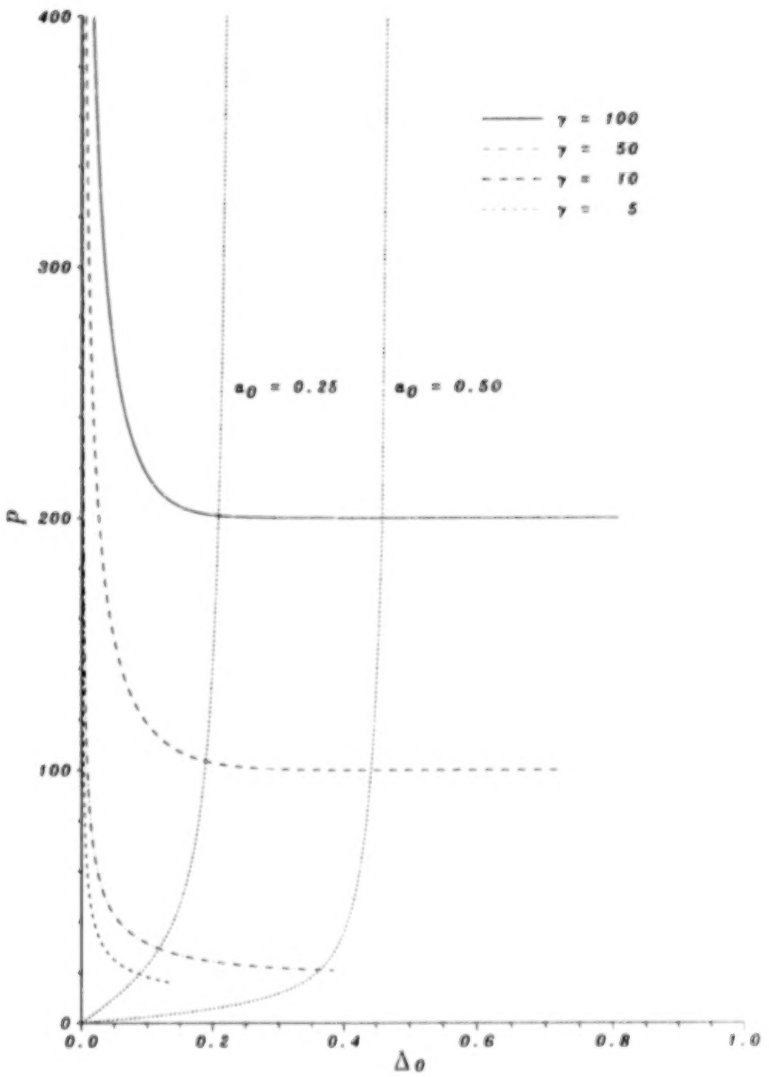

Fig. 6. Prepropagation and Lift Zone/Bond Point Propagation Paths (γ = 5, 10, 50, 100): Applied Load vs. Load Edge Deflection

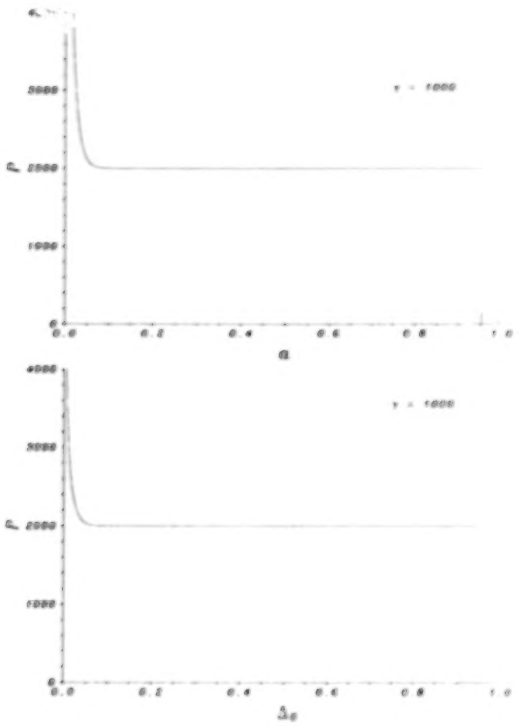

Fig. 7. Lift-Zone/Bond Pt. Propagation Paths (γ = 1000): (a) Applied Load vs. Bond Zone Boundary, (b) Applied Load vs. Load Edge Deflection

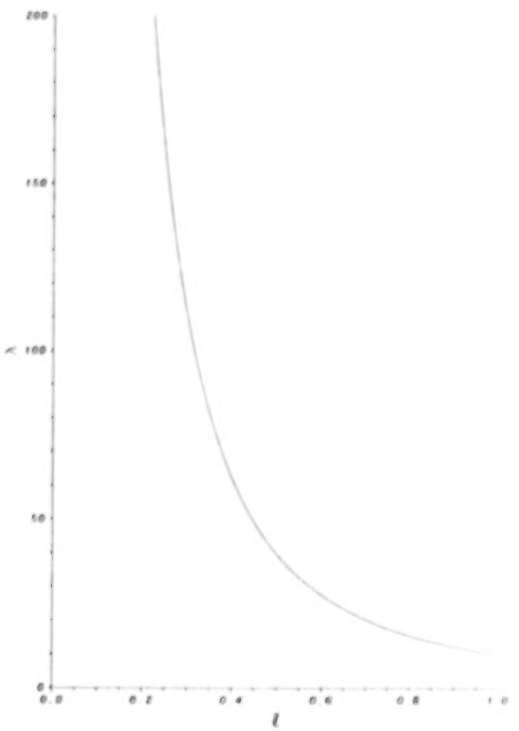

Fig. 8. Internal Force at Inflection Point of Loop as a Function of Loop (Half) Length

Acknowledgments

The author wishes to thank Mr. D.C. Newman of Carnegie Mellon University for performing the numerical calculations, simulations and associated graphics using the MATHLIB Software by Innosoft. Additionally, the author wishes to thank Ms. M. Bellinger of Rutgers University for performing the non-computational graphics. Finally, he would like to thank Ms. Bellinger for bringing her acute observations to his attention, thus motivating this study.

References

1. Bottega, W.J.: Peeling of a Cylindrical Layer. Int. J. Fracture, Vol. 38, No. 1, 1988, pp. 3-14.

A NEW BEAM THEORY
USING
FIRST-ORDER WARPING FUNCTIONS

C.A. IE and J.B. KOSMATKA
DEPARTMENT OF APPLIED MECHANICS AND ENGINEERING SCIENCE
UNIVERSITY OF CALIFORNIA, SAN DIEGO
LA JOLLA, CA 92093

BASIC IDEA

Due to a certain type of loading and geometrical boundary conditions, each beam will respond differently depending on its geometrical form of the cross section and its material definition. As an example, consider an isotropic rectangular beam under pure bending. Plane sections perpendicular to the longitudinal axis of the beam will remain plane and perpendicular to the deformed axis after deformation. However, due to the Poisson effect, particles in the planes will move relative to each other resulting in a form of anticlastic deformation. In other words, even in pure bending of an isotropic beam, each cross section will deform in the plane.

If the material of the beam above is replaced by a generally anisotropic material, then the cross sections will not only deform in the plane, but also out of plane. Hence, in general, both in-plane deformations and out-of-plane warping will exist and depend on the geometrical form and material definition of the cross sections and also on the loadings.

For the purpose of explanation, an analogy is made. The geometrical forms of the bodies of each individuals are unique. Hence, different sizes of clothes are needed. Finding the sizes of clothes for individuals is like determining the warping functions in beams.

A new beam theory using first-order warping functions is introduced. Numerical examples will be presented for an isotropic beam with rectangular cross section. The theory can be extended for composite beams. (Fig. 1.)

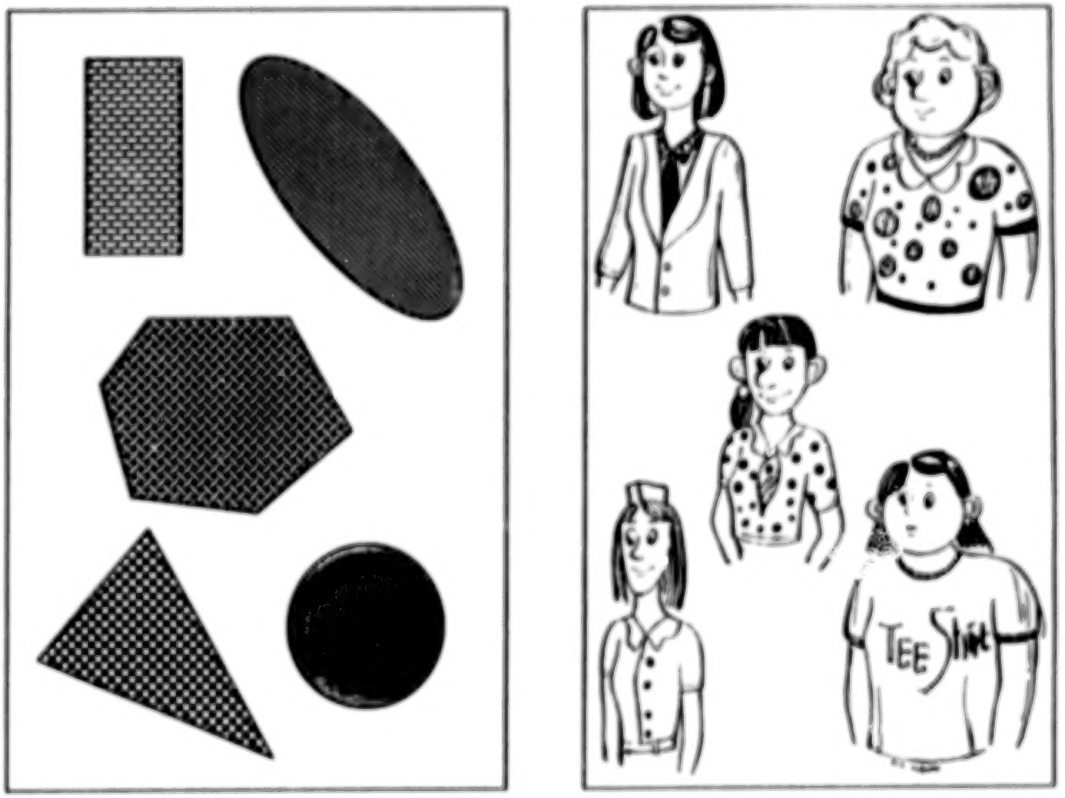

Figure 1. Analogy between determining the (first-order) warping functions and the proper size of clothes for individuals.

CANTILEVER BEAM

Consider the case of an isotropic rectangular cantilever beam with a tip loading (P). For the purpose of **comparison** to the St. Venant elasticity solution, St. Venant boundary stresses shall be taken into account. These self-equilibrated boundary stresses are shown in the figure below. XYZ is the system coordinate ; L is the length ; H is the height, and B is the thickness of the beam. Comparison will be made with respect to the **plane stress** St. Venant elasticity solution. Hence, the comparison will be more valid as the thickness goes to zero. (Fig. 2.)

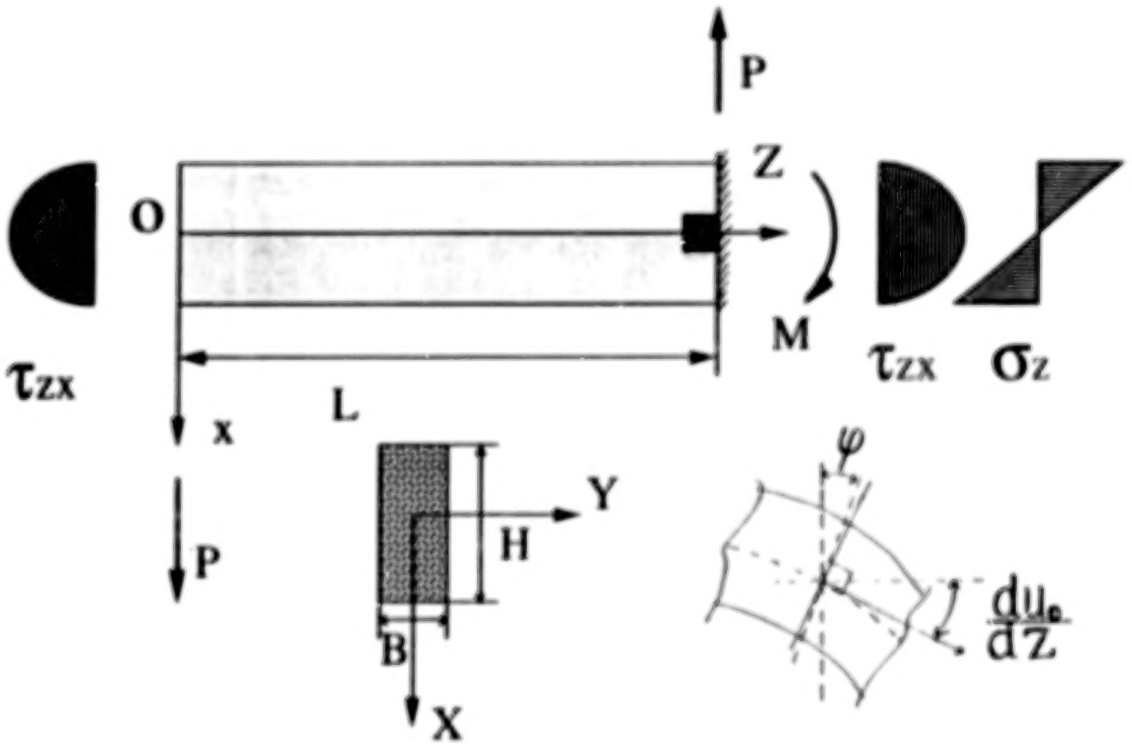

Figure 2. Cantilever beam with its boundary conditions.

ASSUMED DISPLACEMENT FIELD

The u,v,w are displacement components parallel to the x,y,z coordinate axis (refer to figure 2.). u_0 is the transverse displacement of the axis of the beam parallel to the x coordinate axis. φ is the bending rotation of the beam axis and its positive sense is defined as in the direction of the positive y axis. M and Q are the bending moment and shear force, respectively. q is the distributed load. U and V are the in-plane deformation functions parallel to the x and y coordinate axis, respectively. W is the out-of-plane warping function parallel to z coordinate axis. E is the Young modulus, and I is the moment of inertia of the cross section.

Strains are computed from the first set of equations. From Hooke's law [$\{\sigma\} = [C]\{\varepsilon\}$], stresses can be calculated. Using the definition of moment, M can be solved in terms of E, I and φ. The final form of the displacement field is as shown in the second set of equations. The detail is as follows.

By definition of moment,

$$M(z) = \int_A x\,\sigma_z\,dA$$

Assuming that (in consistency with using only the first-order warping functions) $Q'(z) = -\varphi(z) = 0$, the moment will be expressible as being $M(z) = -EI\varphi'(z)$. By equilibrium $Q(z) = M'(z) = -EI\,\varphi''(z)$. Substituting M and Q into the first set of equations, the final form of the displacement field is obtained.

It is important to note that no assumption is being made except the assumed displacement field itself. (Fig. 3.)

$$u(x,y,z) = u_o(z) + M(z)\,\bar{U}(x,y) \qquad v(x,y,z) = M(z)\,\bar{V}(x,y)$$

$$w(x,y,z) = -x\,\varphi(z) + Q(z)\,\bar{W}(x,y)$$

where

$$\bar{U}(x,y) = -\frac{\upsilon}{2EI}(x^2 - y^2) \qquad \bar{V}(x,y) = -\frac{\upsilon}{EI}\,x\,y$$

$$\bar{W}(x,y) = \bar{W}(x) = -\frac{2+\upsilon}{6EI}\,x^3$$

Final Model

$$u(x,y,z) = u_o(z) + \varphi'(z)\,U(x,y) \qquad v(x,y,z) = \varphi'(z)\,V(x,y)$$

$$w(x,y,z) = -x\,\varphi(z) + \varphi''(z)\,W(x)$$

where now

$$U(x,y) = \frac{\upsilon}{2}(x^2 - y^2) \qquad V(x,y) = \upsilon\,x\,y$$

$$W(x) = \frac{2+\upsilon}{6}\,x^3$$

Figure 3. Proposed model in a case of rectangular cross section.

LAYOUT OF THE NODAL POINTS

The finite-element model is developed using a layout of the nodal points as shown below. The layout is chosen such that all terms in the strain energy expression are taken into account. The minimum order of polynomials that is required for φ based upon the strain energy expression is three. Hence a four-node layout is required for φ. A five-node layout is selected for u_0 because, from the physical point of view, u_0 is one order higher. Other polynomials could also be selected (Fig. 4.)

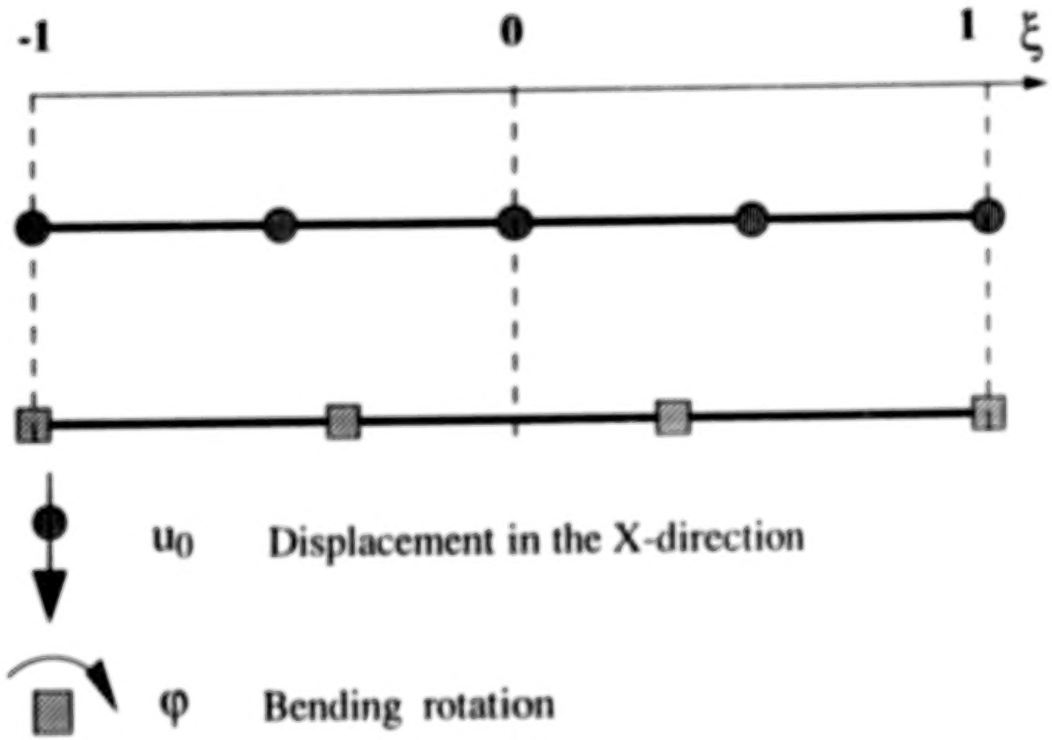

Figure 4. Layout of the nodal points in the finite-element model.

FINITE-ELEMENT MODEL

Using the principle of stationary potential energy a finite-element model is obtained. The term $\{\delta M\}$ in the equation is due to the fact that, instead of applied concentrated resultant forces, 'applied' St. Venant distributed stresses (through the cross section) are to be considered. If applied concentrated resultant forces do exist in the reality, then this term will vanish. The term $\{\delta m\}$ is present due to the fact that the distributed forces are applied on the upper surface of the beam. These additional terms exist because a beam theory that accounts for in-plane deformations and out-of-plane warping is used. Had an Euler-Bernoulli beam theory been used (or likewise Timoshenko beam theory), all these terms will vanish no matter how the loads are applied. All other terms are the usual terms that result when developing a finite-element model based upon an Euler- Bernoulli theory. For example

$$\{f\} = \int q\,[N]^T\,dz$$

where q is the distributed load and [N] are the shape functions. (Fig. 5.)

$$u_o(z) = \sum_{j=1}^{5} u_{oj}\,\phi_j(z)$$

$$\varphi(z) = \sum_{j=1}^{4} \varphi_j\,\theta_j(z)$$

u_{oj} , φ_j are Lagrangian type shape functions.

Equilibrium equations

$$\begin{bmatrix} [K^{11}]_{5\times5} & [K^{12}]_{5\times4} \\ [K^{21}]_{4\times5} & [K^{22}]_{4\times4} \end{bmatrix} \begin{pmatrix} \{u_o\}_{5\times1} \\ \{\varphi\}_{4\times1} \end{pmatrix} = \begin{pmatrix} \{P\}_{5\times1} \\ \{M\}_{4\times1} \end{pmatrix} + \begin{pmatrix} \{0\}_{5\times1} \\ \{\delta M\}_{4\times1} \end{pmatrix} + \begin{pmatrix} \{f\}_{5\times1} \\ \{\delta m\}_{4\times1} \end{pmatrix}$$

Figure 5. Finite-element model.

TIP DISPLACEMENT OF A CANTILEVER BEAM

A semi-logarithmic plot of aspect ratio versus nondimensionalized tip displacement is shown below where the tip displacement is nondimensionalized by dividing by the Euler-Bernoulli solution for a given load and geometry. Aspect ratio is defined as the length divided by the height of the beam. The Poisson ratio is taken equal to 0.25. All theories are in agreement for slender beams. For this type of loading,the elasticity solution, the proposed theory, and the Timoshenko using k equal to 2/3 are in perfect agreement. Using a k factor equal to 0.8475 [1] in the Timoshenko theory results in a stiffer beam (compare to using k equal to 2/3).

Solutions were calculated for extremely long slender beams (L/H = 100) to insure that the current beam element converged to the Euler-Bernoulli solution and did not "shear-lock". All calculations were performed assuming that B/L is equal to 1/8000. This selection was made to insure that the current model can be directly compared to the plane stress elasticity solutions. (Fig. 6.)

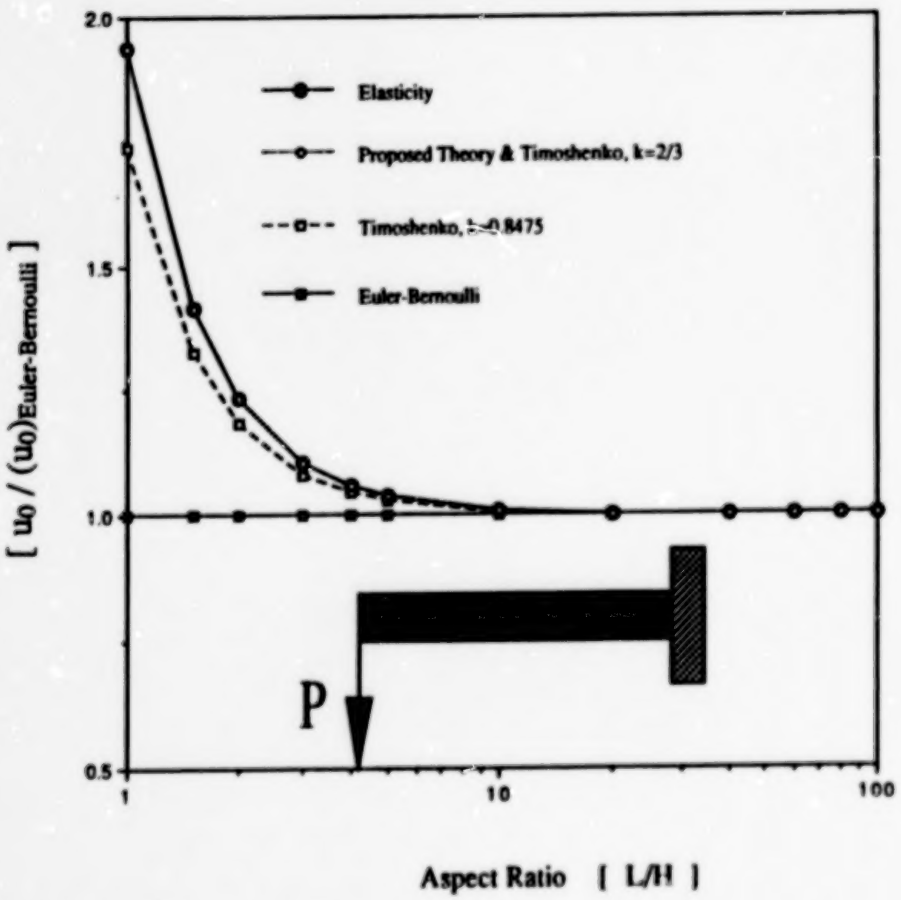

Figure 6. Tip displacements of a tip-loaded cantilever beam.

NORMAL STRESSES AT THE ROOT OF A CANTILEVER BEAM

Consider a case of the cantilever beam with an aspect ratio equal to three. The abscissa is the nondimensionalized normal stresses with respect to the Euler-Bernoulli normal stress at the top of the surface, i.e., $\bar{\sigma}_z$. The ordinate is the nondimensionalized X-coordinate where the top and bottom surfaces of the beam are defined as -1 and 1, respectively. As can be seen, all theories are in perfect agreement. (Fig. 7.)

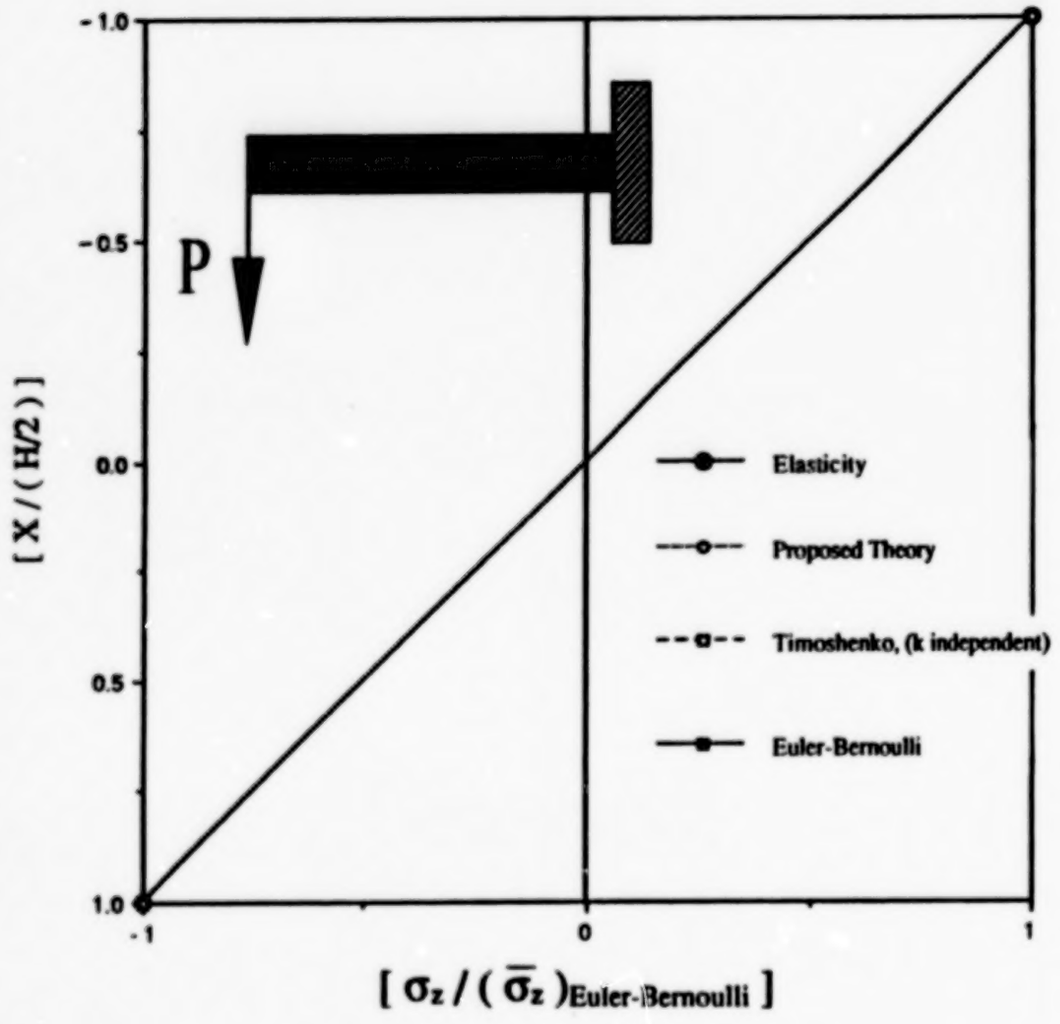

Figure 7. Normal stress at the root of a tip-loaded cantilever beam.

TRANSVERSE SHEAR STRESSES AT THE ROOT OF A CANTILEVER BEAM

Nondimensionalized shear stresses with respect to the elasticity shear stress at x equal to zero are made, i.e., nondimensionalized with respect to $\bar{\tau}_{zx}$. The ordinate is the nondimensionalized X-coordinate. The results from the proposed theory are in perfect agreement with the elasticity solutions. If the Timoshenko theory is applied, constant shear stress distribution is obtained. In fact, their values are equal to the average shear stress, i.e., P/A where A is the area of the cross section and P is the applied concentrated load. In this case, they do not depend on the value of the shear correction factor (k). Hence, the shear correction factor will influence the stiffness and shear strains of the beam, but not the shear stresses. Since the shear stresses are independent of k, then the shear strains must vary proportionally to the inverse of k. For an Euler-Bernoulli beam, a contradiction exists. If shear stresses are computed from the shear strains, then their values will vanish. On the other hand, from the equilibrium point of view, shear stresses cannot be zero. Using the principle of equilibrium, shear stresses can be obtained. (Fig. 8.)

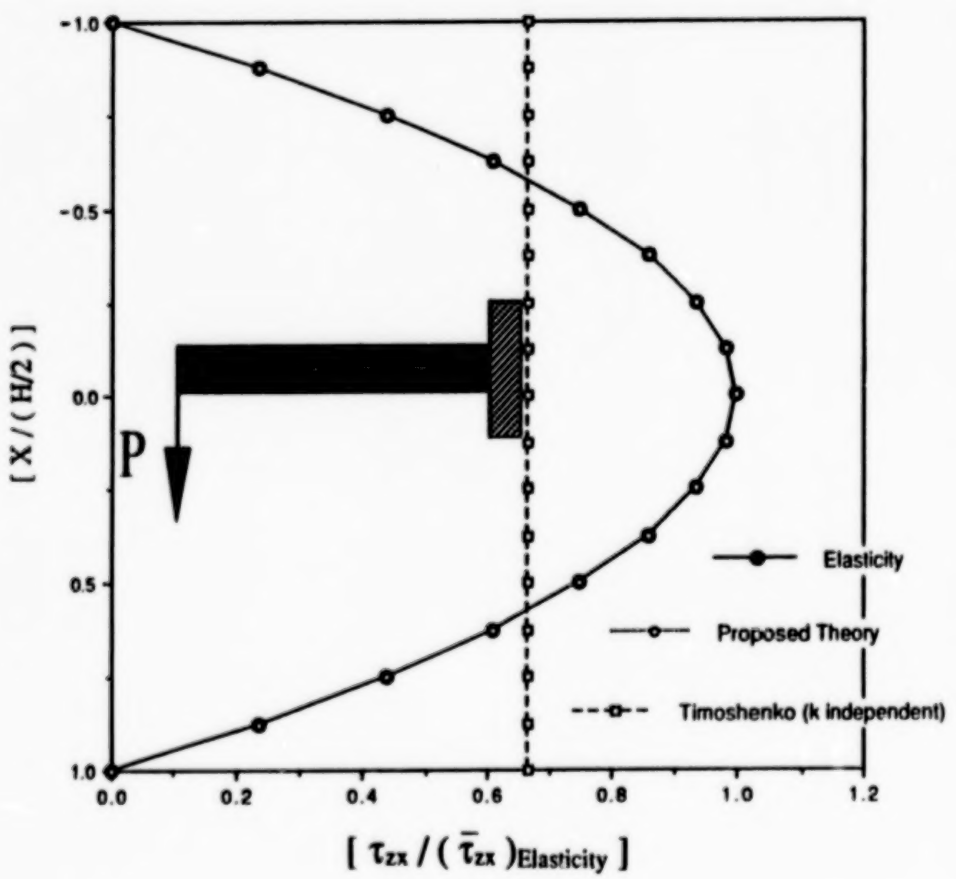

Figure 8. Transverse shear stresses at the root of a cantilever beam.

TABLE OF COMPARISON FOR THE STRESS COMPONENTS OF A CANTILEVER BEAM

Results from the theory of elasticity for the stresses are available. Due to the computational round-off errors, the coefficients ε_i will exist in the proposed theory. These terms become smaller as the value of B (the thickness) goes to zero. If truncation errors could be eliminated, the ε_i terms will go to zero as B goes to zero. This is due to the fact that the out-of-plane warping function W(x,y) was taken from the plane stress solution, which is then only a function of x, i.e., W = W(x). This is done mainly for the purpose of comparison and simplicity. In order for the current comparison to be valid, the thickness of the beam should be taken very small (B --> 0). As one can see, apart from the round-off errors, the proposed theory is in perfect agreement with the elasticity solution for the whole body (plane). (Fig. 9.)

$$\sigma_z = \varepsilon_1 x z^2 + \underline{c_1 x z} + \varepsilon_2 x^3 + \varepsilon_3 x$$

$$\tau_{zx} = \varepsilon_4 z^3 + \varepsilon_5 z^2 + \varepsilon_6 x^2 z + \varepsilon_7 z + \underline{c_2 x^2} + \underline{c_3}$$

$$\sigma_x = \sigma_y = \varepsilon_8 x^3 \qquad \tau_{yz} = \tau_{xy} = 0$$

	Proposed Theory Elasticity	Timoshenko Elasticity	Euler-Bernoulli Elasticity
c_1	1.00	1.00	1.00
c_2	1.00	0.00	0.00
c_3	1.00	0.67	0.00
$\varepsilon_i \rightarrow 0$ as B (the thickness) goes to 0			

Figure 9. Comparison of the stress components relative to the elasticity solutions.

SIMPLY SUPPORTED BEAM

Since the model is developed for tip loadings, it may have slight deficiencies for analyzing beams with higher-order distributed loads. In this example, the effects of the higher-order warping functions will be shown. Although it is possible to extend the model incorporating some degree of higher-order warping functions, for beam-type structures it may not be necessary. Higher-order warping functions play an important role for beams with small aspect ratios (closer to solid structures). But, as the aspect ratio gets smaller, the St. Venant solution becomes trivial in the practical sense (in reality). Another way of defining beams is as follows. A structure (structural element) can be considered as being a beam if the higher-order warping functions play insignificant roles. (Fig. 10.)

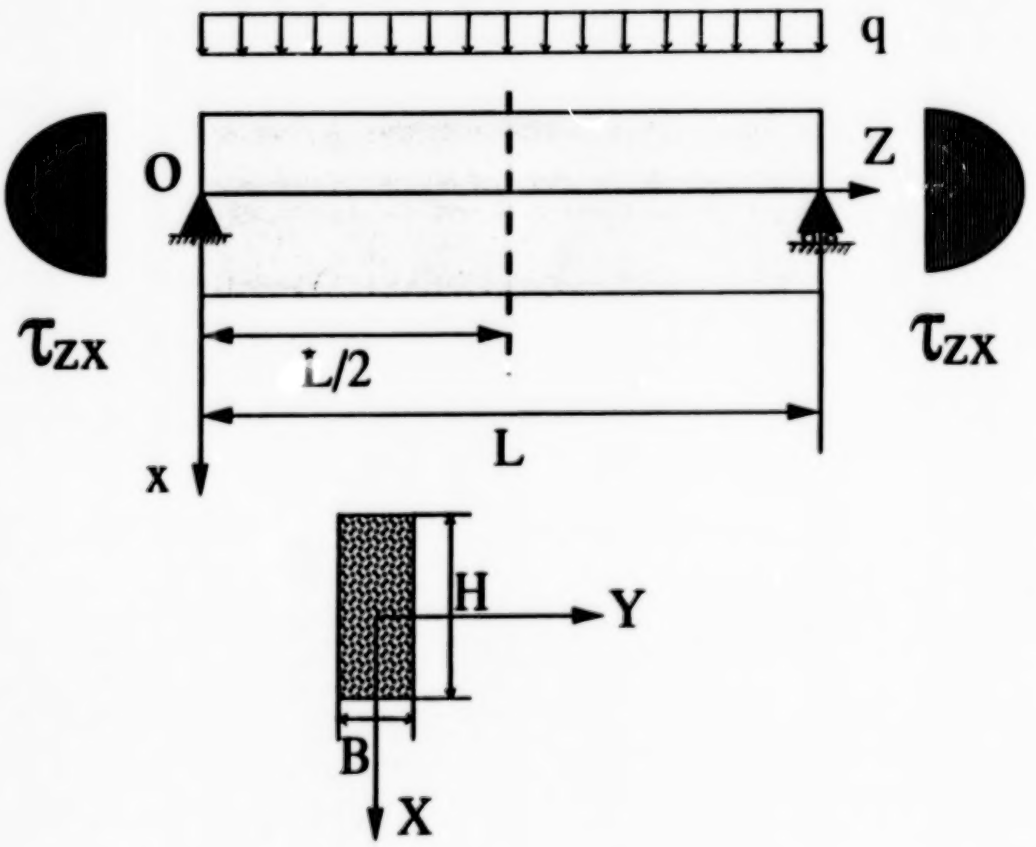

Figure 10. Simply supported beam with its boundary conditions.

MID-LENGTH DISPLACEMENT OF A SIMPLY SUPPORTED BEAM

It is very interesting to note that, although the Timoshenko theory for k equal to 2/3 gives the exact results (for the displacements) in the case of a cantilever beam, it gives the most flexible structure in the case of simply supported beams with constant distributed load. The proposed theory still gives very accurate results for the displacements. As can be seen, the effect of higher-order warping functions in the displacements, in this typical case, is very insignificant. (Fig. 11.) The effects in the stresses can be seen in the next figure.

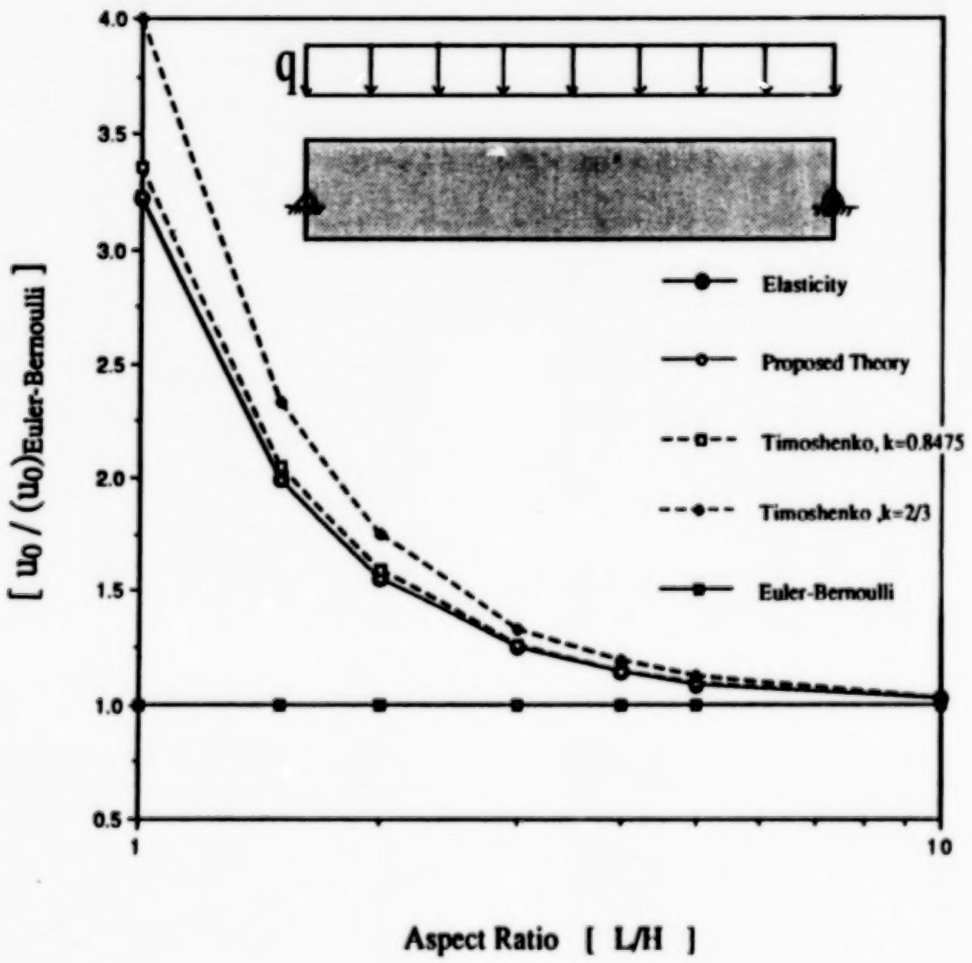

Figure 11. Displacements at mid-length of a simply supported beam.

NORMAL STRESSES AT MID-LENGTH OF A SIMPLY SUPPORTED BEAM

Consider the case of a simply supported beam with a uniformly distributed load where the aspect ratio (L/B) is equal to three. Nondimensionalized normal stresses are with respect to the Euler-Bernoulli stress on the bottom surface of the beam. It is important to note that the elasticity solution results in a cubic normal stress distribution as opposed to linear as suggested by the Euler-Bernoulli or Timoshenko beam theories. (Fig. 12.) In the next figure, a closer look at the lower portion of the cross section is presented.

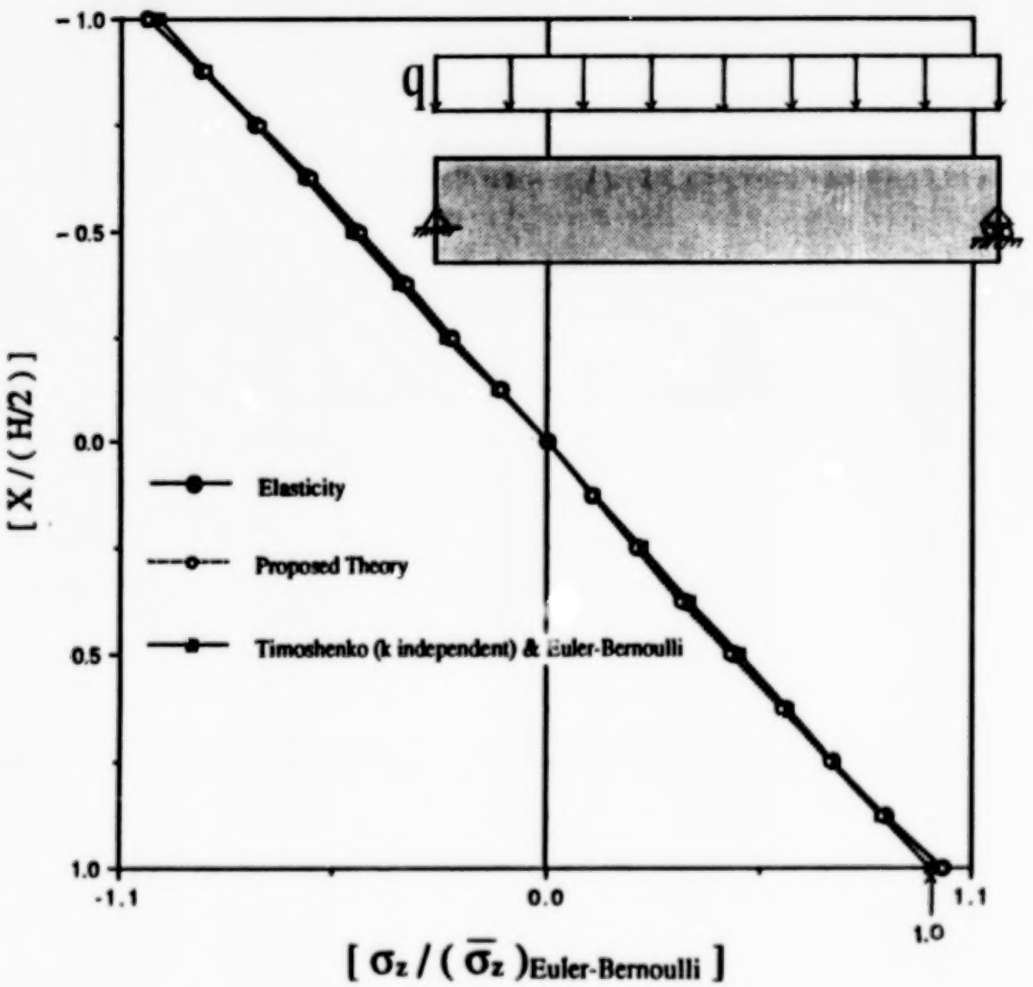

Figure 12. Normal stresses at mid-length of a simply supported beam.

NORMAL STRESSES AT MID-LENGTH FOR THE LOWER PORTION OF THE CROSS SECTION

As can be seen, the elasticity solution gives higher normal stresses at the top and bottom of the beam compared to the Euler-Bernoulli or Timoshenko beam. For this typical numerical example (with an aspect ratio equal to three), the elasticity normal stress at the bottom (or the top) is 3 percent higher, and the proposed theory gives 2.7 percent higher. This effect is due to the presence of distributed load or, in other words, due to the presence of higher-order warping functions. As the aspect ratio gets smaller, its effect will be more significant. (Fig. 13.)

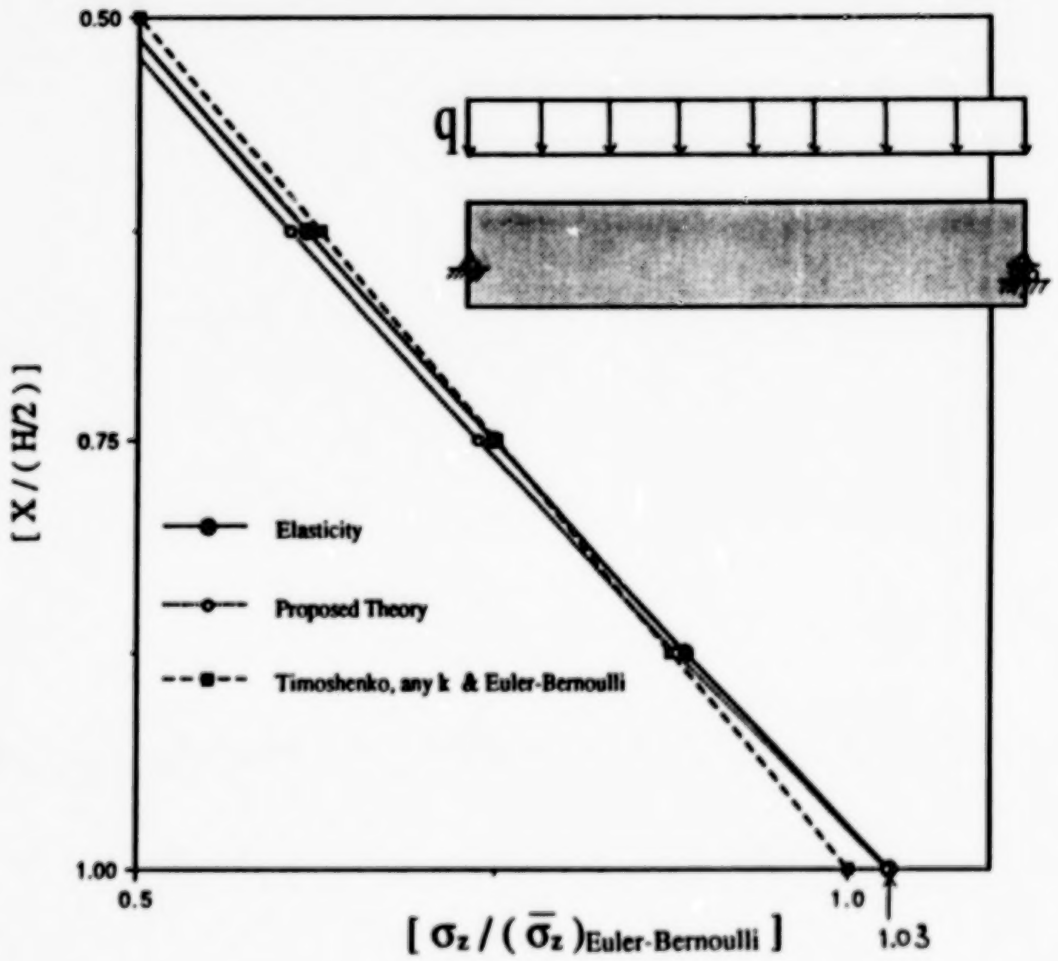

Figure 13. Detail of figure 12 for lower portion of the cross section.

TRANSVERSE SHEAR STRESSES AT LEFT-END OF A SIMPLY SUPPORTED BEAM

The same nondimensionalization as is found in figure 8 is made. The proposed theory results in perfect agreement with the elasticity solution. Again, the Timonshenko beam gives a constant shear stress distribution which is equal to R/A where R is the reaction force at the left end. (Fig. 14.)

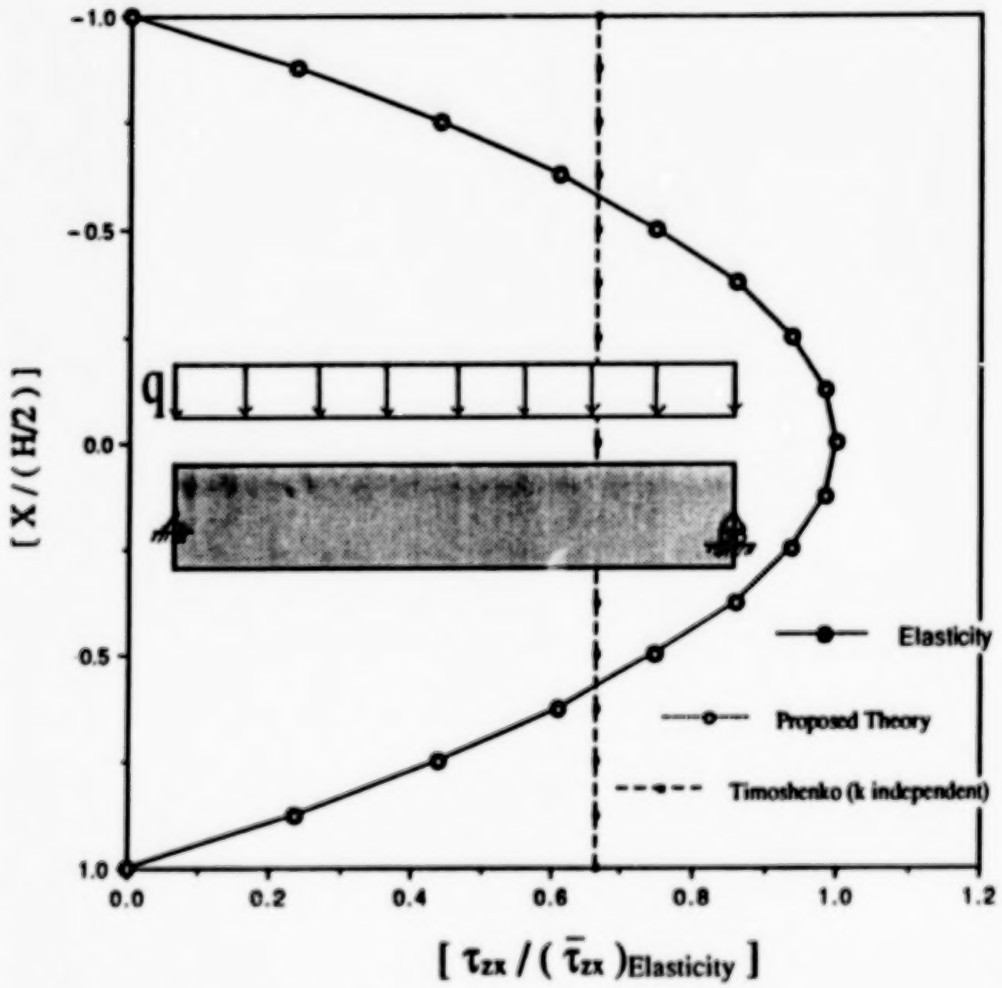

Figure 14. Shear stresses at the left-end of a simply supported beam.

TABLE OF COMPARISONS FOR THE STRESS COMPONENTS OF A SIMPLY SUPPORTED BEAM

All underlined terms exist in the plane stress elasticity solution. The terms with the coefficients h_1 and h_2 are the nonclassical terms and become important only for beams with very small aspect ratios. As a matter of fact, these two terms, found in the expression of σ_z, are self-equilibrated in the section planes. Obviously both the Timoshenko and Euler-Bernoulli beam theories cannot capture these higher-order terms. The proposed theory is still able to capture these two terms. Although it is not accurate inside the body of the beam, it gives an accurate result at the top and bottom of the beam, which are, in fact, the most important points (for normal stresses) for practical purposes.

Due to the presence of the distributed load, the stress component σ_x will not vanish. The proposed theory gives a meaningless result in the sense that it does not satisfy the boundary conditions at the top and bottom of the beam. This is not surprising because the theory accounts for only first-order warping functions. Although it is possible to extend the theory incorporating higher-order warping functions, it may not be necessary for practical purposes. It is important to note that for this typical beam structure, the most important stress components are σ_z and τ_{zx}. (Fig. 15.)

$$\sigma_z = \underline{c_1 x z^2} + \underline{c_2 x z} + \underline{h_1 x^3} + \underline{h_2 x}$$

$$\tau_{zx} = \varepsilon_1 z^3 + \varepsilon_2 z^2 + \underline{c_3 x^2 z} + \underline{c_4 z} + \underline{c_5 x^2} + \underline{c_6}$$

$$\sigma_x = \underline{c_7 x^3} + \underline{c_8 x} + \underline{c_9} \qquad \sigma_y = d_1 x^3 \qquad \tau_{yz} = \tau_{xy} = 0$$

	Proposed Theory Elasticity	Timoshenko Elasticity	Euler-Bernoulli Elasticity
c_1	1.00	1.00	1.00
c_2	1.00	1.00	1.00
h_1	1.35	0.00	0.00
h_2	1.63	0.00	0.00
c_3	1.00	0.00	0.00
c_4	1.00	0.67	0.00
c_5	1.00	0.00	0.00
c_6	1.00	0.67	0.00
In the proposed theory, $\sigma_x = \sigma_y = d_1 x^3$; $d_1 \to 10^4$.			

Figure 15. Comparison of the stress compoments relative to the elasticity solutions of a simply supported beam.

FUTURE STUDIES

Future studies will include vibration analysis, methods to determine the warping functions for a typical beam cross section, geometrical nonlinearity, and an extension for composite beams. Basically the proposed theory will be extended for general cross sections and material definition (composite beams) such that they can be applied for any special case. (Fig. 16.)

FUTURE STUDIES :

- ---> **VIBRATION ANALYSIS**
- ---> **METHOD TO DETERMINE WARPING FUNCTIONS**
- ---> **GEOMETRIC NONLINEARITY**
- ---> **COMPOSITE BEAMS**

Figure 16. Future studies.

REFERENCES

1. Cowper, G. R. : The Shear Coefficient in Timoshenko's Beam Theory. ASME Journal of Applied Mechanics, June 1966, pp. 335-340.

PROBABILISTIC STRUCTURAL ANALYSIS BY EXTREMUM METHODS

AVINASH M. NAFDAY

EQE Engineering, Inc.

Costa Mesa, California

STRUCTURAL MODELS FOR SYSTEM RELIABILITY EVALUATION

Evaluation of structural system reliability is based on the determination of probabilistic response of structures. The study of probabilistic behavior of structural systems requires an underlying structural analysis model. The current system reliability analysis procedures utilize the structural analysis methods basically developed with a deterministic point of view. The applicability of these methods when dealing with a random situation needs examination. It may be that methods of structural analysis that are quite suitable for deterministic analysis are not as suitable for probabilistic analysis and vice versa. Development of structural system models especially suited for random state variables may be more efficient and likely to lead to important insights into random structural behavior. A recent National Science Foundation Workshop on Structural System Reliability held at the University of Colorado, Boulder [1] also emphasized the need for the development of structural analysis models from the probabilistic viewpoint.

The objective of this paper is to demonstrate discrete extremum methods of structural analysis as a tool for structural system reliability evaluation. Specifically, linear and multiobjective linear programming models for analysis of rigid plastic frames under proportional and multiparametric loadings, respectively, are considered. Kinematic and static approaches for analysis form a primal-dual pair in each of these models and have a polyhedral format. Duality relations link extreme points and hyperplanes of these polyhedra and lead naturally to dual methods for system reliability evaluation.

- **DIRECT METHOD**
  - **Formulation of the global limit state surface**
  - **Computation of probability of random variables having an outcome in the safe set**

- **INDIRECT METHOD**
  - **Identification of all failure modes**
  - **Computation of the probability of failure of individual modes**
  - **Evaluation of system reliability from modal probabilities**

LIMITATIONS OF CURRENT APPROACHES

It is known that the structural problems can be analyzed by idealizing these mathematically as either continuous or discrete models, leading respectively to the solution of differential or algebraic equations/inequalities. The underlying solution principles can be based on the solution of simultaneous equations or the use of extremum principles. In the sixties, Schmit and coworkers [2] briefly explored extremum methods for the deterministic structural analysis problems but found them to be not competitive with solution methods for simultaneous equations. However, in the use of simultaneous equations procedure for probabilistic structural analysis, one has to solve the structural analysis problem repeatedly for different realizations of random variables and this is computionally costly. Use of extremum principles, on the other hand, elucidates the mathematical structure of the problem corresponding to various random realizations of state variables. This structure is extremely coherent with a definite pattern about the solutions of the problem. An understanding of such patterns leads one to gain important insights into response under random variables without analyzing the structure for all such combinations. This coupled with use of recent computational advances in algorithms [3] and vector processing of information on supercomputers are likely to make these methods extremely attractive for use in probabilistic analysis. For example, recent research [4] shows extremum methods to be ideally suited for structural analysis required in the system reliability assessment of structures with rigid plastic material behavior.

- **STRUCTURAL ANALYSIS FOR RELIABILITY EVALUATION**
  - **Discrete/Continuous models**
  - **Classical methods, elastic/plastic**
  - **Extremum methods**
- **RESPONSE PATTERNS**
  - **Polyhedral response regions**
  - **Other response regions**
- **ADVANTAGES OF EXTREMUM METHODS**

EXTREMUM METHODS FOR STRUCTURAL ANALYSIS

Structural analysis requires both the calculation of the distribution of forces throughout the structure and the displaced state of the system under the action of applied loads. One of the fundamental features of structural analysis is the possibility of using either forces or displacements as basic variables, with the respective approaches referred to as static and kinematic methods. The algebraic relationship of the static and kinematic approaches are the mathematical transpose of each other, a feature known as the static-kinematic duality. If the structure is statically determinate, the number of equations is same as the number of variables, and the forces and displacements can be found easily from the solution of system of algebraic equations. For statically indeterminate structures, additional conditions reflecting the material constitutive relations must be introduced.

As an example, for redundant frame structures, partial satisfaction of structural constraints generates a subspace in R^n containing the solutions of interest and the final solution can be reached by some optimality criterion. The optimal solution gives the result corresponding to the solution by traditional methods. The power of the extremum methods, however, is that all the suboptimal solutions may also be obtained from the model, and these suboptimal solutions correspond to various random realizations of the variables. This set of available solutions has a rich underlying mathematical structure and such patterns have recently been studied for rigid plastic frames under proportional and multiparametric loading [4].

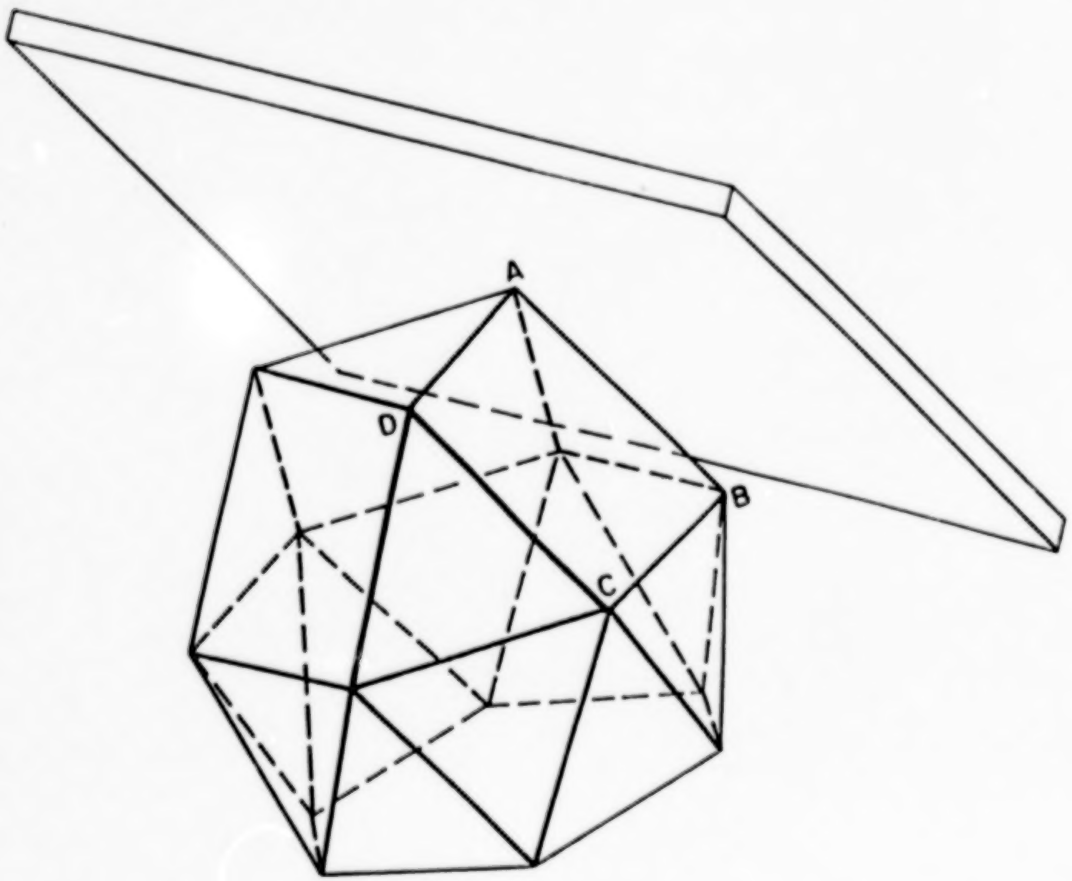

RIGID PLASTIC FRAMES WITH PROPORTIONAL LOADING

The problem of limit analysis of frames in which the plastic behavior is activated by a single stress resultant (such as flexure) may be formulated in terms of a Linear Programming (LP) model [5]. Plastic hinges are assumed to form at a set of discrete locations ($j = 1, 2, \ldots, J$) and the plastic moment capacity at the j^{th} section is denoted by Mp_j. Models formulated from dual structural consideration of static and kinematic principles have been shown to be a primal-dual pair in the LP format. The variables are M_j - moment at section j, $M_j = M_j^+ - M_j^-$ where M_j^+ and M_j^- represent the positive and negative values of moments; θ_j - rotation at section j; t_k - a coefficient indicating the contribution of the k^{th} elementary mode to collapse, $t_k = t_k^+ - t_k^-$ and λ^+, λ - collapse load factors for the kinematic and static LP's respectively. The parameters are θ_{kj} - hinge rotation of elementary mechanism k at joint j, e_k - external work associated with elementary mechanism k, M - number of equations of equilibrium and Mp_j - member capacity at section j.

KINEMATIC LP

$$\lambda = \text{Min} \left[\sum_{j=1}^{J} Mp_j \left(\theta_j^+ + \theta_j^-\right)\right]$$

$$\text{s.t.} \quad \theta_j^+ - \theta_j^- = \sum_{k=1}^{M} t_k \, \theta_{kj} \qquad j = 1, \ldots, J$$

$$\sum_{k=1}^{M} t_k \, e_k = 1$$

$$\theta_j^+, \theta_j^- \geq 0$$

STATIC LP

$$\lambda = \text{Max} \; \lambda^-$$

$$\text{s.t.} \quad \sum_{j=1}^{J} \theta_{kj} \, M_j = \lambda^- e_k \qquad k = 1, \cdots, M$$

$$-M_{p_j}^- \leq M_j \leq +M_{p_j}^+ \qquad j = 1, \cdots, J$$

DUALITY RELATIONS

A study of the geometric structure of the primal and dual models shows the constraint regions for both to be polyhedral. The failure modes of the frame are given by the extreme points of the kinematic constraint region and the facets of the static constraint region. Duality transformations of LP actually map extreme points of one model to the hyperplanes of the other and vice versa. More generally, 1-dimensional subspaces of the model in R^n are linked to (n-1) dimensional subspaces of the other model.

For primal, the random material properties specified by vector $\underline{Mp}$ occur only in the objective function and these determine the failure mode of the frame since the solution must surely belong to at least one of the extreme points. Therefore, unlike other procedures that require repeated solutions of structural model, one just needs to explore the polyhedral region for identifying the solution for a different (random) $\underline{Mp}$ vectors. Similarly, the vector $\underline{Mp}$ occurs only in the right hand side of static LP model and failure modes (facets) can be generated from the dual variables.

- **DUALITY**
  - **Static/Kinematic**
  - **Mathematical programming**
- **PHYSICAL INTERPRETATION**
  - **Limit states/Failure modes**
  - **Hyperplanes/Extreme points**
  - **Relationships**

RIGID PLASTIC FRAMES WITH MULTIPARAMETRIC LOADING

Proportional loading indicates a system of concentrated loads, each of which is proportional to a parameter, λ. However, the actual loading on the structures may not satisfy the restriction of proportional loading. It is necessary, in such cases, to consider the independent variation of load factor parameters for the various loads acting on the frame. A static multiobjective linear programming (MOLP) model has recently been formulated. Q (q = 1, 2, ..., Q) denote independent load parameters and C_{kj} and D_{kq} are the constant coefficients. Unlike scalar optimization problems, the vector optimal solutions are not completely ordered and there is no unique 'optimal' solution. The notion of an optimal solution is replaced by the concept of weak noninferior solution.

The geometrical structure of the MOLP static model shows that it has two different associated polyhedra instead of just one, as in LP models. These polyhedral regions are defined by the feasible regions of the MOLP model in the objective (load) space and decision (basic variable) space, respectively. The two polyhedral feasible regions have frontiers made up of only polyhedral facets. It has been shown [6] that maximal facets of these polyhedra correspond to the failure modes of the structure and union of all maximal facets gives the global limit surface for the frame.

STATIC MOLP MODEL

$$\text{Max} \quad \underline{\bar{\lambda}} = \text{Max}\{\lambda_1, \cdots, \lambda_Q\}^T$$

$$\text{s.t.} \quad \sum_{j=1}^{J} C_{kj} M_j - \sum_{q=1}^{Q} D_{kq} \lambda_q = 0$$

$$k = 1, \cdots, M$$

$$-M_{pj}^{-} \leq M_j = \leq M_{pj}^{+}$$

$$j = 1, \cdots, J$$

RESPONSE REGIONS

These response patterns for frames define the limits of variation of random variables and once such patterns are generated for a given structure, different solutions corresponding to any random vector must belong to the defined regions. Therefore, by considering powerful algorithmic methods developed in mathematical and computer science literature for extremum problems, alternative structural responses can be predicted without reanalysis of the structure. Often, it is possible to further simplify the procedure in some cases, based on the decomposition of parametric space. These procedures decompose the parametric space into mutually exclusive (non-overlapping) and collectively exhaustive subdomains corresponding to various failure modes [7]. This enables one to replace the consideration of an infinite number of parameter combinations with a finite number of parametric regions, which are also polyhedral. Multiparametric procedures lead to partitioning of both the load and basic variable space. All these procedures do not in any way depend on the probabilistic information. The probability considerations can be subsequently introduced to evaluate structural system reliability. This facilitates investigation of different loading conditions and probabilistic assumptions since reliability evaluations can be obtained without any further structural analyses.

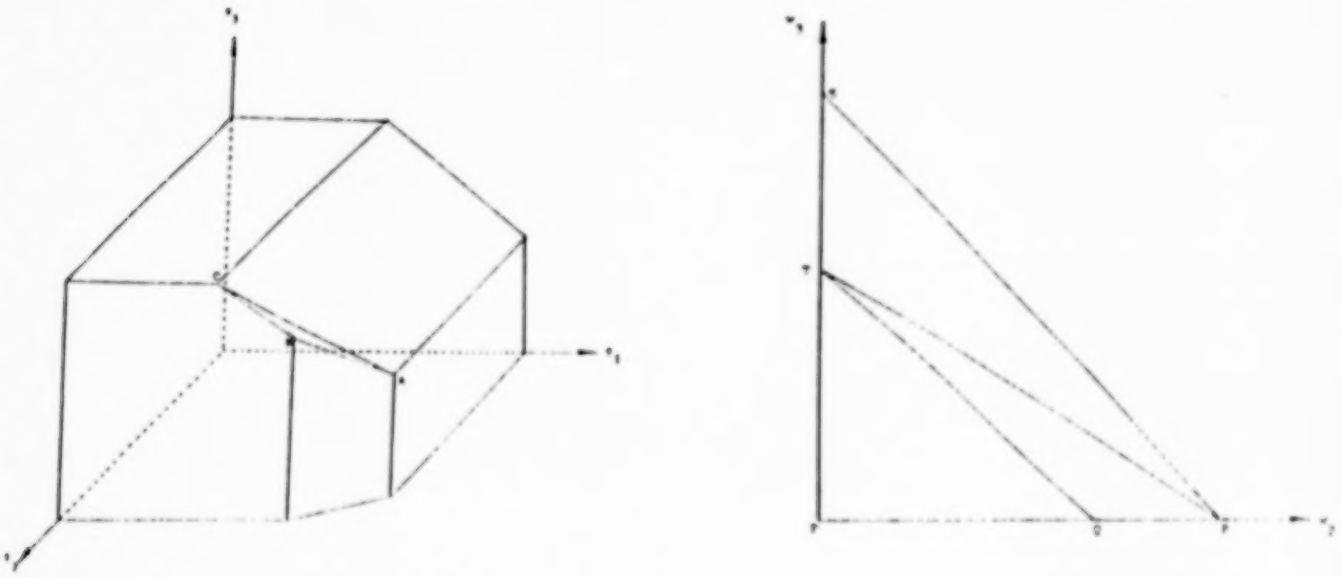

SYSTEM RELIABILITY EVALUATION

System reliability evaluation of frames for ultimate collapse is simplified by the use of structural responses generated by extremum procedures. For example, in the static case, a method has been proposed [8] which replaces the safe polyhedral response region of the frame with an analytically tractable region of equivalent volume, where the term volume is to be interpreted in a broad sense, since the volume may be of different dimensions and order. Reliability can be computed from the properties of the substituted region, which can be a parallelotope, hypersphere, hyperellipsoid, or any other suitable form. Use of hyperspherical equivalent region leads to the expression for structural system reliability in terms of the chi-square distribution.

System reliability evaluation of frames for ultimate collapse by the kinematic approach requires the enumeration of the failure modes, calculation of the probability of failure for each mode and then computation of the overall reliability by suitable aggregation. A simulation approach that exploits the special structure of the kinematic model has been proposed [9]. Load and resistance proportionalities are determined by each simulation, and the associated failure mode is identified as an extreme point of the LP model. The procedure gains its efficiency from the fact that every simulation derives an associated failure condition and its probability which are then combined into a system reliability.

- **SYSTEM RELIABILITY - STATIC APPROACH**
  - **Replacement of response regions by an equivalent region**
  - **Concept of equivalence**
  - **Hypersphere, parallelotope, hyperellipsoid**
- **SYSTEM RELIABILITY - KINEMATIC APPROACH**
  - **Generation of failure modes**
  - **Simulation procedure**

CONCLUSIONS

Extremum methods of structural analysis offer significant promise for advances in the analysis of random structural systems and their reliability assessment. The complexity of the physical problem and the randomness of the variables makes the solution otherwise intractable. Fortunately, the mathematical nature of the problem lends itself to mathematical programming formulations and use of powerful algorithmic procedures. This has been illustrated by consideration of rigid plastic frames subject to collapse by flexural action. Linear and multiobjective linear programming models were discussed for structural systems analysis under proportional and multiparametric loading, respectively. Duality relations between the static and kinematic approaches for each of these models and their response patterns lead naturally to alternative methods for system reliability evaluation.

Author's ongoing research aims to demonstrate the use of extremum methods for the reliability analysis of different structural systems for varying material behavior, structural dynamics problems and stability analysis. It is planned to explore structural behavior patterns with the objective of gaining insights into random structural behavior, dual relationships of patterns from static and kinematic considerations, causes of redundancy and the feasibility of using insights for the development of simplified and efficient computational methods for structural reanalysis and system reliability evaluation.

- **PROMISE OF EXTREMUM METHODS**
- **EXTENSIONS**
  - **Other structures**
  - **Material behavior models**
  - **Structural dynamics problems**
  - **Stability analysis**
- **REDUNDANCY**
- **STRUCTURAL REANALYSIS**
- **SIMPLIFIED METHODS FOR SYSTEM RELIABILITY**

REFERENCES

1. Frangopol, D.M. (Ed), "New Directions in Structural System Reliability," National Science Foundation Workshop on System Reliability Concepts and Techniques in Structural Analysis, Design and Optimization, University of Colorado, Boulder, September 12-14, 1988.

2. Schmit, L.A., F.K. Bogner, and R.L. Fox, "Finite Deflection Discrete Element Analysis using Plate and Shell Discrete Elements," AIAA Journal, Vol. 6, No. 5, 1968.

3 Karmarkar, N., "A New Polynomial-Time Algorithm for Linear Programming," Proceedings of the 16th Annual ACM Symposium on Theory of Computing, pp. 302-311.

4 Nafday, A.M., "Extremum Methods of Structural Analysis for System Reliability Assessment," Doctoral dissertation submitted to the Johns Hopkins University, Baltimore, February, 1987.

5. Cohn, M.Z., S.K. Ghosh, and S.R. Parimi, "Unified Approach to the Theory of Plastic Structures," Journal of Engineering Mechanics Division, American Society of Civil Engineers, Vol. 98, No. EM5, Oct. 1972, pp.1133-1158.

6. Nafday, A.M., R.B. Corotis, and J.L. Cohon, "Multiparametric Limit Analysis of Frames: Part I and II," Journal of Engineering Mechanics, American Society of Civil Engineers, Vol. 114, No. 3, 1988.

7. Nafday, A.M. and R.B. Corotis, "Parametric Decomposition for system reliability Evaluation," Second IFIP Conference on Reliability and Optimization of Structural Systems (Ed. P. Thoft Christensen), September 26-28, 1988, London, U.K.

8. Nafday, A.M., R.B. Corotis, and J.L. Cohon, "System Reliability of Rigid Plastic Frames," Reliability and Risk Analysis in Civil Engineering (Ed. N. C. Lind), ICASP-5, University of Waterloo, Canada, 1987.

9. Nafday, A.M. and R.B. Corotis, "Structural System Reliability using Linear Programming and Simulation," Journal of Structural Engineering, American Society of Civil Engineers, Vol. 115, No.10, October, 1989.

Probabilistic Failure Assessment with Application to Solid Rocket Motors

Darrell L. Jan, Barry D. Davidson, and Nicholas R. Moore
Jet Propulsion Laboratory
California Institute of Technology
Pasadena, California

Probabilistic Failure Assessment with Application to Solid Rocket Motors

Darrell L. Jan, Barry D. Davidson, and Nicholas R. Moore
Jet Propulsion Laboratory
California Institute of Technology

Introduction

A quantitative methodology is being developed at JPL for assessment of risk of failure of solid rocket motors. This probabilistic methodology employs best available engineering models and available information in a stochastic framework. The framework accounts for incomplete knowledge of governing parameters, intrinsic variability, and failure model specification error. Earlier case studies have been conducted on several failure modes of the Space Shuttle Main Engine (refs. 1,2,3). This paper describes work in progress on application of this probabilistic approach to large solid rocket boosters such as the Advanced Solid Rocket Motor for the Space Shuttle. Failure due to debonding has been selected as the first case study for large solid rocket motors (SRMs) since it accounts for a significant number of historical SRM failures. Impact of incomplete knowledge of governing parameters and failure model specification errors is expected to be important.

Debond Failure in SRMs

SRM failure modes generally fall into the categories of debonding, nozzle failure, propellant cracking, combustion instability, field joint failure, O-ring failure, and case burst. As an initial case study, this work is focussing on failure due to debonding. Motivation for looking at debond failure is clear, as stated in reference 4:

> It is probably a conservative estimate that well over half of all mishaps (and this includes the latest space shuttle disaster) are due to the flame front prematurely reaching the chamber walls, or getting into places where it should not. Usually the cause is a failure of the propellant-liner bond, or the propellant-to-insulation bond, and sometimes insulation to chamber wall bond.

The problem of solid propellant debonding has received considerable attention in the literature. For example, in reference 5, a finite element computer code was developed for evaluation of the state of stress in solid propellant case liner bond regions. Also, a closed form fracture mechanics solution which accounts for the dissimilar material properties on either side of the bondline was proposed for predicting debond growth. Reference 6 discussed both stress-strain and fracture mechanics techniques for predicting bondline failures.

The underlying chemistry and environment of the bond region are quite complex. These issues are addressed in references 7 and 8. However it may not be necessary to incorporate all of the complexity considered in these references in order to satisfactorily assess reliability. Inherent variability of various parameters in the bonded region may be accounted for through the statistical approach described briefly below, and in detail in reference 1.

The Debond Failure Mode. The sequence of events leading to failure by debonding is shown in Figure 1. Failure due to debonding begins as a defect, or crack, in the bond region, referred to as the "Initial State" in Figure 1. This defect may occur as a result of normal manufacturing processes, or perhaps as a result of foreign particle inclusion. In general there will be a distribution of size and locations of a number of defects. These defects may grow prior to launch as a result of induced bondline stresses from shipping

and handling loads, thermal cycling, and moisture absorption. Additional defect growth may result from vibrations during launch, axial acceleration, case pressurization, aerodynamic heating, or vibrational loads. The result can be a defect of a certain size and location such that the flame front can enter the defect region. The debonded region contributes additional surface area for burning. This can lead to uneven burn and increased pressure. If the pressure becomes higher than the design pressure, it can cause mechanical deformation and further defect growth. Case burn-through becomes a possibility, and detonation can result if the pressure rise is rapid enough (ref. 9).

The Probabilistic Failure Assessment (PFA) Methodology.

The PFA Methodology developed at JPL is a quantitative technique for estimating reliability warranted by the available information. (See reference 1 for a detailed description of PFA.) For cases of unacceptable risk, PFA identifies areas where design improvement and/or additional data are required.

The core of the PFA approach consists of analytical engineering models which characterize failure phenomena in terms of governing parameters. Such failure models typically express a failure parameter such as burst pressure, flaw size, or flaw growth rate, as a function of "drivers." These drivers, i.e., the governing parameters, determine the value of the failure parameter. The drivers usually include geometry and dimensions, loads and environmental conditions, and relevant material properties for the operating environment.

In this probabilistic approach, the drivers are characterized by probability distributions These probability distributions express uncertainty regarding driver values within the ranges of possible values. The accuracy of the failure model is treated as another driver which is probabilistically characterized. The probability distributions for the drivers are derived from available information regarding uncertainty of their values. The drivers are characterized using the information that exists at the time of the analysis. There is no specific information requirement for any driver.

The driver distributions reflect incomplete knowledge and limited information regarding driver values as well as intrinsic variability. The criteria of not overstating the available information in the driver probability distributions must be observed in order to appropriately represent the risk that results from incomplete knowledge and limited information.

Performance, weight, and cost requirements that propulsion systems must meet may not permit consistently, verifiably conservative values for analysis parameters to be used in all cases. Deterministic analyses for such applications must be "calibrated" by means of directly relevant past experience with applications that are similar in terms of the knowledge of input parameters, the validity of engineering models under the conditions of an application, and variability of manufacturing processes.

When deterministic analyses are used in applications that are removed from the directly relevant experience base, as is often the case for launch vehicle propulsion systems, the uncertainty or risk associated with their results increases. Since a deterministic analysis provides no quantitative risk estimate, an assessment of risk incurred as a result of having chosen any specific set of values for the governing parameters of the analysis must be left to the vicissitudes of judgment formed in the absence of directly relevant experience.

Deterministic analyses of failure modes under such conditions of limited information thus becomes arbitrary. Launch vehicle propulsion systems are invariably subject to some number of failure modes for which the governing parameters may not be well known, e.g.,

the knowledge of loads and/or local environments may be significantly uncertain and the validity of analytical models used to characterize failure phenomena may be questionable. Under such conditions of limited information and uncertain analyses, the implicit consideration of risk by means of qualitative judgments based on deterministic analysis of failure modes is inadequate.

In contrast, the PFA Methodology quantitatively accounts for driver specification error through appropriate formulation of the driver probability distribution. Application of a Monte Carlo technique using the driver distributions, coupled with the engineering model, produces a set of simulated failures. These simulated failures are then fit to a parametric failure distribution which is treated as a Bayesian prior distribution. This prior distribution is then modified using Bayesian updating to incorporate test and flight experience. The result is a posterior probability distribution for the failure mode. Overall mission risk can be estimated by aggregation of critical failure mode results.

The resultant risk may be judged to be acceptable or unacceptable. If risk is unacceptable, the framework of the PFA analysis facilitates the procedure for choosing actions which will reduce the risk. The effect on risk, for example, of acquiring additional data, improving the engineering model, or making design changes, can be determined directly and quantitatively.

Application of PFA Methodology to Debonding.

At this writing, a flowchart for the engineering model for debonding has been developed. The model, shown in Figure 2, incorporates the processes described in the debond failure mode description above. Standard nomenclature is used: K_I and K_{II} are the mode I and mode II stress intensity factors, respectively. It is expected that some parts of the flowchart will require more detail while other parts represent unnecessary detail, and will be revised. For example, finite element and finite difference calculations are incorporated in the flowchart loop. These would be extremely demanding of computational time if they were required to be within the Monte Carlo analysis. Considerations of this type have been encountered before (refs. 2 & 3), and some techniques have been found which help minimize cpu time. Modifications of the Monte Carlo approach and alternative methods will also be considered.

It is important to reiterate that the risk assessment will be made using available information--no additional program to develop data is required (although advantage will be taken of such opportunities, in particular appropriate information from the Solid Propellant Integrity Program, ref. 10, will be utilized). For example, variability or scarcity of data in material properties can be accounted for statistically. If the resultant risk is unacceptable, the structure of the PFA methodology can suggest options which will have the greatest impact on the risk estimate. Possible options include design or processing changes, improved inspection capability, acquisition of additional materials characterization data, and reduction in uncertainty of engineering models.

Interaction with experts in the SRM industry have been and will continue to play an important role in technical development of this program.

Acknowledgments

This research described in this paper was carried out by the Jet Propulsion Laboratory, California Institute of Technology, under a contract with the Air Force Astronautics Laboratory and the National Aeronautics and Space Administration.

DEBOND FAILURE PROCESSES

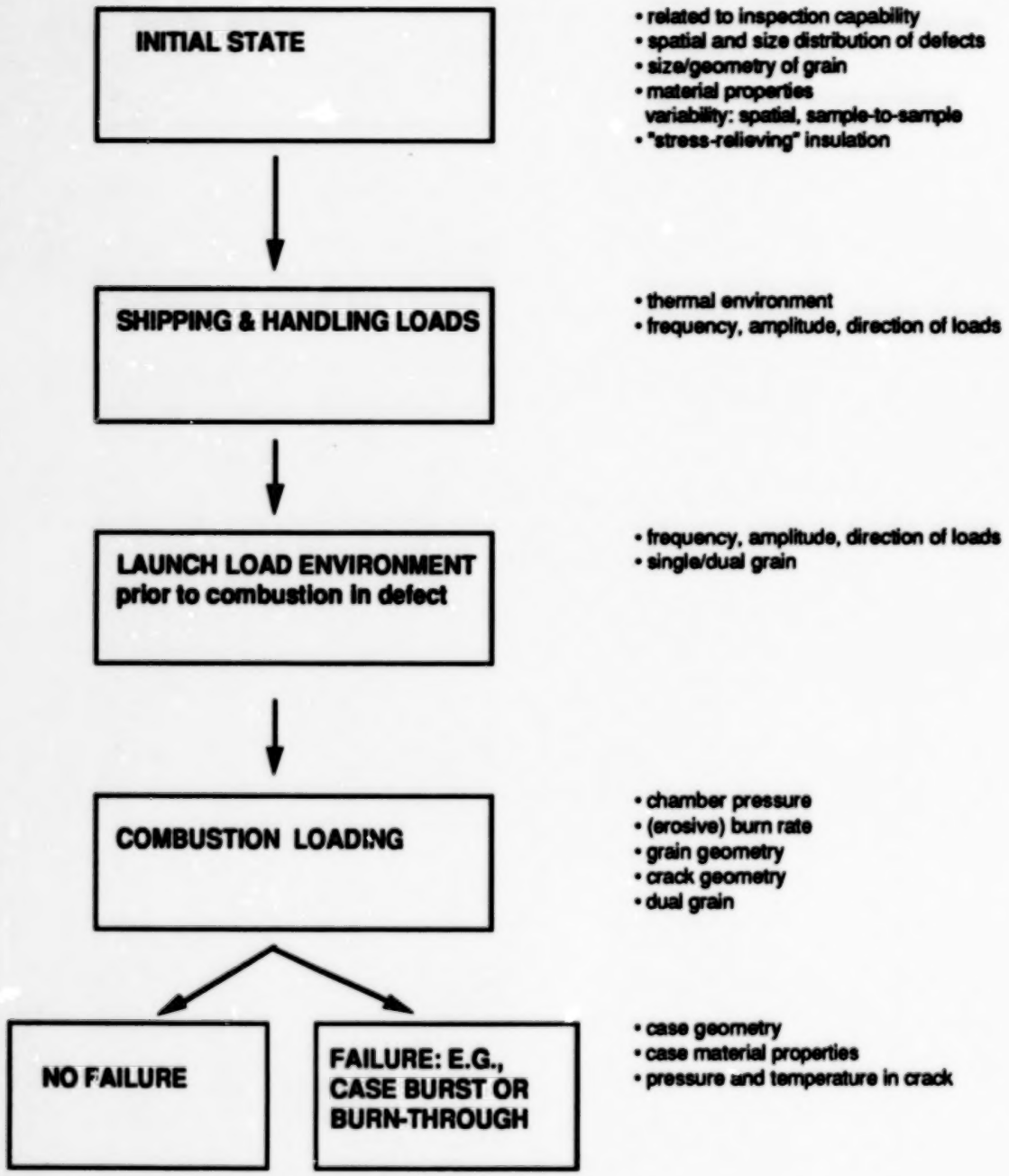

Figure 1. Diagram of debonding processes. Comments to the right of the boxes represent a partial list of relevant factors.

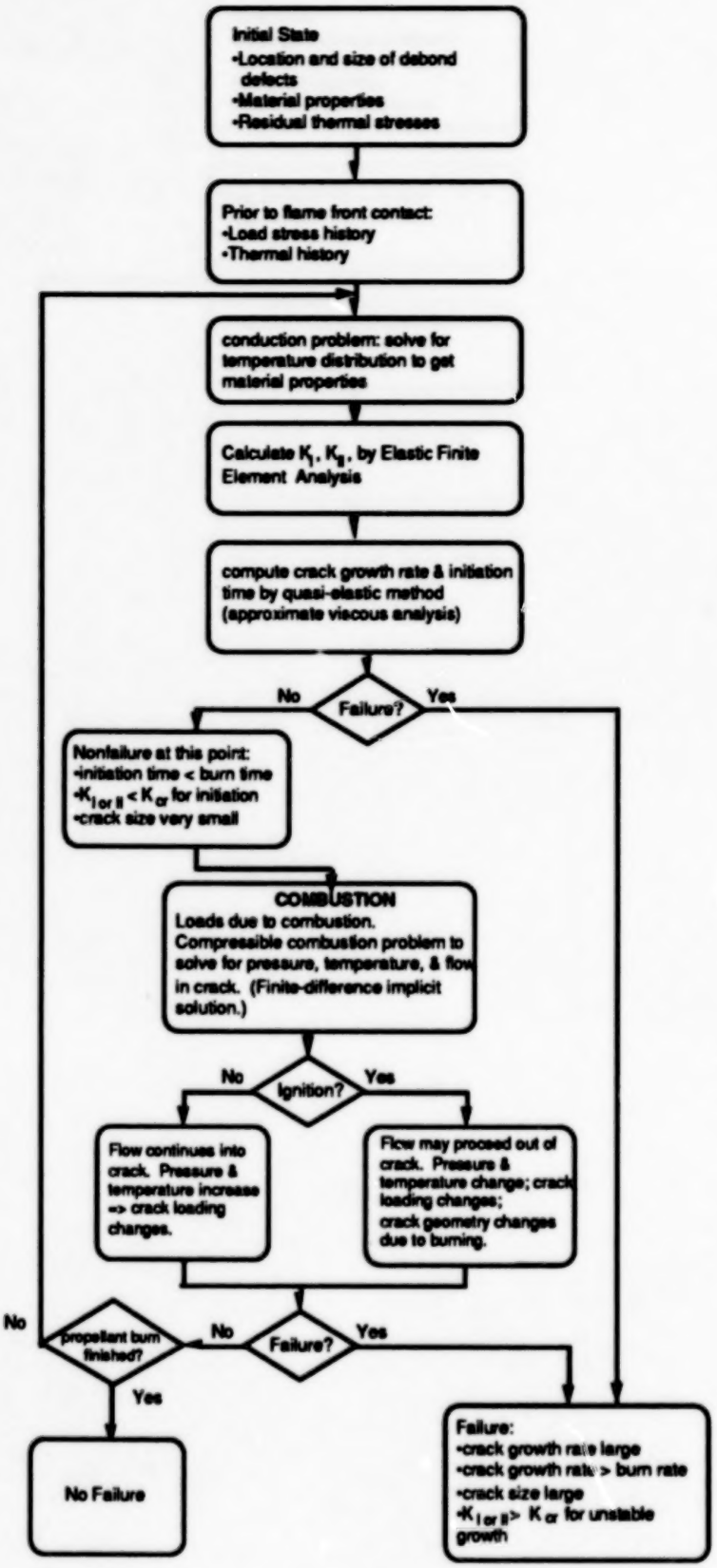
Initial State
•Location and size of debond defects
•Material properties
•Residual thermal stresses
Prior to flame front contact:
•Load stress history
•Thermal history
conduction problem: solve for temperature distribution to get material properties
Calculate K_I, K_{II}, by Elastic Finite Element Analysis
compute crack growth rate & initiation time by quasi-elastic method (approximate viscous analysis)
No
Failure?
Yes
Nonfailure at this point:
•initiation time < burn time
•$K_{I \text{ or } II} < K_{cr}$ for initiation
•crack size very small
COMBUSTION
Loads due to combustion. Compressible combustion problem to solve for pressure, temperature, & flow in crack. (Finite-difference implicit solution.)
No
Ignition?
Yes
Flow continues into crack. Pressure & temperature increase => crack loading changes.
Flow may proceed out of crack. Pressure & temperature change; crack loading changes; crack geometry changes due to burning.
No
propellant burn finished?
No
Failure?
Yes
Yes
No Failure
Failure:
•crack growth rate large
•crack growth rate > burn rate
•crack size large
•$K_{I \text{ or } II} > K_{cr}$ for unstable growth

Figure 2. Flowchart of PFA debond model.

References:

1. Moore, N., et al, "A Methodology for Probabilistic Prediction of Structural Failures of Launch Vehicle Propulsion Systems, " AIAA 31st Structures, Structural Dynamics, and Materials Conference, April, 1990.

2. Newlin, L., et al, " Probabilistic Low Cycle Fatigue Failure Analysis with Application to Liquid Propulsion Rocket Engines," AIAA 31st Structures, Structural Dynamics, and Materials Conference, April, 1990.

3. Sutharshana, S., et al, " Probabilistic High Cycle Fatigue Failure Analysis with Application to Liquid Propulsion Rocket Engines," abstract submitted to the 31st Structures, Structural Dynamics, and Materials Conference, April, 1990.

4. Oberth, Adolf. E.: Principles of Solid Propellant Development. CPIA Publication 469, September 1987.

5. Francis, E. C.; Deverall, L. I., Carlton, C. H., Zitzer, H. J., Knauss, W. G., Becker, E. B., Dunham, R. S.: Case Liner Bond Analysis, AFRPL-74-23, July 1974.

6. Predictive Techniques for Failure Mechanisms in Solid Rocket Motors, AFRPL-TR-79-87, January 1980.

7. Liu, E. K.; McCamey, R. K.: Ballistic Missile Bonding Technology, AFRPL-TR-86-084, June 1987.

8. Fitzgerald, J. E.; Hufferd, W. L.: Handbook for the Engineering Structural Analysis of Solid Propellants, CPIA Publication 214, May 1971.

9. Kumar, M.; Kuo, K.K.: Chapter 6. Flame Spreading and Overall Ignition Transient, in Fundamentals of Solid Propellant Combustion, K. K. Kuo, editor, AIAA Progress in Astronautics and Aeronautics series, 1984.

10. Annual Review of the Bondlines Work Package of the Solid Propellant Integrity Program, held at Science Applications International Corporation, December 12-13, 1989.

GLOBAL OPTIMIZATION METHODS FOR ENGINEERING DESIGN

Jasbir S. Arora

OPTIMAL DESIGN LABORATORY

College of Engineering
The University of Iowa
Iowa City, IA 52242-1593

PROBLEM DEFINITION

The problem is to find a global minimum for the Problem P. Necessary and sufficient conditions are available for *local optimality*. However, global solution can be assured only under the assumption of convexity of the problem. If the constraint set S is compact and the cost function is continuous on it, existence of a global minimum is guaranteed. However, in view of the fact that *no global optimality conditions* are available, a global solution can be found only by an *exhaustive search* to satisfy Inequality (5). The exhaustive search can be organized in such a way that the entire design space need not be searched for the solution. This way the computational burden is reduced somewhat.

Problem P: Find a design variable vector $\mathbf{x}$ to minimize a cost function

$$f(\mathbf{x}) \text{ for } \mathbf{x} \in S \subset R^n \tag{1}$$

where S is the constraint set defined as

$$S = \{\mathbf{x} \mid g_i(\mathbf{x}) = 0,\ i = 1 \text{ to } p;\ g_i(\mathbf{x}) < 0,\ i = (p+1) \text{ to } m\} \tag{2}$$

Local Minimum $\mathbf{x}^*$

$$f(\mathbf{x}^*) \leq f(\mathbf{x}) \text{ for all } \mathbf{x} \in N(\mathbf{x}^*,\delta) \cap S \tag{3}$$

$$N(\mathbf{x}^*,\delta) = \{\mathbf{x} \mid \|\mathbf{x}-\mathbf{x}\| < \delta\} \tag{4}$$

Global Minimum $\mathbf{x}^*$

$$f(\mathbf{x}^*) \leq f(\mathbf{x}) \text{ for all } \mathbf{x} \in S \tag{5}$$

GLOBAL OPTIMIZATION ALGORITHMS

Most global optimization methods developed in the literature are for the unconstrained problems. It is generally assumed that the constraints can be handled by adding a penalty term to the cost function. Therefore, unconstrained algorithms can be useful. Some of the methods date as far back as 1960s. In the following, we outline some of the algorithms that have been presented in the literature.

The Tunneling Method

The tunneling method was initially developed for unconstrained problems and then extended to the constrained problems [1]. The basic idea of the method is to first find a local minimum $\mathbf{x}^*$ for the function $f(\mathbf{x})$. Any reliable and efficient method can be used in this step. Once this has been done another starting point is found that is different from $\mathbf{x}^*$ but has cost function value as $f(\mathbf{x}^*)$. This can be expressed as a problem of finding root of the nonlinear equation

$$f(\mathbf{x}) = f(\mathbf{x}^*) \tag{6}$$

that is different from $\mathbf{x}^*$. Again, any reliable and efficient algorithm for finding roots of nonlinear equations, such as the stabilized Newton's method can be used. Once the root of Eq. (6) has been obtained, the method to determine local minimum of $f(\mathbf{x})$ is used to determine the new solution point. The process is repeated until there is no other root of Eq. (6) except $\mathbf{x} = \mathbf{x}^*$. The nonlinear function defined in Eq. (6) or its modification is called the tunneling function. The phase where root of Eq. (6) is sought is called the *tunneling phase*.

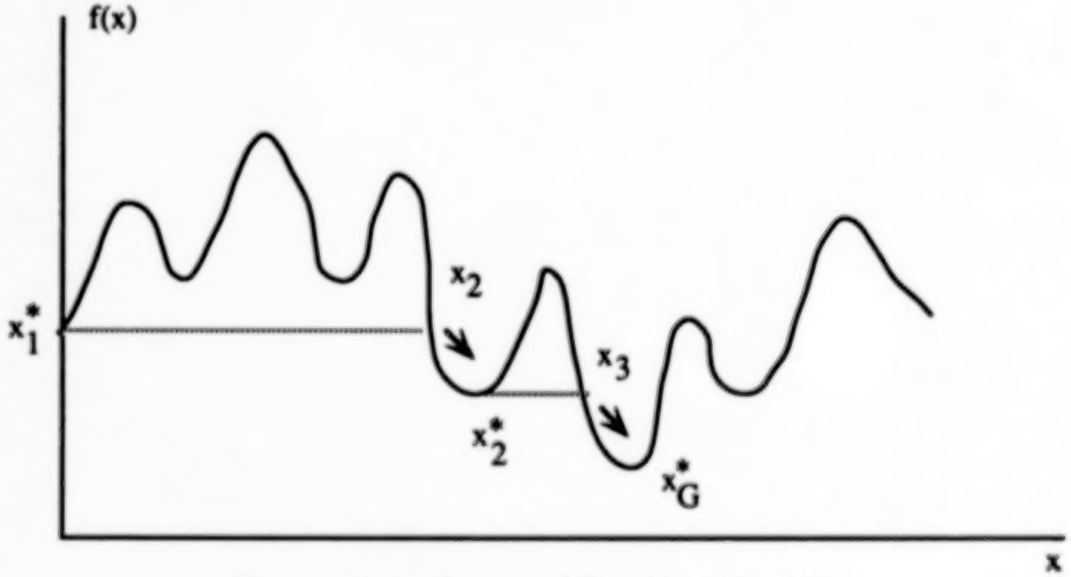

Figure Basic Concept of Tunneling Algorithm. The Algorithm tunnels below irrelevant minima and approaches the global minimum in an orderly manner [1].

GLOBAL OPTIMIZATION ALGORITHMS (Cont'd)

Stochastic Methods

These methods are based on statistical concepts [2,3].

Random Search
- Global-Local Phase
- Multistart
- Region of Attraction
- Clustering Method

The Annealing Algorithm

This algorithm, also based on probabilistic concepts, can be used to find global optimum solution [4].

Can be used for discrete variables
Analogy between Combinatorial Optimization and Annealing Process
Concept of Statistical Mechanical System
H(x): Hamiltonian (total energy)

Boltzmann-Gibbs Distribution:

$$p(x) = \frac{1}{Z} \exp\{-H(x)/T\} \tag{7}$$

where T is a temperature and Z is a normalization constant (statistical sum).

Let x^* be the equilibrium configuration of the system, i.e.,

$$H(x^*) = \min_{x \varepsilon S} H(x) \tag{8}$$

Then the probability of the equilibrium state is maximal, i.e.,

$$p(x^*) = \max_{x \varepsilon S} p(x) \tag{9}$$

The Genetic Algorithm

This method is also in the category of stochastic search method, such as the simulated annealing [5,6], in that both methods have their basis in *natural processes*.

Suitable for Discrete Variable Optimization

Three Operators:
1. Reproduction
2. Crossover
3. Mutation

ZOOMING ALGORITHM FOR GLOBAL MINIMUM SOLUTION

This new global minimization algorithm combines a local minimization algorithm with successive refinements of the feasible region to eliminate regions of local minimum points to "zoom-in" on the global solution. The basic idea is to initiate the search for a local minimum from any point - feasible or infeasible point. Once a local minimum point has been found, the problem is redefined such that the current solution is eliminated from any further search. The search process is reinitiated and a new minimum point is found. The process is continued until no other minimum point can be found.

Once a local minimum point has been obtained, the problem is redefined by adding an additional constraint as follows:

minimize $f(\mathbf{x})$

subject to

$$g_i(\mathbf{x}) = 0, \quad i = 1 \text{ to } p$$

$$g_i(\mathbf{x}) \leq 0, \quad i = (p+1) \text{ to } m$$

$$f(\mathbf{x}) \leq \gamma f(\mathbf{x}^*) \tag{10}$$

where $f(\mathbf{x}^*)$ is the cost function value at the current minimum point and γ is any number between 0 and 1 if $f(\mathbf{x}^*) > 0$, and $\gamma > 1$ if $f(\mathbf{x}^*) < 0$. Constraint of Eq. (10) can be written differently as follows:

$$f(\mathbf{x}) \leq c \tag{11}$$

$$f(\mathbf{x}) \leq f(\mathbf{x}^*) - r\,|f(\mathbf{x}^*)| \tag{12}$$

where $c < f(\mathbf{x}^*)$ and $0 < r < 1$.

EXAMPLE ILLUSTRATING THE CONCEPT

Minimize $f(x) = -(x_1 - 1.5)^2 - (x_2 - 1.5)^2$

subject to

$$x_1 + x_2 - 2 \leq 0$$
$$-x_1 \leq 0, \quad -x_2 \leq 0$$

There are three local minimum points:

1. (0,2), f = -2.5
2. (2,0), f = -2.5
3. (0,0), f = -4.5

The figure illustrates the basic concept of zooming algorithm.

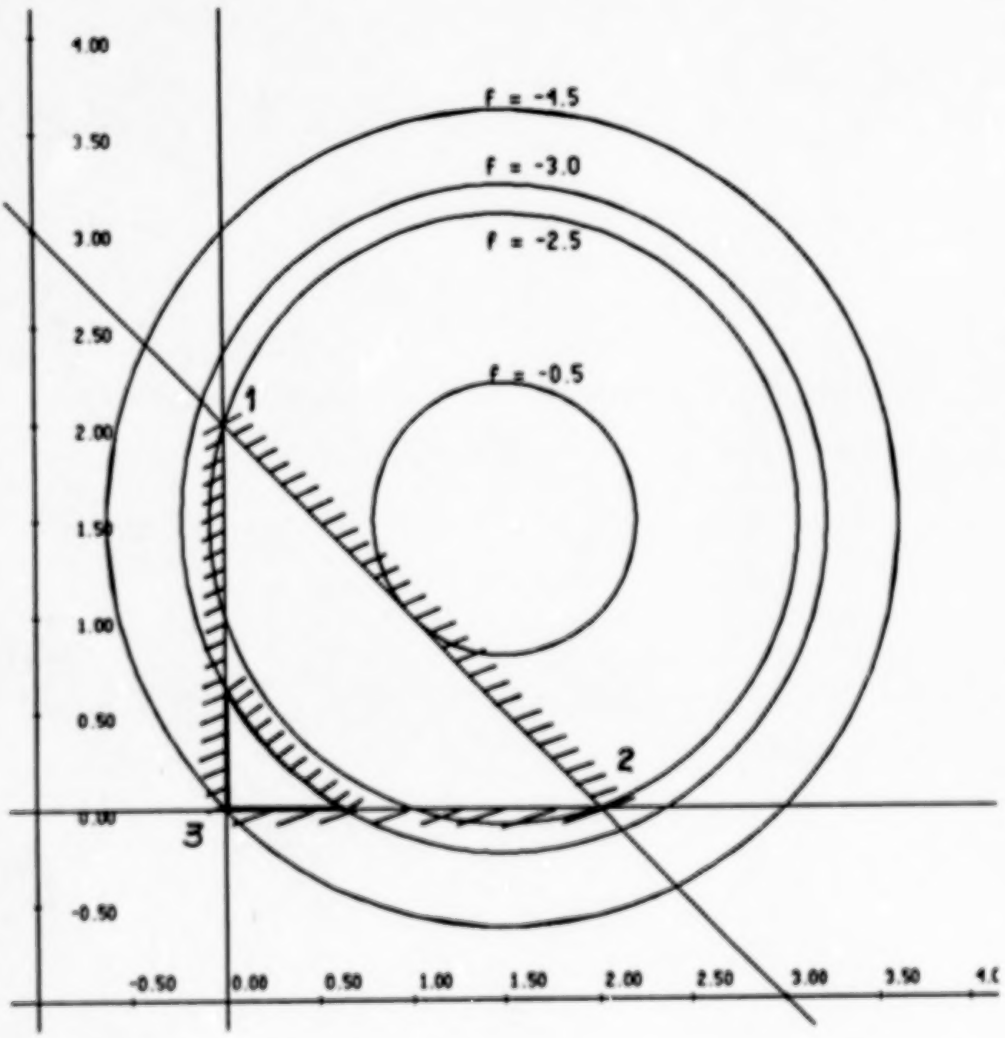

Figure: Graphical Solution for the Example

NUMERICAL EXAMPLE

Minimize $f(x) = 9x_1^2 + 18x_1x_2 + 13x_2^2$

subject to

$$x_1^2 + x_2^2 + 2x_1 = 16$$

This problem has two local minimum points:

1. (2.5945,-2.0198), f = 19.291
2. (-3.7322,3.0879), f = 41.877

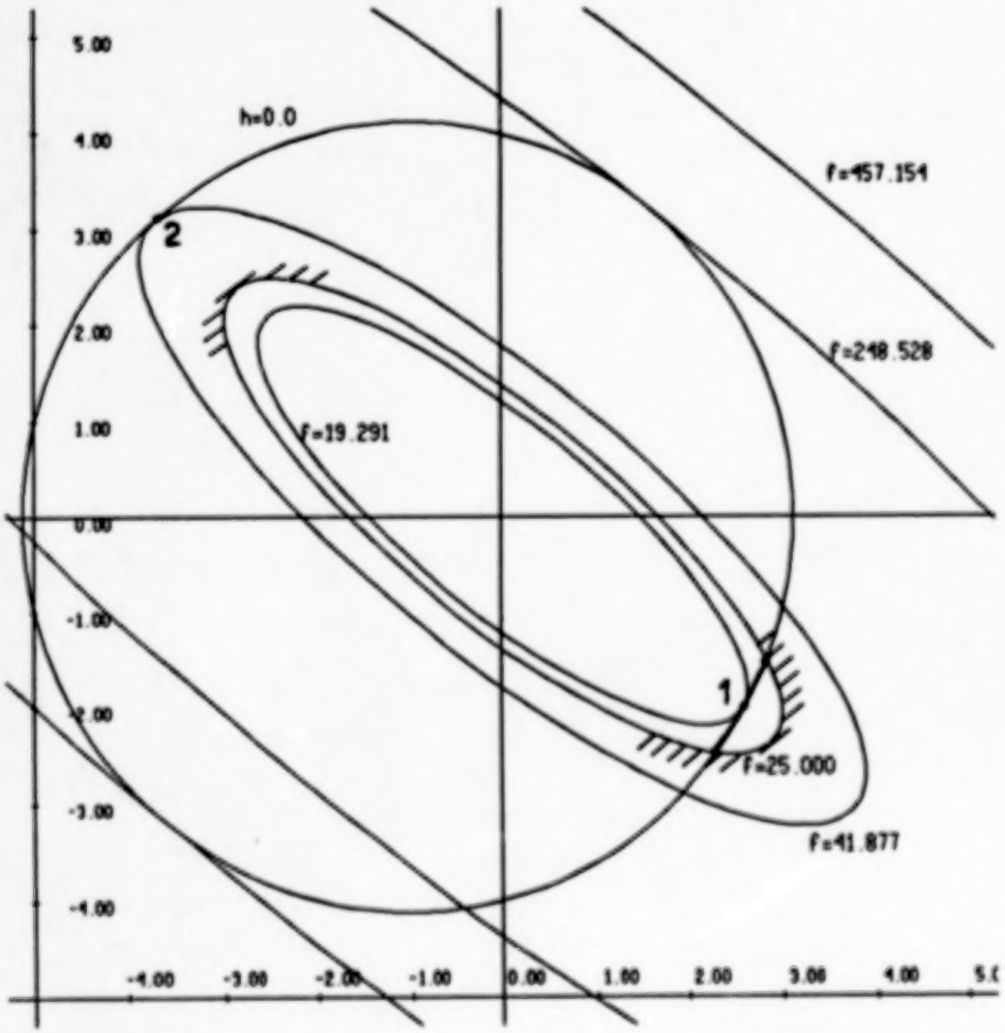

Figure: Graphical Solution for the Example

NUMERICAL EXAMPLE

Minimize $f = 2x_1 + 3x_2 - x_1^3 - 2x_2^2$

subject to

$$x_1 + 3x_2 \leq 6$$
$$5x_1 + 2x_2 \leq 10$$
$$x_1, x_2 \geq 0$$

This problem has four local minimum points:

1. (0,0), f = 0.0
2. (2,0), f = -4.0
3. (0,2), f = -2.0
4. (1.38462,1.53846), f = -0.003654

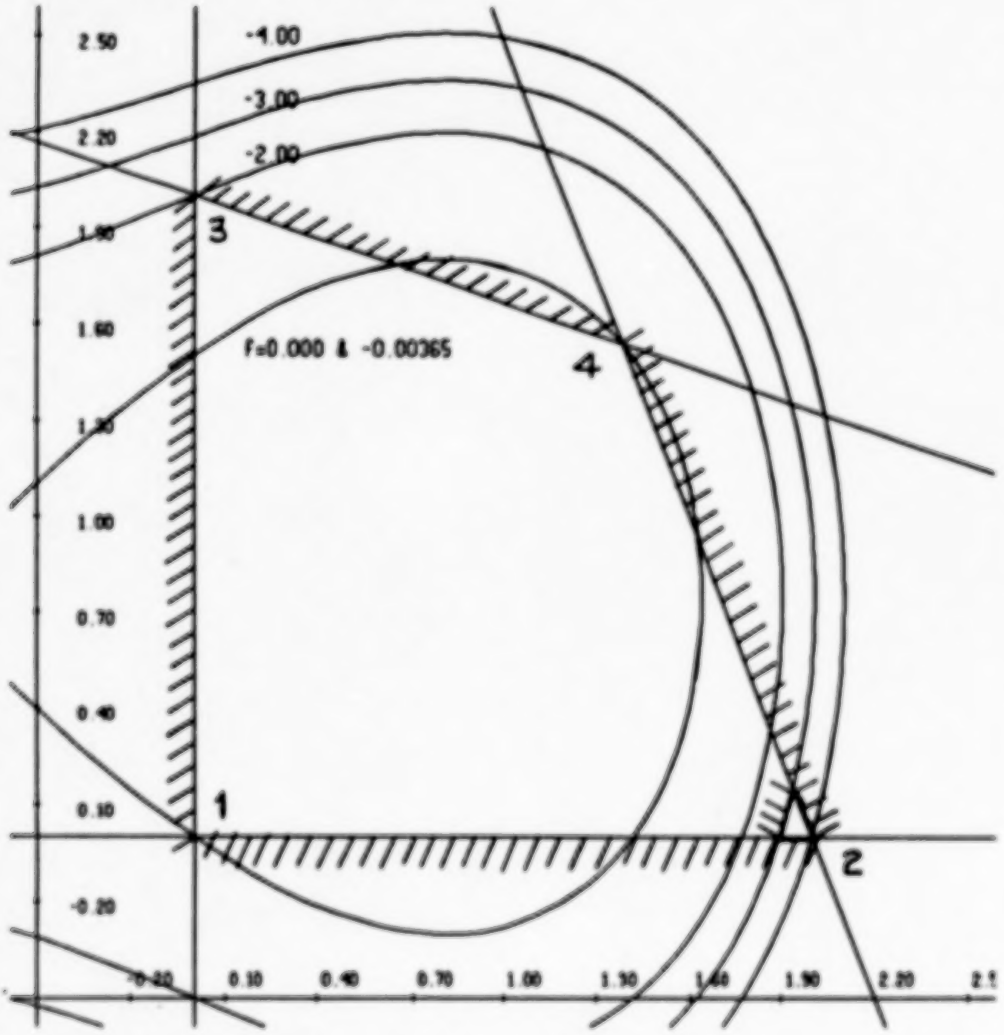

Figure: Graphical Solution for the Example

SIMULTANEOUS CONTROL AND DESIGN OF STRUCTURES

Problem Formulation [7,8]

State Equation: $\dot{\mathbf{x}} = \mathbf{A}\mathbf{x} + \mathbf{B}\mathbf{f}$

$$\mathbf{A} = \begin{bmatrix} \mathbf{0} & \mathbf{I} \\ -\boldsymbol{\omega}^2 & -2\boldsymbol{\zeta}\boldsymbol{\omega} \end{bmatrix}, \quad \mathbf{B} = \begin{bmatrix} \mathbf{0} \\ \boldsymbol{\phi}^T\mathbf{D} \end{bmatrix}$$

Performance Index:

$$PI = \int_0^t [(\mathbf{x},\mathbf{Q}\mathbf{x}) + (\mathbf{f},\mathbf{R}\mathbf{f})]dt$$

State Feedback Control Law:

$$\mathbf{f} = -\mathbf{G}\mathbf{x}, \quad \mathbf{G} = \mathbf{R}^{-1}\mathbf{B}^T\mathbf{P}$$

$$\mathbf{A}^T\mathbf{P}^T - \mathbf{P}\mathbf{B}\mathbf{R}^{-1}\mathbf{B}^T\mathbf{P} + \mathbf{P}\mathbf{A} + \mathbf{Q} = \mathbf{0}$$

Close-Loop System: $\dot{\mathbf{x}} = \bar{\mathbf{A}}\mathbf{x}$

$$\bar{\mathbf{A}} = \mathbf{A} - \mathbf{B}\mathbf{G}$$

Complex Eigenvalues and Damping of Close-Loop System

$$\lambda_i = \tilde{\sigma}_i \pm j\,\tilde{\omega}_i$$

$$\xi_i = -\tilde{\sigma}_i/(\tilde{\sigma}_i^2 + \tilde{\omega}_i^2)^{1/2}$$

EXAMPLE: ACOSS-IV Model

Minimize weight, $W = \Sigma \rho_i A_i L_i$

subject to $\xi_j^* - \xi_j \le 0, \quad j = 1,2,..$

$\omega_j^* - \tilde{\omega}_j \le 0, \quad j = 1,2,..$

$A_{i\ell} - A_i \le 0,$

$\tilde{\omega}_1 = 1.341, \quad \tilde{\omega}_2 \ge 1.3, \quad \xi_i = 0.1093, \quad i = 1 \text{ to } 4$

For Global Solution: $W \le W^*$

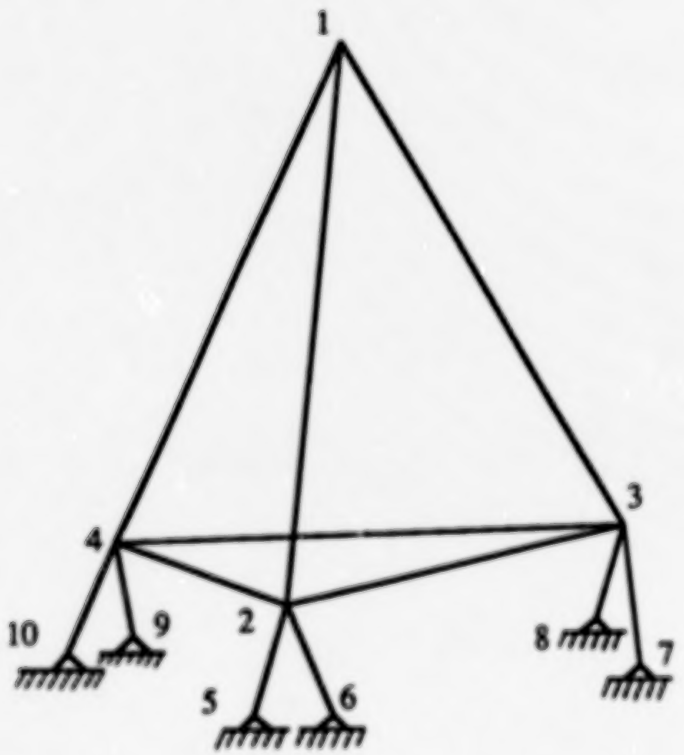

Figure: ACOSS-IV Model

RESULTS FOR 12-BAR ACOSS-IV MODEL

Problem No. →	1	2	3	4	5
Cost Constraint (W*)	100.0	28.00	24.00	20.75	19.00
Optimum Weight	31.25	28.00	23.29	20.75	No sol.
No. of Iterations	35	26	36	28	35

Starting Point for all problems:

$A_i = 1000$ for i = 1,2,5,6; $A_i = 100$ for others

$A_{i\ell} = 10$, i = 1 to 12

Convergence criteria:

Constraint Feasibility $\leq 0.1\%$

$\|\text{Search Direction}\| \leq 0.01$

CONCLUSIONS

1. Zooming algorithm for global optimizations appears to be a good alternative to stochastic methods. More testing is needed.

2. A general, robust, and efficient local minimizer is required. IDESIGN [9] was used in all numerical calculations which is based on a sequential quadratic programming algorithm.

3. Since feasible set keeps on shrinking, a good algorithm to find an initial feasible point is required. Such algorithms need to be developed and evaluated.

REFERENCES

1. Levy, A.V. and Gomez, S., 1985, "The Tunneling Method Applied to Global Optimization," in *Numerical Optimization 1984*, P.T. Boggs et al., Eds., Society for Industrial and Applied Mathematics, Philadelphia, PA.

2. Rinnooy Kan, A.H.G. and Timmer, G.T., 1985, "A Stochastic Approach to Global Optimization," in *Numerical Optimization 1984*, P.T. Boggs, et al., Eds., Society for Industrial and Applied Mathematics, Philadelphia, PA.

3. Rinnooy Kan, A.H.G., Boender, C.G.E., and Timmer, G.T., 1985, "A Stochastic Approach to Global Optimization," in *Computational Mathematical Programming*, K. Schittkowski, Ed., Series F: Computer and System Sciences, Vol. 15, Springer-Verlag, pp. 281-308.

4. Elprin, T., 1988, "Monte Carlo Structural Optimization in Discrete Variables with Annealing Algorithm," *Int. J. for Num. Meth. in Engrg.*, Vol. 26, pp. 815-821.

5. Goldberg, D.E. and Kuo, C.H., 1987, "Genetic Algorithms in Pipeline Optimization," *J. of Computing in Civil Engrg.*, Vol. 1, No. 2, April, pp. 128-141.

6. Hajela, P., 1989, "Genetic Search - An Approach to the Nonconvex Optimization Problem," proceedings of the 30th AIAA/ASME/ASCE/AHS Structures, Structural Dynamics and Materials Conference, Mobile, Alabama, April, pp. 165-175.

7. Khot, N.S., Eastep, F.E. and Venkayya, V.B., "Optimal Structural Modifications to Enhance the Optimal Active Vibration Control of Large Flexible Structures," *AIAA Journal*, Vol. 24, No. 8, August 1986, pp. 1368-1374.

8. Grandhi, R.V., "Structural and Control Optimization of Space Structures," *Computers and Structures*, Vol. 31, No. 2, 1989, pp. 139-150.

9. Arora, J.S., *IDESIGN User's Manual*, Optimal Design Laboratory, College of Engineering, The University of Iowa, Iowa City, IA 52242 USA, 1989.

EXPONENTIAL APPROXIMATIONS IN OPTIMAL DESIGN

A. D. Belegundu, M. AIAA
Mechanical Engineering Department
The Pennsylvania State University
University Park, PA 16802

S. D. Rajan
Civil Engineering Department
Arizona State University
Tempe, AZ 85287

J. Rajgopal
Department of Industrial Engineering
University of Pittsburgh
Pittsburgh, PA 15261

Abstract

One-point and two-point exponential functions have been developed and proved to be very effective approximations of structural response. The exponential has been compared to the linear, reciprocal and quadratic fit methods. Four test problems in structural analysis have been selected. The use of such approximations is attractive in structural optimization to reduce the numbers of exact analyses which involve computationally expensive finite element analysis.

1. INTRODUCTION

The use of detailed, computationally expensive, finite element models has motivated researchers to develop approximations of structural response. These approximations are useful for re-design particularly with use of optimization techniques, where the number of finite element analyses can be significantly reduced. The problem considered here is to construct local approximations using function values and derivatives of the structural response at one or two design points. The term local approximation used here means that the approximation is valid only in the vicinity of the current design point and is different from global approximation methods based on simplified design models or reduced basis techniques which seek to approximate the response in the entire design space.

Specifically, let $\underline{x}$ be the current design point, where $\underline{x} = (x_1, x_2, \ldots, x_n)^T$ is a design variable vector. Let $g(\underline{x})$ be a structural response such as element stress or fundamental frequency, which enters as a constraint function in an optimal design formulation. The problem is to construct a local approximation, $g_a(\underline{x})$, based on the function value and derivatives evaluated at $\underline{x}^0$ and possibly another design point. Then, subsequent evaluations of the structural response in the neighborhood of $\underline{x}^0$ can be estimated using g_a rather than the exact response g which will involve finite element computations. A variation of this problem is as follows: Let $\underline{p}$ be a direction vector in design space which has been determined to be desirable in terms of reducing the cost function subject to constraints. Usually, $\underline{p}$ is determined by solving a linear program or quadratic program in optimization algorithms. Now, let $\underline{x}^1$ be a second design point along p such that $\|\underline{x}^1 - \underline{x}^0\|$ represents a move limit along $\underline{p}$. The problem is now to develop a (local) line approximation $g_a(\underline{x})$ such that $g_a(\underline{x}) \approx g(\underline{x})$ for points $\underline{x}$ along the line joining $\underline{x}^0$ and $\underline{x}^1$, given by

$$\underline{x} = (1-\zeta)\,\underline{x}^0 + \zeta\,\underline{x}^1, \quad 0 \le \zeta \le 1 \tag{1}$$

Here, the approximation g_a is to be constructed using structural response information at $\underline{x}^0$ and possibly $\underline{x}^1$.

A comparison of various approximation methods has been carried out by Haftka, *et. al.* (ref. 1) and Haftka (ref. 2). The methods include linear and quadratic Taylor series expansions involving first order and second order sensitivity analysis (refs. 3-5), approximations based on use of reciprocal design variables (refs. 6, 7) and convex approximations (ref. 8). Recently, force approximations have been used by Vanderplaats (ref. 9). Use of rational polynomials may be found in Ref. 10. In this paper, exponential approximations of the form

$$g_a = C \prod_{i=1}^{n} x_i^{a_i} \tag{2}$$

are considered and compared with linear, reciprocal and quadratic polynomial methods. It is noted the exponential approximation discussed in Ref. (1) is of a different form than that in (2). The motivation for choosing exponential approximations of the form in (2) is discussed below.

2. BASIS FOR EXPONENTIAL APPROXIMATIONS

The motivation for approximating structural response using the exponential form in (2) is discussed in this section, as also the basis for use of reciprocal variables and force approximations. The basis for most approximations comes from the equation

$$\sigma(A) = \frac{P}{A} \tag{3}$$

which states that stress = element force/area. Area A is the design variable here.

Reciprocal Variables

The choice of reciprocal design variables is natural, since choosing $x = 1/A$ as a variable results in $\hat{\sigma} = \sigma(1/x)$ being linear in x:

$$\hat{\sigma}(x) = P\,x \tag{4}$$

In the x-space, larger more limits can be imposed on changes in design, leading to faster convergence. Now, in a statically indeterminate truss, the stress function is of the form

$$\sigma(A) = \frac{P(A)}{A} \tag{5}$$

The force P is no longer a constant, but dependent on design. The choice of $x=1/A$ is still beneficial as it tends to linearize the stress function. In general, a first order Taylor service expansion of $g(\underline{x})$ in the reciprocals of the variables $y_i = 1/x_i$, $i=1, \ldots, n$, written in terms of the original variables, x_i, is given by

$$g_a(\underline{x}) = g\left(\underline{x}^0\right) + \sum_{i=1}^{n} \left(x_i - x_{io}\right)\left(\frac{x_{io}}{x_i}\right)\partial g / \partial x_i \tag{6}$$

Force Approximations

The idea here is to approximate P(A) in (5) by Taylor series as opposed to $\sigma(A)$, and obtain

$$\sigma_a(A) = \frac{P(A_o) + \dfrac{dP}{dA}(A_o)\ (A - A_o)}{A} \tag{7}$$

In the case when P is a constant, the approximation yields $\sigma_a = P/A$ which is exact. Otherwise, curvature information is retained in (7) and yields a superior approximation to the conventional tangent approximation $\sigma_a = \sigma(A_o) + \partial\sigma/\partial A \cdot (A-A_o)$.

Exponential Approximations

The approximation introduced in this paper is now discussed. Equation (3) may be re-written as

$$\sigma(A) = P\,A^{-1} \tag{8}$$

Thus, the stress is seen to be exponentially related to design variable A. This is the basis for approximating structural response in n-dimensional space by

$$g_a(\underline{x}) = C \prod_{i=1}^{n} x_i^{a_i}$$

where $x_1, x_2, ..., x_n$ are non-negative design variables. Choice of constants C and a_i are discussed in the next section.

A second and more general basis for exponential approximations lies in the concept of 'elasticity', a quantity used by economists and also relevant in nonlinear stress-strain constitutive laws. Consider a function $g = g(x)$, where $x > 0$ is a scalar variable. The elasticity of the function is defined as

$$e_g = \frac{d(\ln g)}{d(\ln x)} \tag{9a}$$

or,

$$e_g = \frac{dg/g}{dx/x} \tag{9b}$$

Physically, elasticity may be considered to be in the limit, the percentage change in the function due to a percentage change in the variable. For instance, $g=x^3$ has a value $e_g=3$, and $g=px^{-1}$ has $e_g = -1$. The exponents a_i in (2) may be considered to be estimates of the elasticity at the current design point.

In this section, reciprocal and force approximation methods have been introduced using the fundamental equation $\sigma = P/A$ as a basis. Work is being done to generalize these methods to be applicable to frames and certain elasticity problems as well. The exponential method of approximation has both $\sigma=P/A$ as a basis as well as the concept of elasticity of a function. One advantage of exponential approximations of the form in (2) is that, for $C > 0$, the function g_a is a monomial, which opens up the possibility of geometric programming (ref. 11).

3. CONSTRUCTION OF THE EXPONENTIAL APPROXIMATION

The problem is to find the coefficient C and exponents a_i, i=1, ..., k, such that the approximate function $g_a(\underline{x}) = C \prod_{i=1}^{n} x_i^{a_i}$ closely matches the exact function $g(\underline{x})$ in a neighborhood of the current point $\underline{x}^0$. One-point and two-point approximations will now be given.

1-Point Approximation

Here, constants C and $\{a_i\}$ are determined using information only at one point $\underline{x}^0$. The technique is based on matching the function value and shapes of g_a and g. This technique has been used in the context of unconstrained geometric programming where general functions are reduced to posynomial form. Morris (ref. 11) discusses an application of this concept to structural design problems. We have, upon taking logarithms,

$$\ln g_a = \ln C + \sum_{i=1}^{n} a_i \ln x_i \tag{10}$$

Differentiating with respect to x_j yields

$$\partial g_a / \partial x_j = g_a \left[\frac{a_j}{x_j} \right] \tag{11}$$

Note that $g_a(\underline{x}^0) = g(\underline{x}^0)$. Equating $\partial g_a/\partial x_j$ in (11) to the exact slope $\partial g/\partial x_j$ at $\underline{x}^0$ yields the exponents

$$a_j = \frac{x_j \, \partial g / \partial x_j}{g} \Big|_{\underline{x}^0} \tag{12}$$

The coefficient C is then obtained from $g_a(\underline{x}^0) = g(\underline{x}^0)$ as

$$C = g / \prod_i x_i^{a_i} \Big|_{x_0} \tag{13}$$

2-Point Approximation

Information at two points are used to construct the exponential approximation. Let $\underline{x}^0$ be the current design point and $\underline{x}^1$ be a second point, which usually is a point along a desired search direction in design space. The quantities $g(\underline{x}^0)$, $\nabla g(\underline{x}^0)$ and $g(\underline{x}^1)$ are now used to determine C and $\{a_i\}$. A least squares formulation is adopted herein. The variable C and $\{a_i\}$ are obtained from the minimization problem

$$E = \frac{1}{2} \left\{ \left(g_0 - C \prod_{i=1}^{n} x_{i0}^{a_i} \right)^2 + \left(g_1 - C \prod_{i=1}^{n} x_{i1}^{a_i} \right)^2 + \sum_{j=1}^{n} \left(\frac{\partial g_0}{\partial x_j} - C \prod_{i=1}^{k} x_{i0}^{a_i} \bullet \ln x_j \right)^2 \right\} \tag{14}$$

The minimization of the least squares objective function E is carried out using a modified Newton algorithm, with a Levenberg-Marquardt correction to the Hessian when descent is not obtained (ref. 12). The algorithm requires the gradient vector

$$\nabla E = \left(\partial E / \partial C, \partial E / \partial a_1, \cdots, \partial E / \partial a_n \right) \tag{15}$$

and the Hessian

$$H_E = \begin{bmatrix} \partial^2 E / \partial C^2 & \partial^2 E / \partial C \partial a_1 \cdots & \partial^2 E / \partial C \partial a_n \\ & \partial^2 E / \partial a_1^2 \cdots & \partial^2 E / \partial a_1 \partial a_n \\ \text{symmetric} & \ddots & \partial^2 E / a_n^2 \end{bmatrix} \tag{16}$$

These derivatives are computed from analytically derived expressions. The least squares algorithm is given below.

Algorithm 2-Point Exponential

Step 1. Choose the initial estimates of C and $\{a_i\}$ from (12), (13), and $\varepsilon_o = 0.001$

Step 2. Solve

$$\left(\underline{H}_E + \varepsilon \underline{I}\right)\underline{\delta} = -\nabla E^T \tag{17}$$

and update $C_{new} = C + \delta_1$, $(a_i)_{new} = a_i + \delta_{i+1}$, $i = 1, \ldots, n$.

Step 3. Evaluate E_{new}. If $E_{new} < E$ the set $C = C_{new}$, $\{a_i\} = \{a_i\}_{new}$, reduce ε, say, $\varepsilon = \varepsilon/10$ (if $\varepsilon < \varepsilon_o$, set $\varepsilon = \varepsilon_o$) and go to step 2. If $E_{new} > E$, then increase $\varepsilon = 10.\varepsilon$ and go to step 2.

The procedure above is terminated when relative and absolute reductions in E for three consecutive iterations are less than a specified tolerance.

4. TEST PROBLEMS AND RESULTS

Four test problems relating to structural design have been considered. The 1-point and 2-point exponential approximations developed in Section 3 are examined. Comparison of the approximation to the original function is done along a line joining two design points $\underline{x}^0$, $\underline{x}^1$, or at points $\underline{x}$ where

$$\underline{x} = (1-\zeta)\,\underline{x}^0 + \zeta\,\underline{x}^1 \tag{18}$$

where ζ is scalar variable, $0 \le \zeta \le 1$. For comparison, the linear (tangent) approximation based on

$$g_a(\underline{x}) = g(\underline{x}^0) + \nabla g(\underline{x}^0) \bullet (\underline{x} - \underline{x}^0) \tag{19}$$

the reciprocal-linear approximation given in (6), and the quadratic polynomial along the line given by

$$g_a(\zeta) = a + b\zeta + c\zeta^2 \tag{20}$$

where coefficients a, b, c are obtained from $g(\underline{x}^0)$, $g(\underline{x}^1)$ and $dg/d\zeta$ (at $\zeta=0$) $= \nabla g(\underline{x}^0) \bullet (\underline{x}^1 - \underline{x}^0)$. Thus, the 1-point exponential, linear, and reciprocal require only $g(\underline{x}^0)$, $\nabla g(\underline{x}^0)$, while the 2-point exponential and quadratic polynomial require, in addition, $g(\underline{x}^1)$. The error between g and g_a along the line is shown both graphically as well as quantitatively through a relative error criterion

$$\text{RELEER} = \sqrt{\sum_{i=1}^{N} \left[(g_i - g_{ai})/g_i\right]^2} \tag{21}$$

and a maximum error criterion

$$\text{MAXERR} = \max_{1 \le i \le N} |g_i - g_{ai}| \tag{22}$$

Above, $g_i = g(x(\zeta_i))$ is the exact function evaluated at the i^{th} discretization point along the line in (18), g_{ai} is the approximate function evaluated at ζ_i, and N, the number of discretization points, is chosen equal to 20.

Cantilever Beam

The axial stress function in a cantilever beam of rectangular cross section, subjected to axial and transverse loads, is given as

$$\sigma(\underline{x}) = \frac{1000}{x_1 x_2} + \frac{6000}{x_1 x_2^2} \tag{23}$$

where x_1, x_2 are the width and depth of the cross section, respectively. The choice of design points is $\underline{x}^0 = (1,2)^T$ in., $\underline{x}^1 = (5,8)^T$ in.

Referring to Fig. 1, the 2-point exponential is in excellent agreement with the original function. The 1-point exponential behaves just as well as the 2-point exponential and is not shown in the figure. The exponential approximation to $\sigma(\underline{x})$ in (23) is of the form

$$\sigma_a(\underline{x}) = 6727.2\, x_1^{-0.891}\, x_2^{-1.750} \tag{24}$$

The quadratic polynomial (Fig. 1), as well as the tangent and reciprocal approximations behave very poorly. The values of RELEER and MAXERR in (21), (22) for this problem are given in Table 1. It is noted that various choices of $\underline{x}^0$ and $\underline{x}^1$ have shown the same trend.

Table 1. Cantilever Beam

Approximation Method	Relative Error	Maximum Error
1-point exponential	0.493	13.1
2-point exponential	0.492	13.0
Linear (tangent)	700.0	0.165 E5
Reciprocal	105.4	0.022 E5
Quadratic Polynomial	96.9	0.033 E5

Tension-Compression Spring

The shear stress function in a spring design problem, with x_1 = coil diameter and x_2 = wire diameter, is given by

$$\tau(\underline{x}) = \frac{8000\,x_1}{\pi\,x_2^3}\left[\left(\frac{4x_1 - x_2}{4x_1 - 4x_2}\right) + 0.615\,\frac{x_2}{x_1}\right] \tag{25}$$

For this problem, $\underline{x}^0 = (1.0, 0.3)^T$ and $\underline{x}^1 = (0.3, 0.05)^T$ in. As with the beam, the 2-point and 1-point exponentials are also in close agreement with the original function. Table 2 provides an error summary for all the methods. The linear, reciprocal and quadratic polynomial are poor by comparison (Fig. 2). Other choices of $\underline{x}^0$, $\underline{x}^1$ show the same trend for this problem.

Table 2. Tension-Compression Spring

Approximation Method	Relative Error	Maximum Error (x 10^6)
1-point exponential	0.091	0.496
2-point exponential	0.088	0.067
Linear (tangent)	2.464	7.265
Reciprocal	1.640	5.876
Quadratic Polynomial	11.060	3.539

Three Bar Symmetrical Truss

The natural frequency of a three bar truss (ref. 3) with x_1, x_2 = cross sectional areas, is described by the function

$$\omega(\underline{x}) = \frac{x_1}{2\sqrt{2}\,x_1 + x_2} \tag{26}$$

Two sets of design points, leading to different performances, are chosen. These sets are

$$\begin{aligned} &\text{I.} \quad \underline{x}^0 = (3,4)^T \text{ in}^2 \quad , \quad \underline{x}^1 = (10,5)^T \text{ in}^2 \\ &\text{II.} \quad \underline{x}^0 = (5,5)^T \text{ in}^2 \quad , \quad \underline{x}^1 = (1,10)^T \text{ in}^2 \end{aligned} \tag{27}$$

Set I: Referring to Fig. 3 and Table 3, the 2-point exponential based on the best fit formulation yields the best approximation, with

$$\omega(\underline{x}) = 0.2877\,x_1^{0.261}\,x_2^{-0.342} \tag{28}$$

The 1-point exponential is poorer, with

$$\omega(\underline{x}) = 0.2635\ x_1^{0.32}\ x_2^{-0.32} \tag{29}$$

Set II: Along the search direction, the original function is quite flat. In fact, the 1-point exponential provides a relatively poor approximation because of the flat nature of the function. The quadratic polynomial is best here. Even though the 2-point exponential is second-best, (Fig. 4), the best-fit nature of the approximation, while averaging the error, does not provide an interval within the line where the error is small. This may cause difficulty for designs near the optimum. Finally, the use of reciprocal variables does not show any advantage over the direct variables for this case.

Table 3. Three Bar Symmetrical Truss

	(Set I)		(Set II)	
Approximation Method	Relative Error	Maximum Error	Relative Error	Maximum Error
1-point exponential	0.247	0.0286	1.386	0.065
2-point exponential	0.059	0.0053	0.605	0.028
Linear (tangent)	0.810	0.100	1.210	0.060
Reciprocal	0.199	0.022	1.902	0.060
Quadratic Polynomial	0.128	0.012	0.074	0.004

Ten Bar Truss

The ten cross sectional areas of the truss shown in Fig. 5 are the design variables. Points $\underline{x}^0$ and $\underline{x}^1$ are chosen as the initial and optimum design obtained in Ref. (1), as

$$\underline{x}^0 = (5., 5., 5., 5., 5., 5., 5., 5., 5., 5.)^T \text{ in}^2$$

and

$$\underline{x}^1 = (7.94, 0.1, 8.06, 3.94, 0.1, 0.1, 5.74, 5.57, 5.57, 0.1)^T \text{ in}^2 \tag{30}$$

Again, both 1-point and 2-point exponentials provide excellent approximations. The number of design variables do not seem to affect their quality. Interestingly, the reciprocal approximation provides equally good results, but to within a certain distance from $\underline{x}^0$. Near $\underline{x}^1$, the reciprocal abruptly diverges (Fig. 6). With smaller move limits, of course, the reciprocal will be excellent for this problem. The quadratic polynomial provides a good approximation for this problem. Error estimates are given in Table 4.

Table 4. Ten Bar Truss

Approximation Method	Relative Error	Maximum Error
1-point exponential	0.088	1.528
2-point exponential	0.021	0.204
Linear (tangent)	0.689	7.907
Reciprocal	0.599	13.980
Quadratic Polynomial	0.081	0.803

5. CONCLUSIONS

Exponential functions of the form $C \prod_i x_i^{a_i}$ have been used to approximate structural response. Both 1-point and 2-point approximations have been used to determine C and $\{a_i\}$. The 1-point involves matching function and derivative values at the current design. The 2-point method is based on minimizing a least squares function by modified Newton's method. The basis for exponential approximations is from two sources: one is from structural theory, where $\sigma = P/A$ can be written as $\sigma = PA^{-1}$, while the other is from economics, where a function $g = cx^a$ has an elasticity equal to the exponent a. The restriction of exponential approximations is $x_i > 0$. An advantage is that the approximating function is valid for any type of structure or type of structural response. Further, the exponential approximations when applied to the cost and constraints of an optimal design problem have the potential for being used in conjunction with geometric programming which can effectively solve the subproblem.

Results on three out of the four structural problems considered have shown that the exponential functions have provided excellent approximations, with essentially no error, even for large distances in the design space. The linear, linear-reciprocal and quadratic polynomial are much inferior.

On one of the problems involving natural frequency of a 3-bar truss, it is observed that the function is essentially flat or linear. In this case, the 2-point exponential (based on a best-fit) does better than the 1-point, but the quadratic polynomial is superior, Thus, for linear or nearly linear functions, the linear approximation is to be preferred. For other cases, the exponential has shown to be a powerful method of approximation.

Acknowledgment

We thank S. Hariharan at the University of Michigan for his helpful suggestions.

REFERENCES

1. Haftka, R.T., Nachlas, J.A., Watson, L.T., Rizzo, T., and Desai, R.: Two-Point Constraint Approximations in Structural Optimization. Computer Methods in Applied Mechanics and Engineering, 60, 1987, pp. 289-301.

2. Haftka, R.T.: First and Second Order Constraint Approximations in Structural Optimization. Computational Mechanics, 3, 1988, pp. 89-104.

3. Haug, E.J. and Arora, J.S.: Applied Optimal Design. Wiley, New York, 1979.

4. Belegundu, A.D.: Müller -Breslau's Principle in Adjoint Design Sensitivity Analysis. Mech. Struct. & Mach., 17(3), 1989, pp. 333-347.

5. Fleury, C.: Efficient Approximation Concepts Using Second Order Information Proc., 29th AIAA/ASME/ASCE/AHS Structures, Structural Dynamics and Materials Conference, Paper 88-2435, Part 3, 1988, pp. 1685-1695.

6. Storaasli, O.O., and Sobieski, J.: On the Accuracy of the Taylor Approximation for Structure Resizing AIAA J., 12(2), 1974, pp. 231-233.

7. Noor, A.K., and Lowder, H.E.: Structural Reanalysis via a Mixed Method. Comput. & Structures, 5(1), 1975, pp. 9-12.

8. Miura, J., and Schmit, L.A.: Second Order Approximation of Natural Frequency Constraints in Structural Synthesis. Internat. J. Numer. Meths. Engrg., 13, 1978, pp. 337-351.

9. Vanderplaats, G.N., and Salajegheh, E.: A New Approximation Method for Stress Constraints in Structural Synthesis. Proc. AIAA/ASME/ASCE/AHS Structures, Structural Dynamics and Materials Conference, Monterey, CA, 1987.

10. Whitesell, J.E.: Rational Approximants in Structural Design Reanalysis. ASME J. Mechanisms, Transmission, and Automation in Design, 106, 1984, pp. 114-118.

11. Morris, A.J. (Ed): Foundations of Structural Optimization. John Wiley & Sons. 1982.

12. Gill, P.E. and Murray, W. (Eds.).: Numerical Methods for Constrained Optimization. Academic Press, 1974.

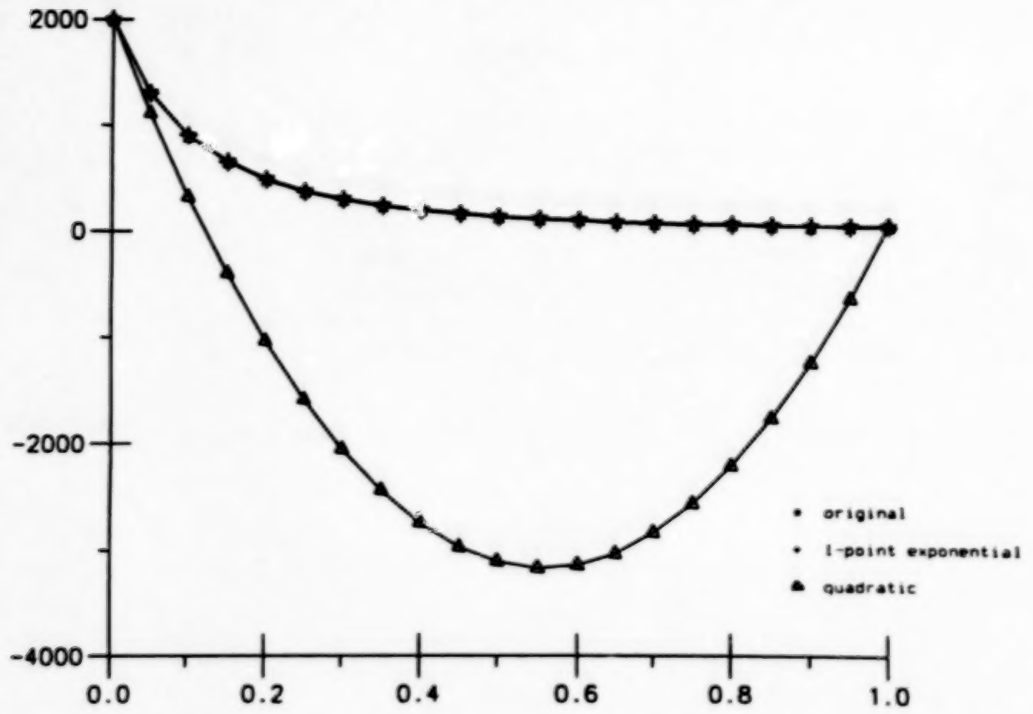

Figure 1. Approximations for the Cantilever Beam.

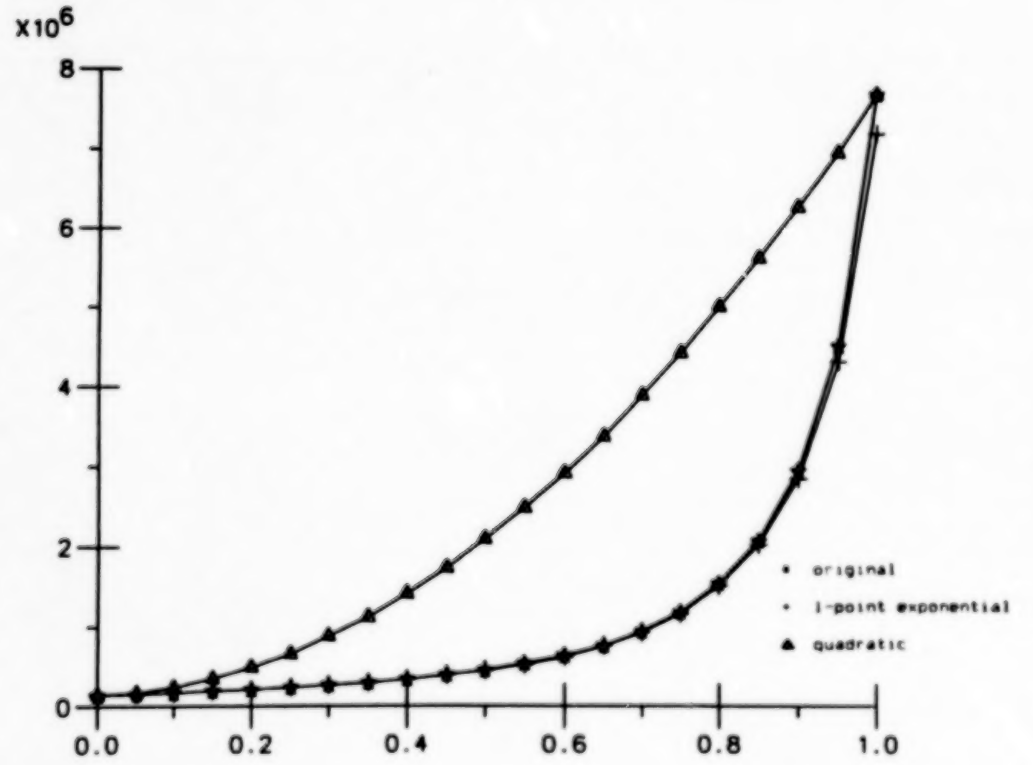

Figure 2. Approximations for the Tension-Compression Spring.

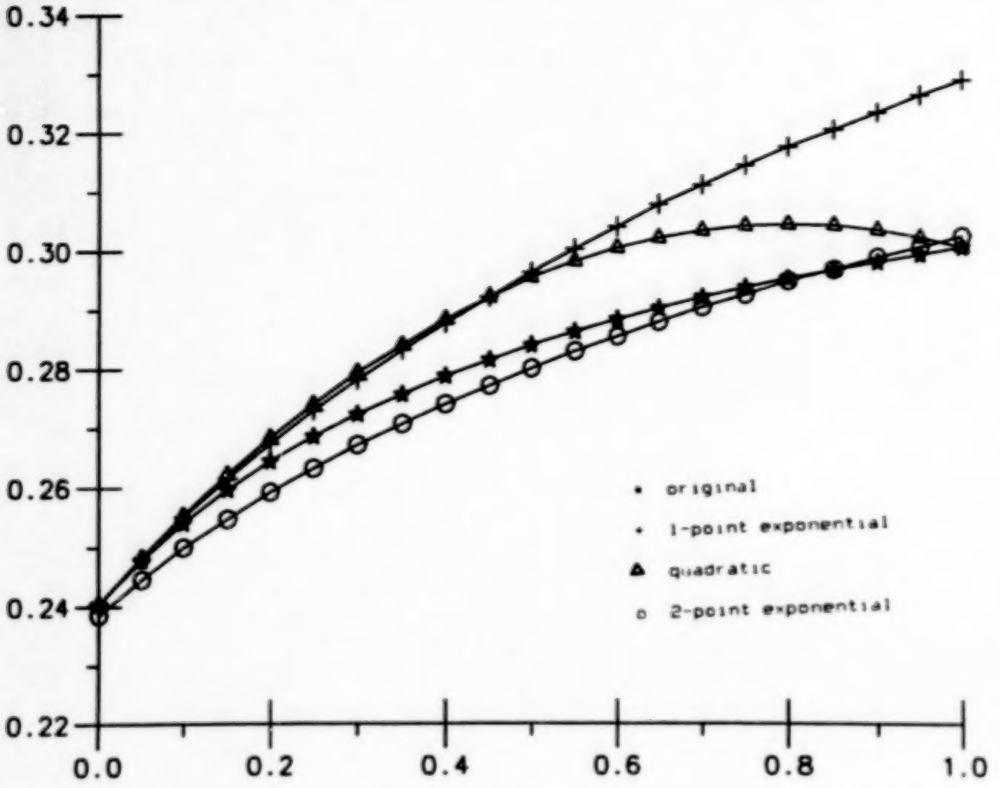

Figure 3. Approximations for the Three Bar Truss - Case I.

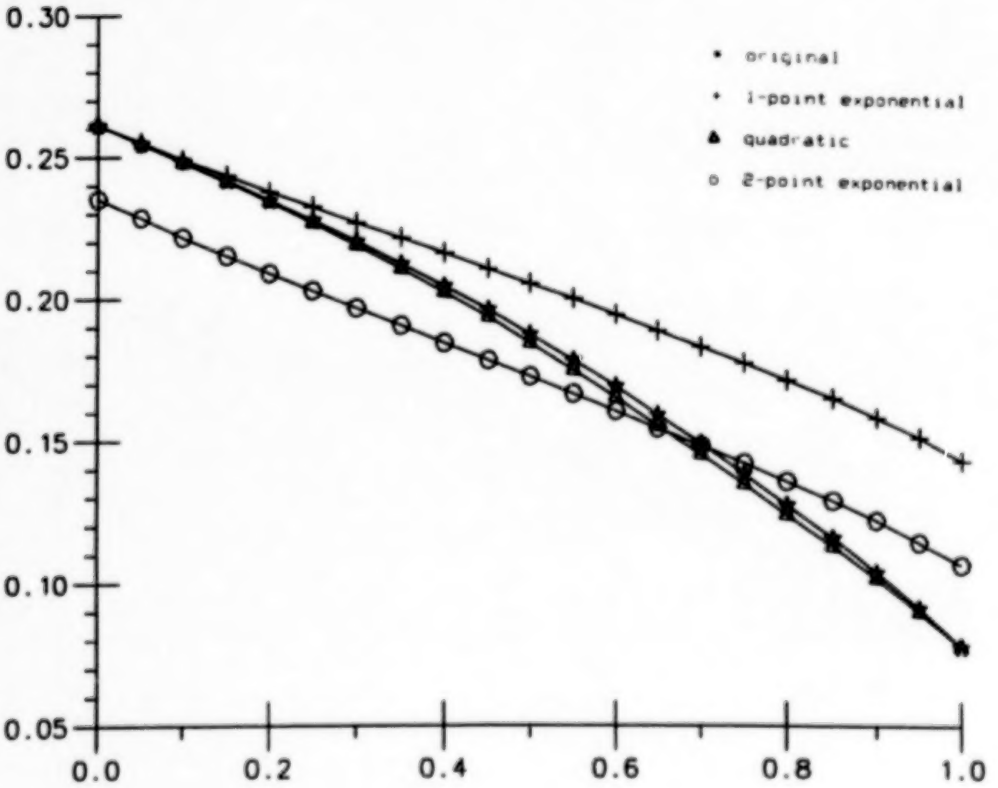

Figure 4. Approximations for the Three Bar Truss - Case II.

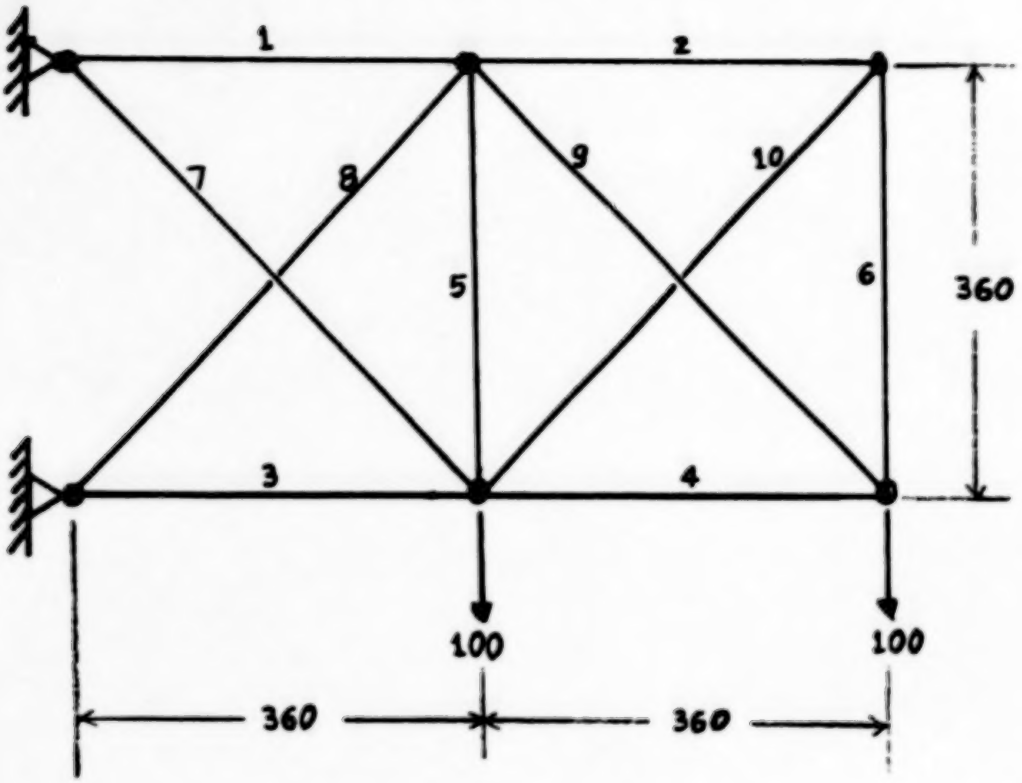

Figure 5. Ten Bar Truss Problem.

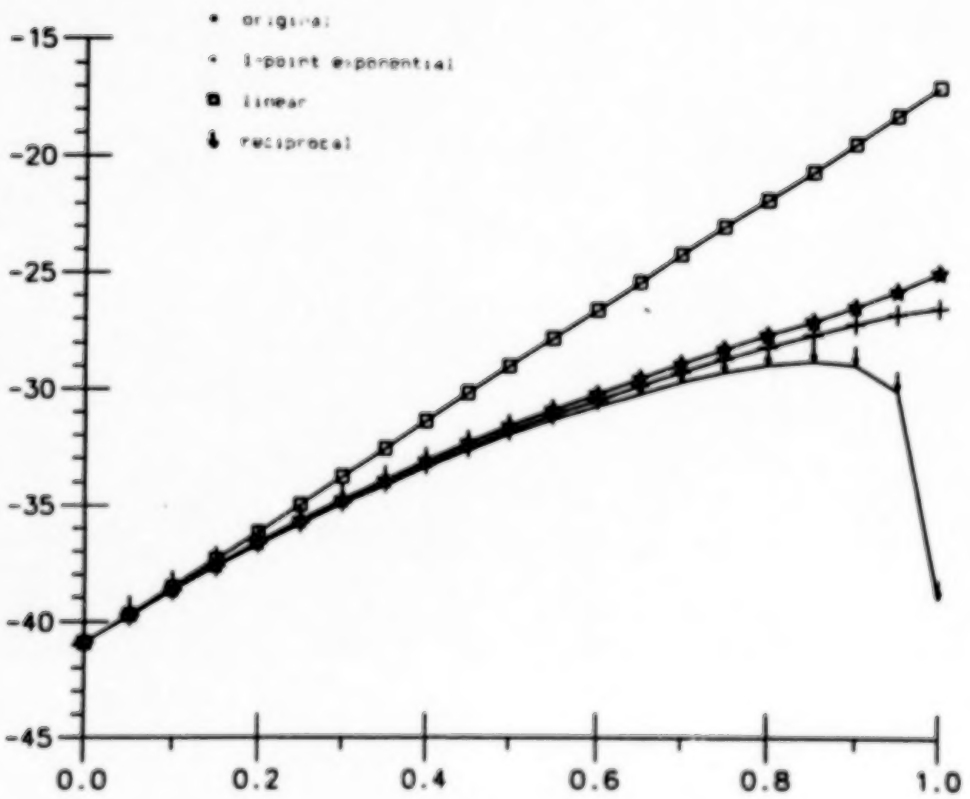

Figure 6. Approximations for the Ten Bar Truss.

CONSERVATIVE BUFFERING OF APPROXIMATE NONLINEAR CONSTRAINTS+

H.L. Thomas* and L.A. Schmit**
University of California, Los Angeles
Los Angeles, California

---

* Graduate Research Assistant, Student Member AIAA. Currently, Research Engineer, VMA Engineering, Goleta, California.

** Professor of Engineering and Applied Science, Fellow AIAA, Fellow ASCE.

+ This research was supported by NASA Research Grant NSG 1490.

INTRODUCTION

In engineering design practice behavior is usually predicted based on some known nominal design. However, when the design is fabricated it will differ from the nominal design because of manufacturing tolerances. In order to generate nominal designs that will still satisfy behavior constraints in the presence of manufacturing tolerances, engineers resort to the use of safety factors, over and above those introduced to account for other uncertainties (e.g. in load conditions, material properties, analysis modeling). The accurate selection of the values of these manufacturing tolerances safety factors is dependent on the capability of the engineer to determine the sensitivity of the critical constraints to changes in the design variables. This process usually leads to overly conservative designs.

The task of choosing safety factors is much more difficult in structural synthesis because: 1) it is not known which constraints will be active at the final design, 2) as the design changes during the synthesis process the sensitivities of the constraints with respect to the design variables also change, and 3) the imposition of the safety factors themselves may change the set of critical constraints. These difficulties can be overcome with the approximation concepts approach to structural synthesis by buffering the approximate constraints with quantities that are related to the design variable tolerances and the accurate sensitivities of the constraints with respect to the design variables. Designs generated by this approach tend to be feasible but not overly conservative.

Problems:

- Design variable tolerances lead to analysis errors.
- Choice of accurate safety factors is dependent on engineers intuition.

Difficulties in Structural Synthesis:

- Critical constraints in the final design are not known.
- Sensitivities of constraints with respect to design variables change during synthesis process.
- Safety factors may change the set of critical constraints.

Solution:

- Use the approximation concepts approach to structural synthesis with the constraints buffered by values that are related to the constraint sensitivities and design variable tolerances.

Figure 1

MATHEMATICAL PROBLEM STATEMENT

The structural synthesis problem is stated as: Minimize the weight of a structure (W) that is a function of the design variables ($\mathbf{Y}$) subject to m constraints (displacements, stresses, and frequencies) ($g_j(\mathbf{Y})$). The n design variables are member cross sectional dimensions and nonstructural masses. The design variables are constrained to be in some specified range ($Y_i^L \le Y_i \le Y_i^U$).

The design variables have tolerances $\pm\Delta Y_i$. These tolerances may be a percentage (k_i) of the current design variable values.

$$\text{Minimize} \quad W(\mathbf{Y})$$

$$g_j(\mathbf{Y}) \le 0 \qquad j = 1, 2, 3, \ldots m$$

$$\text{subject to}$$

$$Y_i^L \le Y_i \le Y_i^i \qquad i = 1, 2, 3, \ldots n$$

with design variable tolerances $\pm \Delta Y_i$

which may be a percentage of the current design variable value:
$\pm \Delta Y_i = \pm k_i Y_i$

Figure 2

APPROXIMATION CONCEPTS APPROACH TO STRUCTURAL SYNTHESIS

In the approximation concepts approach to structural synthesis an approximate optimization problem is constructed and solved at each design iteration. The use of approximations that better capture the behavior of the actual problem will, in general lead to faster design convergence. Linear Taylor Series Approximations were first used to form approximate problems (Ref. 1). It was observed that displacements and stresses were functions of the reciprocals of the design variables in statically determinate structures. This led to the use of approximations with respect to the inverse of the design variables (Ref. 2). The use of a mixture of linear and reciprocal (hybrid) approximations, based on the sign of the partial derivatives, was found to be a more conservative approximation (Ref. 3) and led to a convex design space (Ref. 4).

More complex and accurate nonlinear approximations, which capture certain explicit nonlinearities of the problem, can be constructed if approximations are formed with respect to intermediate design variables (Ref. 2) such as beam section properties (Ref. 5), and if intermediate response quantities (Ref. 2) such as member forces for stress constraints (Ref. 6) and modal energies for frequency constraints (Ref. 7) are approximated.

Linear Approximation:
$$\tilde{g}_L(\mathbf{Y}) = g(\mathbf{Y}_o) + \sum_{i=1}^{n} \frac{\partial g(\mathbf{Y})}{\partial Y_i}(Y_i - Y_{io}) \tag{1}$$

Reciprocal Approximation:
$$\tilde{g}_R(\mathbf{Y}) = g(\mathbf{Y}_o) + \sum_{i=1}^{n} (-Y_{io}^2)\frac{\partial g(\mathbf{Y})}{\partial Y_i}\left(\frac{1}{Y_i} - \frac{1}{Y_{io}}\right) \tag{2}$$

Hybrid Approximation: Mixture of Linear and Reciprocal Approximations based on the sign of $\frac{\partial g(\mathbf{Y})}{\partial Y_i}$ (assuming $Y_i > 0$)

Intermediate Variables:
$$\tilde{g}_{IV}(\mathbf{Y}) = g(\mathbf{Y}_o) + \sum_{j} \frac{\partial g(\mathbf{X})}{\partial X_j}[X_j(\mathbf{Y}) - X_j(\mathbf{Y}_o)] \tag{3}$$

(Linear Approximation)

For Beam Bending:
$$\tilde{g}_{IV}(h,b) = g(h_o,b_o) + \sum_{j} \frac{\partial g(h_o,b_o)}{\partial I_j}[I_j(h,b) - I_{oj}] \tag{4}$$

Intermediate Response Quantities
$$\tilde{g}_{IR}(\mathbf{Y}) = \frac{\tilde{\sigma}(\mathbf{Y})}{\sigma_a} - 1.0 = \frac{\tilde{M}(\mathbf{Y})c}{I\sigma_a} - 1.0 \tag{5}$$

(Forces in Beam Bending)

where
$$\tilde{M}(\mathbf{Y}) = M_o(\mathbf{Y}) + \sum_{i=1}^{n} \frac{\partial M(\mathbf{Y})}{\partial Y_i}(Y_i - Y_{io}) \tag{6}$$

Figure 3

FIRST ORDER CONSTRAINT BUFFERING

One approach used to buffer the constraints, introduced in Ref. 8, is to add a padding term to the constraint function that is equal to the sum of the absolute value of the tolerance on each of the design variables multiplied by the sensitivity of the constraint with respect to the design variable (Eq. 7). This approach has the advantage that it gives good results when the constraints are nearly linear in the design variables. The drawback to this approach is that when the constraint function is nonlinear, due to the use of intermediate design variable or intermediate response quantity concepts, the padding term is still a linear function of the tolerances on the design variables. This can lead to designs that are not conservative enough.

Another drawback to this approach is that the first order derivatives of the constraint functions may contain second order quantities if intermediate design variables and response quantities are used. These second order terms cannot be neglected since they can be larger than the first order terms. Calculation of the second order terms can be quite difficult, since the analytical expression can be very complex. The finite difference technique can be used to calculate the second order terms; however the error associated with this technique may become large, especially if the first order derivatives where generated by finite difference. The second order terms could be approximated by using an approximate Hessian matrix (see Ref. 9), but there are also errors associated with this technique.

$$\tilde{g}^{p}(\mathbf{Y}) = \tilde{g}(\mathbf{Y}) + \sum_{i=1}^{n} \left| \Delta Y_i \frac{\partial g(\mathbf{Y})}{\partial Y_i} \right| \tag{7}$$

$$\tilde{g}_L^{p}(\mathbf{Y}) = g(\mathbf{Y}_o) + \sum_{i=1}^{n} \frac{\partial g(\mathbf{Y})}{\partial Y_i}(Y_i - Y_{oi}) + \sum_{i=1}^{n} \left| \Delta Y_i \frac{\partial g(\mathbf{Y})}{\partial Y_i} \right| \tag{8}$$

$$\tilde{g}_R^{p}(\mathbf{Y}) = g(\mathbf{Y}_o) + \sum_{i=1}^{n} (-Y_{oi}^2) \frac{\partial g(Y)}{\partial Y_i}(1/Y_i - 1/Y_{oi}) + \sum_{i=1}^{n} \left| \Delta(1/Y_i) \left(\frac{Y_{oi}}{Y_i} \right)^2 \frac{\partial g(\mathbf{Y})}{\partial Y_i} \right| \tag{9}$$

Figure 4

BUFFERING OF NONLINEAR CONSTRAINTS

A more accurate buffered constraint, which captures the explicit nonlinearity in high quality approximations, can be constructed by using the values of the design variables at their upper or lower tolerance values, depending on the sign of the derivative of the constraint with respect to each design variable, in the constraint function. For example, in a structure with displacement constraints the values of the member cross sectional dimensions at their lower tolerances would be used in the constraint function. The lower tolerance value is used, as opposed to the upper tolerance, because the lower values lead to larger displacements (the sign of the derivative of the displacement with respect to the design variable is negative). Since the tolerance is included in the constraint function, all of the nonlinearity that is captured by the constraint function is also present in the buffered constraint. Note that the accurate calculation of the first derivatives of the constraints with respect to the design variables is the same and as simple as the method that is used for unbuffered constraints. The only difference is that the value of the design variable is replaced by its upper or lower tolerance value.

If constraints are formed using intermediate design variables, then the values of the design variables at their upper or lower tolerance values are used to calculate the buffered value of the intermediate design variables. Note that in some cases, such as frequency constraints, some of the design variables associated with an intermediate design variable may be at their upper tolerance values while the others are at their lower tolerance values.

$$\tilde{g}^B(\mathbf{Y}) = \tilde{g}(\mathbf{Y}^B) \tag{10}$$

$$\text{where } Y_i^B = \begin{cases} Y_i + \Delta Y_i & \text{if } \dfrac{\partial g(\mathbf{Y})}{\partial Y_i} \geq 0 \\ Y_i - \Delta Y_i & \text{if } \dfrac{\partial g(\mathbf{Y})}{\partial Y_i} < 0 \end{cases}$$

$$\tilde{g}_L^B(\mathbf{Y}) = g(\mathbf{Y}_o) + \sum_{i=1}^{n} \frac{\partial g(\mathbf{Y})}{\partial Y_i}(Y_i^B - Y_{oi}) \tag{11}$$

$$\tilde{g}_R^B(\mathbf{Y}) = g(\mathbf{Y}_o) + \sum_{i=1}^{n} (-Y_{oi}^2)\frac{\partial g(\mathbf{Y})}{\partial Y_i}\left(\frac{1}{Y_i^B} - \frac{1}{Y_{oi}}\right) \tag{12}$$

$$\tilde{g}_{IV}^B(\mathbf{X}(\mathbf{Y})) = \tilde{g}(\mathbf{X}^B(\mathbf{Y}^B)) \tag{13}$$

Figure 5

EXAMPLE

Consider a rectangular cantilevered beam of height h and width b loaded by a moment M at the tip. If the intermediate response quantity approach is used, then the approximate stress is calculated using the approximate moment. In statically determinate problems such as this one, this is trivial since the approximate moment is constant. Hence, the approximate stress is exact.

The approximate stress is calculated using the value of b and h. The buffered approximate stress is calculated using the buffered values of b and h. Since the stress is greater when the values of b and h are smaller, the values of b and h at their lower tolerances are used in the buffered constraint approximation. Note that the constraint is a nonlinear function of the design variable tolerance (Eq. 18). The buffered value of the stress is also exact. Therefore, when the design is fabricated and the manufacturing tolerances are at their lower values, the stress constraint will not be violated. Equation 19 is the first order form of the buffered constraint. Although this type of buffered constraint is exact for linear approximations, there is some error when it is used with nonlinear approximations because the buffering is only a linear function of the design variable tolerances.

$$\tilde{g} = \frac{\tilde{\sigma}}{\sigma} - 1 \; ; \; \tilde{\sigma} = \frac{6\tilde{M}}{bh^2} \tag{14}$$

$$\tilde{g}^B = \frac{\tilde{\sigma}^B}{\sigma_a} - 1 \; ; \; \tilde{\sigma}^B = \frac{6\tilde{M}^B}{b^B (h^B)^2} \tag{15}$$

$$\tilde{M}^B = \tilde{M} = M \tag{16}$$

$$b^B = b - \Delta b \quad , \quad h^B = h - \Delta h \tag{17}$$

$$\tilde{\sigma}^B = \frac{6M}{(b - \Delta b)(h - \Delta h)^2} \tag{18}$$

$$\tilde{\sigma}^F = \frac{6M}{bh^2} + \left| \Delta b \left(\frac{-6M}{b^2 h^2} \right) \right| + \left| \Delta h \left(\frac{-12M}{bh^3} \right) \right| \tag{19}$$

Figure 6

REFERENCES

1. Schmit, L.A. and Farshi, B., "Some Approximation Concepts for Efficient Structural Synthesis," *AIAA Journal*, Vol. 12, May 1974, pp. 692-699.

2. Schmit, L.A. and Miura, H., "Approximation Concepts for Efficient Structural Synthesis," NASA CR 2552, March 1976.

3. Starnes, J.R. Jr. and Haftka, R.T., "Preliminary Design of Composite Wings for Buckling, Stress and Displacement Constraints," *Journal of Aircraft*, Vol. 16, Aug. 1979, pp. 564-570.

4. Fleury, C. and Braibrant, V., "Structural Optimization - A New Dual Method Using Mixed Variables," *International Journal for Numerical Methods in Engr.*, Vol. 23, 1986, pp. 409-428.

5. Vanderplaats, G.N. and Salajegheh, E., "An Efficient Approximation Technique for Frequency Constraints in Frame Optimization," *International Journal for Numerical Methods*, Vol. 26, 1988, pp. 1057-1069.

6. Vanderplaats, G.N. and Salajegheh, E., "A New Approximation Method for Stress Constraints in Structural Synthesis," *AIAA Journal*, Vol. 27, March 1989, pp. 352-358.

7. Canfield, R.A., "An Approximation Function for Frequency Constrained Structural Optimization," *Proceedings of the Second NASA/Air Force Symposium on Recent Advances in Multidisciplinary Analysis and Optimization*, AIAA, Hampton, VA, Sept. 28-30, 1988, pp. 937-953.

8. Bennett, J.A. and Lust, R.V., "Conservative Methods for Structural Optimization," *Proceedings of the AIAA/ASME/ASCE/AHS/ACS 30th Structures, Structural Dynamics and Materials Conference*, AIAA, Washington, D.C., April 1989, pp. 546-552.

9. Vanderplaats, G.N., *Numerical Optimization Techniques for Engineering Design: With Applications*, McGraw - Hill, Inc., New York, NY, 1984, Chap. 3.

Evaluation of Alternatives for Best-Fit Paraboloid for Deformed Antenna Surfaces

Menahem Baruch
Faculty of Aerospace Engineering
Technion, Haifa 32000, Israel

and

Raphael T. Haftka
Department of Aerospace and Ocean Engineering
Virginia Polytechnic Institute and State University
Blacksburg, Virginia 24061

Abstract

Paraboloid antenna surfaces suffer performance degradation due to structural deformation. A first step in the prediction of the performance degradation is to find the best-fit paraboloid to the deformed surface. This paper examines the question of whether rigid body translations perpendicular to the axis of the paraboloid should be included in the search for the best-fit paraboloid. It is shown that if these translations are included the problem is ill-conditioned, and small structural deformation can result in large translations of the best-fit paraboloid with respect to the original surface. The magnitude of these translations then requires nonlinear analysis for finding the best-fit paraboloid. On the other hand, if these translations are excluded, or if they are limited in magnitude, the errors with respect to the restricted "not-so-best-fit" paraboloid can be much greater than the errors with respect to the true best-fit paraboloid.

Introduction

Paraboloid antenna surfaces suffer performance degradation due to structural deformation. A first step in the prediction of the performance degradation is to find the best-fit paraboloid to the deformed surface. The process of finding this best-fit paraboloid has received some attention in the past, (e.g. Refs. 1,2) but there is no clear agreement on a procedure that should be followed. In particular, questions that arise are whether it is acceptable to change the focus length in choosing the best-fit paraboloid and which rigid

body motions should be included in moving from the original paraboloid to the best-fit one. The present paper attempts to shed some light on this second question.

The choice of rigid body modes to be considered is associated with ill-conditioning of the numerical process of obtaining the best-fit paraboloid. If z denotes the paraboloid axis symmetry, then the ill-conditioning is associated with translations in the x and y directions. Because antenna surfaces are typically shallow paraboloids, finding x and y translations required to move the original paraboloid to the best-fit one leads to an ill-conditioned set of equations. It is possible to eliminate these translations by, for example, setting them to be equal to the corresponding translations at the apex. However, it is not clear how much is lost in terms of the root mean square (rms) surface error. This paper shows that not including these translations can indeed result in substantial increase in rms errors, but that to include them one must resort to complicated and costly nonlinear calculations. This is demonstrated first by the simpler case of a best-fit parabola.

Best-Fit Parabola

The undeformed shape of the parabola is given as

$$y_1 = ax_1^2$$

The distortions in the x_1 and y_1 directions are given by ξ and η (see Figure 1) so that

a point A moves to position A'. The best-fit parabola is given as

$$y = cx^2 \tag{2a}$$

$$c = a + b \tag{2b}$$

The two coordinate systems shown in Figure 1 have unit vectors $\bar{i}_1$ and $\bar{j}_1$ associated with the undeformed parabola, and $\bar{i}$ and $\bar{j}$ associated with the best-fit parabola.

The radius vector $\overline{R}_A$ from the apex of the original parabola to A' is given as

$$\overline{R}_A = (x_A + \xi)\bar{i}_1 + (ax_A^2 + \eta)\bar{j}_1 \tag{3}$$

The closest point to A' on the best-fit parabola is denoted B (Figure 1) and has the coordinates $[x_B, (a+b)x^2\beta]$ in the (x, y) coordinate system. The radius vector from the origin of the original parabola to β is given as

$$\overline{R}_B = \beta_1\bar{i}_1 + \beta_2\bar{j}_1 + x_B\bar{i} + (a+b)x_B^2\bar{j} \tag{4}$$

where β_1 and β_2 are the coordinates of the origin of the best-fit parabola. Denoting the angle between the x, and x axes as β_3 we have

$$\bar{i}_1 = \bar{i}\cos\beta_3 - \bar{j}\sin\beta_3 \tag{5a}$$

$$\bar{i}_2 = \vec{i}\sin\beta_3 + \bar{j}\cos\beta_3 \tag{5b}$$

Using Eqs. (5) we can obtain from Eqs. (3) and (4) the error $\overline{v}$ of A' with respect to the best-fit parabola

$$\overline{v} = \overline{R}_B - \overline{R}_A = (x_B - \overline{x}_A)\bar{i} + [(a+b)x_B^2 - \overline{y}_A]\bar{j} \tag{6}$$

where $(\overline{x}_A, \overline{y}_A)$, the coordinates of A' in the best-fit coordinate system are given as

$$\overline{x}_A = (x_A + \xi)\cos\beta_3 + (ax_A^2 + \eta)\sin\beta_3 - \beta_1\cos\beta_3 - \beta_2\sin\beta_3 \tag{7a}$$

$$\overline{y}_A = -(x_A + \xi)\sin\beta_3 + (ax_A^2 + \eta)\cos\beta_3 + \beta_1\sin\beta_3 - \beta_2\cos\beta_3 \tag{7b}$$

The point β on the best-fit parabola is found by minimizing $\|\overline{R}_B - R'_A\|$ with respect to x_β. In the present work this is done with a Newton-Raphson iteration using x_A as an initial guess (x_B is the solution to a cubic equation).

The parameters $b, \beta_1, \beta_2, \beta_3$ are found by minimizing the root-mean-square (rms) distortion

$$\nu_{rms}^2 = \frac{1}{2h}\int_{-h}^{h} \nu \cdot \nu dx \cong \sum_{i=1}^{n} c_i \nu^2(x_i) \tag{8}$$

where $\pm$h are the limits of the parabola, c_i are quadrature weight and x_i are points where the deformed parabola coordinates are given. In this work the minimization was performed by a conjugate-gradient method using finite-difference derivatives.

Instead of performing this nonlinear analysis it is standard practice to linearize the problem. First we set $\cos\beta_3 = 1$, $\sin\beta_3 = \beta_3$ and neglect higher order terms in Eqs. (7) (assuming $\xi, \eta, \beta_1, \beta_2, \beta_3$ are small) to get

$$\overline{x}_A = x_A + \xi + ax_A^2\beta_3 - \beta_1 \tag{9a}$$

$$\overline{y}_A = -x_A\beta_3 + ax_A^2 + \eta - \beta_2 \tag{9b}$$

Next we use a linear approximation to the minimum distance as follows: We set $x_B = x_A$ in Eq. (6) and take only the component of $\bar{\nu}$ normal to the best-fit parabola at $x_B = x_A$. This normal $\overline{n}$ is given as

$$\overline{n} = \frac{\bar{j} - 2(a+b)x_A\bar{i}}{\sqrt{1+4(a+b)^2 x_A{}^2}} \tag{10}$$

Neglecting higher order terms the normal component of ν can be written as

$$\nu_n = \overline{\nu} \cdot \overline{n} = -\nu_\circ + \ell^T \alpha \tag{11}$$

where

$$\nu_\circ = (\eta - 2ax_A\xi)/\sqrt{1+4a^2x_A^2} \tag{12}$$

and

$$\ell^T = [x_A^2, -2ax_A, 1, xa + 2a^2x_A^3]/\sqrt{1+4a^2x_A^2} \tag{13}$$

The rms error is now defined as

$$\nu_{rms}^2 = \frac{1}{2h}\int_{-h}^{h} \nu_n^2 dx \tag{14}$$

To minimize it we differentiate Eq. (14) with respect to α to obtain

$$\frac{1}{2h}\int_{-h}^{h} \nu_n \frac{\partial \nu_n}{\partial \alpha_j} dx = 0 \qquad j = 1, ..., 4 \tag{15}$$

Using Eq. (11), Eq. (15) becomes

$$A\alpha = f \tag{16}$$

where

$$A = \int_{-h}^{h} \ell\ell^T dx = \sum_{i=1}^{n} c_i \ell_i(x_i)\ell_i^T(xi) \tag{17a}$$

$$f = \int_{-h}^{h} \nu_o \ell dx = \sum_{i=1}^{n} c_i \nu_o(x_i)\ell(x_i) \tag{17b}$$

The matrix A is almost singular so that small deformations ξ, η can result in large values of β_1 (the x-translation) and β_3 (the rotation). We can minimize ν_{rms}^2 with an additional limitation on the size of α of the form

$$\alpha^T \alpha \leq \xi \tag{18}$$

and this leads to a system of equations

$$(A + \lambda I)\alpha = f \tag{19}$$

where λ is a Lagrange multiplier (chosen to satisfy Eq. (18)) and I the identity matrix.

Best-Fit Paraboloid

The derivations for the paraboloid parallel the derivations for the parabola given in the previous section. The undeformed shape of the paraboloid is given as

$$z_1 = a\rho_1^2 \tag{20}$$

in a coordinate system shown in figure 2. The distortions in the ρ_1, θ_1 and z_1 directions are given by ξ, η and ζ, respectively, so that point A in Figure 2 moves to position A$'$.

The best-fit paraboloid is given as

$$z = c\rho^2 \tag{21a}$$

$$c = a + b \tag{21b}$$

The radius vector $\bar{R}'_A$ from the apex of the original paraboloid to A' is given as

$$\bar{R}'_A = [(\rho_A + \xi)cos\ \theta_A - \eta\ sin\ \theta_A]\bar{i}_1$$

$$+[(\rho_A + \xi)sin\ \theta_A + \eta\ cos\ \theta_A]\ \bar{j}_1 + (a\rho_A^2 + \zeta)\bar{k}_1$$

$$= x'_A\bar{i}_1 + y'_A\bar{j}_1 + z'_A\bar{k}_1 \tag{22}$$

The closest point to A' on the best-fit paraboloid is denoted B (Figure 2) and has the cylindrical coordinates $[\rho_B, \theta_B, (a+b)\rho_B^2]$ in the (x, y, z) cordinate system. The radius vector from the origin of the original paraboloid to B is given as

$$\bar{R}_B = \beta_1\bar{i}_1 + \beta_2\bar{j}_1 + \beta_3\bar{k}_1 + \rho_B\ cos\ \theta_B\bar{i} + \rho_B\ sin\ \theta_B\bar{j} + (a+b)\ \rho_B^2\bar{k} \tag{23}$$

where now β_1, β_2 and β_3 are the coordinates of the apex of the best-fit paraboloid in the $(x_1,\ y_1,\ z_1)$ system. The relationship between the unit vectors in the original and best-fit systems is given as

$$\begin{Bmatrix} \bar{i}_1 \\ \bar{j}_1 \\ \bar{k}_1 \end{Bmatrix} = T \begin{Bmatrix} \bar{i} \\ \bar{j} \\ \bar{k} \end{Bmatrix} \tag{24}$$

where

$$T = \begin{bmatrix} 1 & 0 & 0 \\ 0 & cos\beta_4 & -sin\beta_4 \\ 0 & sin\beta_4 & cos\beta_4 \end{bmatrix} \begin{bmatrix} cos\beta_5 & 0 & sin\beta_5 \\ 0 & 1 & 0 \\ -sin\beta_5 & 0 & cos\beta_5 \end{bmatrix} \begin{bmatrix} cos\beta_6 & -sin\beta_6 & 0 \\ sin\beta_6 & cos\beta_6 & 0 \\ 0 & 0 & 1 \end{bmatrix} \tag{25}$$

and β_4, β_5 and β_6 are rotations around the axes x_1, y_1, z_1, respectively.

Using Eq. (25) we can obtain from Eq. (22), (23) and (24) the error $\bar{\nu}$ of A' with respect to the best-fit paraboloid.

$$\bar{\nu} = \bar{R}_B - \bar{R}'_A = (\rho_B \cos\theta_B - \bar{x}_A)\bar{i} + (\rho_B \sin\theta_B - \bar{y}_A)\bar{j} + (c\rho_B^2 - \bar{z}_A)\bar{k} \quad (26)$$

where $(\bar{x}_A, \bar{y}_A, \bar{z}_A)$, the coordinates of A' in the best-fit coordinate system, are given as

$$\begin{Bmatrix} \bar{x}_A \\ \bar{y}_A \\ \bar{z}_A \end{Bmatrix} = T^t \begin{Bmatrix} x'_A - \beta_1 \\ y'_A - \beta_2 \\ z'_A - \beta_3 \end{Bmatrix} \quad (27)$$

The point B on the best-fit paraboloid is found by minimizing $\| \bar{\nu} \|^2$ with respect to ρ_B and θ_B. Doing so we obtain

$$\theta_B = \theta_A + \phi \quad (28)$$

where

$$tan\phi = \frac{\bar{y}_A \cos\theta_A - \bar{x}_A \sin\theta_A}{\bar{x}_A \cos\theta_A + \bar{y}_A \sin\theta_A} \quad (29)$$

and ρ_B is the solution of the cubic equation

$$2c^2\rho_B^3 + \rho_B(1 - 2c\bar{z}_A) - (\bar{x}_A \cos\theta_B + \bar{y}_A \sin\theta_B) = 0 \quad (30)$$

which is closest to ρ_A. The parameters $b, \beta_1, ..., \beta_6$ are found by minimizing the root-mean-square (rms) distortion

$$\nu_{rms}^2 = \frac{1}{\pi h^2} \int_0^h \int_0^{2\pi} \bar{\nu}.\bar{\nu}\rho d\theta \cong \sum_{i=1}^{\eta} c_i \nu^2(\rho_i, \theta_i) \quad (31)$$

where h is the limit of ρ for the paraboloid. As in the case of the parabola the minimization was performed by a conjugate-gradient method using finite-difference derivatives. As in the case of the parabola we consider also a linear analysis setting $cos\beta_i = 1,\ sin\beta_i = \beta_i$ for $i = 4, 5, 6$. The linear approximation to the minimum distance is obtained by a similar procedure to the two-dimensional case: We set $\rho_B = \rho_A$ and $\theta_B = \theta_A$ in Eq. (26) and take only the component of $\bar{\nu}$ normal to the best-fit paraboloid at $\rho_B = \rho_A$ and $\theta_B = \theta_A$. The normal $\bar{n}$ is given by

$$\bar{n} = \frac{\bar{k} - 2c\rho_A cos\theta_A \bar{i} - 2c\rho_A sin\theta_A \bar{j}}{\sqrt{1 + 4c^2\rho_A^2}} \tag{32}$$

Neglecting higher-order terms the normal component of $\bar{\nu}$ can be written as

$$\nu_n = \bar{\nu}.\bar{n} = -\nu_0 + \ell^t \alpha \tag{33}$$

where

$$\nu_0 = (\zeta - 2a\rho_A\xi)/\sqrt{1 + 4a^2\rho_A^2} \tag{34}$$

and

$$\ell^T = [\rho_A^2, -2a\rho_A cos\theta_A, -2a\rho_A sin\theta_A, 1, \rho_A sin\theta_A(1+2a^2\rho_A^2), -\rho_A cos\theta_A(1+2a^2\rho_A^2)]$$

$$/\sqrt{1 + 4a^2\rho_A^2} \tag{35}$$

and

$$\alpha^t = [b, \beta_1, \beta_2, \beta_3, \beta_4, \beta_5] \tag{36}$$

Note that, as expected because of axial symmetry, η and β_6 do not influence the error.

The rms error is again defined as

$$\nu_{\text{rms}}^2 = \frac{1}{\pi h^2} \int_0^h \int_0^{2\pi} \nu_n^2 \rho d\rho d\theta \tag{37}$$

and the minimization again leads to a system of linear equations.

$$A\alpha = f \tag{38}$$

where

$$A = \int_0^h \int_0^{2\pi} \ell \ell^t \rho d\rho d\theta = \sum_{L=1}^{n} c_i \ell_i(\rho_i, \theta_i) \ell_i^t(\rho_i, \theta_i) \tag{39a}$$

$$f = \int_0^h \int_0^{2\pi} \nu_0 \ell \rho d\rho d\theta = \sum_{L=1}^{n} c_i \nu_0(\rho_i, \theta_i) \ell(\rho_i, \theta_i) \tag{39b}$$

Results for Best-Fit Parabola

To illustrate the problems associated with finding the vector α which defines the best-fit parabola consider a distortion of the form

$$\xi = \xi_C (1 - \cos \frac{2\pi x}{h}) \tag{40}$$

with $\eta = 0$. A parabola with a/h = 0.2 corresponding to focal length over diameter ratio of 0.625 was used. The best-fit parabola was calculated for a very small disturbance $\xi_C/h = 0.005$. The best-fit parabola corresponding to this distortion was calculated three different ways:

(i) By using conjugate gradient optimization procedure to minimize ν_{rms}^2 based on the nonlinear expressions in Eqs. (6) and (8). The resulting surface error is denoted ν_{NL}.

(ii) By solving the linearized problem Eq. (16). The corresponding linear approximation to the surface distortion is denoted ν_L.

(iii) By solving the size-limited problem, Eq. (19) for various values of λ.

The results are summarized in Table 1. The first line shows the results obtained with conjugate gradient minimization of the nonlinear expression for the error. It is seen that the rms value of the error can be reduced by a factor of three. However, there is great amplification of the disturbance with the normalized translation β_1/h being equal to 0.1571. The linear analysis based on Eq. (16) yielded similar values for the components of α. However, because of the large values of these components the prediction of that linear analysis was erroneous. The predicted rms value of 4.9×10^{-4} compares with a nonlinear value of 6.37×10^{-3}. Thus while the linear analysis predicted a reduction of the initial rms by a factor of 3 the nonlinear analysis predicted that the best-fit linear parabola actually *increased* the error by a factor of three and a half.

The next three lines in Table 1 include size-limited solutions obtained from Eq. (19) with various values of λ. It is seen that as λ is increased the size of α decreases so that the linear and nonlinear predictions become close. However, this is accompanied with substantial increase in the best-fit rms error. The last line in the table shows a 3-variable

solution obtained by setting β_1 to the apex x-translation (zero here). This solution is close to the large-λ solution from Eq. (19).

Table 1 shows that we have a dilemma in the construction of a best-fit parabola. Linear analysis requires that we eliminate one of the variables or restrict the size of the solution. These limitations, however, substantially increase the error rms of the now 'not-so-best-fit' parabola. The alternative nonlinear solution is complex and costly.

This type of difficulty is not encountered when the distortion does not require β_1 and β_3 for its correction. As an example consider a distortion of the form

$$\xi = \xi_s \sin \frac{2\pi x}{h} \tag{41}$$

The results of the nonlinear and linear solutions are shown in Table 2 for a substantial value of $\xi_s/h = 0.04$. It is seen that there is hardly any difference between the linear and nonlinear solutions.

Results for Best-Fit Paraboloid.

Similar results were obtained for the best-fit paraboloid for $a/h = 0.2$. For example, a distortion of the form

$$\zeta = \zeta_s \sin(\pi\rho/\mathrm{h})\sin\theta \tag{42}$$

was considered, and the results for $\zeta_s/h = 0.001$ are summarized in Table 3. The first column shows the results of the nonlinear analysis coupled with the conjugate gradient

minimization. The rms error is reduced by about a factor of 7, however there is again amplification of the distortion due to the ill-conditioning of the problem with $\beta_2/h = 0.09$. The linear analysis shown in the second column produces very similar solution, predicting even better reduction in rms (about a factor of 10). However, when the nonlinear solution is analyzed using the nonlinear analysis we find that the error actually *increased* by a factor of 3.

The next three columns in Table 3 show the size-limited solutions based on Eq. (19). It is seen that, as we put more and more stringent limits on the magnitude of the solution, the agreement between the linear and nonlinear solution improves. However, much of the reduction in the error is lost, so that we have a 'not-so-best-fit-paraboloid'. Similar results are obtained by setting β_1 and β_2 equal to x and y translation of the apex (zero for the example) and solving a reduced 4-variable problem.

While this dilemma of how to calculate the best-fit-paraboid is difficult, there is a bright side to it. The linear analysis gives a reasonable idea of the magnitude of error reduction possible with the best-fit paraboloid.

Concluding Remarks

An investigation of alternatives for calculating the best-fit paraboloid to a deformed paraboloid surface was investigated. In particular we focused on the ill-conditioning as-

sociated with the translations perpendicular to the axis of the paraboloid. It was shown that this ill-conditioning results in disturbance amplification so that small deformation can result in large translations and rotations for the best-fit paraboloid. It was also found that eliminating the two translations or restricting their magnitude may result in large increases in rms errors.

The amplification of translations and rotations for the best-fit paraboloid results in grossly inaccurate prediction by linear analysis of the rms error. However, the linear analysis may be less inaccurate in predicting the achievable reduction in rms error.

Acknowledgment

This research was supported in part by NASA grant NAG-1-224

References.

1. Brondess, S.M. and Utku, S., "Computation of Weighted Root Mean Square of Path Length Changes Caused by Deformers and Imperfections of Rotational Paraboloidal Antennas", JPL, TM 33-118, 1963.

2. Ludwig, a., "Computer Programs for Antenna Feed System Design and Analysis", JPL TM 32-979, 1967.

Table 1: Best-fit parabola with various fitting schemes, $\xi_c/h = 0.005$, initial error $\nu_{orms}/h = 1.75 \times 10^{-3}$

Fitting scheme	b/h	β_1/h	β_2/h	β_3/h	ν_L/h	ν_{NL}/h
					rms values	
4-variable						
nonlinear	.00104	.1571	.00426	.05854		4.90×10^{-4}
linear	0.	.1574	0.	.05844	4.90×10^{-4}	6.37×10^{-3}
$\lambda = .00001$	0.	.1238	0.	.05844	4.90×10^{-4}	3.90×10^{-3}
$\lambda = .0001$	0.	.0426	0.	.0146	8.91×10^{-4}	9.74×10^{-4}
$\lambda = .0002$	0.	.0248	0.	.00785	9.89×10^{-4}	9.95×10^{-4}
$\lambda = .0005$	0.	.0113	0.	.00267	1.07×10^{-3}	1.07×10^{-3}
3-variable	0.	0.	0.	-.00163	1.13×10^{-3}	1.13×10^{-3}

Table 2: Best-fit parabola with various fitting schemes, $\xi_c/h = 0.04$, $\nu_{orms}/h = 8.69 \times 10^3$

Fitting scheme	b/h	β_1/h	β_2/h	β_3/h	ν_L/h	ν_{NL}/h
					rms values	
nonlinear	.0142	0.	-.00228	0.		6.02×10^{-3}
linear	.0141	0.	-.00225	0.	5.69×10^{-3}	6.02×10^{-3}

Table 3: Best-fit parabola with various fitting schemes, $\zeta_s/h = 0.001$, initial error $\nu_{orms}/h = 4.868 \times 10^{-4}$

Fitting scheme	6-variable					4-variable
	nonlinear	linear				
		$\lambda = 0$	$\lambda = 5 \times 10^{-6}$	$\lambda = 2 \times 10^{-5}$	$\lambda = 5 \times 10^{-5}$	
b/h	2.33×10^{-4}	0.	0.	0.	0.	0.
β_1/h	0.	0.	0.	0.	0.	0.
β_2/h	-0.09055	-0.09055	-0.06281	-0.03280	-0.01686	0.
β_3/h	1.41×10^{-3}	0.	0.	0.	0.	0.
β_4/h	-0.03366	-0.03366	-0.02313	-0.01174	0.00569	7.12×10^{-4}
β_5/h	0.	0.	0.	0.	0.	0.
ν_L/h		5.19×10^{-5}	1.12×10^{-4}	2.14×10^{-4}	2.70×10^{-4}	3.29×10^{-4}
ν_{NL}/h	6.91×10^{-5}	1.47×10^{-3}	7.05×10^{-4}	2.79×10^{-4}	2.73×10^{-4}	3.29×10^{-4}

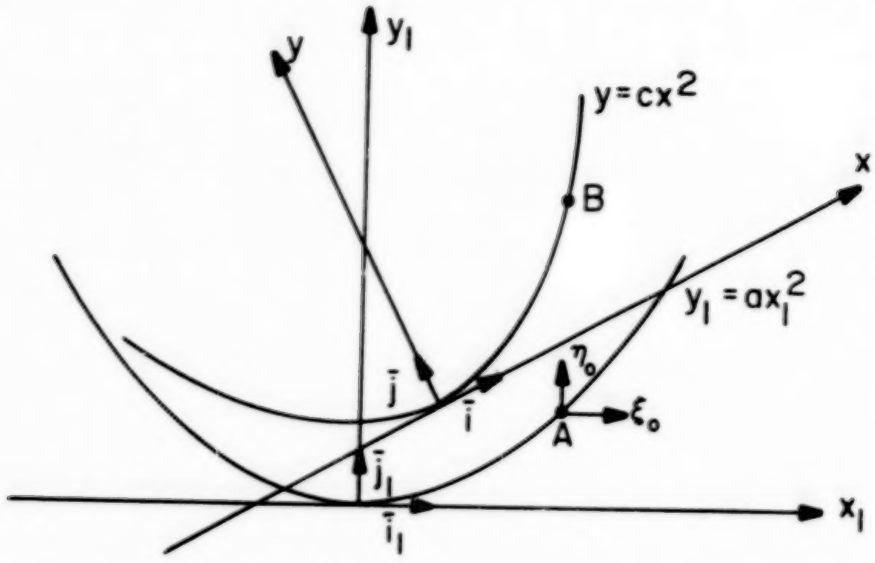

Figure 1: Parabola geometry

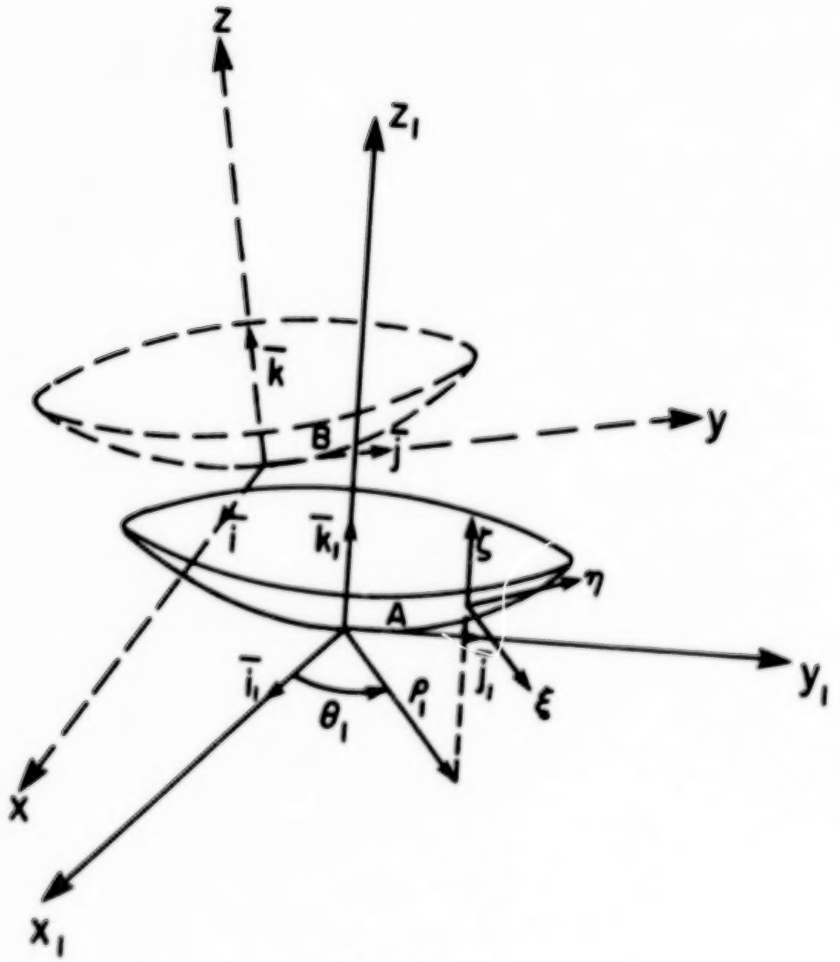

Figure 2: Paraboloid Geometry

SESSION 43 (W2)
WORK-IN-PROGRESS II

Combined Design of Structures and Controllers for Optimal Maneuverability

Jer Ling*, Pierre Kabamba**, and John Taylor†

The University of Michigan

Ann Arbor, MI 48109-2140

†Professor, Department of Aerospace Engineering. **Associate Professor, Department of Aeropace Engineering. *Graduate Student, Department of Aerospace Engineering.

Abstract

This paper presents approaches to the combined design of structures and controllers for achieving optimal maneuverability. A maneuverability index which directly reflects the minimum time required to perform a given set of maneuvers is introduced. By designing the flexible appendages, the maneuver time of the spacecraft is minimized under the constraints of structural properties, and of the post maneuver spillover being within a specified bound. The spillover reduction is achieved by making use of an appropriate reduced order model. The distributed parameter design problem is approached using assumed shape functions, and finite element analysis with dynamic reduction. Solution procedures have been investigated. Approximate design methods have been developed to overcome the computational difficulties. Some new constraints on the modal frequencies of the spacecraft are introduced in the original optimization problem to facilitate the solution process. It is shown that the global optimal design may be obtained by tuning the natural frequencies to satisfy specific constraints. We quantify the difference between a lower bound to the solution for maneuver time associated with the original problem and the estimate obtained from the modified problem, for a specified application requirement. Numerical examples are presented to demonstrate the capability of this approach.

I. Introduction

Large space structures such as antennas or space stations will be very flexible, not only because of the high cost of transportation of structures from Earth to space, but also because they will be constructed or deployed in orbit and will not need to withstand large launching and gravity loads. However, when a space structure is very flexible, its active control system can excite and otherwise significantly interact with its flexible modes. Thus, the idea arises of achieving the best flexible mode suppression for attitude maneuver of spacecraft. The control problem of time-optimal, rest to rest, slewing of a flexible spacecraft through a large angle has been investigated [1]. In that work, a specific spacecraft is modelled using a reduced order model, and the time-optimal control history of this modelled system is derived. In some time critical applications, it is required that the maneuver be performed as rapidly as possible. As a consequence, structural optimization is considered so as to further minimize the maneuver time. The whole design process, the idea of combined design of controllers and structures for optimal maneuverability, is considered in this work.

Traditionally, the overall design problem for actively controlled space structures is treated via an iterative two-part scheme. Redesign of the structure including sensor and actuator placement is performed in one stage, and then the control law is modified for the resulting system to complete an iteration cycle. Generally different design objectives apply in the separate steps. More recently, the need to integrate the design of a structure and its control system has been recognized. An integrated approach is justified simply on the basis that structural and control purposes are substantially coupled. Bodden and Junkins [2] presented a method for eigenvalue optimization with sequential or simultaneous design of structure and control. Khot, Oz, Venkayya, and Eastep [3-5] considered structural optimization, including constraints on control gain norm and transient behavior of the control system, based on a linear-quadratic model of the controller. Hale, Lisowski, and Dahl's [6,7] treatment of the problem of simultaneous structure and control design for a maneuvering spacecraft resulted in a linear-quadratic optimization problem. Bendsoe, Olhoff, and Taylor [8] presented an algorithm for integrated design of the structure and its control system which includes a constraint to limit the control spillover into the unmodelled modes. Lust and Schmit [9] presented a control-augmented structural synthesis methodology in which the structural member sizes and active control system feedback gains are treated simultaneously as independent design variables. Onoda and Haftka [10] considered the optimization of the total cost of the structure and control system subject to constraints on the magnitude of the response to a given disturbance involving both rigid-body and elastic modes. Lim and Junkins [11] presented an idea for optimizing the robustness of structures and structural controllers, using homotopy and sequential linear programming algorithms. Khot [12] presented algorithms for design of minimum weight structures with the goal of improving system dynamics by use of a closed-loop control system.

Most of the developments on simultaneous design of structures and controllers reported in the literature use simple linear feedback control laws and quadratic performance indices. Practical constraints such as limitation on the amplitude of the control effort generally are not taken into account. The use of such relatively narrow forms of problem statements may have serious implications in terms of the usefulness of the results. It is understood, for example, that the use of performance indices expressed as linear/quadratic functionals is generally inappropriate unless loop transfer recovery techniques [13-16] are incorporated into the formulation. Furthermore, the constraints usually used in literature are on the closed-loop eigenvalue distribution and structural frequencies. These constraints are not as direct to the application problem as constraints on rise time, maximal displacement, or maximal stress. The consideration of performance degradation of the optimal system coming from the control and observer spillover is also generally not included.

In the present work, we examine the problem of fully coupled design for a spacearaft and its associated control. The design of the structural system and control is to be integrated so as to optimize with respect to a single cost function. The objective is chosen to reflect the maneuverability of this structure/control system, i.e. the time required to perform a given maneuver or set of maneuvers. Various forms of Mission Specification can be reflected in the definition of the performance index. Ours includes criteria related to sets of maneuvers with specified probability of occurrence. This performance index is generally more meaningful than the usual LQG index with minimum weight. The 'minimum time' objective is appropriate for application in slewing or other retargeting maneuvers. Furthermore, the problem is formulated in a way to accommodate in explicit form of various practical constraints, such as limits on control action and performance error (control spillover). Also, the formulation is consistent with a nonlinear bang-bang form of optimal control design.

The spacecraft is modeled as a linear, elastic, undamped, nongyroscopic system. The necessary-and-sufficient condition for the time-optimal rest-to-rest control problem can be considered as a mapping from the structural dynamic properties to the optimal maneuver time. The maneuverability is optimized by updating design parameters. Characteristics of the problem and problem solving procedures have been investigated. Approximate design methods have been developed to overcome the computational difficulties. Numerical examples are presented to demonstrate the capability of those approaches.

II. Combined Design of Structures/Controllers - Problem Formulation

Consider the linearized rotational dynamics of a flexible spacecraft where control inputs are used to actively control the rigid body mode and flexible modes. The spacecraft is modeled as a linear, elastic, undamped, nongyroscopic system. There is a rigid central body, as shown in Figure 1, to which N ($N \geq 2$) identical flexible appendages are attached with uniform spacing between them. Along the appendages, there might be some kinds of distributed or concentrated payload masses for practical usage. The spacecraft may be very large and flexible. The spacecraft is to be controlled by a single torque actuator located on the central body and m torquers located at identical locations on each of the N appendages. The amplitude of the torque applied by each torquer is limited. The objective of the control design is to time-optimally slewing the spacecraft through a specified angle θ, and achieve flexible mode suppression at the end of the maneuver. Assume that the appendage displacements, slopes and central body rotation rates remain small and the appendages are inextensible. The appendage displacements are restricted to a plane orthogonal to the central body's axis of rotation.

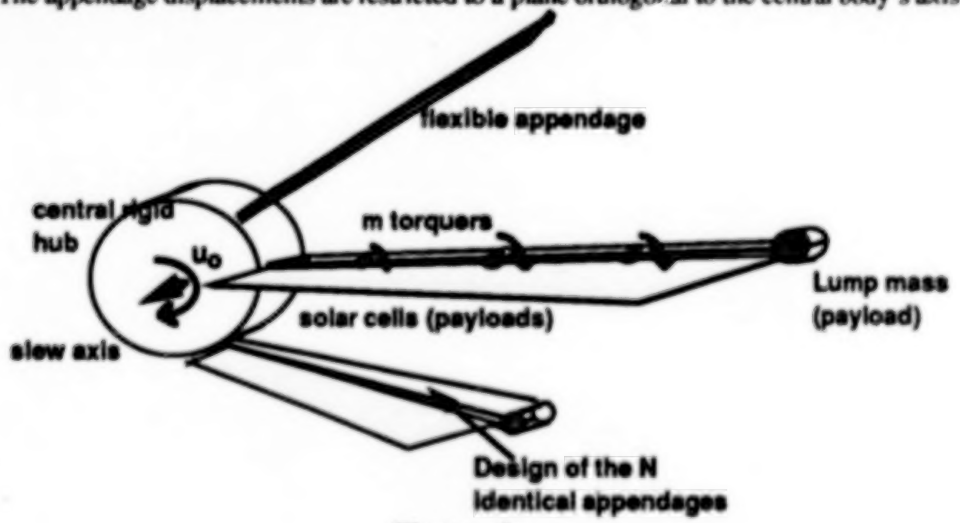

Figure 1

The design parameters of the appendages can be the cross section, stiffness or density of the material, layouts of the composite material or the location of torquer actuators along the appendage. Let the design parameter vector be $\xi \in R^N$, implying that the structural dynamics properties are implicit functions of ξ.

Maneuverability Index

The maneuverability, formulated as a maneuverability index, reflects the cost required to perform a given maneuver or set of maneuvers. The mission profile is specified by giving the probability density function $p(\theta)$ of the required

maneuver amplitude θ. Let $t_f^*(\theta)$ be the optimal maneuver time for maneuver θ, and $t_f^*(\theta)$ is a function of the structural design parameter vector ξ. Therefore the maneuverability index is also a function of ξ. We define the maneuverability index as

$$\mu^*(\xi) = \int_{-\infty}^{+\infty} p(\theta) \cdot t_f^*(\theta) d\theta \,, \tag{2.1}$$

For example, let $p(\theta) = \delta(\theta - \theta^*)$ then $\mu^*(\xi) = t_f^*(\theta^*)$. In other words, the maneuverability index represents the expected value of the optimal maneuver time for a given mission profile. The structural design problem is then to optimize $\mu^*(\xi)$ with respect to ξ.

Optimal Design Problems

Assume that the structural design parameter ξ is restricted to belong to a compact set Ξ, which represents feasible designs. Assume that the design of the appendages will not change the characteristic of the torquers along the appendages. In other words, the amplitude limits of the torquers remain the same for all values of the design parameters. Therefore, we can formulate the optimal combined structure/control design problem as :

$$\mu = \min_{\Xi} \mu^*(\xi)$$

where Ξ is the space of structural design variables
subject to two sets of constraints :

I. a. Material resource constraint,
   b. Geometric configuration constraints :
      such as the max. and min. thickness limits of cross section,
   c. Dynamic response constraints :
      such as the max. stress and displacement limits,

and, II. The post-maneuver control spillover is within a specified bound. (2.2)

Constraint II takes into account the perfor nance degradation associated with the uns odelled dynamics.

We approach the distributed parameter design of the cross section of the appendage using assumed shape functions. For example, let the design parameter of the cross section be the thickness distribution. We assume that the thickness function, h(x) (x is the location along the appendage) is represented via a linear combination of a set of assumed shape functions. This approach uses the same idea as design variable linkage [17].

The distributed infinite degree-of-freedom system is approximated with finite elements. We discretize the spacecraft into a finite number of elements and then perform modal analysis. There are two kinds of mathematical models for design and analysis. Let subscript $\mathfrak{E}$ indicate a quantity derived based on the control evaluation model. The number of modes in this model is the number of degrees of freedom in the finite element analysis (let it be n in this paper). Assuming this model to represent the exact dynamic system, we can evaluate the performance of the controlled system on it. Let subscript $\mathfrak{R}$ indicate a quantity derived based on the control design model. The control design model is the model on which we obtain the optimal-time maneuver law. We assume there are r ($r << n$) vibrational modes retained in this model. The natural frequency and mode shape of the modes in the control design model can be easily obtained from the control evaluation with the dynamic reduction method.

Results of the Linear Time-Optimal Control Problems

Results presented in this section were obtained in the recent paper [1]. The optimal control characterized here is based on a control design model, or so called reduced order model, which has one rigid body mode and r undamped flexible modes. There are $2*(r+1)$ state variables in this system. The problem of time-optimal rest-to-rest slewing maneuver can be formulated as

Problem $M(\theta)_{\mathfrak{R}}$:

$$\min \; t_f(\theta) \tag{2.3}$$

Subject to :

$$\dot{x} = A\, x(t) + B\, u(t)$$

$$|u_j(t)| \le U_j \;;\; j = 0, 1, \ldots, m$$

where u_0 is related to the control input at the central rigid body and $u_1, u_2, \ldots u_m$ are related to the m

torquer actuators along the appendages. U_j ; $j = 0, 1, \ldots, m$ are the corresponding amplitude limits.

$$x(0) = (0, 0, \ldots, 0)^t \text{ , where } (\ )^t \text{ denotes transpose.}$$

$$x(t_f) = (\theta, 0, \ldots, 0)^t$$

$\mathbf{A}$ = Block diag$[\mathbf{A}_i]$, $\mathbf{B}$ = Block col $[\mathbf{B}_i]$, where

$$\mathbf{A}_i = \begin{bmatrix} 0 & 1 \\ 0 & 0 \end{bmatrix} \quad ; \ i = 0,$$

$$\begin{bmatrix} 0 & \omega_i \\ -\omega_i & 0 \end{bmatrix} \quad ; \ \omega_i \text{ is the natural frequency, } i = 1, 2, \ldots, r$$

$$\mathbf{B}_i = \begin{bmatrix} 0 & 0 & \cdots & 0 \\ \beta_0^i & \beta_1^i & \cdots & \beta_r^i \end{bmatrix} \quad ; \ i = 1, 2, \ldots, r \tag{2.4}$$

Let the solution for problem $M(\theta)_{\mathcal{R}}$ be $t_f^*(\theta)$.

Theorem 1.1. Let t_f^* be the optimal maneuver time. For all θ, Problem $M(\theta)_{\mathcal{R}}$ has a unique solution t_f^*.

Theorem 1.2. For a given θ, the optimal control law is of bang-bang type, and is symmetric around $t_f^*/2$, i.e.

$$u(t_f^*/2 - t)^* = -u(t_f^*/2 + t)^*, \quad 0 \le t \le t_f^*/2 .$$

Reference [1] treats the general multiple control case, where there are m+1 control inputs. However, for simplicity, herein we assume that only one control input is used to control the maneuver, that is, the scalar control case. This assumption means that the N torque actuators on the appendages and the actuator on the rigid central body taken together represent one control input.

Theorem 1.3. Assume there are k switching times between 0 and $t_f^*/2$, and let them be t_i, $i = 1,2,\ldots k$. Let J^* be the total rotational moment of the spacecraft, and $(p_0^0, 0, p_0^1, 0, \ldots, p_0^r, 0)$ be the costate variable at mid-maneuver time. Then the optimal maneuver time and the switching times satisfy as necessary and sufficient conditions, the following system of nonlinear algebraic equations :

$$(t_f^*)^2 - 2(t_k)^2 + 2(t_{k-1})^2 - \cdots + 2(-1)^k (t_1)^2 = \theta J^*/U_0 , \tag{2.5}$$

$$\cos(\omega_i t_f^*/2) - 2\cos(\omega_i t_k) + 2\cos(\omega_i t_{k-1}) - \ldots + 2(-1)^k \cos(\omega_i t_1) + (-1)^{k+1} = 0$$

$$i = 1, 2, \ldots r \tag{2.6}$$

$$\begin{bmatrix} U_0 t_f^*/2 & U_0 \sin(\omega_1 t_f^*/2) & \cdots & U_0 \sin(\omega_r t_f^*/2) \\ t_k & \sin(\omega_1 t_k) & \cdots & \sin(\omega_r t_k) \\ \vdots & \vdots & & \vdots \\ t_1 & \sin(\omega_1 t_1) & \cdots & \sin(\omega_r t_1) \end{bmatrix} \begin{Bmatrix} p_0^0 \\ \beta_0^1 p_0^1 \\ \vdots \\ \beta_0^r p_0^r \end{Bmatrix} = \begin{Bmatrix} -1 \\ 0 \\ 1 \\ 0 \\ 0 \end{Bmatrix} \tag{2.7}$$

and two inequality equations :

$$t_f^*/2 > t_k > t_{k-1} > \ldots > t_2 > t_1 > 0$$

$$p_0^0 t + \sum_{i=1}^{r} \beta_j^i p_0^i \sin(w_i t) \neq 0 \tag{2.8}$$

$$\text{where } 0 \le t \le t_f^*/2 \quad t \neq t_i \quad i = 1, 2, \ldots k$$

To solve for the optimal control history, we need first assume the number of switching times, say k, then try to find the solutions $\{ t_j , j = 1, 2, \ldots k \}$ and $\{ p_0^i , i = 0, 1, 2, \ldots r \}$ for (2.5)-(2.7). If (2.5)-(2.7) really admit solutions and they satisfy (2.8) as well, by uniqueness of the solution of the optimal control problem, we have the unique solution.

We have found that, in general, k is always equal to r. Only when { ω_i , i = 1, 2, ... r } satisfy some special conditions, k is less than r. For the case where k is equal to r, Theorem 1.3 can be simplified by omitting (2.7).

Reduced Order Model

We now consider how many flexible modes should be retained in the reduced order model. The question is answered by analyzing the degradation in the performance of the designed system on the control evaluation model. This performance degradation is associated with 'unmodelled dynamics' of the uncontrolled residual modes in the control evaluation model (from r+1-th term to n-th term). The effects, therefore, result in post maneuver free vibration of the system, due to control spillover. We need to make sure these vibrations have amplitudes within a specified performance error bound during the optimization.

There are two ways to quantify the performance degradation : (i). the residual or spillover energy $\mathcal{E}_r(t)$, and (ii). the pointing error of the rigid central body after completion of the maneuver $\theta_e(t)$ (where $t \geq t_f^*/2$). From the recent investigation on these [1], the latter is the better one because the maximum pointing error continues to decrease as we suppress additional modes at the final time, while the spillover energy does not necessarily decrease. Also [1] gives three closed form expressions for the upper bound $|\theta_e(t)|$, based on the control evaluation model. Among them, the most useful according to our experience is

$$|\theta_e(t)| \leq 2[(2 + 2k)U_d/J^{*2}] \sum_{i=r+1}^{n} (\beta_0^i)^2 \; ; \quad t \geq t_f^*/2, \tag{2.9}$$

We use this upper bound to determine the size of the control design model in order to obtain a prespecified post-maneuver pointing accuracy of the rigid central body.

Characteristics of the Optimal Design Problem

Theorem 2.
Suppose the number of flexible modes retained in the model is fixed. The optimal maneuver time solved from the (2.5)-(2.8) is a continuous function of the structural design variables, ξ.
Corollary 1. The objective function, $\mu(\xi)$, is a continuous function of ξ.
Corollary 2. There exists a solution to the optimal design problem (2.2).

We have observed that the objective function is always a differentiable function of the structural design variables, ξ. Consider the generic case where k is equal to r. The optimal maneuver time can be obtained from (2.5)-(2.6). Actually (2.5)-(2.6) represent a system of implicit equations of the form :

$$F(t_f^*, t_1, \omega, \beta, J^*) = 0. \tag{2.10}$$

The gradient of the optimal maneuver time with respect to structural parameters can be obtained using the Implicit Function Theorem as follows : Let $x=(t_f^*, t_1)$ and $y=(\omega, \beta, J^*)$

Theorem 3. (Implicit Function Theorem)
Suppose (x_0, y_0) is such that $F(x_0, y_0) = 0$ and $F(x_0, y_0) \in C^k$, and the Jacobian matrix $[\partial F/\partial x]$ is nonsingular (regular) at (x_0, y_0). Then there exist a neighborhood of y_0, say $N(y_0)$, and a mapping $G : N(y_0) \to R^n$ such that $x_0 = G(y_0)$ and $G(y_0) \in C^k$, and $F(G(y), y) = 0$ on $N(y)$. Moreover, we have

$$[\partial G/\partial y]|_{y0} = -[\partial F/\partial x]^{-1}_{x0, y0} [\partial F/\partial y]_{x0, y0} \tag{2.11}$$

By the Chain Rule, we can obtain the gradient of the objective function with respect to the design parameters. A candidate optimal design must satisfy the Kurash-Kuhn-Tucker necessary conditions [18]. We use mathematical programming to find it.

From (2.10), t_f^* is an implicit function of (ω, β, J^*). Furthermore, for the generic case where k is equal to r, t_f^* actually is a function of ω and J^* only. We show the behavior of $t_f^*(\omega, J^*)$ for the simplest case where there is only one flexible mode in Figures 2 and 3.

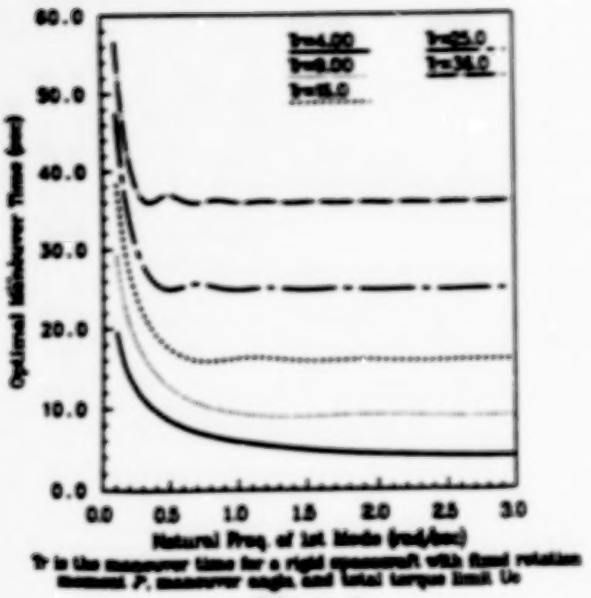

Figure 2.

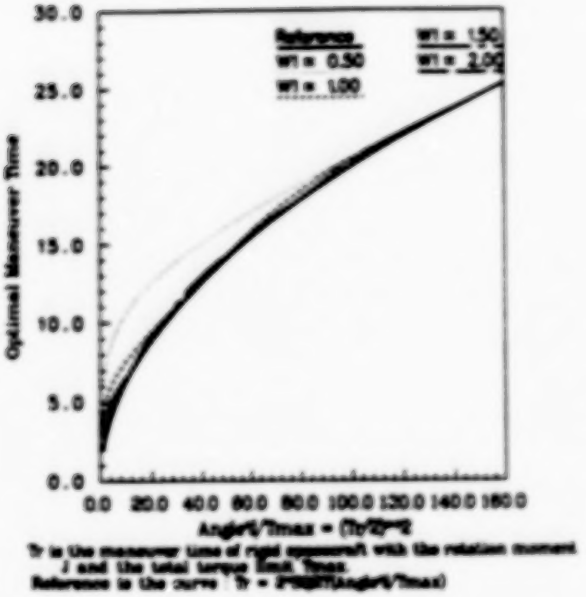

Figure 3.

We have found the following results : Assume a spacecraft has only one flexible mode.

(i). For a spacecarft with very small ω_1 (usually a very flexible spacecarft), t_f^* is quite large. On the other hand, for a spacecraft with large ω_1 (as shown in the Figure 2, greater than 2.0), t_f^* is almost the same as that of the equivalent rigid spacecraft.

(ii). For a spacecraft with $\theta J^*/U_0 \geq 120.0$ (the torquer limit is very small or the maneuver angle is very large), t_f^* is almost the same as that of the equivalent rigid spacecraft.

Of course, a typical spacecraft has more than one flexible mode, and we can not say much about it. However, Figure 2 and 3 provide important information. If the spacecraft is very flexible or the torquer limit is very large (usually this implies very large maneuver speed), the result of the optimal design can provide substantial improvement.

Problem Solving Algorithm

The control design model is chosen according to the analysis of control spillover. In order to take advantage of Theorem 2, we assume that the control design model is fixed during the optimization and formulate the optimization procedure as

$\mathcal{P}_1$:

Begin with a reasonable baseline design of the spacecraft.

Step 0 : Set up the reduced model by (2.9). (Set the value of r)
Step 1 : Initialize the design variables.
Step 2 : Get the cross section of the appendage for the current value of the design variables.
Step 3 : Finite Element Analysis.
Step 4 : Calculate the natural frequencies of the modes in the reduced model by the Dynamic Reduction Method.
Step 5 : Solve the time-optimal control problem to obtain the optimal maneuver time.
Step 6 : Find the next values of the design variables by the Nonlinear Programming.
Step 7 : If the result is convergent, Step 8. Otherwise, go to Step 2.
Step 8 : If the spillover constraint (ii of (2.2)) is satisfied, then Stop. Otherwise, Step 0.

Although the algorithm $\mathcal{P}_1$ is able to solve the optimal structural design problem (2.2), unfortunately, in our experience, there exist a lot of numerical difficulties associated with it :

i). To solve the time-optimal control problem, we need to know the number of switching times.
ii). Actually the set of nonlinear equations (2.5-2.7) admit many solutions, of which only one satisfies the inequality conditions (2.8). Thus, even though we have a good nonlinear equation solver, it would not be able to guarantee to find the solution we want.

Given all the difficulties above, it seems a formidable task to solve the optimal design problem by $\mathcal{P}_1$ without any simplification, especially if one expects to find the global optimal design. Therefore, we introduce approximate design methods as described in the next section.

III. Approximate Design Method

The fundamental idea of this solution procedure is to formulate an approximate design problem without violating any constraint of the original problem. The solution of the approximate design problem is a 'near-optimal design' in the sense that there is little difference of objective function between the two solutions. We need to quantify the difference without solving the original problem and make it as small as possible. However, there is a trade-off between accuracy and efforts for solving problems. Thus an important capability of the approximation algorithm is that we can adaptively upgrade the approximation procedure to obtain a reasonable result according to the specific application requirement. Since design models can not exactlly represent the real system, it is unreasonable to concern oneself so much about a relatively small improvement of accuracy of the solution based on a design model. In this section we introduce two approximate design methods : the Adaptive Frequency Tuning method, and the Minorant method. The former one is suitable for the single maneuver case; the latter one requires more computation work but is suitable for the multimaneuver case.

Frequency Tuning Approach

There are two basic assumptions :

Assumption 1. : The natural frequencies of the modes retained in the reduced order model can be freely assigned by adjusting the values of the design variables.

Assumption 2. : During the design iteration, the mass distribution of the appendage is taken to be independent of the stiffness distribution, i.e., the total rotational moment of the spacecraft, J^* , does not change when the stiffness distribution is modified.

Considering (2.5, 2.6), if for a spacecraft the natural frequencies of all modes in the reduced order model happen to satisfy :

$$\omega_i \cdot t_f^* = j_i \cdot 4\pi \quad , \quad i = 1,2, \ldots\ldots r \tag{3.1}$$

where t_f is the maneuver time and j_i is some integer multiplier,

then, the solution in terms of switching times and the optimal maneuver time satisfy :

$$k = 0 \text{ , and } \quad t_f^* = 2\sqrt{\theta J^* / U_0} \tag{3.2}$$

It also satisfies the inequality condition (2.8). Thus we solve the time-optimal control problem for $\{\omega_i, i = 1,2, \ldots r$ satisfying (3.1) $\}$. Moreover, (3.2) imply that there is no switch of the control history between 0 and $t_f^*/2$, and only one switch at the mid-maneuver. This means that all flexible modes in the reduced model are dead beat at the end of maneuver by the same control which maneuvers a rigid body of the same value of total rotational moment J^*. We have the new optimization problem :

$$\mathcal{P}_2 \qquad \min_{\Xi} \; t_f^* = 2\sqrt{\theta J^* / U_0}$$

subject to :

the constraints I and II of (2.2), and (3.1) (3.3)

Proposition : Under the Assumptions 1 and 2 above, the solution of $\mathcal{P}_2$ solves our original problem, (2.2), and it is a global optimum.

The rigid-body control strategy is the simplest to implement, and we don't need to solve any nonlinear equations (2.5-2.7). Furthermore the optimal design of appendage which satisfies (3.1) may be very flexible (in the sense that natural frequencies of the first few flexible modes are very small), and very light (in the sense that J^* is small). This idea for design appears to be original.

Adaptive Upgrade Algorithm

Unfortunately, Assumption 2 above is not always satisfied in general applications. For example, in designing an appendage of rectangular cross section with high density material, the stiffness is highly coupled with the design of mass distribution. Actually, $\mathcal{P}_2$ implicitly assumes that the global optimal design of the appendages is such that the time-optimal control is the same as the rigid-body control strategy. We restrict ourselves to solve the original problem in a subspace of the feasible design variable space. Therefore, the result of $\mathcal{P}_2$ in general does not apply and needs to be modified or upgraded.

We first quantify the index of improvement in approximation as the difference of objective function between the exact optimal design (the solution of original problem) and the solution of approximate design problems. Let tf be the maneuver time of the exact optimal design, which is equal to the minimum of t_f^* over the entire feasible design space.

Also we note that μ is equal to $\int p(\theta_i) \cdot tf(\theta_i)\, d\theta_i$. Let tf^a, μ^a be the approximated solution of tf and μ respectively.

Then we introduce : Index of approximation : $\mathcal{I}_0 = |tf^a - tf|$ or $|\mu^a - \mu|$ (3.4)

An approximated solution is better if the index of approximation is smaller. However, this doesn't mean the two designs are close to each other. For example, they may be substatially different in shape. In order to avoid difficulties in computing tf, we modify (3.4) : $\mathcal{I}_1 = |tf^a - \mathcal{L}^b(tf)|$ or $|\mu^a - \mathcal{L}^b(\mu)|$,

where $\mathcal{L}^b(\cdot)$ is a lower bound of $\cdot$, and it is very easy to compute. (3.5)

Also, we have $\mathcal{L}^b(\mu) = \int p(\theta_i)\, \mathcal{L}^b(tf(\theta_i))\, d\theta_i$ (3.6)

There are two ways to define such a lower bound :

(i). the maneuver time for a rigid spacecraft with the least fesible total rotational moment I^*:

$$\mathcal{L}^b_1(tf) = 2\sqrt{\theta I^* / U_0} \tag{3.7}$$

It is usually unreasonable to define the lower bound in this way because (3.7) is very conservative. The appendage with the least total rotational moment is usually too slender, too flexible, and likely requires a long maneuver time.

(ii). the optimal maneuver time of the optimal design which is based on a reduced model with only one flexible mode. Let the superscript 1 of tf indicate that the value is based on a reduced model with only one flexible mode. Thus

$$\mathcal{L}^b_2(tf) = tf^1 = \text{minimum of } t_f^{*1} \text{ over the entire feasible design space.} \tag{3.8}$$

Since we need more maneuver time for the reduced model with more flexible modes, we know tf^1 is a lower bound of the maneuver time for the design problem of any reduced order model. We need some computation effort to calculate tf^1; however, the calculation is not very difficult. It is more reasonable to define the lower bound of the maneuver time to be tf^1.

We propose the modified approximate problem $\mathcal{P}_3$ according to the following facts :

Fact 1 : For a specified reduced order model with r flexible modes, we can divide the feasible design space into :

$\mathcal{D}_0$: { ξ : the time-optimal control history of this design admits only one switch at mid-maneuver, without any switch in $(0, t_f^*/2)$ },

$\mathcal{D}_1$: { ξ : the time-optimal control history of this design admits at most one switch in $(0, t_f^*/2)$ },

$\mathcal{D}_2$: { ξ : the time-optimal control of this design admits at most two switches in $(0, t_f^*/2)$ },

.....

and $\mathcal{D}_0 \subseteq \mathcal{D}_1 \subseteq \mathcal{D}_2 \subseteq \mathcal{D}_3 \subseteq$ ..... (3.9)

Fact 2 : t_f^* over $\mathcal{D}_r \geq t_f^*$ over $\mathcal{D}_{r+1}$ (3.10)

Fact 3 : the solution of (2.2) is the t_f^* over $\mathcal{D}_r$ for some $r \geq 0$.

Actually, the solution of $\mathcal{P}_2$ is nothing but tf over $\mathcal{D}_0$. Similarly, $\mathcal{P}_3$ is the problem of solving for tf over $\mathcal{D}_r$, $r \geq 1$, adaptively upgrading with respect to the index of improvement, and with a stopping criterion based on sufficiently small change of improvement. We can eventually obtain the exact global optimal design if the upgrade goes on. However, we have restricted ourselves to solveing for tf over $\mathcal{D}_r$, $r \leq 2$.

The Minorant Design Method

$\mathcal{P}_2$ and $\mathcal{P}_3$ are not suitable for the general multiple maneuver case because it is difficult to find ω_i , i = 1,2, ... r which satisfy (3.1) for many different maneuvers, $\{\theta_i\}$. In this section we discuss an algorithm, the minorant method, which is more difficult to implement, but, suitable for the multiple maneuver case. While solving the time optimal control problem, we find that for any design of spacecraft, $t_f^{*r+1} \geq t_f^{*r}$; however, the difference becames smaller and smaller as r increases. From our numerical studies, it is observed that the maneuverability is most influenced by the total rotational moment J*, and then from the few lowest flexible modes. An appendage with smaller total rotational moment or with more rigidity, in the sense that the natural frequencies of the lowest few flexible modes are large tends to be very maneuverable.

$\mathcal{P}_4$ is based on the following assumption and fact.

Assumption : For any fesible design of the spacecraft $\xi \in \Xi$, we have $| t_f^*(\xi)^{i+2} - t_f^*(\xi)^{i+1} | \leq | t_f^*(\xi)^{i+1} - t_f^*(\xi)^i |$, i ≥ 0, where the superscript i indicate that the quantity is obtained based on a reduced model with i flexible modes.

Fact 4 : $| tf^{i+2} - tf^{i+1} | \leq | tf^{i+1} - tf^i |$, i ≥ 0, and $| tf^i - tf^r | \to 0$ as r and i are sufficiently large. Furthermore, $|\mu^{i+2} - \mu^{i+1}| \leq |\mu^{i+1} - \mu^i|$, i ≥ 0, and $|\mu^i - \mu^r| \to 0$ as r and i are sufficiently large.

$\mathcal{P}_4$:

Step 1 : Let i = 0, and Solve μ^i by $\mathcal{P}_1$.

Step 2 : Obtain the index of improvement $\mathcal{I}$. If there is no relative change of improvement, stop. Otherwise, i = i+1. Go to Step 1.

The exact optimal design can be obtained for i = r. However, we do not go beyond i ≥ 2. The capability of $\mathcal{P}_4$ will be investigated later with numerical examples.

IV Numerical Examples

In our examples, we consider designing appendages by adjusting the cross section. We use practical examples with realistic scale and material. Furthermore, we try to investigate the design of large flexible space structures, such as huge antenna or space stations.

In what follows, we perform the modal analysis with the finite element method, and model the flexible spacecraft with one rigid body mode and twenty flexible modes. There are r flexible modes, obtained by the dynamic reduction method, retained in the reduced order model for control design. The reduced order model is specified according to the post-maneuver spillover constraint. In the examples, we specify the maximum angular deviation of the central rigid body post maneuver as 0.05 deg. The appendages are I-beams (as shown in Figure 4). Our goal is to obtain the optimal flange depth distribution of the appendages, and assume the width of the web, and thickness of the web and flange to be constant. The flange depth is symmetric about a central line passing through the cross section. We use two spline polynomials as the assumed shape functions to describe the half flange depth :

$$h_1(x) = c_1 + (c_2/L)x + (c_3/L)^2 x^2 + (c_4/L)^3 x^3, \qquad 0 \leq x \leq L/2$$

$$h_2(x) = h_1(L/2) + h_1'(L/2)(x - L/2) + (c_5/L)^2 (x - L/2)^2 + (c_6/L)^3 (x - L/2)^3, \quad L/2 \leq x \leq L$$

where c_i, i = 1, 2, ... 6 are design variables. (4.1)

We note that all design variables c_i , i = 1, 2, ... 6 are almost of the same order, and h(x) and dh(x)/dx are continuous at x = L/2.

We consider a spacecraft with two identical flexible appendages. For simplicity, we assume the appendages are made of a single uniform material.

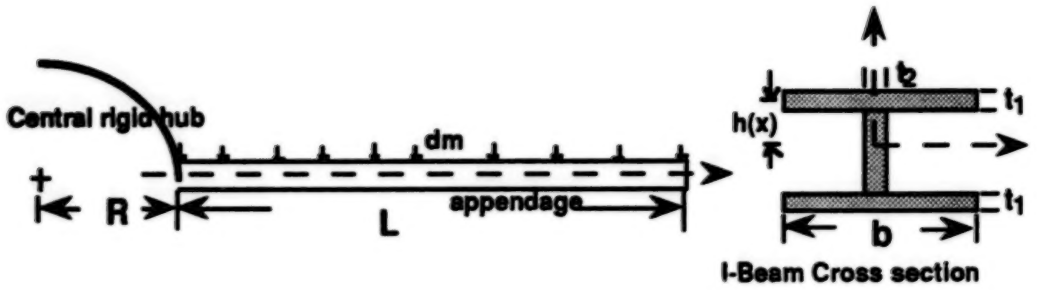

Figure 4 Design of the cross section of appendages

We begin solving the problem by finding a reasonable number of modes in the reduced order model. We use a reasonable baseline design with flange equal 4.00 cm. As shown in Table 1, we note that it is appropriate to retain three flexible modes for a postmaneuver maximum angular deviation to be guaranteed less than 0.05 deg.

Number of modes retained in the model	0	1	2	3	4	5	6	7
Max. angle deviation post maneuver (deg)	1.495	0.082	0.0113	2.6e-3	8.3e-4	3.2e-4	1.5e-4	7.1e-5

Table 1.

Spacecraft Data	
Appendage material density, ρ	1880.00 kg/m^3
Appendage Material Elasticity, E	2.76E11 N/m^2
Radius of the rigid central body, R	12.00 m
Mass of the rigid central body	4500.00 kg
Length of one appendage, L	50.00 m
Maximum torque available, U0	3.0 E4 N-m
Width of the web, b	5.00 cm
Thickness of the web, t1	1.75 cm
Thickness of the flange, t2	0.75 cm
Distributed pay load mass, dm	9.00 kg/m
Concentrated pay load mass (at x = L), M	None
The resource constraint of two appendages	450.0 kg
The minimal flange depth	2.00 cm
The maximal flange depth	12.00 cm

Case 1 : Single maneuver case

Command slew angle, θ 90.00 deg

Thus the exact solution is tf, which is equal to t_f^{*3} over the entire feasible design space.

Result :

(a). $\mathcal{L}^b_1(tf) = 2\sqrt{\theta J * U_0} = 21.9814$ sec, but t_f^{*3} of this design is 24.6213 sec.

(b). $\mathcal{L}^b_2(tf) = tf^1 = 22.3126$ sec, and t_f^{*3} of this design is 22.41457 sec. The switching times between 0 and t_f^{*3} of the time-optimal control history are 1.5547E-8, 0.21945, 0.48124 sec (one switching time is almost zero).

(c). From $\mathcal{P}_2$: tf over domain $\mathcal{D}_0$ is 22.3218 sec. Let it be tf^a.

$|tf^a - \mathcal{L}^b_2(tf)| = 9.2E\text{-}3$. We can accept this design as the solution (as shown in Fig. 5).

Properties of this optimal design of Case 1 :

Structural mass of two appendages	379.687 kg
Total pay load mass along the appendages	900.00 kg

Total mass of the spacecraft	5779.687 kg
Total rotational moment	2375330.68 kg-m^2
Natural frequency ω_i , i = 1, 2, ..., 4	0.5642, 1.6942, 4.4738, 8.9745 (rad/sec)
The max. angle deviation from the uncontrolled modes	0.00908 deg
Number of switches between 0 and $t_f^*/2$ of the time-optimal control history :	None

Case 2 : General Multiple Maneuvers

The set of maneuvers are $\{ \theta_i \} = \{9, 15, 30, 45, 60, 90 \text{ (deg)} \}$, and assume that they occur at the same frequency. Thus the objective function (maneuverability index) is

$$\mu(\xi) = \frac{1}{6} \sum_{i=1}^{6} t_f^*(\theta_i) \qquad (4.3)$$

The solution μ equals μ^{*3} over the entire feasible design space.

Result :

(a). $\mathcal{L}^6_1(\mu) = \sqrt[2]{\theta J^* \mu_0} = 13.1753$ sec.

(b). $\mathcal{L}^6_2(\mu) = \mu^1 = 15.0436$ sec, and μ^{*3} for this design is 15.30617 sec.

As $\mathcal{P}_4$: if we let $\mu^a = 15.30617$, we have $|\mu^a - \mathcal{L}^6_2(\mu)| = 0.26257$, as 1.7454 %.

(c). μ^2 is 14.8580 sec, and μ^{*3} for this design is 14.96326 sec.

As $\mathcal{P}_4$: if we let $\mu^a = 14.96326$, we have $|\mu^a - \mathcal{L}^6_2(\mu)| = 0.06526$, as 0.4392 %. We accept it as the solution (as shown in Fig. 5).

(d). We investigate the exact solution by $\mathcal{P}_1$ and obtain μ^3 is 14.9455 sec.

Properties of this optimal design of Case 2 :

Structural mass of two appendages	425.075 kg
Total pay load mass along the appendages	900.00 kg
Total mass of the spacecraft	5825.075 kg
Total rotational moment	2379168.55 kg-m^2
Natural frequency ω_i , i = 1, 2, ..., 4	0.8460, 2.0276, 5.5051, 10.6193 (rad/sec)
The max. angle deviation from the uncontrolled modes	0.02436 deg
Number of switches between 0 and $t_f^*/2$ of the time-optimal control history :	Three

V. Conclusion and Future Work

The problem of combined design of structures and controls for optimal maneuverability of an elastic spacecraft has been considered. The main results of the present work are

i). The problem formulation is consistent with bang-bang forms of time optimal controls.

ii). The performance degradation constraint is considered in the design problem.

iii). The optimal design problem is well defined. There always exists a solution.

iv). The optimization is done by mathematical programming.

v). The gradient of the objective function is computed using the Implicit Function Theorem.

vi). Efficient and practical approximate methods have been developed.

Our experience with various numerical examples leads to the following assertions :

i). The best structural designs often are those for which the designs of mass distribution and stiffness distribution have very little coupling.

ii). The benefit of multiple controls is not apparent, since we can use scalar control to achieve good results.

Since spacecraft structure is modelled to be linear, with small displacement and inextensible deformation, the performace for a realistic system which violates these assumptions is worth investigating. The constraints of structural dynamic response, such as maximal displacement and stress, should be considered in the examples as well. Those topics are indicated for future study.

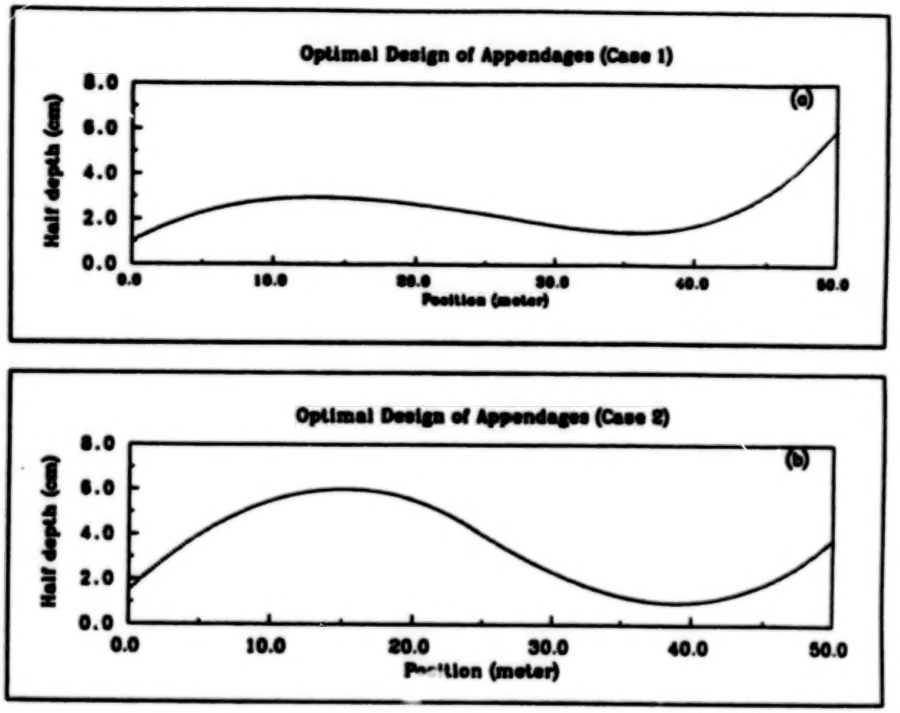

Figure. 5

VI. References

1. G. Singh, P. T. Kabamba, and N. H. McClamroch, "Planar, Time-Optimal, Rest-to-Rest Slewing Maneuvers of Flexible Spacecraft," Journal of Guidance, Control, and dynamics, Vol. 12, No. 1, pp. 71-81, Jan.-Feb. 1989.
2. D. S. Bodden and J. L. Junkins, "Eigenvalue Optimization Algorithms for Structure/Controller Design Iterations," Journal of Guidance and Control, pp. 697-706, Nov.-Dec. 1985.
3. N. S. Khot, F. E. Eastep, and V. B. Venkayya, "Optimal Structural Modifications to Enhance the Optimal Active Vibration Control of Large Flexible Structures," AIAA Paper 85-0627, April 1985.
4. N. S. Khot, F. E. Eastep, and V. B. Venkayya, "Simultaneous Optimal Structural/Control Modifications to Enhance the Vibration Control of Large of a Large Flexible Structure," AIAA Paper 85-1925, Augist 1985.
5. N. S. Khot, H. Oz, R. V. Grandhi, F. E. Eastep, and V. B. Venkayya, "Optimal Structural Design with Control Gain Norm Constraint," AIAA Journal, Vol. 26, No.5, pp. 604-611, May 1988.
6. A. L. Hale and R. J. Lisowski, "Optimal Simultaneous Structural and Control Design of Maneuvering Flexible Spacecraft," in Proceedings of the 4th VPI & SU/AIAA Symposium, pp. 1-16, Virginia Polytechnic Institute, Blacksburg, VA, June 1983.
7. A. L. Hale, R. J. Lisowski, and W. E. Dahl, "Optimal Simultaneous Structural and Control Design of Maneuvering Flexible Spacecraft," Journal of Guidance and Control, Vol. 8, pp. 86-93, 1984.
8. M. P. Bendsoe, N. Olhoff, and J. E. Taylor, "On the Design of Structure and Controls for Optimal Performance of Actively Controlled Flexible Structures," Mech. Struct. & Mach., 51(3), pp. 265-295, 1987.
9. R. V. Lust and L. A. Schmit, "Control-Augmented Structural Synthesis," AIAA Journal, Vol. 26, pp. 86-95, January 1988.
10. J. Onoda and R. T. Haftka, "An Approach to Structure/Control Simultaneous Optimization for Large Flexible Spacecraft," AIAA Journal, Vol. 25, No. 8, pp. 1133-1138, August 1987.

13. M. G. Safonov and M. Athans, "Gain and Phase Margin for Multiloop LQG Regulators", IEEE Trans. Auto. Control, Vol. AC-22, pp. 173-179, 1977.
14. N. A. Lehtomaki, N. R. Sandell and M. Athans, "Robustness Results in Linear Quadratic Gaussian Based Multivariable Control Designs", IEEE Trans. Auto. Controll, Vol. AC-26, pp. 75-93, 1981.
15. J. C. Doyle, "Guaranteed Margins for LQG Regulators", IEEE Trans. Auto. Control, Vol. AC-23, pp.756-757, 1978.
16. J. C. Doyle and G. Stein, "Robustness with Observers," IEEE Trans Auto. Control, Vol. AC-24, No. 4, pp.607-611, 1979.
17. T. L. Fetterman and A. K. Noor, "Computational Procedures for Evaluating the Sensitvity Derivatives of Vibration Frequencies and Eigenmodes of Framed Structures," NASA Contractor Report 4099, 1987.
18. R. T. Haftka, Elements of Optimal Structural Design, Klumer Academic Publishers, 1985.

GROUND TEST PROGRAM FOR NEW ATLAS PAYLOAD FAIRINGS

Michael J. Robbins
General Dynamics/Space Systems Division
San Diego, California

GROUND TEST PROGRAM FOR NEW ATLAS PAYLOAD FAIRINGS

Introduction

An extensive ground test program is currently being undertaken by General Dynamics/Space Systems Division to verify the design of the metal payload fairings for the new family of Atlas launch vehicles, the first of which will be launched this summer. Two new designs, an 11-foot and a 14-foot diameter version of the payload fairings (see Figure 1), are now available to mission planners seeking to accommodate the widest variety of mission requirements. While the 14-foot diameter version was developed for the commercial Atlas I program, and the 11-foot diameter fairing was developed for the U.S. Air Force Atlas II vehicle, once both production lines are at full capacity, the selection of a fairing will be dictated by the size of the satellite payload. These new fairing designs replace the 10-foot diameter, honeycomb fiberglass payload fairings which were flown on previous Atlas/ Centaur launch vehicles. The new metal fairings feature a larger payload envelope, greater ease of manufacturing and modification, have more consistent quality control properties, provide better EMI shielding for the satellite payload, and do so at costs and weights comparable to the old fiberglass fairing.

Both the 11-foot and 14-foot diameter designs are of aluminum skin, frame, and stringer construction and are built at the General Dynamics Services Company plant in Harlingen, Texas. The main structural purposes of the payload fairing are to protect the satellite payload during the ascent phase and to provide an aerodynamic forward surface for the launch vehicle. After the vehicle has cleared the atmosphere, the payload fairing is no longer required, and it is jettisoned both to save weight and to allow for the separation of the Centaur upper stage and the spacecraft. Both the 11-foot and 14-foot designs use a method of separation similar to that originally used for the 10-foot fiberglass fairing. At the moment of jettison, which occurs about 3 1/2 minutes after

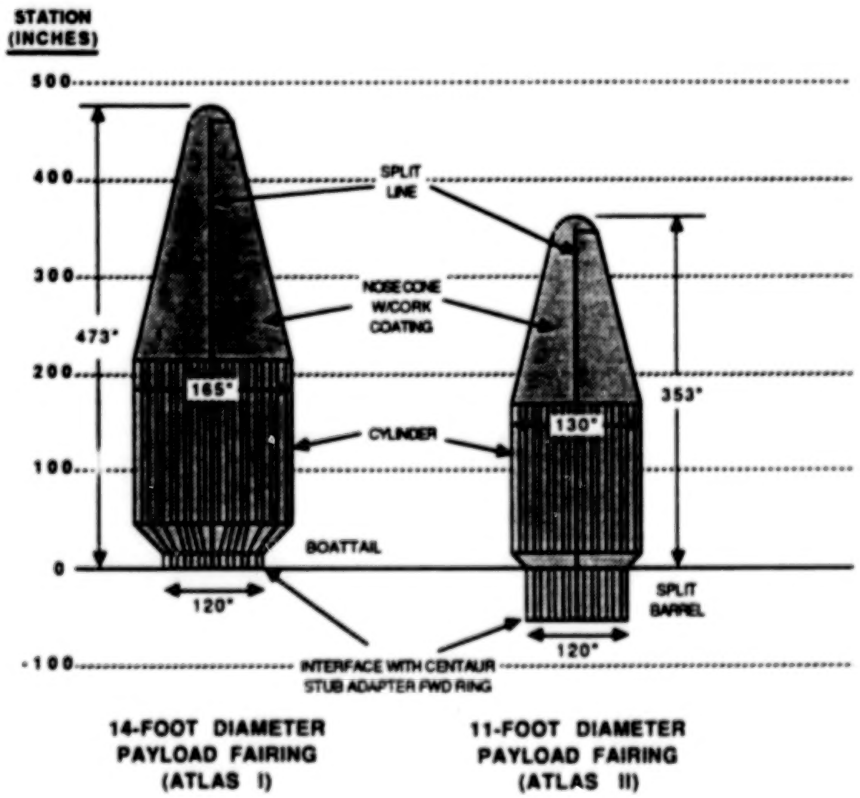

Figure 1. Atlas 11-Foot and 14-Foot Diameter Payload Fairings.

liftoff, explosive bolts fire which allow the two 180-degree halves of the fairing to begin separation. Spring loaded actuators at the top of the cone section push the halves apart, while the aft end of each fairing half begins to rotate on hinges located on the stub adapter. After the fairing halves have rotated about 70 degrees, the hinges allow the fairing to safely and completely separate from the vehicle. Both fairing halves fall back to Earth, where they land in the Atlantic Ocean. No attempt is planned to recover these items.

Five separate ground tests, one of which has already been completed, were planned to gather the necessary data to qualify these new designs for flight. All tests planned will be performed on full-scale payload fairing structures (either dedicated test articles or flight articles). Three tests have been planned for the 14-foot diameter payload fairing and two tests have been planned for the 11-foot diameter payload fairing. All tests of the 14-foot diameter payload fairing must be complete by the planned June 1990 launch for the Combined Release and Radiation Effects Satellite (CRRES) and all tests of the 11-foot diameter payload fairing must be complete in time to support stress and dynamics analyses which must be performed prior to the January 1991 Initial Launch Capability (ILC) date for the Atlas II system.

I. 14-Foot Diameter Payload Fairing Jettison Test

Description: Of the three ground tests planned for the 14-foot diameter version of the new payload fairings, the jettison test is the only one which has been completed as of this writing. This test was successfully performed in December 1989 - January 1990 at the Space Power Facility (SPF) operated by NASA/Lewis Research Center at the Plum Brook Station near Sandusky, Ohio. This site was chosen because it is the largest vacuum chamber in the world, and is the only one in which a full jettison of at least one full payload fairing half could be accomplished. The interior of the chamber consisted of a metal-walled pressure vessel with a 100-foot diameter circular floor and a 120-foot high, domed ceiling. This was surrounded by a thick concrete-walled containment building with a profile which betrays the original intent of the building: to house nuclear powered satellites during test and checkout. Because the facility had not been used since a 1974 Skylab test, a substantial effort was required to reactivate the chamber. Now that the chamber has been proved to be operational, several other jettison tests of payload fairings, including one of the giant Titan IV fairing, have been planned for the NASA Plum Brook SPF.

The test article for the jettison test was a dedicated test fairing which was manufactured to the same engineering prints and quality standards as a regular flight fairing. This article was the first payload fairing completed at the General Dynamics Services Company, Harlingen, Texas assembly plant. From its interface with the Centaur upper stage's stub adapter to the tip of its nose, the new fairing stands 39 1/2 feet high. In the SPF, atop its base fixture and stub adapter, the test article measured in with an impressive height of 52 1/2 feet. Before each completed payload fairing is shipped from its assembly plant, an acceptance test, consisting of a stackmate and a "rotation" test, is conducted to verify that manufacturing tolerances were maintained throughout the entire structure. The rotation test consists of splitting the fairing halves (by a total of no more than one foot at the top of the cone) using a manually activated screwjack in place of the spring loaded actuators. As the fairing halves are gradually rotated on the jettison hinges, clearances at various locations along the splitline longerons are recorded to verify all shear pins are disengaging smoothly.

The jettison test was a simulation of the event described above, wherein the two halves of the payload fairing separate after the launch vehicle clears the Earth's atmosphere. The test program consisted of performing two separate payload fairing jettison events at a simulated altitude of 85,000 feet (chamber pressure = 17 torr). After the inner metal door and the outer concrete chamber doors were closed, an approximately five hour pumpdown was performed, and after a short countdown a switch was flipped, immediately supplying power to the explosive bolts, initiating the jettison event. For each event, one half of the fairing (capped half) was fully

jettisoned, while the other half rotated only fifteen degrees before impacting the catch net (see Figure 2). Both halves were slowed from initial net impact to a full stop by hydraulically actuated brakes which were an integral part of the catch net system. The force used to initiate the jettison event was varied by using only one spring-loaded jettison actuator for the first event, and the full complement of two actuators for the second jettison event. This provided analysts with two data points against which to compare the analytically predicted behavior of the test fairing. After the first jettison event was completed, only a few days were required to reconfigure the fairing assembly for the second event.

Purpose: The primary purpose of the jettison test was to demonstrate that the analytical NASTRAN computer model being used by structural dynamicists and stress analysts to predict fairing behavior during vehicle flight environments is able to accurately predict the behavior of the payload fairing under the jettison test conditions. Pre-test predictions of all test data (pyro shocks, rigid-body motion, fairing half-breathing modes) were made using the analytical computer model. Comparison of test data with these analytical predictions will indicate if any corrections are necessary to the model. Another purpose was to simply demonstrate that the fairing jettison hardware (actuators, hinges, explosive bolts, shear pins, harness disconnects, etc.) functioned properly together. An important element of proper jettison functioning is the mechanical clearance between the fairing hardware as it rotates on the hinges and other critical items on the Centaur upper stage and the satellite payload. Because the fairing half "breathing" or "pinching" mode effectively reduces the static clearance, the intent was to design a fairing which was as stiff as possible. The items which represented potential rotation interferences were simulated during this test, and dynamic clearances were checked to allow comparison with pre-test predictions. In addition to exercising generic payload fairing hardware, the jettison test article subsets of two mylar installations which have been designed for mission-peculiar applications, a thin thermal shield which covers the interior of the cone and cylinder regions, and the pillow-like acoustic blankets for interior noise reduction, were installed inside the fairing test article to verify that the

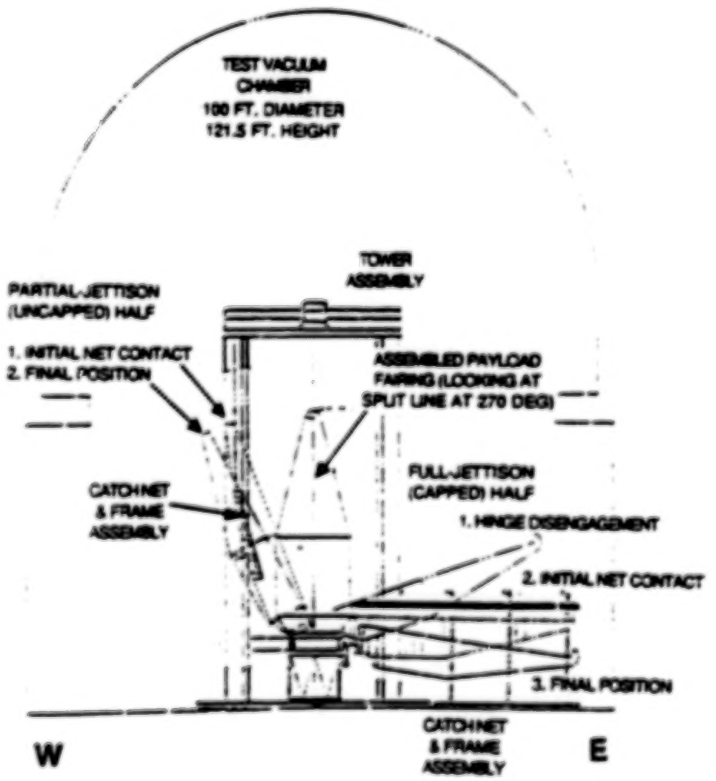

Figure 2. Payload Fairing Jettison Test Catch Net System.

bending associated with the jettison event would not damage either the mylar components or their fastening hardware. It was felt that this verification was necessary to eliminate the possibility that loose mylar could damage the encapsulated spacecraft during the jettison event.

Data Acquisitions: Test instrumentation for the jettison test included 31 channels of low-frequency accelerometer data, intended to measure the lowest vibration modes of the fairing halves and larger scale, rigid-body motions, 21 channels of high-frequency accelerometer data, which measured the shock environment (generated by the 28 explosive bolts) at various sensitive locations on the vehicle structure, and 44 channels of strain gage data, which measured the structural loads in the jettison hinges on which the fairing halves rotate. An analog FM-based data acquistion system was used to record all test data. Events were recorded by fourteen high-speed motion picture cameras and three video cameras. The video cameras were installed mainly to present to the test conductor a real-time image of what was occurring inside the chamber, realizing that there are no windows through which to look. Exactly half of the fourteen high-speed film cameras were focused on clearly visible targets mounted on fairing hardware. This film was later run through a film motion analyzer to produce deflection, velocity, and acceleration data. Clearance indicators, made of thin solder wire, were used to detect any infringement of the payload fairing structure during its jettison rotation into sensitive areas surrounding avionics packages or into the satellite payload envelope.

II. 14-Foot Diameter Payload Fairing Structural Test

Description: This test is currently under way at the Sycamore Canyon test site operated by General Dynamics just north of San Diego, California. During this structural test, the fairing will undergo a series of static test conditions which will determine if the fairing structure will yield at predicted design limit loads (based on loads experienced during the transonic condition) or will fail at design ultimate loads (125% of design limit loads). Because the test article is to be exposed to ultimate structural loads, the dedicated test fairing which was used for the jettison test described above, and which will never fly on an Atlas vehicle, will be used for this test. Four different test configurations (see Figure 3) will be used in order to completely test all of the major structural elements of the payload fairing: upper and lower nose cone (crush pressure and side load), nose dome (crush pressure only), cylinder and boattail (burst pressure and vent fin loads), and the all-up system level configuration (bending moments, shear loads, and axial loads). The last two configurations will be performed in a new test tower constructed last year specifically for the purpose of performing payload fairing testing. Included as part of the all-up system level testing will be test conditions which will reveal stiffness data on the payload fairing structure. It is planned that 27 separate test conditions will be required to fully accomplish the objectives of this test. The following paragraphs describe the major test configurations and the purpose for each of these:

Nose Cone Test Conditions: For the nose cone tests (see Figure 3a), the cone section (21 feet high) will be removed from the fairing cylindrical section and mounted on an airtight base fixture. A negative pressure differential will be established across the nose cone skin which will simulate worst-case crush pressures experienced by this structure during the ascent phase of flight. While the fairing structure is vented at the bottom of the cylinder section, pressure differentials are still experienced during flight at different fairing stations due to the varying aerodynamic pressure profiles. Pressures in the cone region during vehicle ascent are of the crush variety due to the aerodynamic nature and purpose of this structure. A shear load will also be introduced at the top of the cone during these test conditions in order to observe and characterize post-buckling behavior and load carrying capability of the monocoque (no external stringers) cone structure. It should be mentioned that buckling of the structure is expected at high loading conditions and is not to be considered a failure of the structure. There will be a total of four test conditions devoted to nose cone testing.

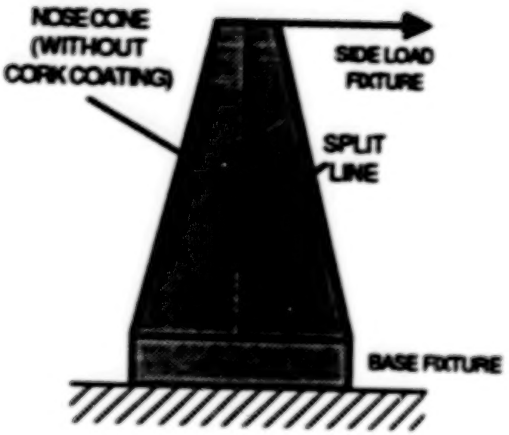

Figure 3a.
Nose Cone Crush Tests.

Figure 3b.
Nose Dome Crush Tests.

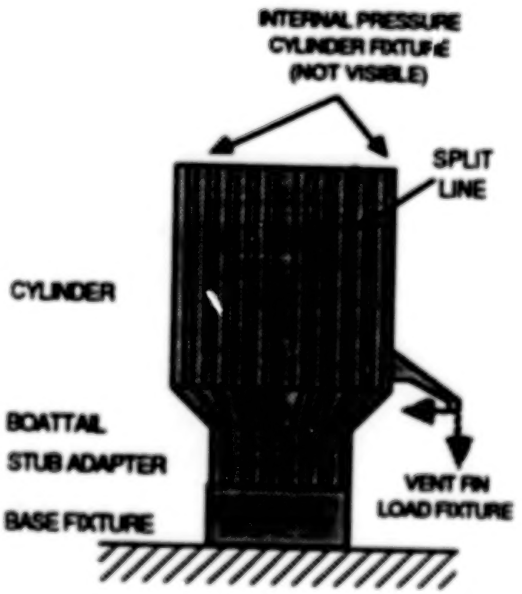

Figure 3c.
Cylinder Burst Tests.

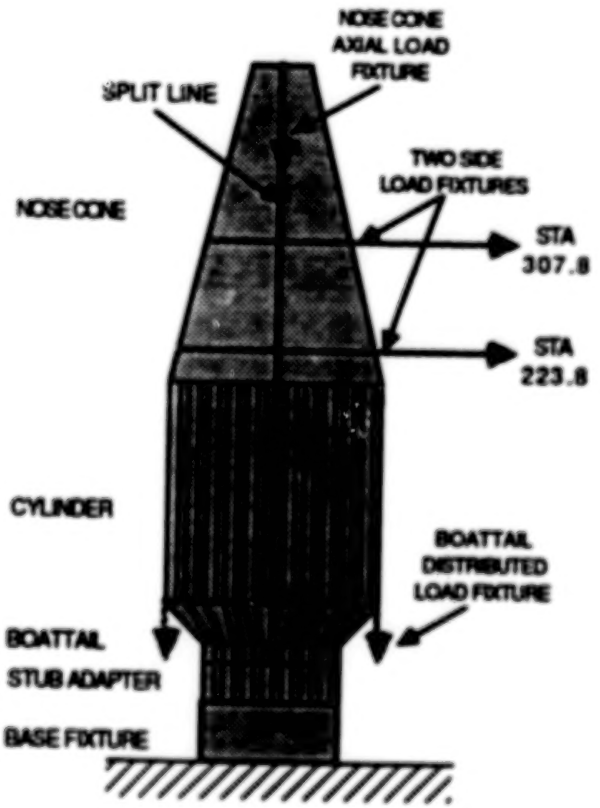

Figure 3d.
All-Up System Tests.

Figure 3. Payload Fairing Structural Test Configurations.

Nose Dome Test Conditions: The nose dome crush pressure test conditions are fairly straightforward, involving only the creation of a negative pressure differential across the nose dome structure, simulating the crush pressures seen during the ascent phase of the vehicle's flight (see Figure 3b). No shear, bending, or other structural loads will be imparted into the nose dome during these tests. There are only two nose dome test conditions.

Cylinder and Boattail Test Conditions: A unique test fixture was required for the cylinder and boattail burst pressure test conditions (see Figure 3c). Pressurizing the entire volume of the cylinder using a flat disk to seal the top of the cylinder (about 22,100 square inches) was not an option because this would have imparted large axial tension loads into the cylinder skin. Instead, a cylinder of a slightly smaller radius will be inserted inside the fairing cylinder, and the small annulus between the two cylinders will be pressurized. The primary goal in these test conditions is to observe the behavior of the explosive bolts and the split line longerons. Gapping of the longerons in the areas between bolts will be measured to characterize this behavior. No shear loads will be imparted to the cylinder or boattail structure during this test, but there will be small loads input into the vent fin structure to observe how flight loads from the vent fin are distributed into the cylinder skin and the backing frames and stringers. There will be a total of four cylinder and boattail test conditions.

All-Up System Level Test Conditions: There are 17 test conditions to be conducted in the fully assembled, all-up test configuration (see Figure 3d), including five stiffness test conditions. In this configuration, the test article will be assembled in exactly the same way that the fairing will sit on top of the Centaur upper stage during the boost phase of flight. Axial loads will be imparted both at the top of the nose cone and at the boattail/ cylinder interface, and side loads will be able to be input at two different stations on the nose cone. The 12 non-stiffness test conditions are constituted by combining three test configurations in four variations: using design limit loads, using design ultimate loads, loading parallel to the split line, and loading perpendicular to the split line. The three configurations are side loading at the upper fixture on the cone (which tests the upper portion of the cylinder), side loading at the lower fixture on the cone combined with maximum axial compression loads, and side loading at the lower fixture on the cone with minimum axial compression loads (both of which test the lower portion of the cylinder, the boattail, and the stub adapter). The maximum axial load condition imparts worst-case compression loads into the skin, longerons, and explosive bolts on the compression side of the fairing, and the minimum axial load condition imparts worst-case tension loads into the skin and longerons on the tension side of the fairing.

Test Instrumentation: About 300 strain gage channels and about 45 deflection transducers will be present on the test article. The strain gage locations are distributed evenly on the various components of the test article structure, but typically only half of the gages will be read for a given test condition. The strain gages are intended to provide an indication of how loads are distributed throughout the test article structure. Deflection transducers are present mainly to provide data on the stiffness of the test article and to monitor deflections of the test article to ensure safe test operations. Load cells on test fixtures and pressure transducers in the test setup will also be monitored to obtain an accurate picture of loads and pressure differentials being input into the test article. A set of digital data loggers will be used for data acquisition system, and data will be delivered to the stress department in personal computer compatible spreadsheet formats.

III. 14-Foot Diameter Payload Fairing Acoustic Test

Description: The acoustic test of the payload fairing will be conducted during May 1990 in General Dynamics/Space Systems Division's Acoustic/Thermal Test Facility (ATTF) at the Kearny Mesa plant in San Diego, California. The ATTF is a dual chamber containing separate acoustic and thermal test chambers. Both chambers are maintained as 100,000 class clean facilities. Its acoustic chamber is one of the largest acoustic test facilities with a floor measuring 33 x 40 feet and a ceiling height of 50 feet (65,000 cubic feet). The chamber is fully reverberant, having a 25-Hz horn, a 50-Hz horn, and two 100-Hz cutoff horns, all mounted on the north wall of the chamber (see Figure 4). The frequency range of the chamber is 25 - 10,000 Hz, and the rated overall sound pressure level is 154 dB. Chamber environments and data acquistion are controlled from the control room on a mezzanine above the chambers. The primary purpose of the ATTF is the environmental testing of large space structures. Currently, the major emphasis of the chamber is on the rigorous checkouts required prior to delivery of the Centaur upper stage of the USAF Titan IV launch vehicle. This checkout includes a full exercise of Centaur avionics control systems while the vehicle LO2 tank is filled with liquid nitrogen and subjected to launch acoustic levels. The vehicle with empty propellant tanks was later subjected to thermal cycling ranging from -40 F to 185 F.

During the acoustic test of the Atlas 14-foot diameter payload fairing, a fully assembled fairing will be subjected to acoustic levels representative of both the launch and Max Q environments. External sound pressure levels for both conditions will approach the rated capacity for the chamber. Empty chamber calibrations will be performed prior to arrival of the test article to better characterize the obtainable sound pressure levels. Various re-configurations of the test article will be performed in order to characterize an 1.) empty, generic fairing, 2.) a generic fairing with a satellite payload, 3.) an empty fairing with the acoustic blanket installation, and 4.) a fairing with the acoustic blanket installation and a satellite payload. Other design features which will be tested are the noise mufflers which are placed over the vent holes in the fairing cylinder section. The flapper doors in the muffler structure (designed to prevent payload contamination and noise intrusion but still allow for venting of internal burst pressures) will be alternately opened and closed to determine their effect on internal noise levels. The noise reduction properties of the fairing structure and the acoustic blanket installation will be fully tested by the completion of the ten test conditions planned (8 at launch levels and 2 at Max Q levels). In order to fully characterize the fairing acoustics, sound decay measurements will be taken inside the fairing structure prior to testing, both with the acoustic blankets installed and with them removed, to determine the reverberant component of the measurements which will be taken internal to the fairing during the actual testing.

Also of interest to the structural dynamicists are the vibrations induced in the fairing structure by this acoustic energy. To investigate this phenomena, accelerometers will be placed on mass simulated avionics packages mounted on the forward end of the Centaur upper stage and on areas of payload fairing skin. By placing microphones very near the avionics packages and the payload fairing skin on which accelerometers are placed, data are gathered which will allow transmissibility studies to be performed. The vibration environments, while significant for the purposes of this test, are expected to be mild enough to allow the use of flight hardware for this test. The second flight payload fairing and the third 14-foot diameter article to come off the line at Harlingen will be used for this test in order to help acheive some schedule compression (the dedicated test article will be committed to the structural test at this time), and because the standard cork and paint installation, which was incompatible with the goals of the structural test, is a requirement for the acoustic test. It was felt that the cork and paint on the nose cone section, bonded on as an ablative for thermal control, would have a significant impact on the acoustic transmissibility of the nose cone skin.

Data Acquisition: Acoustic levels internal to the payload fairing structure will be fully characterized through the use of about 20 microphones positioned both in and around the test article. Several control microphones will also be used to monitor chamber conditions in real time. Vibrational levels associated with the acoustic energy will also be recorded by about 10 triaxial accelerometer placements on sensitive areas of vehicle structure. A state-of-the-art data acquisition

Figure 4. General Dynamics Acoustic Chamber, San Diego, California.

system in the ATTF control room will record all test data and will allow for a wide variety of data presentation formats; 1/3 Octave Band Center Frequency Plots shall be produced for all microphones. Power Spectral Densities (PSDs) will be produced for all data microphones and Accelerometer Spectral Densities (ASDs) of all accelerometer data will also be produced, as will transmissibility plots showing the relationship between microphone and accelerometer data. Because this test is currently scheduled for completion less than one month prior to launch of AC-69, the first commericial Atlas flight, prompt data reduction and presentation will be of utmost importance.

IV. 11-Foot Diameter Payload Fairing Modal Survey Test

Description: This first test of the smaller 11-foot diameter fairing, developed for the USAF Atlas II, will be conducted in two major segments: a "free-free" test condition in which only one half of the fairing will be tested, and a "fixed base" test condition which will be performed on a fully assembled and erected fairing. The free-free conditions will be performed at the General Dynamics operated U. S. Air Force Plant 19 near downtown San Diego, and the fixed base test conditons will be performed at the Sycamore Canyon test facility. The fixed base testing will immediately follow the 14-foot diameter payload fairing structural test and be conducted in the same test tower. The test article will be a dedicated 11-foot diameter test article, constructed to the same engineering prints and quality control criteria as a flight article. This will be the first 11-foot diameter fairing completed by the Harlingen assembly plant and will be the fourth aluminum payload fairing off the production line. Because of suspicions that the thermal control cork coating on the nose cone would introduce significant modal damping, it was determined that it should be included on the test article in order to accurately reflect the properties of the flight article. The 11-foot diameter payload fairing is somewhat shorter than the 14-foot diameter version, measuring 34 feet in height, 5 1/2 feet less than its larger brother. While it is large enough to accommodate the DSCS-III spacecraft, the 11-foot diameter payload fairing is some 1,500 pounds lighter than the 14-foot diameter payload fairing, weighing in at just over 3,000 pounds. This allows for a dramatic increase in payload-weight-to-orbit. The 11-foot fairing is even slightly lighter than the comparably sized 10-foot diameter fiberglass fairing, showing the inherent efficiency of the aluminum skin, stringer, and frame construction. In addition to supplying data on fairing vibrational modes, this modal test will be the primary source of stiffness data on the 11-foot diameter payload fairing structure.

General Dynamics will be assisted in this test effort by Structural Dynamics Research Corporation (SDRC), which is headquartered in Milford, Ohio. SDRC Engineering Services Division, based convieniently in San Diego, will be the primary contract agency. SDRC, which has a great deal of experience in the modal testing field, will:

- perform a pre-test analyses, which will predict mode shapes and frequencies
- determine instrumentation quantities and placements
- install the instrumentation and shakers on the test article
- perform all test operations
- perform all data acquisition
- perform a post-test analysis intended to refine the fairing analytical model
- prepare a test report which presents all test data

Free-Free Test Requirements: The free-free test condition, in which a single fairing half will be excited, is being performed to determine the vibrational modes of a fairing (and split barrel) half which has been separated from its twin half and is free to vibrate at all boundaries. This test condition is being run in lieu of conducting a separate (and very expensive) jettison test of the 11-foot diameter payload fairing. This test condition will provide information on the primary breathing modes and the modes which will load the stub adapter hinges during jettison rotation. About 200 low-frequency accelerometers will be present on the test article to monitor vibration during this condition. The

fairing will be suspended from the ceiling in a concave down (inverted canoe, see Figure 5) orientation and will be supported at three locations by bungee cords. Exciters will be mounted on the floor and will be attached to the split line longerons. Multiple input random excitation will be the primary method of excitation, providing information on all modes below 50 Hz, but for the major modes of interest, sine-sweep excitation will be used to obtain more specific information (linearity, orthogonality, damping, etc.). Orthogonality requirements for the free-free condition are that all off-diagonal terms of the modal mass matrix be less than 0.10. Up to 12 total retakes of contaminated target modes will be permitted to satisfy these requirements.

Fixed Base Test Requirements: In order to determine the vibrational modes of the fully assembled fairing as it sits on the Centaur upper stage for the first 3 1/2 minutes of flight, the fixed base modal configuration will be performed at Sycamore Canyon. The modes of primary interest are the first three bending modes in the vehicle pitch and yaw axes, the first two axial modes, and the first torsional mode. If any of these modes is above 64 Hz, a shell mode pair will be substituted. It is anticipated that about 250 low-frequency accelerometers will be required to monitor vibration during this test condition. As in the free-free condition, multiple input random excitation will be the primary source, characterizing all modes below 50 Hz, and sine-sweep will be used to isolate the specified target modes. Orthogonality requirements are, as in the free-free condition, that all off-diagonal terms of the modal mass matrix be less than 0.10. A total of 18 retakes will be allowed in order to satisfy these requirements for all contaminated target modes.

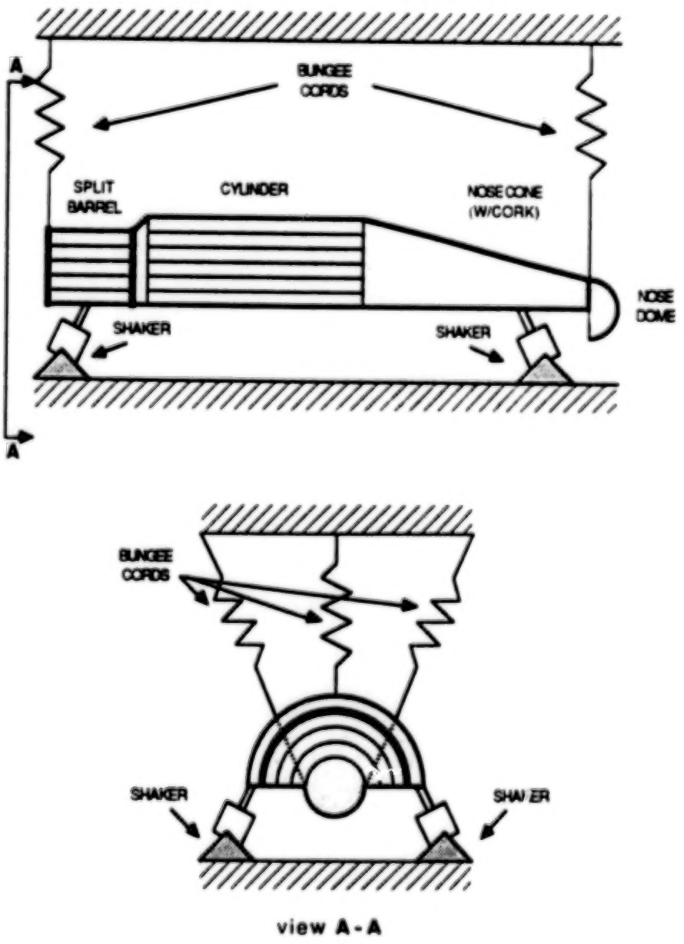

Figure 5. 11-Foot Diameter Payload Fairing Modal Test Free-Free Condition.

V. 11-Foot Diameter Payload Fairing Structural Test

Description: The 11-foot diameter payload fairing structural test will be the last fairing test to be conducted in the Sycamore Canyon test tower. There will be no special setup required for this test as the configuration and the test article for this test are exactly the same as the fixed base configuration for the modal survey test, which it will immediately follow. The goals of this test are very similar to those established for the 14-foot diameter payload fairing structural test: 1.) the fairing structure shall not yield under design limit loads and 2.) the fairing structure shall not fail under design ultimate loads (125% of design limit). As with the 14-foot diameter structural test, there will be a series of static test conditions designed specifically to satisfy the above requirements and additionally to determine the stiffness of the payload fairing structure, serving as a verification of the stiffness data obtained during the previously mentioned modal survey test. This structural test, however will not incorporate any of the component level tests which the 14-foot structural test program did, mainly because some of the structural components tested at that time (upper and lower nose cone, nose dome, and stub adapter) are common between the 11-foot and 14-foot designs and need not be demonstrated again. The only configuration for this test is the fully assembled fairing. No burst or crush pressures will be required during any of the test conditions to be performed in this test program.

Test Conditions: Like the all-up system level tests conducted during the 14-foot diameter structural test program, loading of the 11-foot diameter test article will be accomplished through a combination of axial and side loading. There will be axial loading available through a fixture at the top of the nose cone and side loading available at three locations: the top of the nose cone, near the base of the nose cone, and near the middle of the fairing cylinder section (see Figure 6). By inputing incremental side loads at three stations, a very good approximation of flight shear and bending moment profiles can be obtained, avoiding any seriously overloaded structure. A total of eleven test conditions will be required to complete the structural test program. There will be four standard conditions using maximum axial compression loads combined with design limit and ultimate shear

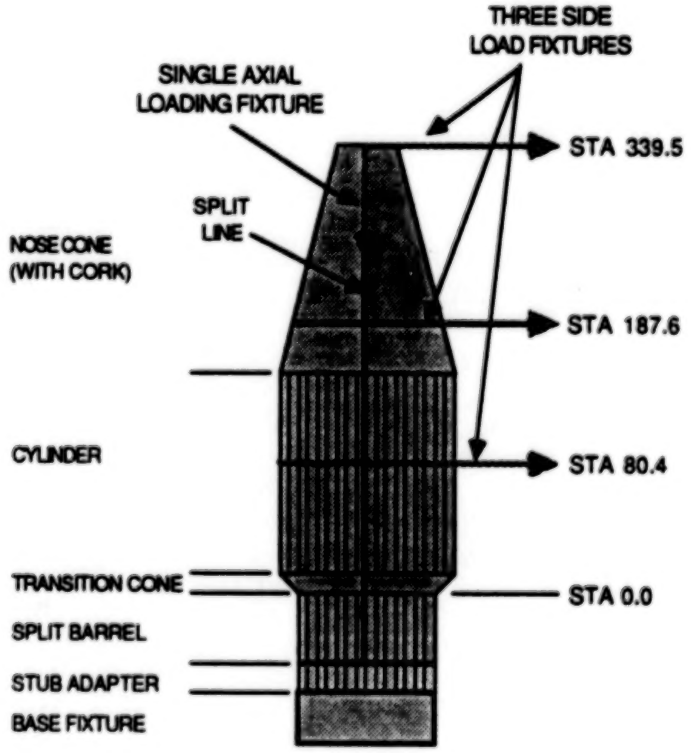

Figure 6. 11-Foot Diameter Payload Fairing Structural Test Loading Fixtures.

loads/bending moments conducted both parallel and perpendicular to the fairing split line. There will also be two test conditions which use mimimum axial compression loads in conjunction with side loads (design limit and ultimate) parallel to the fairing split line. Maximum axial compression relates to the Max Q flight condition and the minimum axial compression case corresponds to loading on the Atlas vehicle at the transonic flight condition. Two test conditions (design limit and ultimate loads) will require that the axis of compression be off the standard axes which are parallel/perpendicular to the split line. This is required because of an air conditioning duct door which is located 30 degrees off the split line. Because of the location of this door at the very top of the fairing cylinder, this structure cannot be designed to a factor of safety of 2.0, and as such must be tested to ultimate loading conditions per the USAF contract. An axis of compression which is off the standard axes requires that a resultant load be reacted, dictating that twice as many load cells be used to impart the test loads. The final three test conditions are the stiffness tests, one each in the standard side load axes (parallel and perpendicular to the split line) using pure side load, and one pure axial load condition.

Data Acquisition: Test instrumentation for the 11-foot diameter payload fairing structural test includes about 80 strain gages and about 35 deflection transducers. Strain gages will be placed in circumferential patterns at the bottom of the lower cone and at the mid-point of the small transition cone between the cylinder and the split barrel. Several explosive bolts shall also be instrumented with strain gages. Deflection transducers will be used mainly to collect stiffness (deflection versus load) data and to monitor test safety during high loading conditions. Load cells connected to the hydraulic load cylinders will also be monitored (maximum of seven hydraulic load cylinders operating during off-axis air conditioning door test conditions) to verify the loads input into the test article. The data acquisition system used on this test will be identical to that used during the 14-foot diameter payload fairing structural test program. A digital data logger will record data on the 3 1/2 -inch floppy disks in standard personal computer spreadsheet format.

Conclusions

To establish the competitiveness of the revitalized family of Atlas launch vehicles (I, II, IIA, and IIAS) a new series of payload fairings, an 11-foot and a 14-foot diameter version, were designed to accommodate the widest possible variety of satellites. Because these aluminum fairings are new designs, the plant at which they are produced is new, and launch customers are very anxious to fly their payloads, an ambitious and efficient test program is essential. Five major tests have been planned for completion within the span of one calendar year. One of these has been completed, with every indication that it was a success, one is currently under way, and two more are scheduled to start in the month of April. Through effective use of test assets, facilities, and personnel, all testing will be completed, allowing the fairing design to be completely characterized and then qualified through analysis prior to first launch of each of the fairings.

DIRECT USE OF LINEAR TIME-DOMAIN AERODYNAMICS IN AEROSERVOELASTIC ANALYSIS: AERODYNAMIC MODEL

J. A. Woods and M. G. Gilbert
Aeroservoelasticity Branch
NASA Langley Research Center
Hampton, Virginia

The work presented here is the first part of a continuing effort to expanding existing capabilities in aeroelasticity by developing the methodology which is necessary to utilize unsteady time-domain aerodynamics directly in aeroservoelastic design and analysis.

The ultimate objective of this study is to define a fully integrated state-space model of an aeroelastic vehicle's aerodynamics, structure and controls which may be used to efficiently determine the vehicle's aeroservoelastic stability.

In this presentation, the current status of developing a state-space model for linear or near-linear time-domain indicial aerodynamic forces is presented.

MOTIVATION:

TO EXPAND EXISTING AEROSERVOELASTIC DESIGN AND ANALYSIS CAPABILITIES TO INCLUDE THE USE OF UNSTEADY TIME-DOMAIN AERODYNAMICS

LONG-TERM OBJECTIVE:

DEVELOP METHODOLOGY TO UTILIZE LINEAR AND NEAR-LINEAR TIME-DOMAIN AERODYNAMICS IN THE SUPERSONIC AND SUBSONIC REGIMES DIRECTLY IN AEROSERVOELASTIC DESIGN AND ANALYSIS.

IMMEDIATE OBJECTIVE:

DEVELOP A TIME-DOMAIN STATE-SPACE MODEL OF TIME-DOMAIN AERODYNAMIC INDICIAL FORCES.

THE INTEGRATED AEROELASTIC MODEL

To understand the importance of this research, it is necessary to consider that several codes [1,2] have been developed in recent years which compute time-domain unsteady aerodynamics, however, the techniques needed to utilize the aerodynamics in aeroservoelastic design have not been fully developed.

One of the only methods devised to date to evaluate the aeroelastic stability of aerospace vehicles in the time-domain has been a general method capable of handling the nonlinear system [3]. This method is expensive as it involves the computation of the aeroelastic system time response which requires solution of the nonlinear small disturbance aerodynamic equations. Further, a frequency decomposition of the response is necessary to evaluate the stability of component modes. The response must be recomputed at several dynamic pressures until a neutrally stable mode is encountered. Other available methods model the aerodynamics directly in the frequency domain.

For linear and near linear systems in supersonic and subsonic flow, however, the vehicle stability may be evaluated without computing the aeroelastic system forced response or transforming forces to the frequency domain. This is accomplished by representing the time-dependent aerodynamic forces in state-space form coupled with a commonly used state-space representation of the structure. Stability is determined by the eigenvalues of the coupled system matrix.

The focus of this presentation is, again, on the formulation of the aerodynamic portion of the integrated model.

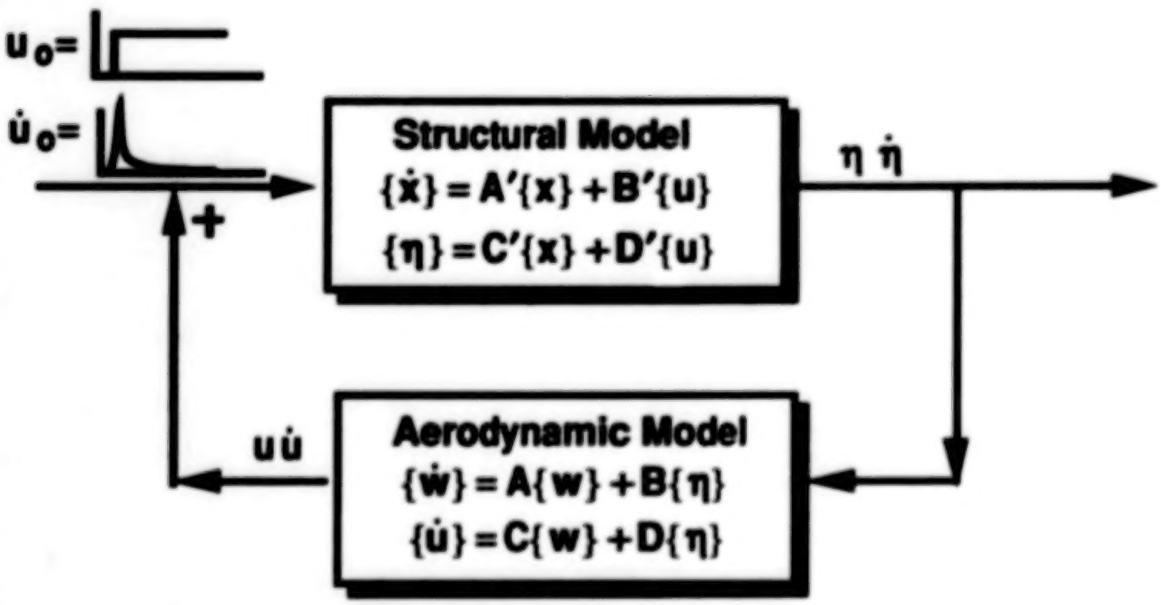

Figure 1. Schematic block diagram indicating integration of the aerodynamic model with the structural model.

FORMULATION OF AERODYNAMIC MODEL

The aerodynamic model is derived as the Laplace transform of a commonly used frequency domain approximation modified from ref. 4. It is transformed directly into state-space form.

MODIFIED FREQUENCY DOMAIN APPROXIMATION

$$\overline{Q}(s) = \left(A_0 + A_1 \frac{b}{V} s + \sum_{i=1}^{N} \frac{B_i s}{s + \beta_i \frac{V}{b}} \right) \eta(s)\, \overline{q}$$

STATE-SPACE REPRESENTATION IN TIME DOMAIN

$$\begin{Bmatrix} \dot{w}_1 \\ \dot{w}_2 \\ \vdots \\ \dot{w}_N \end{Bmatrix} = \begin{bmatrix} \beta_1 \frac{V}{b} & 0 & \cdots & 0 \\ 0 & \beta_2 \frac{V}{b} & & \vdots \\ 0 & & \cdots & \beta_N \frac{V}{b} \end{bmatrix} \begin{Bmatrix} w_1 \\ w_2 \\ \vdots \\ w_N \end{Bmatrix} + \begin{bmatrix} 0 & B_1 \\ 0 & B_2 \\ \vdots & \vdots \\ 0 & B_N \end{bmatrix} \begin{Bmatrix} \eta \\ \dot{\eta} \end{Bmatrix}$$

$$\overline{Q}(t) = \overline{q}[1\ 1\ \cdots 1] \begin{Bmatrix} w_1 \\ w_2 \\ \vdots \\ w_N \end{Bmatrix} + \overline{q} \begin{bmatrix} A_0 & A_1 \frac{b}{V} \end{bmatrix} \begin{Bmatrix} \eta \\ \dot{\eta} \end{Bmatrix}$$

APPROXIMATION METHOD

The approximation method involves a least squares approximation to the actual aerodynamic force to determine the scalars A_o, A_1 and B_i. The fit is constrained at t=0 to fit exactly and at large times to equal the asymptotic value of the generalized force. As in the frequency-domain rational function type approximations, aerodynamic poles, β_i, are initially specified.

The aerodynamic forces currently being approximated are the rigid-body forces acting on a NACA0064 airfoil and are due to Dowell [5].

APPROXIMATING FUNCTION

$$\overline{Q}(t) = \left(A_o \eta(t) + A_1 \frac{b}{V} \dot{\eta}(t) + \sum_{i=1}^{N} B_i e^{\beta_i \frac{V}{b} t} \right) \overline{q}$$

CONSTRAINTS ON LEAST SQUARES APPROXIMATION

$$A_o = Q(t_\infty)$$

$$A_1 = \left(Q(0) - \sum_{i=1}^{N} B_i - Q(t_\infty) \right) \frac{V}{b}$$

APPROXIMATION METHOD (CONTI)

A system identification technique frequently used in control system analysis is applied to regenerate the generalized aerodynamic force. Specifically, impulse and step responses of the aerodynamic model are generated using a discrete-time state-transition method. The sum of these responses is the aerodynamic approximation, $\overline{Q}(t) \cong Q(t)$, based on previously determined coefficients and the specified aerodynamic poles.

Due to the discontinuity at t=0 in the impulse input, an assumption is made that at t=0+, initial conditions are real valued. At t=0-, initial conditions are zero. This assumption can be shown mathematically.

STATE TRANSITION EQUATIONS

$$w(t+1) = \Phi w(t) + \Gamma u(t)$$

$$\overline{Q}(t) = C w(t) + D u(t)$$

WHERE

$$\Phi(t) = e^{[A]T} \quad \text{and} \quad \Gamma = \int_0^T e^{[A]\tau} B \, d\tau$$

ASSUMING

$$w(0^-) = 0 \qquad w(0^+) = Bu(0)$$

APPROXIMATION METHOD (CONTI)

Improvements to the aerodynamic approximation are made by updating the aerodynamic poles, β_l, followed by another least squares approximation to recompute the coefficients. To update the poles, the method used by Peterson and Crawley [7] to approximate unsteady aerodynamics in the frequency domain is implemented in the time domain. A norm square-error cost function is defined. In this case, the square of the difference between the actual aerodynamic force and the approximation is used. The incremental change in aerodynamic poles is solved for by inverting the Hessian, $\partial^2 J / \partial\beta_l \partial\beta_k$, in a single term Taylor series expansion of $\partial J / \partial\beta$. The incremental change in β_l is multiplied by a scale factor, α, and added to the current aerodynamic poles. The scale factor, α, is computed using quadratic interpolation [8] to insure that the cost is approaching a local extrema.

The new aerodynamic poles are limited. If a given pole is greater than -0.01, it is set equal to that value until the next parameter update. To prevent a pole from going to $-\infty$ and ill-conditioning the system matrix later on, the pole is limited to a value which would produce no more than a 99.5% decrease in magnitude of the exponential over a given time step.

The two step procedure of computing system coefficients and updating aerodynamic states is repeated until the cost function has been minimized.

SQUARE ERROR COST FUNCTION

$$J(\beta)=\left[Q(t)-\overline{Q}(t,\beta)\right]^T\left[Q(t)-\overline{Q}(t,\beta)\right]$$

NEWTON RAPHSON STEP

$$\{\delta\beta_l\}=[H]^{-1}\left\{\frac{\partial J}{\partial\beta_l}\right\}$$

WHERE,

$$H=\frac{\partial^2 J}{\partial\beta_l\partial\beta_k}$$

AERODYNAMIC POLE UPDATE

$$\beta_{new}=\beta_o+\alpha\,\delta\beta_l$$

CONSTRAINTS ON AERODYNAMIC POLES

$$\beta\le -0.01 \qquad \text{AND} \qquad \beta\ge \ln(0.005)/\Delta t$$

PRELIMINARY RESULTS

Table I briefly describes some of the progress which has been made up to this time. Four sets of initially specified aerodynamic poles, associated coefficients and the initial cost are indicated as well as the minimum cost quantities. The first set of poles is a subset of the poles which were used by Dowell to generate the aerodynamic forces. Dowell's zero pole was not included for stability reasons and because the A_1 term serves the same purpose of providing a constant term at t=0. The other sets of poles represent "random" selections between a small negative number and -1.0, -2.0 and -3.0.

A minimum cost was obtained for each of these sets of poles. The poles close to those of the generating function produced the lowest cost. Minimum cost increases from there as the range of initial poles widens. It is noted that finding a minimum isn't always guaranteed. For some sets of initial poles, the least-squares fit doesn't converge or the program determines a local maxima instead of a local minima.

One of the immediate observations which can be made from Table I is that the aerodynamic poles tend to decrease in magnitude as the cost is minimized. The same trend occurs as other rigid body forces are being approximated. The implication is that the fit improves at large times and degrades at small times. In terms of reduced frequencies, this means that the high frequency components of the curve are not being fit well. Thus, a weighted least-squares fit and a weighted square error function will be considered to improve the approximation at small times.

Finally, an assumption made in the quadratic interpolation subroutine which computes parameter step size is that when the square-error cost is computed for the "step-ahead" coefficients remain constant . From Table I, this appears to be a valid assumption, as over the entire range of parameter updates, coefficients have remained fairly unchanged.

PRELIMINARY RESULTS

LIFT DUE TO PLUNGE
6 POLE APPROXIMATIONS

Initial Data					Minimum Cost Results				
Poles*	Coefficients	A_0	A_1	Cost	Poles*	Coefficients	A_0	A_1	Cost
-0.1	-0.433	0.999	0.034	0.0170	-0.091	-1.24	0.999	-0.036	0.0012
-0.3	-0.51				-0.881	0.805			
-0.8	1.646				-0.148	-0.178			
-1.2	-2.841				-0.528	-0.116			
-1.75	2.19				-1.255	0.402			
-3.5	-0.574				-2.882	-0.123			
-0.2	-3.041	0.999	-0.074	0.0047	-0.185	-3.202	0.999	-0.056	0.0020
-0.4	43.06				-0.33	42.016			
-0.5	-124.97				-0.401	-114.617			
-0.6	121.388				-0.470	103.931			
-0.8	-51.012				-0.613	-37.816			
-1.0	14.162				-0.775	9.256			
-0.334	-6.036	0.999	-0.343	0.1995	-0.243	-5.681	0.999	-0.0997	0.0166
-0.668	46.844				-0.424	42.426			
-1.0	-178.225				-0.590	-152.419			
-1.334	333.826				-0.747	263.921			
-1.668	-299.231				-0.898	-215.887			
-2.0	102.678				-1.049	67.253			
-0.5	-9.818	0.999	-1.266	0.8687	-0.35	-6.406	0.999	-0.421	0.2469
-1.0	89.054				-0.683	42.793			
-1.5	-365.568				-1.03	-137.988			
-2.0	723.748				-1.409	222.239			
-2.5	-678.553				-1.837	-174.33			
-3.0	241.917				-2.343	53.628			

* Poles indicated are $\beta_i \frac{b}{V}$.

Table I. Summary of some aerodynamic poles, coefficients and cost functions.

PRELIMINARY RESULTS (CONTI)

Figure 2 illustrates some of the approximations to the rigid-body forces acting on a NACA0064 airfoil which are currently being obtained. The figure includes a pair of figures for each of four rigid-body aerodynamic forces. The lower figure in each pair contains a comparison between the aerodynamic data and an approximation ma y using the initially specified aerodynamic poles. The norm square-error cost is indicated. The upper figure in each pair indicates the improved approximation after the minimization technique has been applied. Again, the minimum norm square-error cost is indicated. In all cases, aerodynamic data has been normalized with the largest absolute magnitude of force.

As can be seen, the technique does improve the approximation noticeably. In three of the four cases, the cost has been reduced by about 90%. In the case of "Moment Due to Pitch", the cost was observed to remain high even after minimization. This emphasizes the fact that the current method finds only the first extrema in cost. This extrema may be only a local extrema and not a global one.

PRELIMINARY RESULTS

NACA0064 RIGID BODY AERODYNAMIC FORCES

β_o =[−.334 −.668 −1.0 −1.334 −1.668 −2.0]

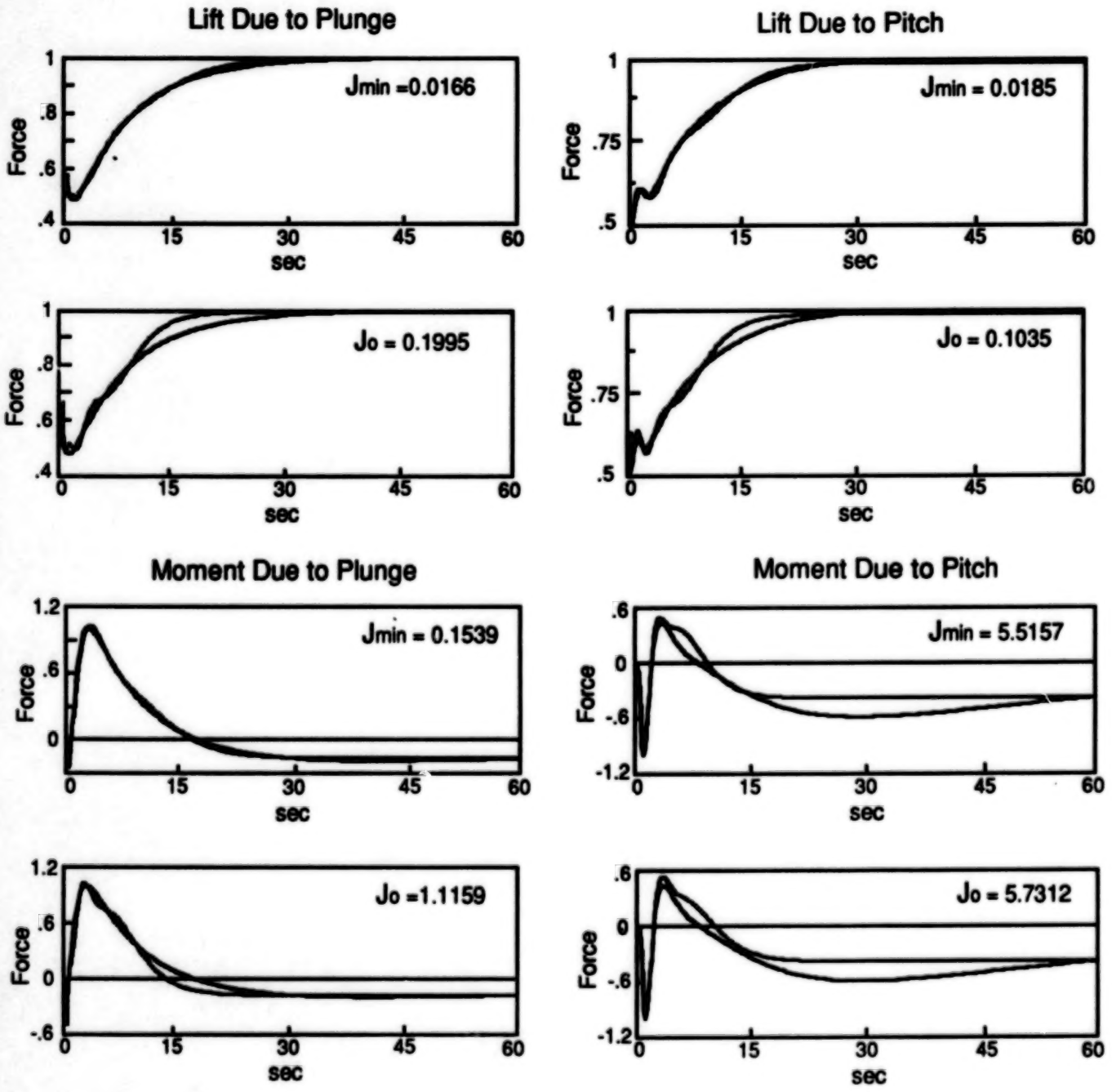

Figure 2. Approximations to NACA0064 airfoil rigid body forces using initial aerodynamic poles and aerodynamic poles computed for minimum cost.

FURTHER DEVELOPMENT

Other methods will be considered to determine minimum cost. The method currently used is effective, but needs modification.

In an effort to improve the fit for small times, a weighted least squares fit will be implemented to determine the coefficients. A weighted square error cost function will also be considered.

Sometimes the program converges to a local maximum instead of minimum. Thus, means of forcing the program to converge on a minimum will be implemented.

FURTHER DEVELOPMENT

- IMPROVE PROCEDURE TO IDENTIFY MINIMUM COST
- INVESTIGATE WEIGHTED LEAST SQUARES APPROXIMATION TO DETERMINE COEFFICIENTS
- INVESTIGATE A WEIGHTED SQUARE ERROR COST FUNCTION
- INVESTIGATE METHODS OF CHANGING THE SEARCH DIRECTION IF A MAXIMUM IS BEING APPROACHED INSTEAD OF A MINIMUM

FURTHER APPLICATIONS

To further evaluate this technique, aerodynamic data generated for a real aircraft by a time-domain aerodynamic code in the subsonic and supersonic flight regimes will be modeled. Both rigid-body and flexible modes will be considered.

Finally, to fulfill the whole purpose of developing this model, methodology will need to be developed to integrate the aerodynamic model effectively with a structural model. Later, control systems will be integrated into the scheme. Using the integrated models, system stability will be evaluated.

FURTHER APPLICATIONS

- APPLY TECHNIQUE TO FLEXIBLE AND RIGID BODY GENERALIZED AERODYNAMIC FORCES ACTING ON A REAL AIRCRAFT

- DEVELOP METHODOLOGY FOR INTEGRATING MODEL WITH DISCRETE-TIME STRUCTURAL MODEL AND PERFORMING STABILITY ANALYSIS FOR ARBITRARY MOTION

REFERENCES

1. Batina, J.T., Seidel, D.A., Bland, S.R., and Bennett, R.M., "Unsteady Transonic Flow Calculations for Realistic Aircraft Configurations," AIAA Paper No. 87-0850, AIAA/ASME/ASCE/AHS 28th Structures, Structural Dynamics and Materials Conference, Monterey, CA, April 6-8, 1987.

2. Blair, M. and Williams, M.H., "A Time-Domain Panel Method for Wings," AIAA Paper No. 89-1323, AIAA/ASME/ASCE/AHS/ASC 30th Structures, Structural Dynamics and Materials Conference, Mobile, Alabama, April 3-5, 1989.

3. Cunningham, H. J., Batina, J. T., and Bennett, R. M., "Modern Wing Flutter Analysis by Computational Fluid Dynamics Methods," ASME Paper No. 87-WA/Aero-9, ASME Winter Annual Meeting, Boston, Mass., Dec 13-18, 1987.

4. Abel, I.A., "An Analytical Technique for Predicting the Characteristics of a Flexible Wing Equipped With an Active Flutter-Suppression System and Comparison with Wind-Tunnel Data," NASA TP 1367, Feb. 1979.

5. Dowell, E. H., "A Simple Method of Converting Frequency-Domain Aerodynamics to the Time-Domain," NASA TM 81844, 1980.

6. Brogan, W.L., Modern Control Theory, Quantum Publishers, Inc., New York, 1974.

7. Peterson, L.D. and Crawley, E.F., "Improved Exponential Time Series Approximation of Unsteady Aerodynamic Operators," Journal of Aircraft, Vol. 25, No. 2, Feb. 1988.

8. Fox. R.L., Optimization Methods for Engineering Design, Addison-Wesley Publishing Co., Reading, Mass., 1971, pp. 51-58.

Computation of Maximum Gust Loads in Nonlinear Aircraft Using a New Method Based on the Matched Filter Approach and Numerical Optimization

Anthony S. Pototzky
Lockheed Engineering and Sciences Company
Hampton, Virginia

Jennifer Heeg and Boyd Perry III
Langley Research Center
National Aeronautics and Space Administration
Hampton, Virginia

Motivation

Time-correlated gust loads are time histories of two or more load quantities due to the same disturbance time history. Time correlation provides knowledge of the value (magnitude and sign) of one load when another is maximum. At least two analysis methods have been identified (references 1 and 2) that are capable of computing maximized time-correlated gust loads for linear aircraft. Both methods solve for the unit-energy gust profile (gust velocity as a function of time) that produces the maximum load at a given location on a linear airplane. Time-correlated gust loads are obtained by re-applying this gust profile to the airplane and computing multiple simultaneous load responses. Such time histories are physically realizable and may be applied to aircraft structures.

Within the past several years there has been much interest in obtaining a practical analysis method which is capable of solving the analogous problem for nonlinear aircraft. Such an analysis method has been the focus of an international committee of gust loads specialists formed by the U. S. Federal Aviation Administration and was the topic of a panel discussion at the Gust and Buffet Loads session at the 1989 SDM Conference in Mobile, Alabama. The kinds of nonlinearities common on modern transport aircraft are indicated in figure 1.

The Statical Discrete Gust method of reference 1 is capable of being, but so far has not been, applied to nonlinear aircraft. As stated in reference 1, to make the method practical for nonlinear applications, a search procedure is essential.

The method of reference 2 is based on Matched Filter Theory and, in its current form, is applicable to linear systems only. The purpose of the current paper is to present the status of an attempt to extend the matched filter approach in reference 2 to nonlinear systems. The extension uses Matched Filter Theory as a starting point and then employs a constrained optimization algorithm to attack the nonlinear problem.

- **Time-correlated gust loads are generated to obtain physically realizable design loads for the analysis and design of aircraft structures**
- **Active control systems of modern aircraft contain significant nonlinearities:**
  - Hardware nonlinearities . . . control surface rate and deflection limits
  - Coded nonlinearities in digital control system
- **The objective is to employ optimization to determine the excitation that produces the maximum gust loads on nonlinear aircraft**
  - Matched filter theory for linear systems provides starting guess

Figure 1

Schematic of Matched Filter Theory as Applied to Linear Systems

Figure 2 contains a schematic of the steps necessary to generate maximum time-correlated gust loads for a linear system using Matched Filter Theory. The signal flow diagram is presented as two paths; the top path illustrates the generation of the system impulse response; the bottom path illustrates the generation of the maximum response of the system.

In the top path, a prefilter (transfer function) representing the gust dynamics is excited by an impulse of unit strength to generate an intermediate gust impulse response which, in turn, is the excitation to the aircraft. Computationally, the time history of the response is carried out until the magnitude of the response dies out to a small fraction of the largest amplitude of the response. The response is normalized by its own root-mean-square (rms) value. This normalized response, reversed in time, is the "matched" excitation waveform for the output y. This becomes the input to the next part of the computational process.

The bottom path illustrates how the maximum response of the system and the critical gust profile are obtained. The matched excitation waveform is applied to the same "known dynamics." The intermediate gust response is referred to as the critical gust profile. The final time histories are time-correlated gust loads. The maximum guaranteed response, y_{max}, is equal to the rms of the impulse response and may be scaled to correspond to the gust intensity levels of interest. It should be mentioned that to obtain both the critical gust profile and the maximum response for a different output, a separate but similar analysis needs to be performed.

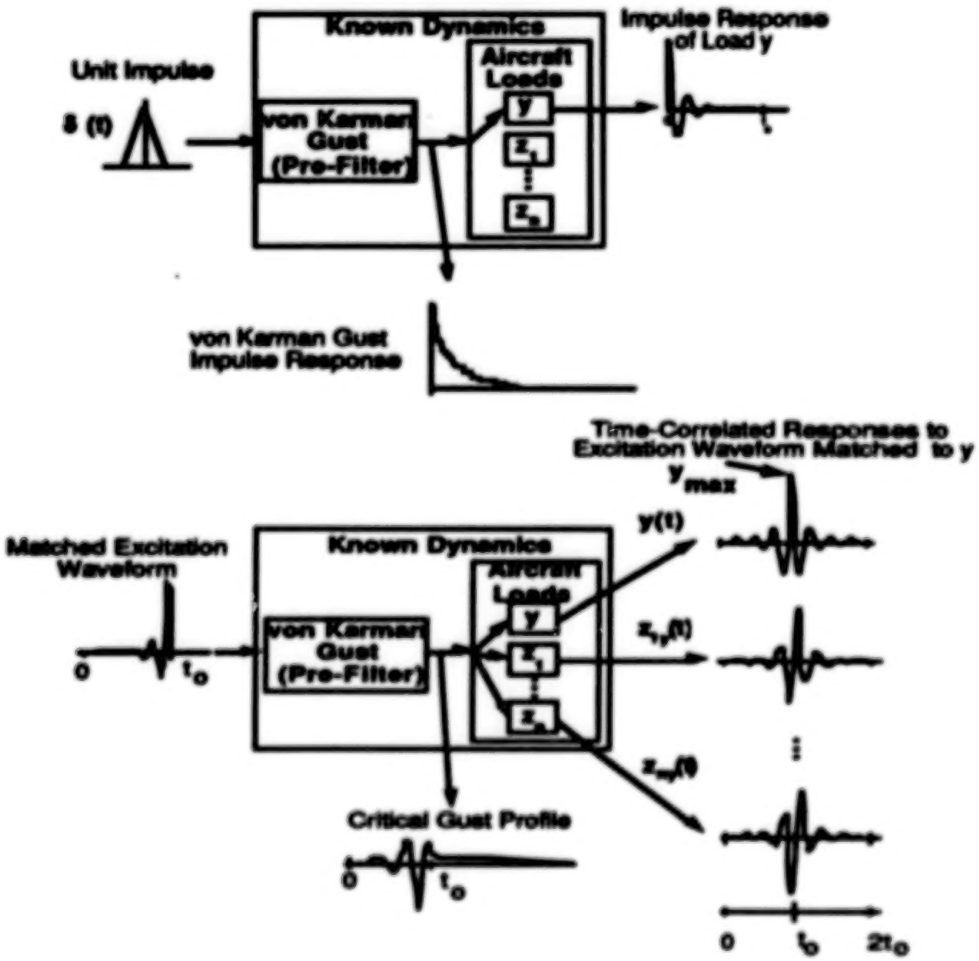

Figure 2

Optimization Scheme to Obtain Maximum Gust Loads for Nonlinear Systems

The objective of the present research is to determine the excitation, with a prescribed rms, that results in a maximized peak gust load response while producing a gust profile of constant energy level (and thus a constant probability level) in an aircraft with a nonlinear element. This figure illustrates how an optimization algorithm may be employed to compute maximized gust loads and their corresponding critical gust profiles for nonlinear systems. The matched filter approach (as described in connection with figure 2) is used to provide an initial estimate of an excitation waveform for turbulence of a given intensity, shown in the upper-left corner of figure 3. The optimization scheme begins with the computation of the coefficients of a set of orthogonal functions in a series approximation to the waveform, normalized to a unit rms. The approximation to the excitation waveform is the input to the gust prefilter, whose output is an iterative gust profile. The gust profile then becomes the input to the nonlinear airplane model. The final output is a time history of the load quantity of interest. Note that the shaded area in the optimization loop is analogous to the "known dynamics" element in figure 2.

The orthogonal approximating function coefficients, which are the design variables in the optimization scheme, are systematically varied by the optimizer until a maximum peak in the load response in obtained. The coefficients are constrained to produce a waveform approximation with a unit rms. Since the approximating functions are orthogonal, Parseval's Theorem allows the rms of the excitation waveform to be written simply as the sum of the squares of the coefficients.

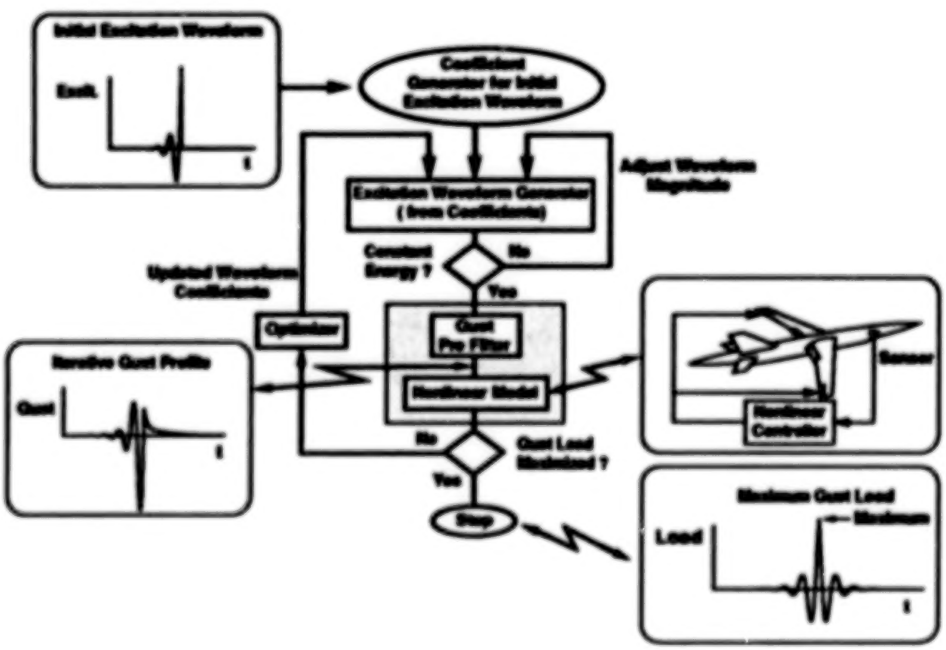

Figure 3

Coefficient Generator Using Fourier Series Approximation

Figure 4 presents an example of approximating the excitation waveform with the coefficient generator. Fourier series has been investigated as a candidate approximating function. The figure shows an initial waveform to be approximated, and two examples of Fourier series approximations. The second plot shows the resultant curve for 41 coefficients. The peak excitation is significantly underpredicted and there is a high frequency oscillation present during the latter portion of the time history. Using 401 coefficients to approximate the excitation sufficiently captures the curve's characteristics, as illustrated in the third plot.

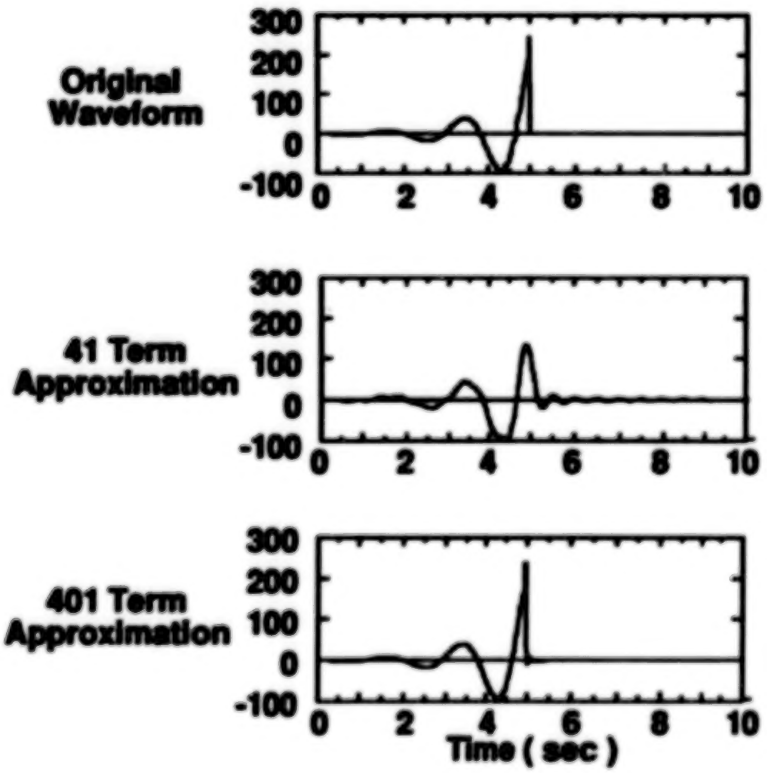

Figure 4

Block Diagram of Aircraft Control System with Nonlinear Element

A simulation model of a drone aircraft was constructed to demonstrate an application of the present method. The model is based on a configuration used to design the gust alleviation control system as discussed in reference 3. Figure 5 shows the block diagram of the simulation model which includes the aeroelastic plant, the gust load alleviation control law, and the nonlinear control element. The shaded block to the left of the plant is the iterative gust profile input. The shaded block to the right of the plant is the wing root bending moment. The maximum absolute value of the wing root bending moment is the objective function.

The plant itself is a linear, s-plane aeroelastic half-model consisting of 2 rigid body modes and 3 flexible modes. Unsteady aerodynamics were obtained using the doublet lattice method (reference 4). The plant model also includes the dynamics for the aileron and elevator control surface actuators. The two-input/two-output control law was obtained using a Linear Quadratic Gaussian design approach with the intent of reducing wing root bending moment. The controller uses the two control surfaces simultaneously.

The original control system design did not contain any nonlinear elements. The nonlinear element defined in the figure is based on a spoiler-driven gust load alleviation system used on the Airbus A320 (reference 5). This nonlinearity is intended to simulate some of the important aspects of an actual system; these aspects include allowing motion only in one direction and preventing motion beyond a deflection limit.

It should be added that wing bending moment response is dominated by the short period dynamics and is characterized by a large overshoot and a smaller undershoot. The objective of the load alleviation system is to reduce the overshoot load above a one g level and to ignore the undershoot loads below this level and the neutral load condition. The nonlinear element in the controller accomplishes this type compensated load reduction.

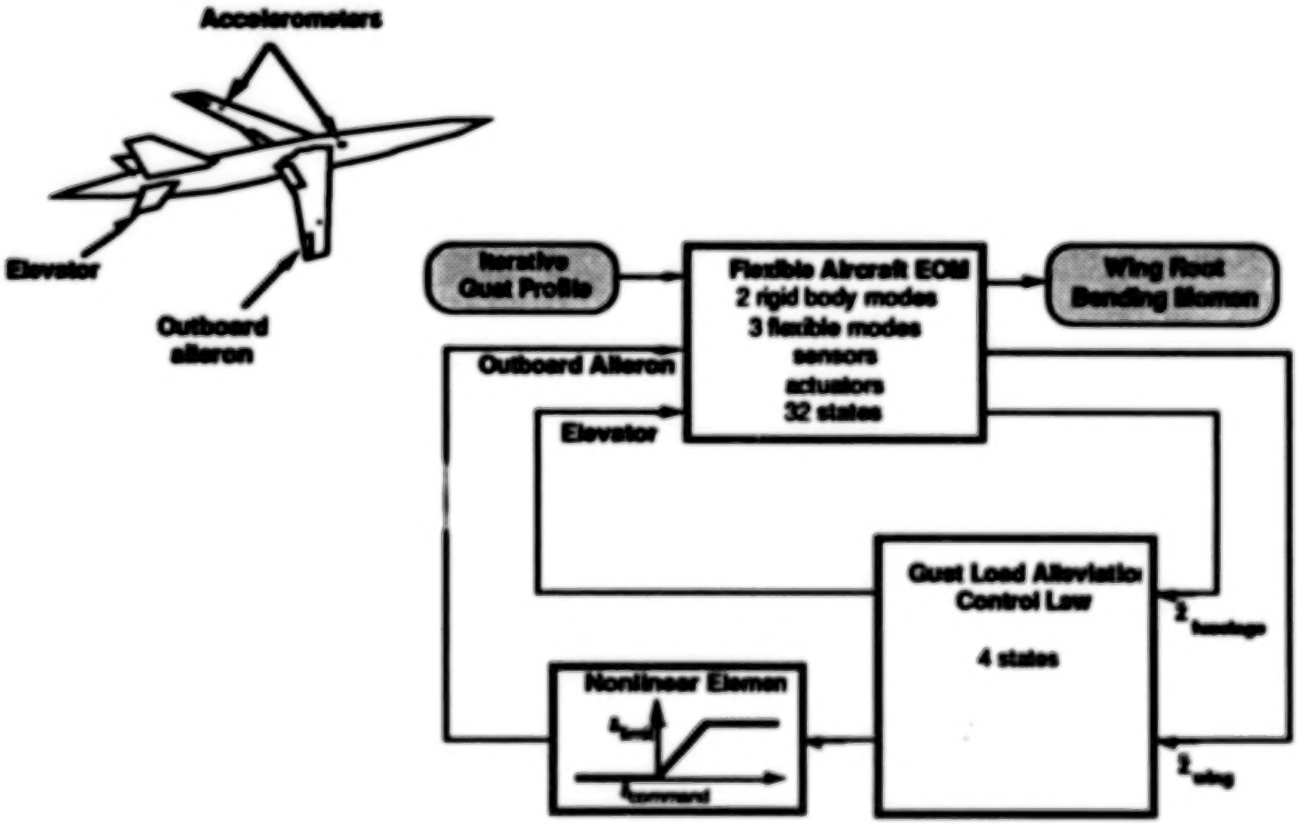

Figure 5

Status

Figure 6 outlines the status of the task. The entire scheme presented in figure 3 has been implemented. The nonlinear control system has been simulated with MATRIX$_X$ SYSTEM_BUILD (reference 6), which uses a high-level interpretive language and nonlinear functions that are built into the program. The simulation is run on a MicroVAX computer. The nonlinear simulation with approximately 2000 time points takes about five minutes clock time to run.

As indicated in figure 4, 401 terms in the Fourier series are necessary for an adequate representation of the initial excitation waveform. Since this is the number of terms used in the implementation, this task required the generation of 200 sine and 201 cosine waveforms for each objective function evaluation.

The optimization is performed using a MATRIX$_X$ Optimization Module (reference 7) that also incorporates a high-level interpretive language. Gradients are generated from within this module using a finite difference method. This part of the computation is estimated to require 402 evaluations (one more than the number of design variables) of the objective functions which means performing the same number of simulations. Using SYSTEM_BUILD and the Optimization Modules, the optimizer was allowed to run for a day and a half clock time and had to be stopped. It was then decided to modify the method to allow more rapid solution of the problem. Figure 7 outlines some of the problems encountered and the possible solutions.

- **Nonlinear control system implemented using MATRIX$_X$ SYSTEM_BUILD**
  - Uses high-level interpretive language
  - Employs built-in nonlinear functions
- **Excitation waveform generator utilized Fourier series**
  - 401 coefficients necessary for good initial waveform approximation
  - Waveform composed of 200 sines, 200 cosines, and 1 constant
- **MATRIX$_X$ Optimization Module used to maximize loads**
  - Objective function is the peak wing root bending moment response
  - Uses equality constraint to maintain constant energy
  - Generates gradients using finite difference method

Figure 6

Research Problems and Proposed Solutions

Figure 7 presents the major research problems identified to date. The central issue is speed. To deal with this problem three areas are being investigated: simulation speed, number of design variables and optimizer speed.

The simulation constructed using SYSTEM_BUILD was run on a MicroVAX. Both the high-level interpretive language of SYSTEM_BUILD and the machine limitations of the MicroVAX contribute to the slowness of the simulation. To overcome this problem, a FORTRAN-based simulation needs to be generated using HYPER_BUILD (reference 8) and run on a faster computer using RemoteSim (reference 9).

The coefficients used to generate the excitation waveform serve as the design variables in the optimization problem. Using Fourier series to approximate the waveform requires an exceptionally large number of coefficients. Other orthogonal functions such as Chebychev polynomials are being investigated to determine their suitability for approximating the waveform. A reduction of the number of coefficients can be achieved by not approximating the discontinuous drop off to zero of the excitation waveform and explicitly setting waveform to zero at that point.

The speed of the optimization module is the third area for possible improvement. Increasing the speed could be accomplished by using a FORTRAN-based optimization module instead of the high-level interpretive language of MATRIXx. Since maintaining the equality constraint is a difficult task to achieve for most optimizers, the number of iterations through the optimizer loop could be reduced by reformulating the equality constraint as an inequality constraint. Gradients currently generated by finite differencing might also be generated analytically. The number of design variables could be reduced by using only the coefficients with the largest gradients. This would also produce a faster optimization.

Problem:
- SYSTEM_BUILD simulations too slow on VAX computers

Solution:
- Fortran-based simulation such as HYPER_BUILD needs to be generated
- Simulation must be executed on faster machine

Problem:
- Exceptionally large number of Fourier coefficients are needed to generate the excitation waveform

Solution:
- Use other orthogonal functions better suited for waveform approximation
- Precomputed polynomial waveforms for later use

Problem:
- MATRIXx Optimization Module too slow

Solution:
- Incorporate a Fortran-based optimization module
- Reformulate equality constraint as inequality constraint
- Generate gradients analytically
- Choose as design variables only those coefficients with the largest gradients

Figure 7

References

1. Jones, J. G.: The Statistical Discrete Gust (SDG) Method in Its Developed Form. AIAA Paper No. 89-1375-CP. April 3-5, 1989.

2. Petotzky, Anthony S.; Zeiler, Thomas A.; and Perry, Boyd III: Time-Correlated Gust Loads Using Matched Filter Theory and Random Process Theory - A New Way of Looking at Things. AIAA Paper No. 89-1374-CP. April 3-5, 1989.

3. Mukhopadhyay, Vivek: Digital Robust Control Law Synthesis Using Constrained Optimization. *Journal of Guidance, Control, and Dynamics*. vol. 12, no. 2, March-April 1989, pp 175-181.

4. Geising, J. P.; Kalman, T. P.; and Rodden, W. P.: Subsonic Unsteady Aerodynamics for General Configurations, Part I: Direct Application of the Nonplanar Doublet Lattice Method. AFFDL-TR-71-5, 1971.

5. Hockenhull, Mark: A Method of Non-Linear Continuous Turbulence Analysis. British Aerospace document BAe/WEY/D/A320/270, Weybridge Surrey KT13 OSF, England. April 21, 1988.

6. SYSTEM_BUILD 7.0 User's Guide: Integrated Systems Inc. October, 1988.

7. MATRIXX Optimization Module User's Guide: Integrated Systems Inc. August, 1988.

8. HYPER_BUILD 7.0 User's Guide: Integrated Systems Inc. October, 1988.

9. RemoteSim User's Guide: Integrated Systems Inc. May, 1988.

PIEZOELECTRICALLY FORCED VIBRATIONS OF ELECTRODED DOUBLY ROTATED QUARTZ PLATES BY STATE SPACE METHOD

R. CHANDER
AEROSTRUCTURES, INC.
ARLINGTON, VIRGINIA

PROCEDURE OUTLINE

The purpose of this investigation is to develop an analytical method to study the vibration characteristics of piezoelectrically forced quartz plates. The procedure is schematically shown in Figure 1, and can be summarized as follows. The three dimensional governing equations of piezoelectricity, the constitutive equations and the strain-displacement relationships are used in deriving the final equations. For this purpose, a state vector consisting of stresses and displacements are chosen and the above equations are manipulated to obtain the projection of the derivative of the state vector with respect to the thickness coordinate on to the state vector itself. The solution to the state vector at any plane is then easily obtained in a closed form in terms of the state vector quantities at a reference plane. To simplify the analysis, simple thickness mode and plane strain approximations are used.

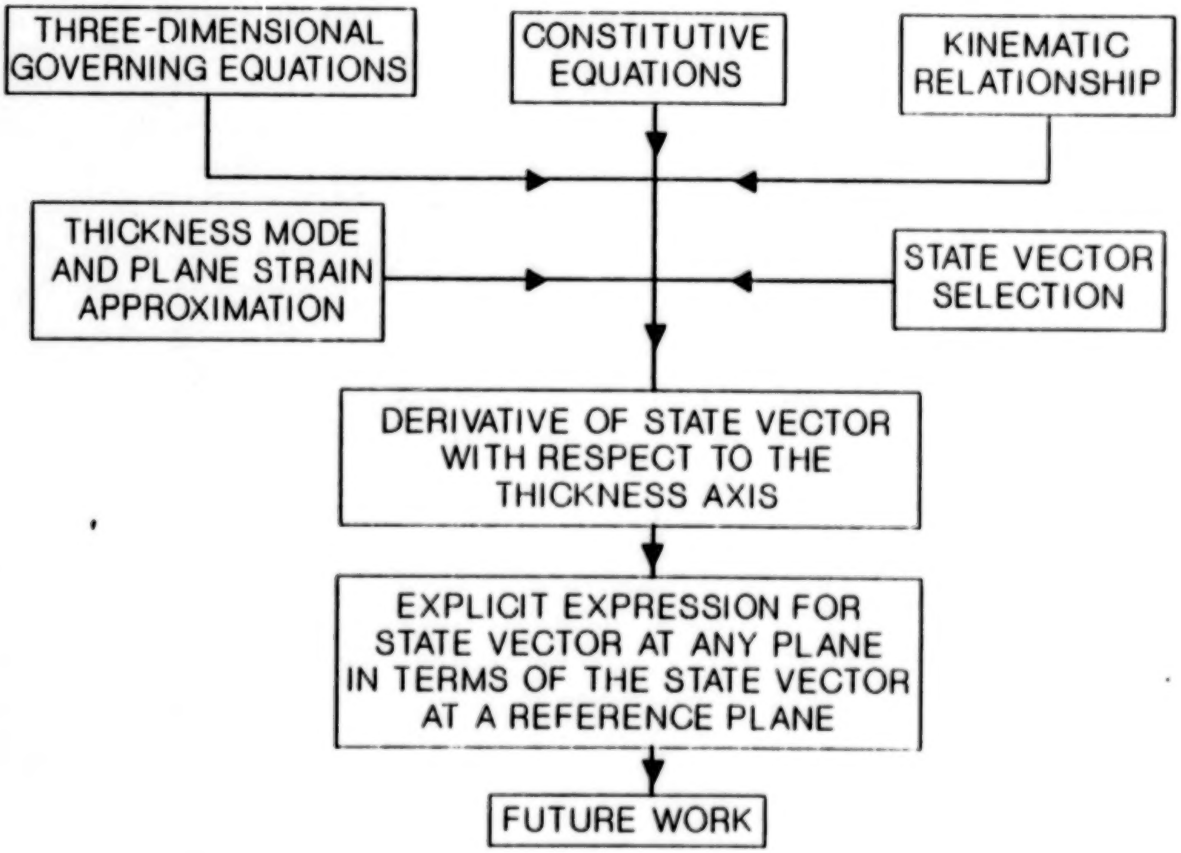
THREE-DIMENSIONAL GOVERNING EQUATIONS
CONSTITUTIVE EQUATIONS
KINEMATIC RELATIONSHIP
THICKNESS MODE AND PLANE STRAIN APPROXIMATION
STATE VECTOR SELECTION
DERIVATIVE OF STATE VECTOR WITH RESPECT TO THE THICKNESS AXIS
EXPLICIT EXPRESSION FOR STATE VECTOR AT ANY PLANE IN TERMS OF THE STATE VECTOR AT A REFERENCE PLANE
FUTURE WORK

Figure 1

The governing equations of piezoelectricity consisting of the equations of motion and the charge equations of electrostatics are given by Equations (1) and (2). The quantities σ_{ij}, u_i and D_i are the components of stress, mechanical and electrical displacements. The constitutive equations are presented in Equations (3) and (4), where C_{ijkl} is the elastic stiffness, and ϵ_{kl}, e_{ijk}, E_i and S_{ij} are respectively the components of mechanical strain, piezoelectric strain constants, electric field and dielectric permitivity. The relationship between mechanical strain and displacement, and the relationship between electric field and electric potential are given in Equations (5) and (6) respectively.

EQUATIONS OF MOTION

$$\sigma_{ij,j} = \rho\, u_{i,tt} \qquad (1)$$

CHARGE EQUATION OF ELECTROSTATICS

$$D_{i,i} = 0 \qquad (2)$$

CONSTITUTIVE EQUATIONS

$$\sigma_{ij} = C_{ijkl}\, \epsilon_{kl} - e_{kij}\, E_k \qquad (3)$$

$$D_i = e_{ijk}\, \epsilon_{jk} + S_{ij}\, E_j \qquad (4)$$

$$\epsilon_{ij} = 0.5\, (u_{j,i} + u_{i,j}) \qquad (5)$$

$$E_i = -\phi_{,i} \qquad (6)$$

Figure 2

The plane x1-x3 is taken to be the plane of the plate, and the x2-direction is considered as the thickness coordinate. The simple thickness mode approximation, in which the various quantities are just functions of the thickness coordinate, is used in the analysis. Also, the system is considered to be under plane strain conditions. Invoking the above assumptions, and using the contracted notation given by Equation (7), the surviving system of equations are presented in Equations (8) through (10). Differentiating the last of the equations (10), using the third of Equation (8) and integrating the resulting equation twice, the expression for ϕ is obtained (Equation 11), where A and B are constants of integration. A constant field does not produce any electric field, hence the constant B in Equation (11) is neglected. Substituting Equation (11) in Equation (10), the expressions for the non zero stress components are obtained, and are given in Equations 12 and 13.

CONTRACTED NOTATION

$$11,\ 22,\ 33,\ 23\ \text{OR}\ 32,\ 31\ \text{OR}\ 13,\ 12\ \text{OR}\ 21 \qquad (7)$$

$$\downarrow$$

$$1,\ 2,\ 3,\ 4,\ 5,\ 6$$

INVOKING SIMPLE THICKNESS MODE AND PLANE STRAIN ASSUMPTIONS

$$\left.\begin{aligned} \sigma_{6,x2} &= \rho\, u_{1,tt} \\ \sigma_{2,x2} &= \rho\, u_{2,tt} \\ D_{2,x2} &= 0 \end{aligned}\right\} \qquad (8)$$

$$\left.\begin{aligned} \epsilon_2 &= u_{2,x2} \\ \epsilon_6 &= 1/2\ u_{1,x2} \\ E_2 &= -\phi_{,x2} \end{aligned}\right\} \qquad (9)$$

$$\left.\begin{aligned} \sigma_2 &= 1/2\ C_{26}\, u_{1,x2} + C_{22}\, u_{2,x2} + e_{22}\, \phi_{,x2} \\ \sigma_6 &= C_{66}\, u_{1,x2} + C_{62}\, u_{2,x2} + e_{26}\, \phi_{,x2} \\ D_2 &= 1/2\ e_{26}\, u_{1,x2} + e_{22}\, u_{2,x2} - S_{22}\, \phi_{,x2} \end{aligned}\right\} \qquad (10)$$

$$\phi = (\ 1/2\ e_{26}\, u_1 + e_{22} u_2\ )/S_{22} + Ax2 + B \qquad (11)$$

$$\sigma_2 = a_{26}\, u_{1,x2} + a_{22}\, u_{2,x2} + e_{22} A \qquad (12)$$

$$\sigma_6 = a_{66}\, u_{1,x2} + a_{62}\, u_{2,x2} + e_{26} A \qquad (13)$$

Figure 3

A state vector (V) defined by Equation (14) is chosen. The derivatives of the state vector with respect to x2 is obtained from Equations (8) through (13) and the resulting expressions are given in Equations (17) through (20). The elements of the matrices B1, B2 and B3 are made up of the material constants and derivatives with respect to x2 and time (t).

STATE VECTOR

$$(V) = [\ (V_1)^T\ (V_2)^T\ ]^T$$
$$(V_1) = [\ u_1\ \sigma_2\ ]^T \quad ; \quad (V_2) = [\ \sigma_6\ u_2\ ]^T \tag{14}$$

$$(V_1)_{,x2} = [\ B_1\ ]\ (V_2) - A\ (b_1) \tag{15}$$

$$(V_2)_{,x2} = [\ B_2\ ]\ (V_1) - A\ (b_2) \tag{16}$$

$$(V)_{,x2} = [\ B_3\ ]\ (V) - A\ (b_3) \tag{17}$$

$$B1 = \begin{bmatrix} 1/a_{66} & -(a_{62}/a_{66})\ \partial/\partial x_2 \\ 0 & \rho\ \partial^2/\partial t^2 \end{bmatrix} \qquad b1 = \begin{bmatrix} e_{26}/a_{66} \\ 0 \end{bmatrix} \tag{18}$$

$$B2 = \begin{bmatrix} \rho\ \partial^2/\partial t^2 & 0 \\ -(a_{26}/a_{22})\ \partial/\partial x_2 & 1/a_{22} \end{bmatrix} \qquad b2 = \begin{bmatrix} 0 \\ e_{22}/a_{22} \end{bmatrix} \tag{19}$$

$$a_{62} = C_{62} + e_{26}e_{22}/S_{22} \quad ; \quad a_{66} = 1/2\ (C_{66} + e_{26}^2/S_{22})$$
$$a_{26} = 1/2\ (C_{26} + e_{22}e_{26}/S_{22}) \quad ; \quad a_{22} = C_{22} + e_{22}^2/S_{22} \tag{20}$$

Figure 4

A solution to the differential equation given in Equation (11) can be easily obtained and is given in Equation (21), where (V0) is the state vector evaluated at x2=0. The analyst has the flexibility of choosing any plane as the appropriate reference plane. The exponential term in Equation (21) can be expressed in an infinite series, and the powers of the matrix B3 can conveniently grouped as shown in Equation (23).

$$V = e^{B3\ x2}\ (V0) + B3^{-1}\ A\ b3$$
$$(V0) = (V)_{x2=0} \qquad (21)$$

$$e^{B3x2}\ (V0) = \left[I + B3\ x2 + (B3\ x2)^2/2! + (B3\ x2)^3/3! + \ldots . \right]\ (V0) \qquad (22)$$

$$B3^2 = \begin{bmatrix} P & 0 \\ 0 & Q \end{bmatrix} \qquad B3^3 = \begin{bmatrix} 0 & B1Q \\ B2P & 0 \end{bmatrix}$$

$$B3^4 = \begin{bmatrix} P^2 & 0 \\ 0 & Q^2 \end{bmatrix} \qquad B3^5 = \begin{bmatrix} 0 & B1Q^2 \\ B2P^2 & 0 \end{bmatrix} \qquad (23)$$

$$[\ P\ ] = [B1]\ [B2]$$
$$[\ Q\ ] = [B2]\ [B1]$$

Figure 5

Using the expressions given in Equation (23), the infinite series expansion for the exponential term can be conveniently grouped as shown in Equation (24). The elements present in Equation (24) can be recognized as a convergent series. The resultant expression is given by Equation (25). Substituting this expression in Equation (21), the final equation for the state vector at any reference plane in terms of the state vector at a reference plane is obtained (Equation 26).

$$e^{B3x2}\,(V0) = \left[I + \begin{bmatrix} 0 & B1 \\ B2 & 0 \end{bmatrix} x2 + \begin{bmatrix} P & 0 \\ 0 & Q \end{bmatrix} x2^2/2! + \right.$$

$$\begin{bmatrix} 0 & B1Q \\ B2P & 0 \end{bmatrix} x2^3/3! + \begin{bmatrix} P^2 & 0 \\ 0 & Q^2 \end{bmatrix} x2^4/4! +$$

$$\left. \begin{bmatrix} 0 & B1Q^2 \\ B2P^2 & 0 \end{bmatrix} x2^5/5! + \ldots. \right] (V0) \qquad (24)$$

$$- \begin{bmatrix} \cosh(x2/P) & B1\sqrt{Q}\sinh(x2/Q) \\ B2/P\sinh(x2/P) & \cosh(x2/Q) \end{bmatrix} (V0) \qquad (25)$$

$$= [R]\,(V0)$$

$$(V) = [R]\,(V0) + A\,[B3]^{-1}\,(b3) \qquad (26)$$

Figure 6

Symbols and Abbreviations

A, B	Constants of integration
a_{ij}	Constant coefficients
C_{ijkl}	Elastic stiffness
D_i	Components of electric displacement
e_{kij}	Components of piezoelectric strain constant
E_k	Components of electric field
S_{ij}	Components of dielectric permittivity
u_i	Components of mechanical displacement
ϵ_{kl}	Components of strain
ϕ	Electric potential
ρ	Mass density
σ_{ij}	Stress components

Analysis of Elastically Tailored Viscoelastic Damping Member

G-S. Chen and B.P. Dolgin

Jet Propulsion Laboratory
California Institute of Technology
Pasadena, California

Introduction

For more than two decades, viscoelastic materials have been commonly used as a passive damping source in a variety of structures because of their high material loss factors. In most of the applications, viscoelastic materials are used either in series with or parallel to the structural load path. The latter is also known as the constrained-layer damping treatment[1,2]. The advantage of the constrained-layer damping treatment is that it can be incorporated without loss in structural integrity, namely, stiffness and strength. However, the disadvantages are that (1) it is not the most effective use of the viscoelastic material when compared with the series-type application, and (2) weight penalty from the stiff constraining layer requirement can be excessive. To overcome the disadvantages of the constrained-layer damping treatment, a new approach for using viscoelastic material in an axial-type structural components, e.g., truss members, was studied in this investigation.

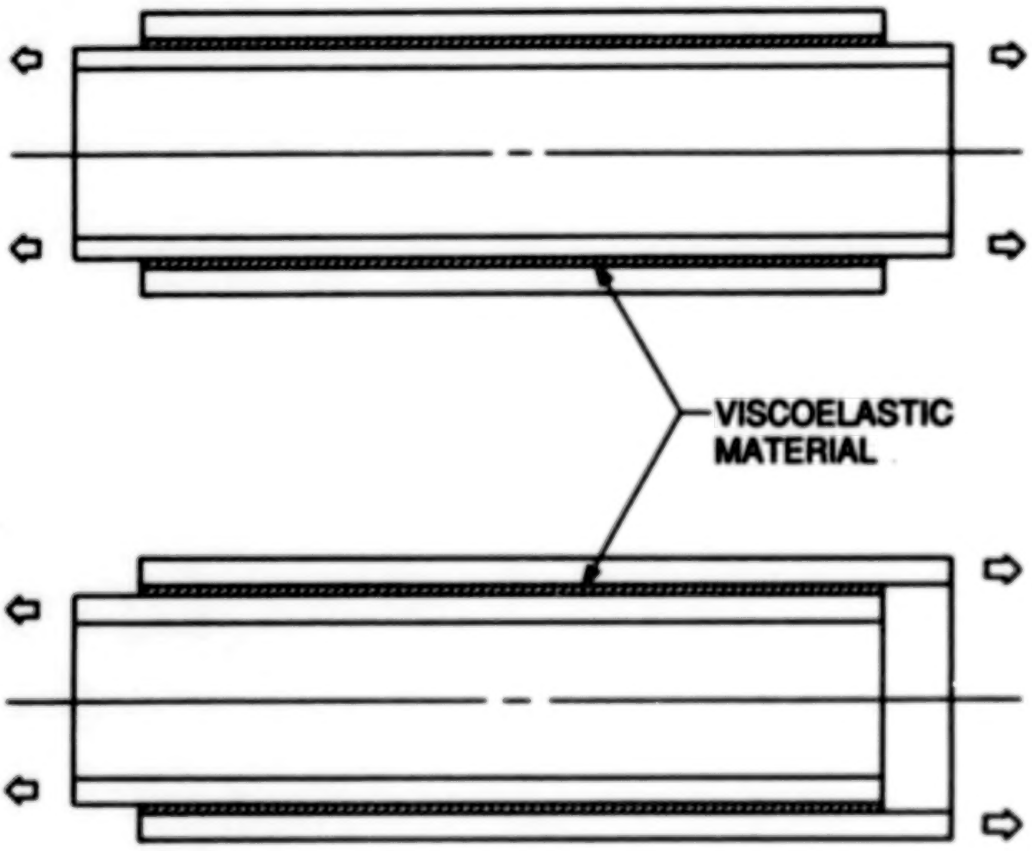

Elastic Tailoring in Composite Structures

It is well known that, with the properly arrangod orientation sequence in layup, composite structure can exhibit various types of deformation coupling when subjected to loading. In certain applications, such anisotropic behavior can be tailored to benefit specific needs. For example, the bending/twisting coupling has been extensively studied for the purposes of aeroelastic tailoring[3,4]. The application of extension/twisting deformation coupling to the constrained-layer damping treatment was explored in Ref. 2. In Refs. 5 and 6, a new approach of applying extension/twisting deformation coupling to damping treatment was proposed for the axial-type truss member. In this approach, the viscoelastic material is embedded in a structural member made of fiber reinforced composite material. By a judicious tailoring, the structural member can exhibit the extension/twisting deformation coupling such that the viscoelastic material is sheared in twisting while the structural member undergoes an axial deformation.

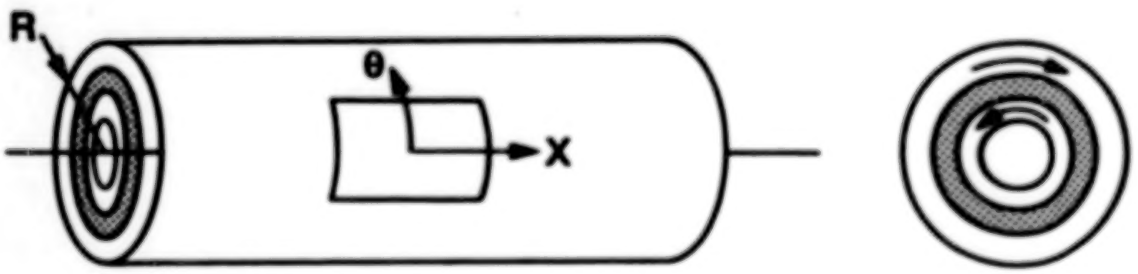

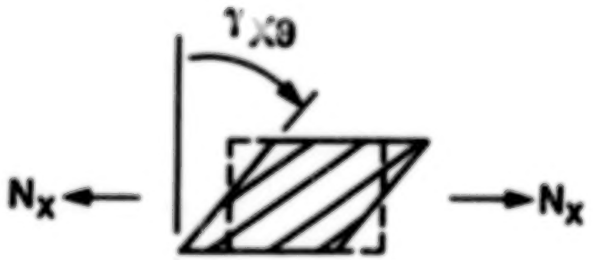

New Material Concept

However, the difficulty with this new approach is that it requires a built-in twisting freedom in the truss member. In reality, such added design complexity is usually forbidden. To avoid such undesirable requirement, a new material concept of using saw-toothed (or V-shaped) fiber in reinforced composite was conceived in Ref. 7. With the V-shaped fiber, a truss member is allowed to undergo twisting deformation at knee-points while its both ends remain fixed. Damping performance was studied on a plane strain model as shown below. The resulting shear strain distribution in the viscoelastic material is a hyperbolic sine function along the member axis which is similar to the result of constrained-layer damping treatment[2]. The member loss factor is estimated from the expression of complex stiffness as

$$K_m = K\cdot\left(1 + \mu\cdot\frac{\tanh\sqrt{\beta}}{\sqrt{\beta}}\right) \qquad \eta_m = \frac{\text{Imaginary } (K_m)}{\text{Real } (K_m)}$$

where

$$\mu = \frac{A_{16}^2}{A_{11}A_{66} - A_{16}^2} \qquad \beta = L^2 \cdot \frac{2G_2}{t_2} \cdot \frac{A_{11}}{A_{11}A_{66}-A_{16}^2}$$

Examining the above expression indicates that the member loss factor is only a function of two parameters. One is the extension/twisting coupling coefficient, μ, which is a function of the composite material properties and its layup. The other is a combined geometry/material parameter, β.

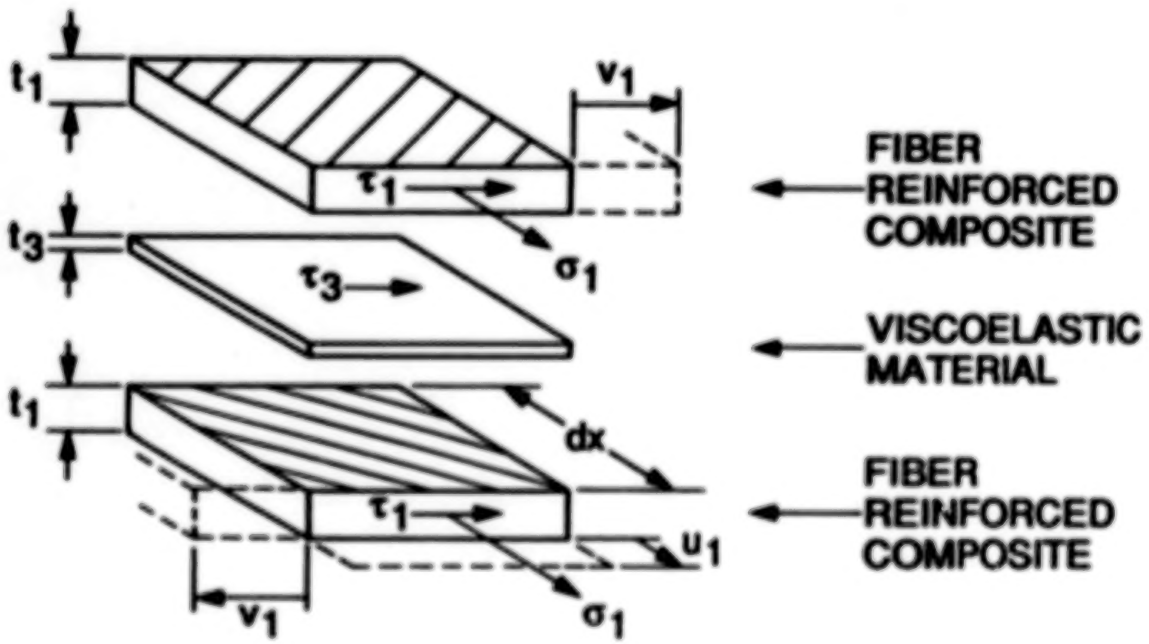

Analysis Model for Waved Fiber Reinforced Composites

The idealized V-shaped fiber is useful in performance trade study. In practice, however, the V-shaped fiber is not really feasible because of its sharp corners. In this investigation, the sine-waved fiber reinforced composite is analyzed for this new damping treatment approach. The analysis model of a truss member made of iso-phased sine-waved fiber reinforced composite is shown below. In this design, the fiber orientation is antisymmetric with respect to the viscoelastic material (VEM) layer, i.e., $[+\theta_n/VEM/-\theta_n]$ layup, such that the twisting deformation in the viscoelastic material is maximized under axial load. Because of the continuously varying fiber orientation, the truss member's elastic properties are varying along the member axis. In this study, a concept of using equivalent homogeneous model with effective elastic properties is proposed to evaluate the member's damping performance. The effective anisotropic properties are estimated in average sense over one quarter of the fiber's spatial wavelength.

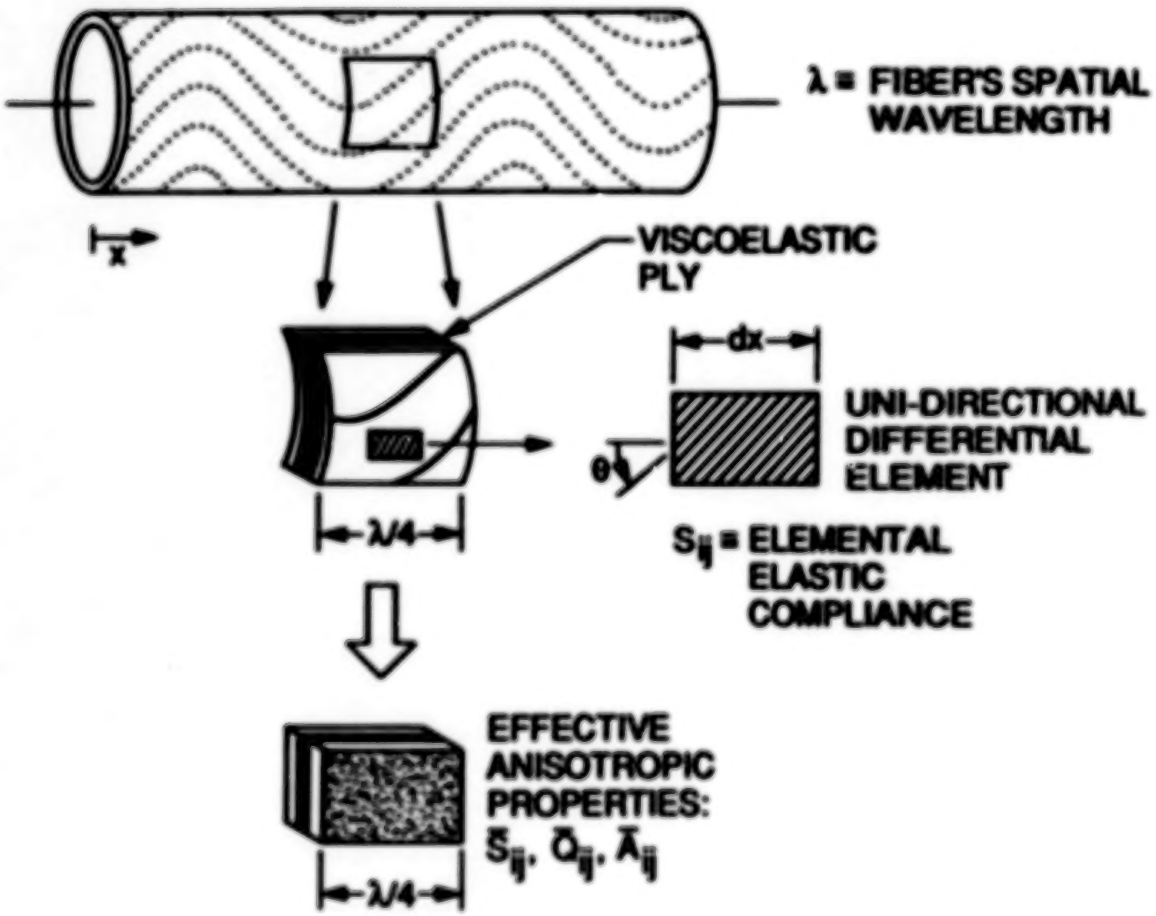

Effective Anisotropic Properties

Spatial dependent strain-stress relation:

$$\{\epsilon\} = [S(\theta)]\ \{\sigma\}$$

where the S_{ij}'s are the elemental elastic compliance and the tangent fiber orientation, θ, is given by

$$\theta = \tan^{-1}\left[\frac{2\pi a}{\lambda} \cdot \cos(2\pi x/\lambda)\right]$$

The effective compliance is

$$\bar{S}_{ij} = \frac{1}{\lambda/4} \cdot \int_0^{\lambda/4} S_{ij}(x) \cdot dx$$

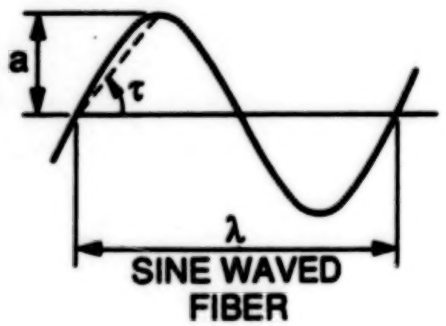

E_L = 40 Msi
E_T = 1.5 Msi
G_{LT} = 0.8 Msi
ν_{LT} = 0.26

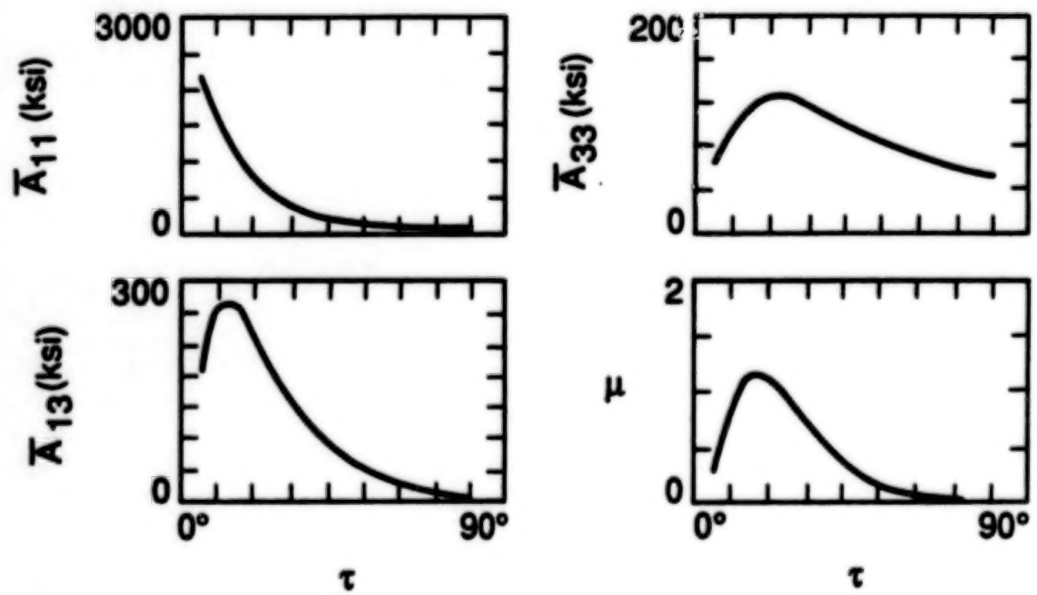

Examples

Given the material loss factor, η_{vem} = 1.0, functional dependency of the member loss factor on the extension/twisting coupling coefficient, μ, and parameter β are illustrated in the following example. It is interesting to note that the β_{opt} is not very sensitive to the variation in μ. For the example of HMS/3501-6, μ_{opt} = 1.2 at τ = 18°, the maximum loss factor attainable is about 17%.

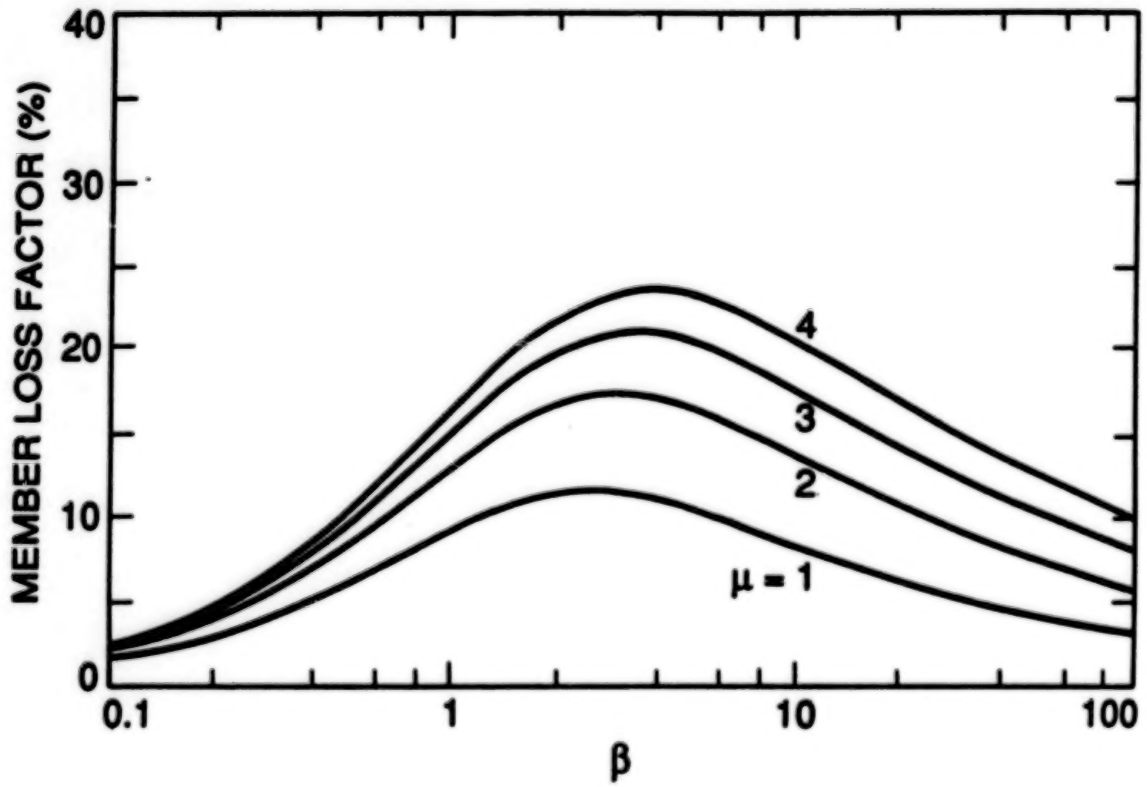

Summary

- o New material concepts, i.e., V-shaped and sine-waved fiber reinforced composite materials, were investigated for the new damping treatment in axial-type structural members.

- o The underlying mechanism of an elastically tailored damping member depends on the extension/twisting deformation coupling in composite materials. As a result, the embedded viscoelastic material is sheared in twisting when the member undergoes axial motion.

- o Shear strain distribution in the viscoelastic material is similar between the extension/twisting coupled damping treatment and the constrained-layer damping treatment.

- o A concept of using an equivalent homogeneous model with effective anisotropic properties was proposed to evaluate damping performance of members made of iso-phased sine-waved fiber reinforced composite material.

- o Numerical examples show that the sine waved-fiber reduces the degree of extension/twisting deformation coupling as compared with the V-shaped fiber reinforced composite material. However, its effect on the β parameter is less critical because the β parameter can be optimized through other geometric parameters.

- o With the optimally selected geometric and material parameters, the attainable loss factor of the elastically tailored damping member ranges from 10-25% which is about in the same performance range of the damping member with constrained-layer damping treatment. The major advantage of the elastically tailored damping member is that there is no additional weight penalty such as the constraining layer of the constrained-layer damping treatment.

References

1. Soovere, J. and Drake, M.L., Aerospace Structures Technology Damping Design Guide, Vol. 2, December, 1985, AFWAL-TR-84-3089.

2. Chen, G-S. and Wada, B.K., "Passive Damping for Space Truss Structures," AIAA SDM Issues of the International Space Station, Williamsburg, VA, April 21, 1988, AIAA Paper 88-2469.

3. Shirk, M.H., Hertz, T.J., and Weisshaar, T.J., "Aeroelastic Tailoring-Theory, Practice, and Promise," Journal of Aircraft, Vol. 23, January, 1986, pp. 6-18.

4. Chen, G-S. and Dugundji, J., "Experimental Aeroelastic Behavior of Forward-Swept Graphite/Epoxy Wings with Rigid-Body Freedom," Journal of Aircraft, Vol. 24, No. 7, July, 1987, pp. 454-462.

5. Barrett, D.J., "A Design for Improving the Structural Damping Properties of Axial Members," Damping Workshop 1989, West Palm Beach, FL, February 8-10, 1989.

6. Dolgin, B.P. and Chen, G-S., "Composite Damping Strut with Viscoelastic Plies," 1989 TMS Fall Meeting, Indianapolis, Indiana, October 1-5, 1989.

7. Dolgin, B.P., "Composite Passive Damping Strut for Large Precision Structures," JPL New Technology Report, NPO-17914, 1989.

STATIC & DYNAMIC AEROELASTIC CHARACTERIZATION OF AN AERODYNAMICALLY HEATED GENERIC HYPERSONIC AIRCRAFT CONFIGURATION

Jennifer Heeg
Michael G. Gilbert
Anthony S. Pototzky

NASA Langley Research Center
Hampton, Virginia

OBJECTIVES

This work-in-progress presentation describes an ongoing research activity at the NASA Langley Research Center to develop analytical methods for the prediction of aerothermoelastic stability of hypersonic aircraft including active control systems. The objectives of this research include application of aerothermal loads to the structural finite element model, determination of the thermal effects on flutter, and assessment of active controls technology applied to overcome any potential adverse aeroelastic stability or response problems due to aerodynamic heating- namely flutter suppression and ride quality improvement. For this study, a generic hypersonic aircraft configuration was selected which incorporates wing flaps, ailerons and all-moveable fins to be used for active control purposes. The active control systems would use onboard sensors in a feedback loop through the aircraft flight control computers to move the surfaces for improved structural dynamic response as the aircraft encounters atmospheric turbulence.

- **Construct a Generic Hypersonic Vehicle to Use in Performing Analytical Studies**

- **Develop and Analyze Aeroelastic Models Incorporating the Effects of Aerodynamic Heating**

- **Apply Active Controls to Compensate for Degraded Dynamic Responses**

  - **Flutter Suppression System**
  - **Ride Qualities Augmentation System**

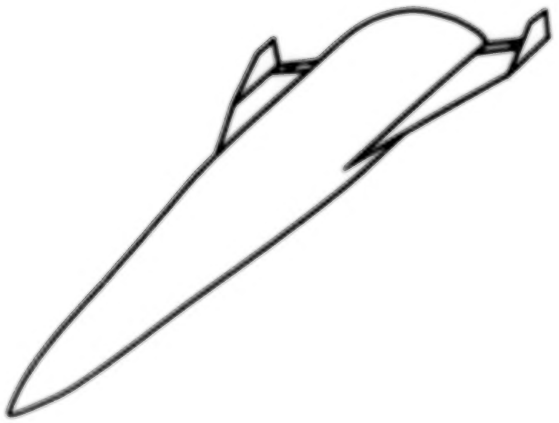

HYPERSONIC ANALYSIS AND DESIGN APPROACH

The current aeroservothermoelastic (ASTE) analysis and design capability is outlined schematically below. The method consists of three primary steps; 1) the determination of thermal loads acting on the structure due to aerodynamic heating, 2) the development of hot and cold aeroelastic mathematical models for flutter analysis including the computation of unsteady aerodynamic forces acting on the structure, and 3) the design, analysis, and simulation of active control laws.

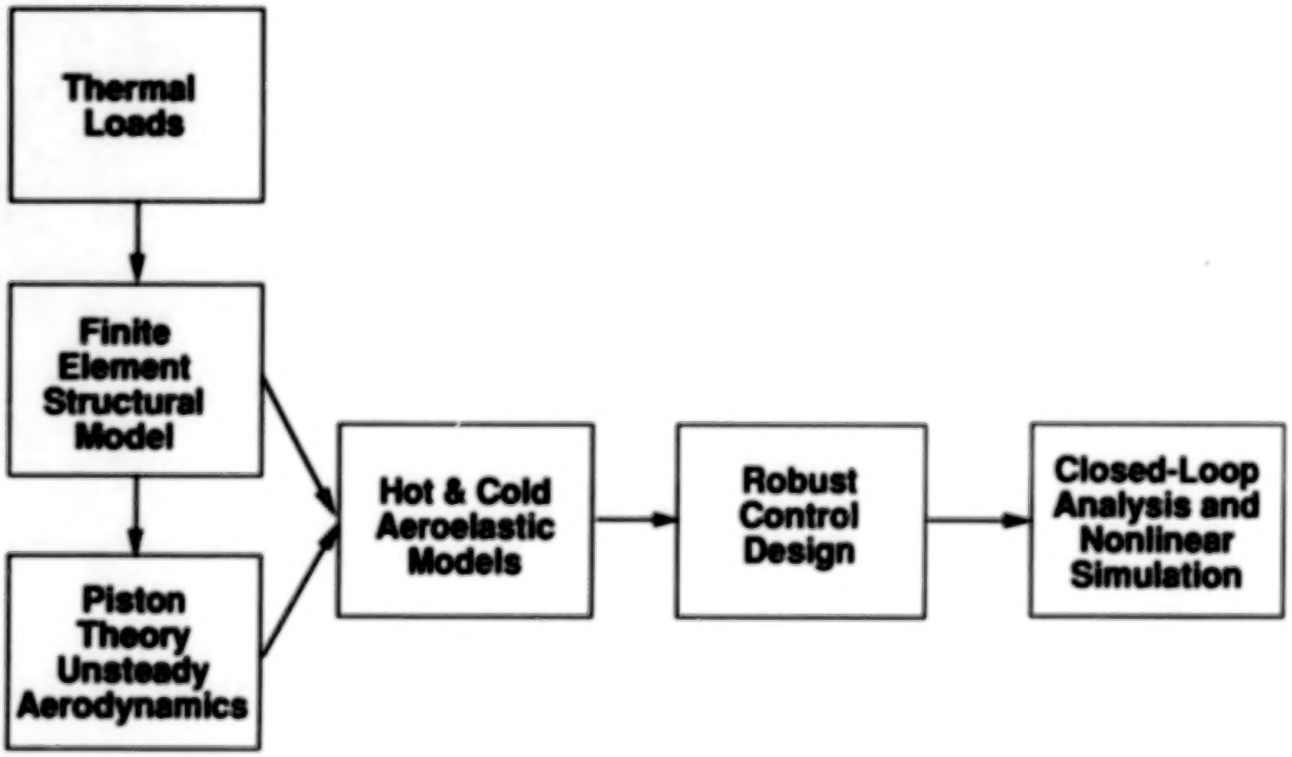

APAS AEROTHERMODYNAMIC MODEL

The Hypersonic Arbitrary Body Program (HABP) of the Aerodynamic Preliminary Analysis System [1] (APAS) was used to model the generic hypersonic aircraft configuration and obtain steady-state aerodynamic forces and heat loads. For a given flight condition (angle-of-attack and control surface deflection), the HABP module was used to compute aerodynamic lift and moment coefficients and aerodynamic center location, as well as the radiation equilibrium wall temperatures on the vehicle. The aerodynamic results were used to calibrate the unsteady aerodynamic force calculations by comparison of pitching moment coefficient and aerodynamic center location. The unsteady aerodynamic force models were then modified to yield compatible results. The radiation equilibrium wall temperatures were used directly as heat loads in the finite element structural model to determine structural stiffness changes caused by thermal stresses and material property changes.

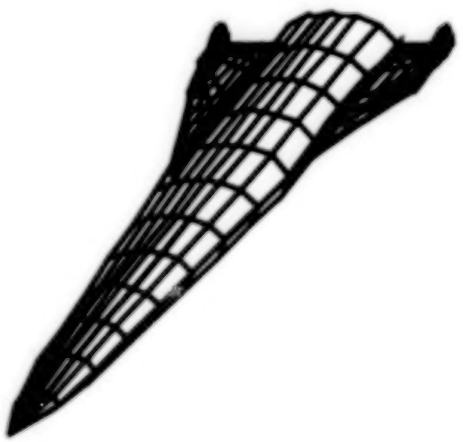

Aerodynamic Preliminary Analysis System (APAS) Hypersonic Arbitrary Body Program (HABP) module used for steady-state aerodynamic calculations

- Radiation equilibrium wall temperatures
- Lift and moment coefficients, aerodynamic center locations

Results used to

- Provide heat loads for thermal structural analysis
- Calibrate unsteady aerodynamic codes

FINITE ELEMENT MODEL

A conventional structural concept was used for the generic aircraft configuration of this study [2]. The fuselage was modeled as an elliptical cross section (width/height ratio 2) consisting of stiffened ring and skin construction. The low-aspect wings were modeled as fully attached to the fuselage consisting of spars, ribs, and skins. The wing leading edge sweep is 70 deg. and the wing section is a 3% circular arc airfoil. A body weight fraction, defined as the weight of the structural material contributing to stiffness divided by gross takeoff weight, of 8.6% was used to determine the required structural mass. Material properties consistent with titanium aluminide were assumed for all structural elements. The wing flaps, ailerons, and all movable fin were modeled separately and attached to the fuselage/wing model by spring stiffness elements modeling actuator stiffness characteristics. The Engineering Analysis Language [3] (EAL) structural analysis code was used to compute hot and cold vibration mode frequencies and mode shapes. The visual appearance and overall character of the mode shapes did not change with variations in temperature, although significant changes did occur in frequencies. Heating effects decreased the frequencies by thirteen to twenty percent.

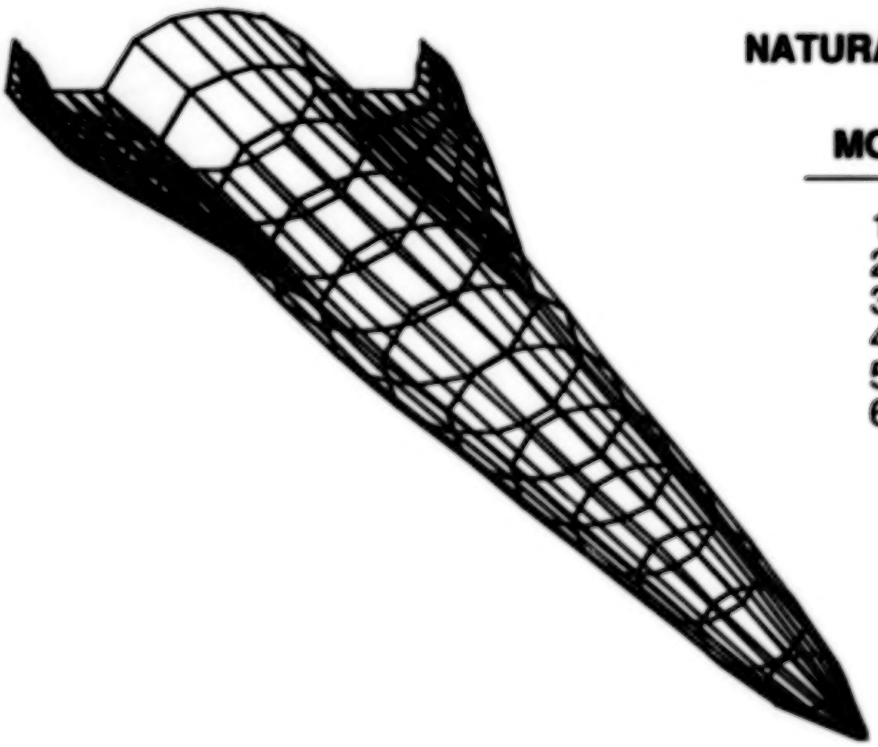

NATURAL FREQUENCIES (Hz)

MODE	COLD	HOT
1	3.01	2.43
2	4.02	3.48
3	7.06	5.67
4	7.70	6.56
5	9.47	7.63
6	10.96	8.84

UNSTEADY AERODYNAMICS - LESSONS LEARNED

Significant problems were encountered in computing valid unsteady aerodynamic forces for use in aeroelastic stability analyses in both subsonic and supersonic flight regimes. For the subsonic case, two versions of the Doublet Lattice Method [4] (DLM) aerodynamic panel code were used, as was a Kernal Function Method [5] (KFM) code. In the case of the DLM, the two versions were inconsistent in force results (both magnitude and phase). This was attributed to nonconvergence of the DLM due to insufficient numbers of aerodynamic boxes. The minimum number of required boxes was later estimated to be on the order of 675, far exceeding reasonable computational cost. Subsonic flutter boundary predictions using the KFM code were erratic, showing wide oscillations in flutter dynamic pressure for small subsonic variations in Mach number. For the supersonic case, the MSC/NASTRAN [6] Mach Box [7] and Piston Theory [8] methods were tried. It was found that the Mach Box result would not compare with analytical solutions for simple check cases. The Piston Theory method was found to be restricted to rigid chords, typically valid for high aspect ratio wings which are very stiff chordwise, and did not include airfoil thickness effects. Two new second-order Piston Theory codes including thickness, camber and chordwise bending effects were written, one in EAL and one in FORTRAN, both taking advantage of an existing aero/structure interface [9]. The FORTRAN version aerodynamic force results were ultimately used for flutter analyses because of consistency with the earlier APAS steady-state results.

SUBSONIC:

Doublet Lattice

- Inconsistent between code versions (ISAC and NASTRAN)
- Estimated 675 aerodynamic boxes required for convergence
- Exceeds inhouse code capability, very expensive in NASTRAN

Kernel Function

- Erratic flutter boundary predictions

SUPERSONIC:

Mach Box

- NASTRAN results do not agree with analytical solutions for simple cases

Piston Theory

- NASTRAN model limited to (a few) rigid chord panels

SUPERSONIC SOLUTION: Write a new piston theory code

- Linked to ISAC aero/structure interface to model nonrigid chords and thickness

PISTON THEORY AERODYNAMIC IMPLEMENTATION

At sufficiently high Mach numbers "local" wave theory is a good approximation to the unsteady aerodynamics. The local pressure is related to the normal free stream velocity in a similar manner as the pressure in a one-dimensional piston chamber is related to the velocity of the piston. A local, linearized pressure equation is represented by the equation shown in the figure. The various aircraft surfaces were represented by trapezoidal panels similar to the one indicated in the figure. The normal velocities over the surfaces were computed using surface spline interpolation with the normal velocities located at the center of each trapezoidal panel. The point forces subsequently created by the piston theory pressures were also concentrated at the center of each panel. The generalized aerodynamic force for each mode was generated by summing these point forces, weighted by the interpolated mode shapes, over the aircraft surfaces. The additional symbols used in the figure are defined as follows: Δp, pressure difference between upper and lower surfaces; ρ, density; a, the local speed of sound; γ, ratio of specific heats; Z, the relation describing the contour, or the thickness of the vehicle component; z, the displacement of the discrete point; and V, the freestream velocity.

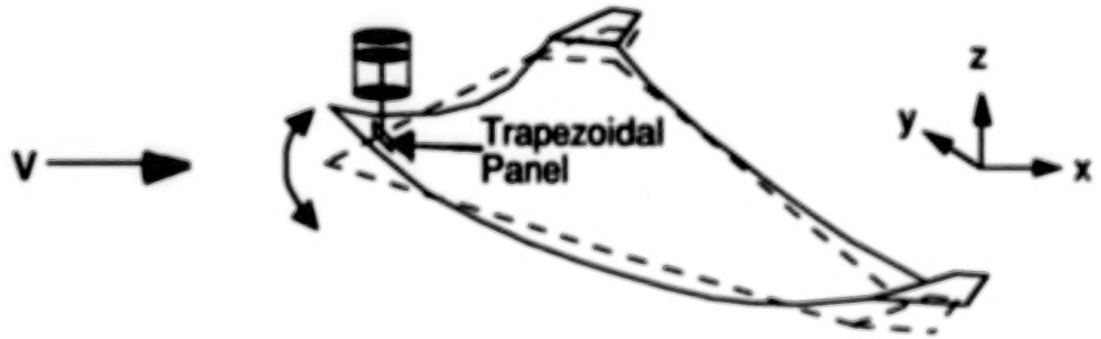

(U) Linearized, second-order equations including thickness effects

$$\Delta p(x,y,t) = -2\rho a\left[1 + G\frac{\partial}{\partial x}Z(x,y)\right]\left[\left(V\frac{\partial}{\partial x} + \frac{\partial}{\partial t}\right)z(x,y,t)\right]$$

$$G = \frac{M^4(\gamma + 1) - 4\beta^2}{2\beta^3} \; ; \; \beta = \sqrt{M^2 - 1}$$

(U) z(x,y,t) calculated at discrete points using surface spline interpolation of mode shape data

(U) Generalized aerodynamic force for each mode computed by numerical integration of the pressure over the surface

AERODYNAMIC MODELING INFLUENCE ON FLUTTER DYNAMIC PRESSURE

The relative importance of the aerodynamic influence of various vehicle components to flutter was evaluated. The importance of the inclusion of a modeling effect was measured by the percent change in flutter dynamic pressure. Four of the effects examined were found to be significant. The baseline analysis contained a restrained flat plate representation of the wing and used the first six flexible modes. Introducing the rigid body plunge and pitch modes into the analysis increased the flutter dynamic pressure by ten percent. Because the structural frequencies are very low, the structural modes are influenced by the short period mode. For this configuration, the rigid body motion helps to dissipate the system's energy into the airstream, thus inhibiting flutter. The addition of a flat plate representation of the fuselage decreases the flutter dynamic pressure by ten percent. Fuselage motion dominates the first and third flexible modes; including this motion in the analysis increases the aerodynamic force input and encourages flutter. Addition of an aerodynamic representation of the vertical fin further decreases the flutter q by ten percent for the same basic reason. The fifth flexible mode has significant vertical fin contributions, making it important to the analysis. The remaining changes to the aerodynamic model are inclusion of the thickness effects of the wing and the fuselage, both of which cause an increase in the flutter dynamic pressure. The wing contour effects changed the flutter value by ten percent, while the fuselage contour effects changed it by only two percent. The final model used for analysis and design incorporated all of the above effects except for fuselage thickness.

Basic Model:

Flat Plate Clipped Delta Wing with 70 Degree Leading Edge Sweep
First 6 Flexible Modes

CHANGE TO MODEL	EFFECT ON $\bar{q}_f$	
▪ Inclusion of Rigid Body Pitch & Plunge Modes	↑ 10 %	
▪ Addition of Flat Plate Fuselage	↓ 10 %	
▪ Addition of Wing Thickness Effects	↑ 10 %	
▪ Inclusion of Flat Plate Vertical Fin	↓ 10 %	
▪ Addition of Fuselage Thickness Effects	↑ 2 %	

ALTITUDE ROOT LOCUS

This figure shows the variation of the eigenvalues associated with the rigid body and first four flexible modes, as altitude is varied. The model used for this typical root locus was the heated structure at Mach 2.0. The arrows indicate decreasing altitude. This analysis was performed at a matched point, so both the density and velocity changed with altitude. Flutter is determined as the cross-over of the imaginary axis. From the figure it is seen that the eigenvalue associated with the third flexible mode moves into the right half plane at a frequency of 43.5 radians per second.

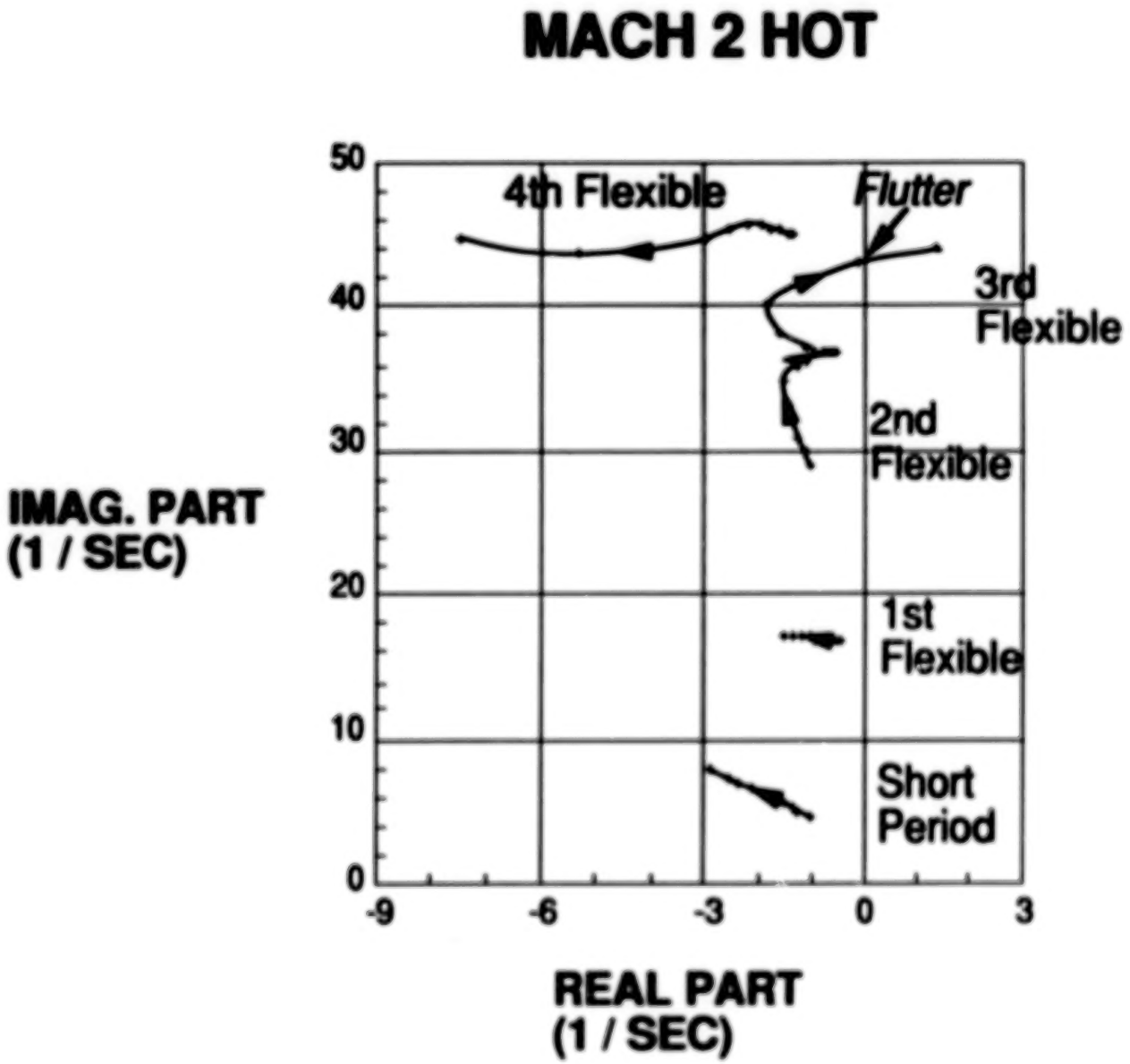

EFFECTS OF MACH NUMBER AND HEAT ON SHORT PERIOD MODE DYNAMICS

The short period mode dynamics are influenced by both the structural properties and by the aerodynamics. The figure shows the changes in short period behavior incurred due to the effects of structural flexibility, heating and Mach number. The six curves represent the trace of the short period eigenvalue in the complex plane as the altitude is varied (altitude decreases from right to left along each curve).

In an aeroelastic system, the roots of any one mode are influenced by the other modes near it. Because the structural frequencies for these configurations are low, in the neighborhood of the rigid body frequency, it is anticipated that they would exhibit a large degree of influence over the short period mode. This influence can be seen by examining the roots of the rigid vehicle versus the eigenvalues after the effects of flexibility have been included. The figure indicates that including flexibility tends to have a destabilizing effect . The effects due to the aerodynamic heating can be seen by comparing the hot and cold data for the same Mach number. At either Mach number, the destabilizing effect of the heating is seen as the roots for the hot data fall further to the right in the s-plane than those corresponding to the cold data.

To determine the effects of the aerodynamics, the curves for the rigid data, the hot data and the cold data must be examined separately. It is seen that as the Mach number is increased, the short period frequency is increased and the damping is decreased. Thus, increasing Mach number also has a destabilizing effect on the short period dynamics.

Comparing the curves in these three ways shows clearly that the Mach number has a much larger influence than either the flexibility or the heating.

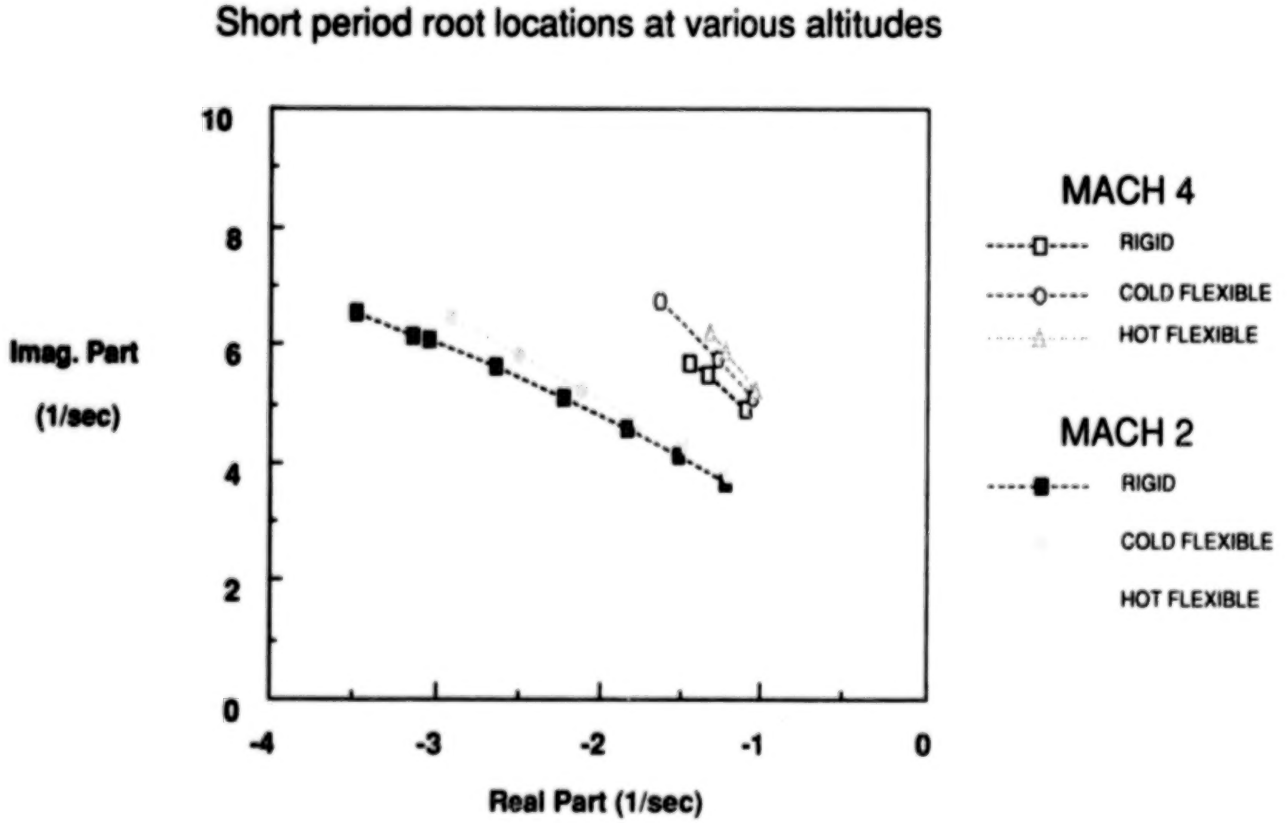

HOT / COLD FLUTTER RESULTS

The flutter characteristics are presented as a set of curves showing regions of instability. The flutter boundaries illustrate the destabilizing effects of both heating and Mach number. The region below either curve represents the region for flutter-free flight. As the Mach number is increased, the flutter dynamic pressure is increased. Heating lowers the flutter boundary over the entire range of Mach numbers, indicating that there will be an instability at lower dynamic pressures.

FLUTTER BOUNDARIES FOR HEATED AND UNHEATED VEHICLES

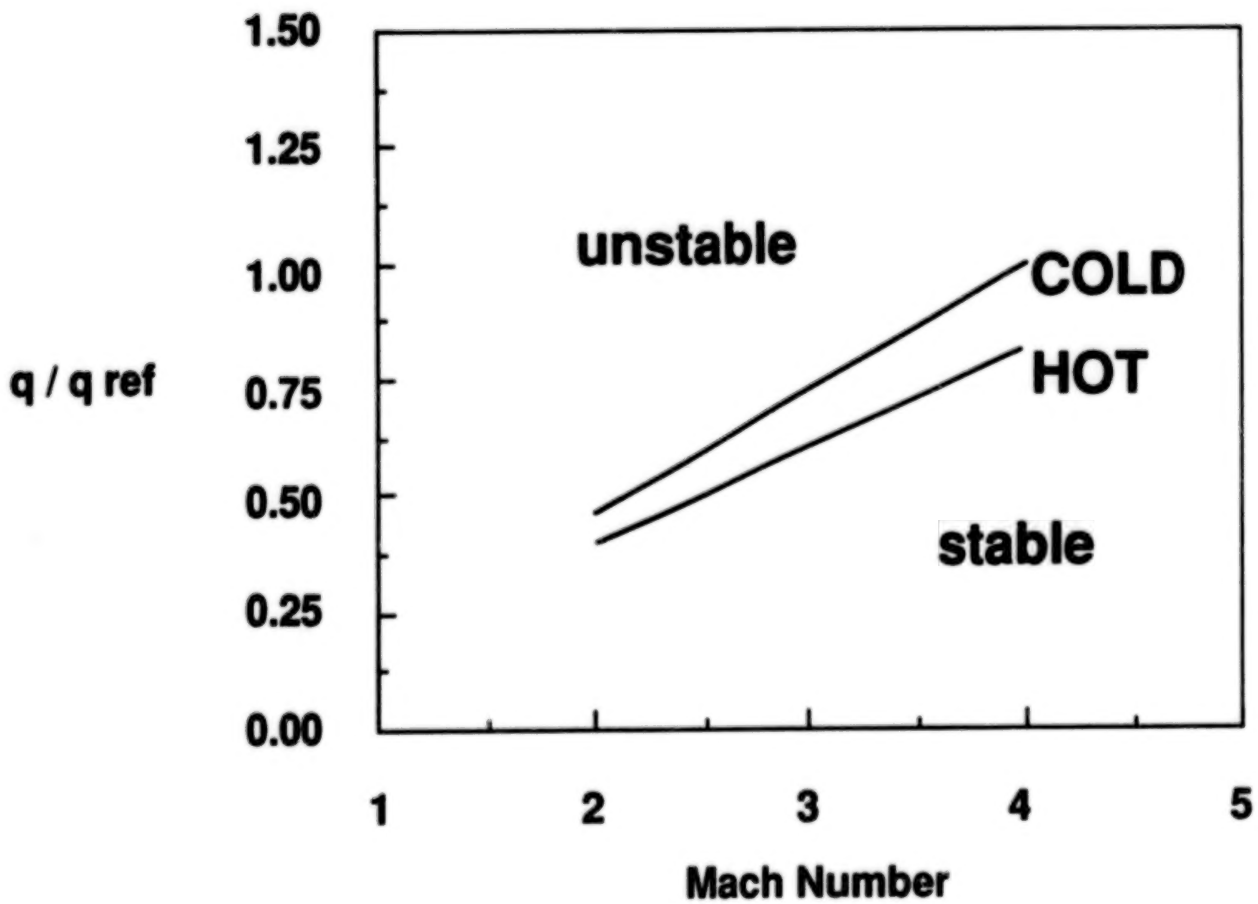

CONCLUSIONS / FUTURE PLANS

An aerothermoelastic analysis method has been developed. The thermal loads due to aerodynamic heating are incorporated into the finite element analysis. Application of the aerothermal effects reduced structural frequencies and lowered the flutter boundary. The flutter was found to be influenced by all components of the vehicle; analyses of hypersonic configurations must consider aircraft flutter versus wing flutter.

Future work in this area will concentrate on control law design and closed loop analysis. Plans include design of a flutter suppression system which will raise the flutter boundary of the heated vehicle up to that of the cold vehicle. Ride qualities improvement will also be a focus in the control law design phase of the project. Additionally, the linear unsteady aerodynamic codes will continue to be evaluated and improved. Flutter boundaries for the heated and unheated vehicles will be defined from the subsonic flight conditions to hypersonic speeds.

CONCLUSIONS

- **Aerothermoelastic Analysis Method Developed**
- **Aerothermal Loads Incorporated into Finite Element Analysis**
    - **Reduced Structural Frequencies**
    - **Lowered Flutter Boundary**
- **Flutter influenced by all vehicle components**
    - **Must Consider Aircraft Flutter Instead of Wing Flutter**

PLANS

- **Further Evaluate and improve Linear Unsteady Aerodynamics Codes**
- **Define Flutter Boundaries for Hot and Cold Vehicles from Subsonic to Hypersonic Speeds**
- **Apply Active Controls to Define Technology Benefits for Hypersonic Aircraft**

REFERENCES

[1] Sova,G. and Divan, P., " Aerodynamic Preliminary Analysis System II, Part II User's Manual," North American Aircraft Operations, Rockwell International.

[2] Spain, C. V., Soistmann, D. L., and Linville, T. W., "Integration of Thermal Effects Into Finite Element Aerothermoelastic Analysis With Illustrative Results", NASP CR 1059, August 1989.

[3] Whetstone,W., "EISI-EAL Engineering Analysis Language Reference Manual," Engineering Information Systems, Inc, San Jose, CA, 1983.

[4] Geising, J. P.,Kalman, T. P., and Rodden, W. P., "Subsonic Unsteady Aerodynamics for General Configurations, Part 1, Vol. 1 - Direct Application of the Nonplanar Doublet-Lattice Method," AFFDL TR-71-5, Part 1, Vol. 1, 1971.

[5] Cunningham, A. M. Jr., " A Steady and Oscillatory Kernal Function Method for Interfering surfaces in Subsonic, Transonic, and Supersonic Flow", NASA CR-144895, 1976.

[6] Rodden, W. P., editor, "MSC/NASTRAN Handbook for Aeroelastic Analysis, Volume 1", Nov. 1987.

[7] Kramer, G. D., and Keylon, G. E., "Prediction of Unsteady Aerodynamic Loadings of Non-Planar Wings and Wing-Tail Configurations in Supersonic Flow", AFFDL-TR-71-108, Part II, 1971.

[8] Morgan, H. G., Huckel, V., and Runyan, H. L., "Procedure for Calculating Flutter at High Supersonic Speed Including Camber Deflections, and Comparison With Experimental Results", NACA TN 4335, Sep. 1958.

[9] Peele, Elwood L., and Adams, William M., Jr., "A Digital Program for Calculating the Interaction Between Flexible Structures, Unsteady Aerodynamics, and Active Controls," NASA TM-80040, January 1979.

STRUCTURAL RISK ASSESSMENT AND AIRCRAFT FLEET MAINTENANCE

Herb Smith Jr.
Lead Engineer

C. R. Saff
Principal Technical Specialist

Structural Research
McDonnell Aircraft Co.
McDonnell Douglas Corporation
P.O. Box 516
St. Louis, MO 63166

Tom F. Christian
WRALC/MMCRA
Air Force Logistics Command
Robins AFB, GA 31098

WEIBULL STATISTICAL ANALYSIS OF FIELD INSPECTION AND AIRCRAFT USAGE DATA HAS BEEN USED TO PREDICT THE RISK OF STRUCTURAL FAILURE

We have described in previous work (ref. 1 and 2) the use of damage tolerance analysis and Weibull statistical analysis in the assessment of structural risk. The interference of the failure distribution and the aircraft life distribution is computed to determine the risk of structural failure. Information from any number of aircraft from different bases can be combined to give a projection of the risk associated with continued operation at the same or modified usage levels.

Three parameter Weibull distributions are determined from the flight usage data and the failure information obtained from field inspection of the aircraft. In the present analysis, deterministic flaw growth analysis is used to project the failure distributions from inspection data.

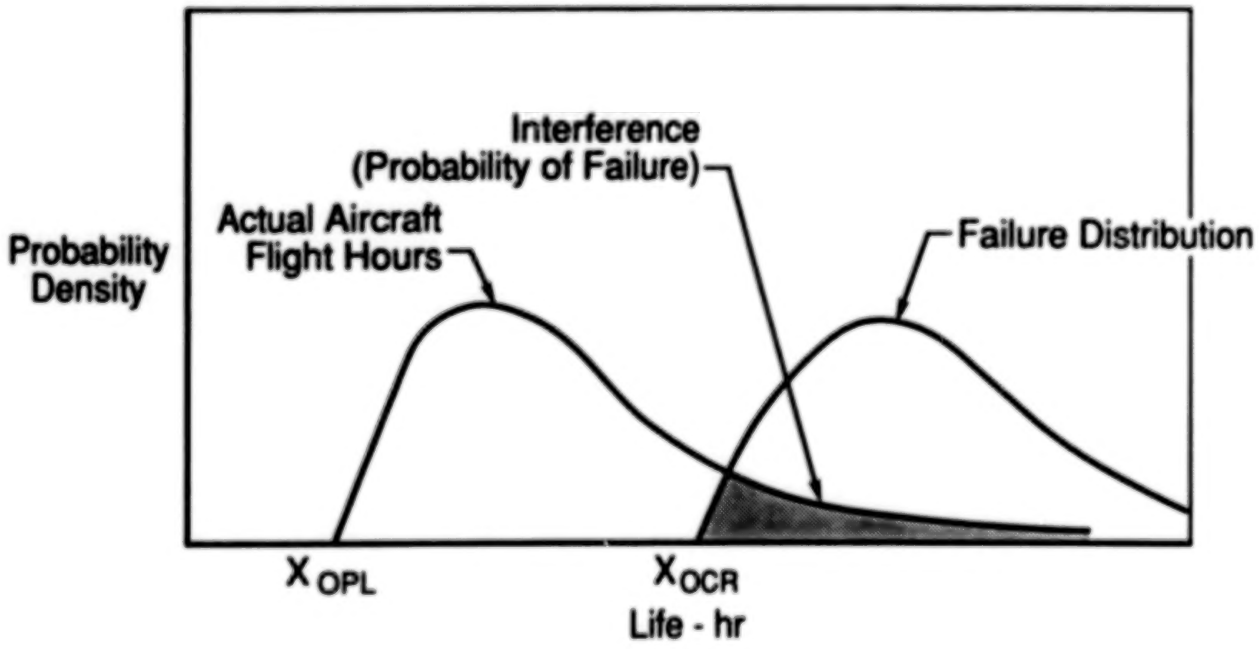

Figure 1

DETERMINATION OF FAILURE DISTRIBUTION FROM FIELD SERVICE INSPECTION DATA

Inspection data is reported for each critical point in the aircraft. The data will indicate either a crack of a specific size or no crack. The crack length may be either less than, equal to, or greater than critical size for that location.

Non-critical length cracks are projected to failure using the crack growth characteristics for that location to find the life when it will be at critical length. Greater-than-critical length cracks are projected back to determine the life at failure, that is, when it was at critical length. The same process is used as in the case of a non-critical crack except that the projection goes the other direction. These points, along with the critical length cracks are used to determine the failure distribution.

To be able to use data from different aircraft to build a common failure distribution, a consistent life variable must be used. Aircraft life varies with the severity of the usage, therefore the number of flight hours for a particular aircraft must be modified by its usage factor to obtain a normalized life which can be compared with that from other aircraft.

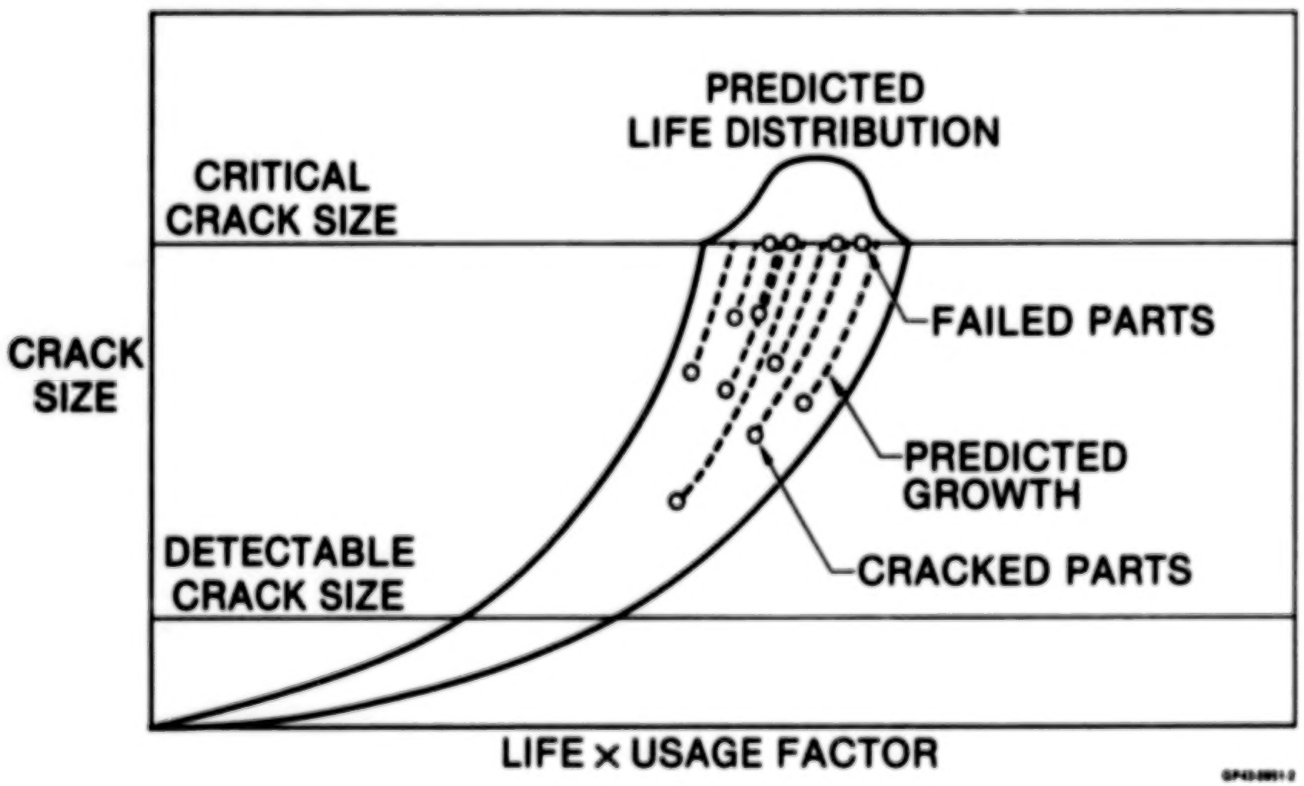

Figure 2

USAGE FACTOR ALLOWS THE COMPARISON OF DATA FROM DIFFERENT AIRCRAFT

The aircraft is designed to a baseline or design spectrum. This is determined from the design mission requirements for the aircraft. The actual usage of the aircraft will vary greatly depending upon where the aircraft is based when it enters service. Some bases fly many more benign flights and others fly more severe flights than the baseline. For flight hours to be compared from one aircraft to another, they must be related to the same severity level or no direct comparison is possible. The usage factor is used to adjust the actual number of flight hours for the difference between the baseline usage and the actual usage of the aircraft. This method has been shown (ref. 3) to accurately account for the effect that usage has on the crack growth characteristics. The usage factor is the ratio of the projected life of the aircraft for the present usage to the baseline life.

$$UF_s = \frac{L_b}{L_s} (> 1.0) \quad UF_m = \frac{L_b}{L_m} (< 1.0)$$

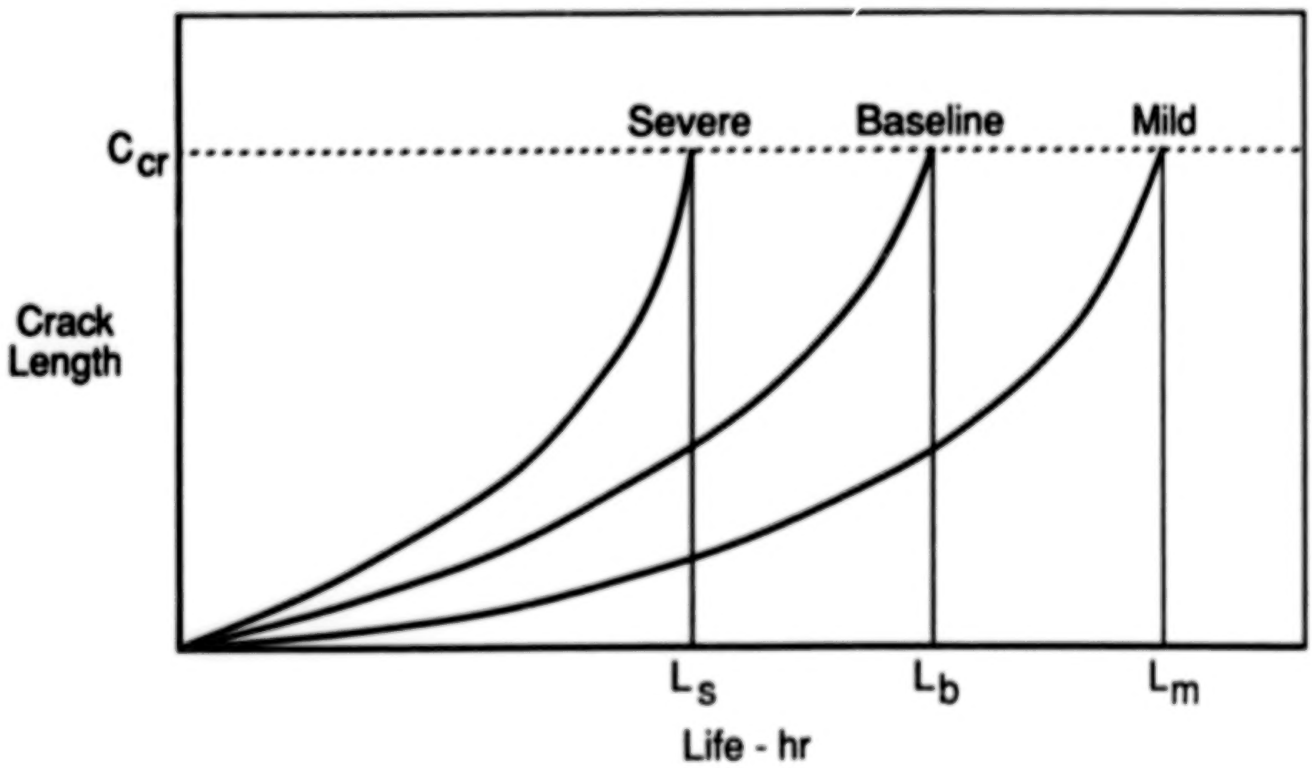

Figure 3

FIELD DATA IS USED TO DETERMINE THE THREE-PARAMETER WEIBULL DISTRIBUTION

Data from field inspections are used to determine the failure and life characteristics of the aircraft under consideration. The distribution of current lives is found from the number of hours (adjusted by usage) recorded for each aircraft. The failure distribution is found from the set of lives associated with the critical crack lengths. Again, the lives must be adjusted for the difference in usage.

Linear regression is used to determine the best 3-parameter Weibull fit to the data. The median ranks are determined for the failed points and take into account the effects of the suspended items (non-cracked aircraft) on the rank values. The minimum expected life is found from a search process which determines what minimum life value gives the best straight line fit to the data.

The difficulty with this process is twofold. First, there are generally only a few cracked parts from which you want to construct the failure distribution. The accuracy of the distribution so computed can be questioned. Second, the growing, or projecting, process assumes that the crack growth characteristics are deterministic.

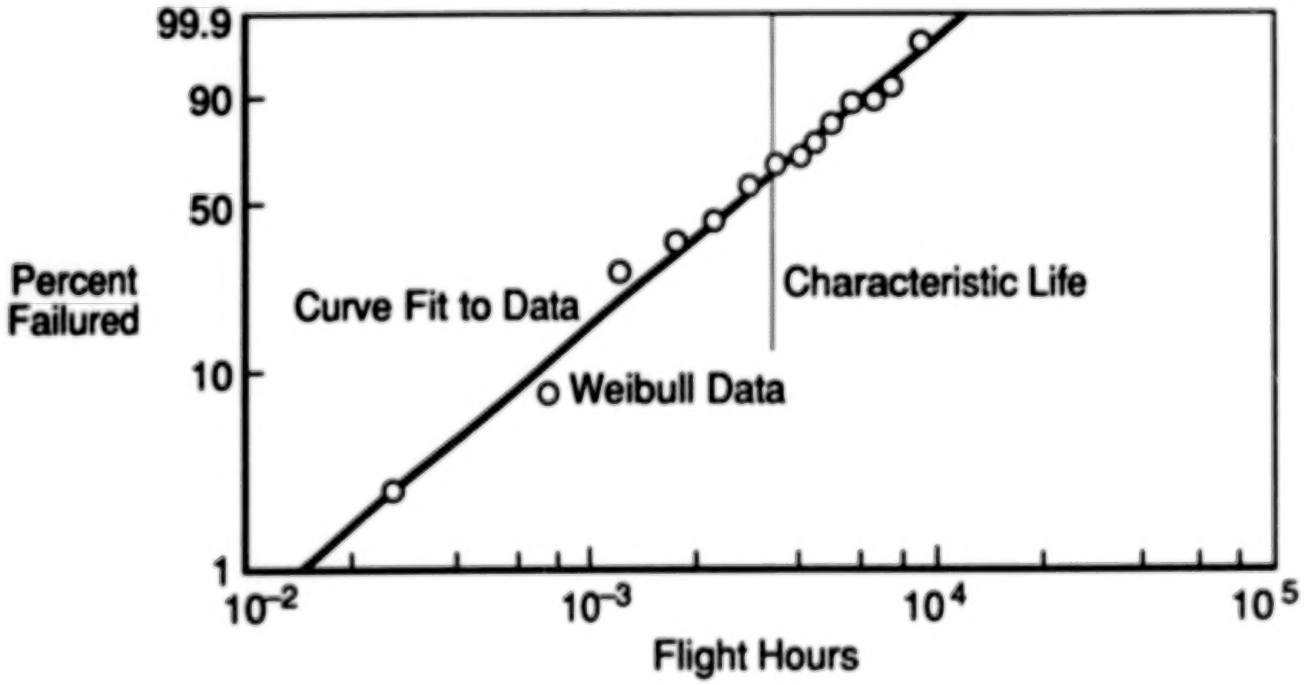

Figure 4

MULTIPLE FAILURE MODES ARE SOMETIMES PRESENT

Failures will sometimes result from several phenomenon. Manufacturing or material defects can precipitate early failures. These will generally occur well before the normal service failures. These failures are of interest, but it is important to separate this behavior from the normal service behavior for fleet management purposes. In addition, it is improper to attempt to fit a Weibull distribution to the combined data set since it does not correctly characterize either behavior pattern. The data set must be pruned to include only the long-term effects of the normal service life if an accurate picture of the failure rate and risk are desired. Generally the bulk of the data will be in this set, with the early failures being few in number.

Similarily, if one wants to concentrate on short-term failures, the data must be pruned of other failure modes. Plotting all data, as shown in this chart, can help identify when more than one failure is represented in the data.

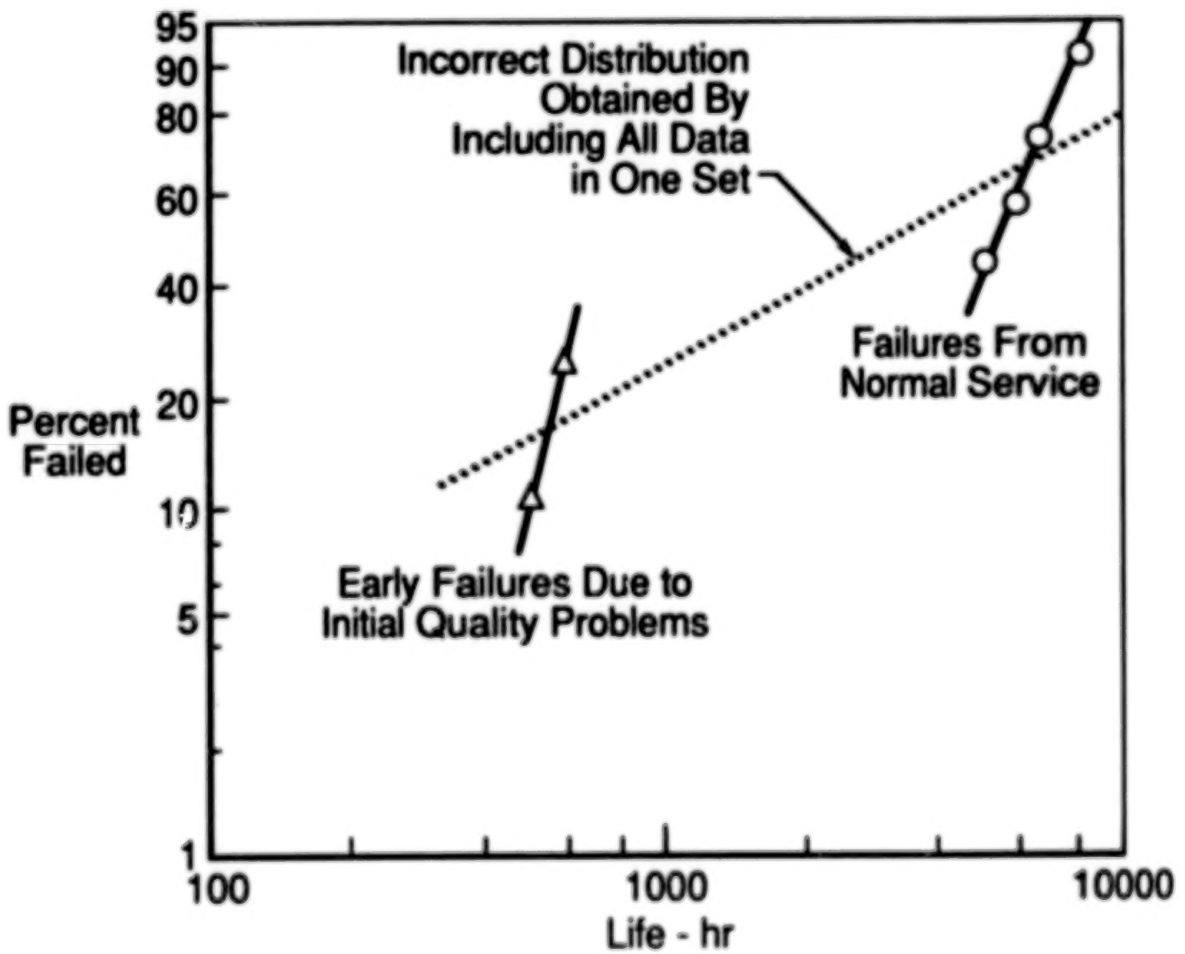

Figure 5

INITIAL INSPECTION DATA FOR 158 AIRCRAFT SHOWS 6 FAILURES

Inspection of 158 fighter aircraft revealed the existence of 6 aircraft with cracks of critical length at a point of concern on the vertical tail. Computation of the Weibull distribution shows that the data fits the curve fairly well, exhibiting a 0.97 correlation coefficient.

Closer examination of the data points indicates that perhaps there are two failure modes present. The first failure at 770 hours seems to be isolated from the remaining five points.

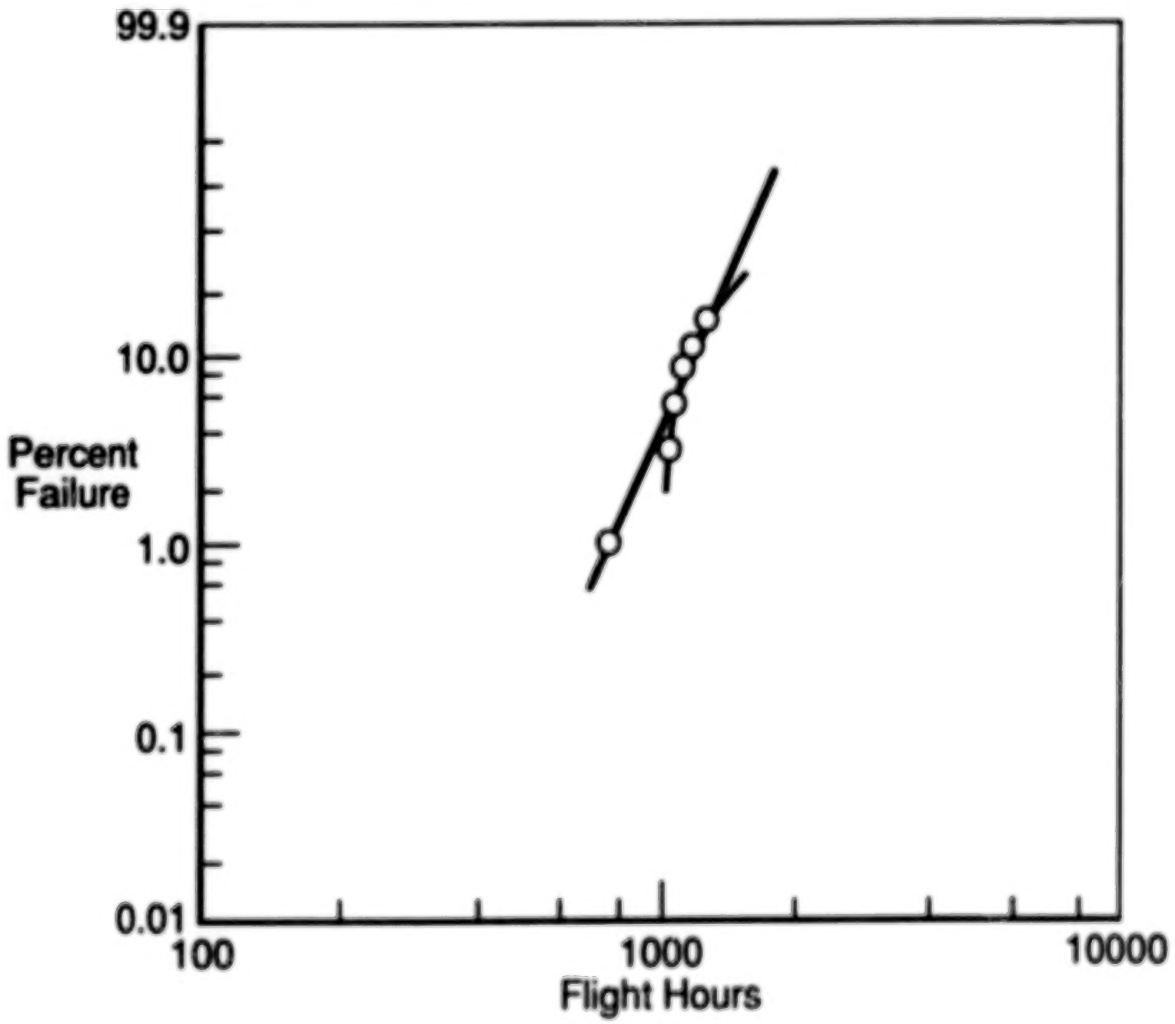

Figure 6

CUMULATIVE PROBABILITY OF FAILURE FOR ORIGINAL DATA

The cumulative probability of failure for the original data set containing six failures is shown. Included on the plot is the 90% confidence band. The confidence band is very important to the decision making process since frequently (as in this case) there are only a few failures from which the fleet commander must reach a decision.

The confidence bands were computed using two different methods. The five and ninety five percent ranks were computed and fit with a Weibull distribution along with the median ranks. This method provides the range for all three Weibull parameters; however, the computation of the ranks and the curve-fitting procedure result in a substantial computation time. The second method utilized the t distribution to compute the confidence band for the linear regression parameters for the curvefit to the median ranks. This process is much faster; however, we obtain no information for the Weibull location parameter. This is a significant loss because the location parameter represents the failure free operating period. The ability to rapidly generate confidence limits for the available data is felt to outweigh this loss.

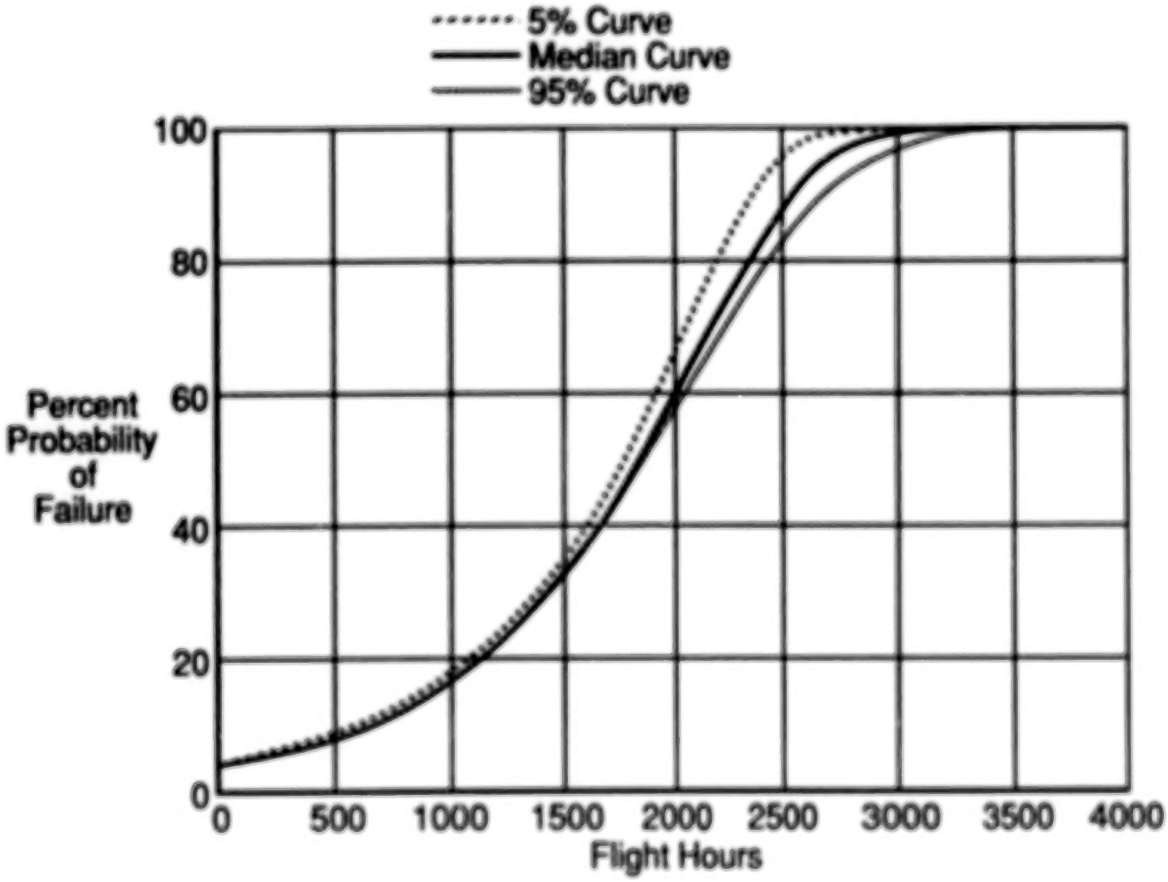

Figure 7

A SUBSEQUENT INSPECTION INCREASED THE DATA SET TO 181 AIRCRAFT WITH 12 FAILURES

Subsequent inspection data increased the sample to 181 aircraft containing 12 aircraft with failures. Again this information was plotted and Weibull distributions determined for the median, five percent, and ninety five percent rank points. These curves are shown along with the result obtained by computing the confidence bands for the linear regression parameters. The two methods compare well, except at the lower end where the variation in the location parameter is felt more strongly.

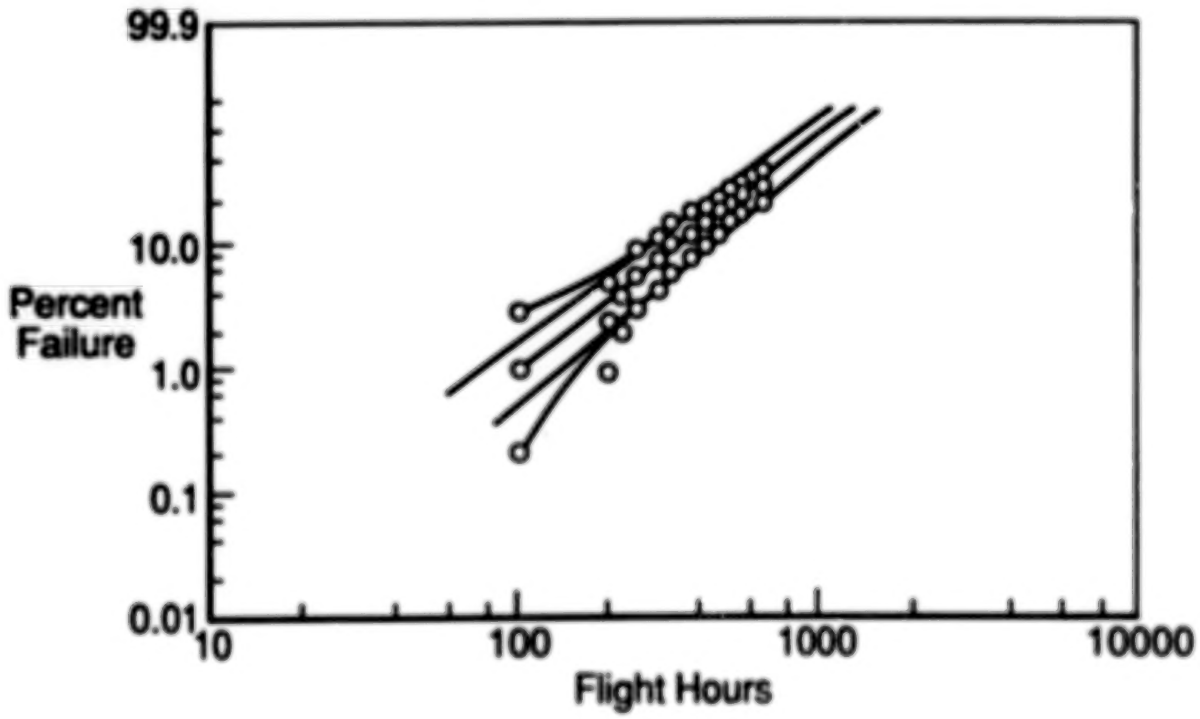

Figure 8

CUMULATIVE PROBABILITY OF FAILURE FOR SECOND DATA SET

The cumulative probability of failure for the second data set containing twelve failures is shown. Included on the plot is the 90% confidence band.

The 90% confidence band is much smaller than that with only six data points, especially at the high probability of failure, indicating that the data set now represents the actual behavior of the failure mechanism to a much higher degree than the original data set. The influence of the early failure has been reduced by the new data points, many of which fell between the first failure at 770 hours and the second failure at 1035 hours in the original set of data.

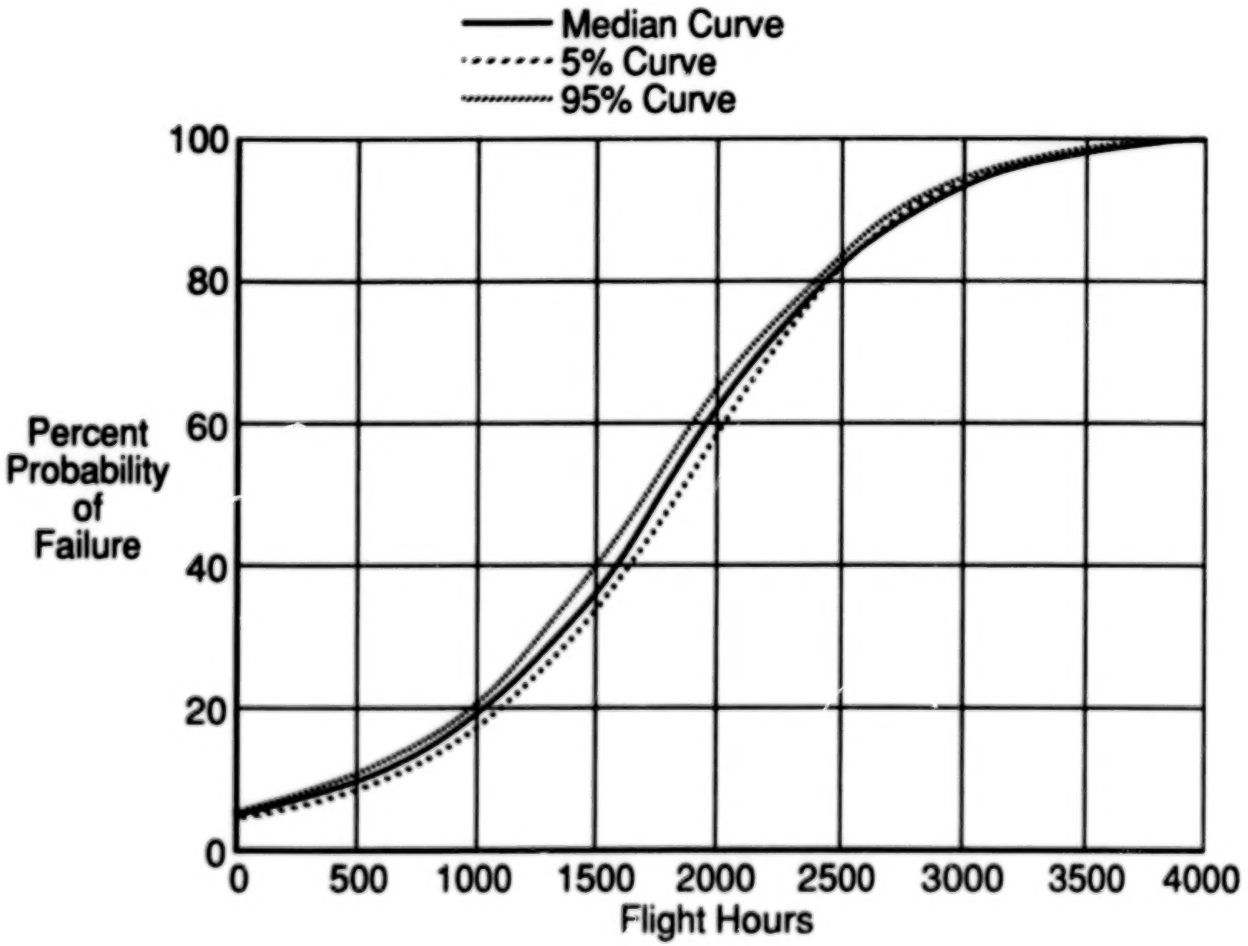

Figure 9

AREAS OF CONTINUING EFFORT

We are continuing our effort in several areas. We will implement a Maximum Likelihood Estimation (MLE) process to determine the Weibull parameters. An iterative procedure is required; however, our experience with the MLE process for two-parameter Weibull curvefits indicates that convergence is very rapid. The linear regression process we are currently using weighs all the points equally in their effect on the regression line, whereas the MLE process weighs the analysis toward the bulk of the data.

The process of projecting cracks to their critical level is accomplished deterministically from the crack growth curve. The crack growth process is, in fact, a random process and thus there is some uncertainty associated with the actual lives at failure. Inspection data is also treated deterministically. Nondestructive Evaluation (NDE) techniques have some uncertainty associated with their ability to detect flaws. The uncertainty, or randomness, of these two phenomena should be included. This uncertainty is best addressed using a Monte Carlo technique at the cost of some additional computation time. The advantage is that we will receive a better picture of the actual risk.

Our current process does not account for the repair of cracked parts and the return of the aircraft to service. We are looking to Renewal Analysis techniques to provide an assessment of such repairs. Repaired aircraft are of particular interest to fleet commanders in planning allocation of resources and logistic needs and to project the maintenance and repair actions required with continued fleet usage.

Maximum Likelihood Estimation of Weibull Parameters

Monte Carlo Simulation Will Allow:

- **Random Crack Growth Characteristics**
- **Uncertainty in Inspection Data**

Renewal Analysis to Account for Replacement of Failed Components

Figure 10

REFERENCES

1. Christian, T.F., Smith, H.G., and Saff, C.R., "Structural Risk Assessment Using Damage Tolerance Analysis and Flight Usage Data", ASME WAM, 7-9 December 1986, Anaheim California.

2. Saff, C.R., Smith, H.G., and Christian, T.F., "Applications of Damage Tolerance Analysis to Structural Risk Assessment", AIAA/ASME/ASCE/AHS 25th Structures, Structural Dynamics and Materials Conference, 6-8 April 1987, Monteray California.

3. Pinckert, R.E., "Damage Tolerance Assessment of F-4 Aircraft", AIAA Paper No. 76-904, Sept. 1976.

DEVELOPING A FRAMEWORK FOR QUALITATIVE ENGINEERING --

Research in Design and Analysis of Complex Structural Systems*

Bruno. M. Franck
Assistant Professor
Forest Products Department
University of Minnesota
St. Paul, Minnesota

*This paper contains references 1-17.

PROBLEM DEFINITION AND CORRESPONDING RESEARCH

The research is focused on automating the evaluation of complex structural systems, whether for the design of a new system or the analysis of an existing one, by developing new structural analysis techniques based on qualitative reasoning. The problem is to identify and better understand 1) the requirements for the automation of design and 2) the qualitative reasoning associated with the conceptual development of a complex system. The long-term objective is to develop an integrated design-risk assessment environment for the evaluation of complex structural systems. The scope of this short presentation is to describe the design and cognition components of the research.

Design has received special attention in cognitive science because it is now identified as a problem solving activity that is different from other information processing tasks [1]. Before an attempt can be made to automate design, a thorough understanding of the underlying design theory and methodology is needed, since the design process is, in many cases, multi-disciplinary, complex in size and motivation, and uses various reasoning processes involving different kinds of knowledge in ways which vary from one context to another. The objective is to unify all the various types of knowledge under one framework of cognition.

This presentation focuses on the cognitive science framework that we are using to represent the knowledge aspects associated with the human mind's abstraction abilities and how we apply it to the engineering knowledge and engineering reasoning in design.

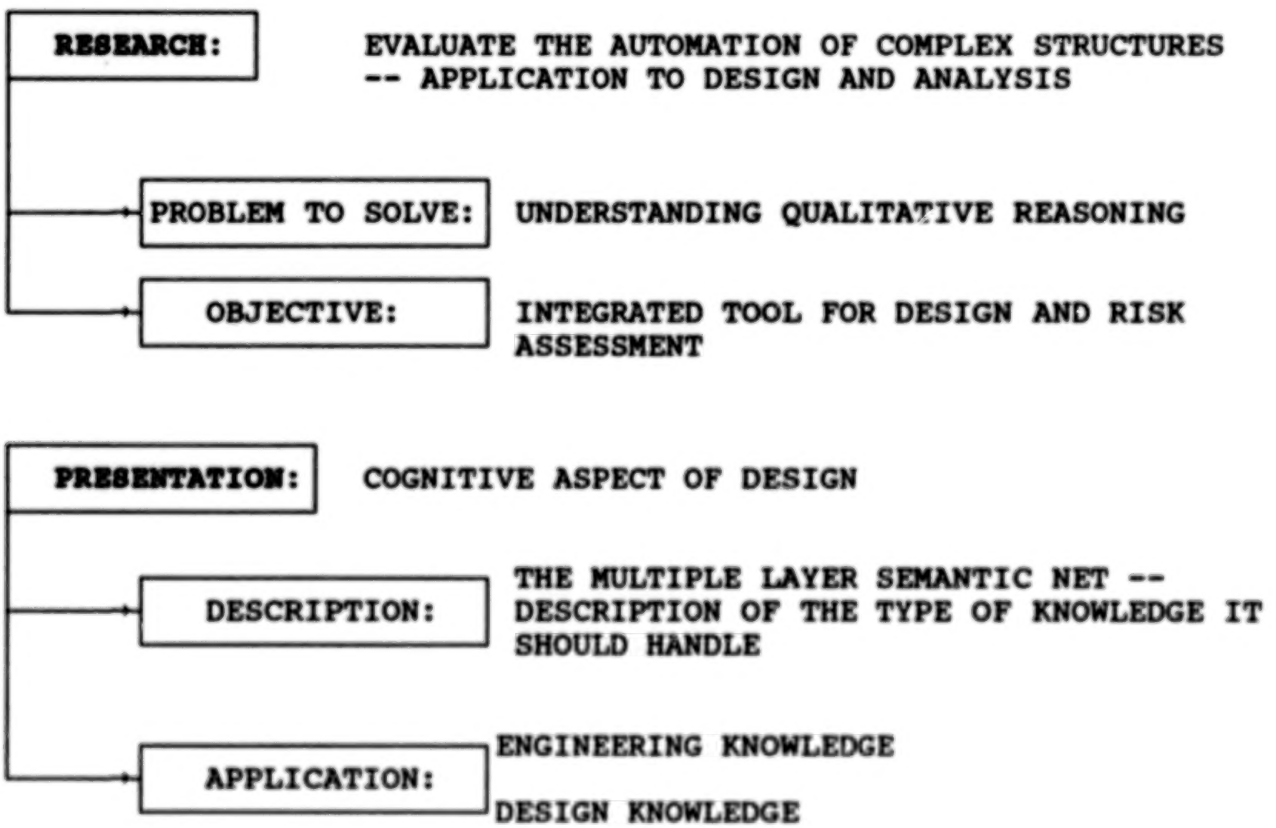

Figure 1

KNOWLEDGE: PROCESSING OF CONCEPTS

The common denominator among diverse entities such as an overall complex system, a component or a sub-assembly of that system, and the design and evaluation processes themselves, is that they can all be represented by formal concepts which, being associated with the human mind, can fundamentally encapsulate models of the reality that surrounds us [2] (percepts and icons). Concepts are organized in conceptual graphs, semantic nets, and schema or prototypes. Procedures can also be represented in semantic nets [7].

Different design reasoning procedures could be represented in various refinements of the same higher-order semantic net which corresponds, at the highest qualitative level, to deriving the structure for a device such that the device can meet a specific function.

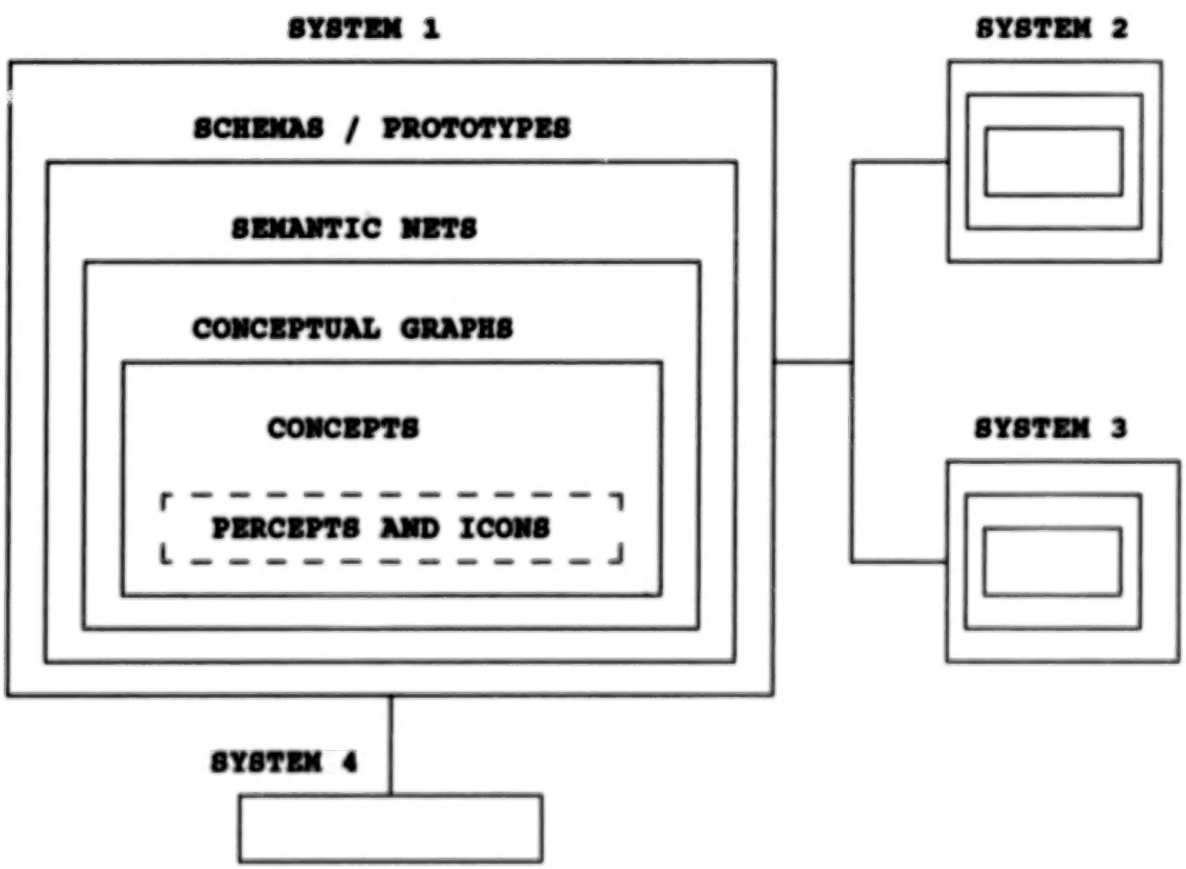

Figure 2

CONCEPTS AS SEMIOTIC PARADIGMS

Each concept associated with a cognitive process has three fundamental components: A semantic component to describe its function (what it is for), a syntactic component to describe its structure (how it is put together), and a pragmatic component to describe how it relates to its context (what are its behavior and the context in which it is used). Pearson [3] attributes these components to cognitive systems and calls such concepts semiotic paradigms.

The physical symbol system [4] and the connection models [5] have the same components in their paradigms, but vary by the emphasis on the level of representational abstraction at which they are described.

Computer models of a device and the corresponding knowledge can be made at various levels of representational abstraction, but they should always have the three semiotic components so that the knowledge can indeed be described and propagated in a manner similar to the actual cognitive process. This will ensure that the full range of engineering discourse, from the qualitative to the quantitative, will be modeled by computer descriptions.

Furthermore, all three semiotic components are described by both a declarative and a procedural statement. The declarative statement describes "what" is needed in design, and the procedural statement covers "how" to use it.

COMPONENTS OF AN ENGINEERING DEVICE	
LINGUISTIC ASPECTS	ENGINEERING ASPECTS
SEMANTIC	FUNCTION
SYNTACTIC	STRUCTURE
PRAGMATIC	BEHAVIOR CONTEXT

Figure 3

KNOWLEDGE STRUCTURE

It is our contention that components of knowledge used in processes apparently as different as design and analysis are, in fact, the same. The description of each component and its processing vary as a function of the particular requirements of a problem situation, but the component itself stays the same. We propose that different design / analysis reasoning procedures can, in fact, be represented as different refinements of the same higher-order semantic net. The various levels of detail required to solve problems correspond to various levels of representational abstraction. The same can be said for the representation of the facts in the domain of knowledge: Functional and structural hierarchies of the components of a complex system can be described at various levels of abstraction.

We therefore propose the Multiple Layer Semantic Net (MLSN) [6] as the cognitive knowledge structure which unifies the representation of the various types of knowledge about facts and reasoning. The MLSN is conceptually a layered semantic net. The nets of each layer are isomorphous to one another in that they represent the same engineering concepts, but their descriptions of the concepts are made at different levels of abstraction. The descriptions are qualitative toward the top of the representation and quantitative toward the bottom.

The rest of this presentation describes the cognitive techniques the MLSN should handle and points out the necessity to provide such a unified structure.

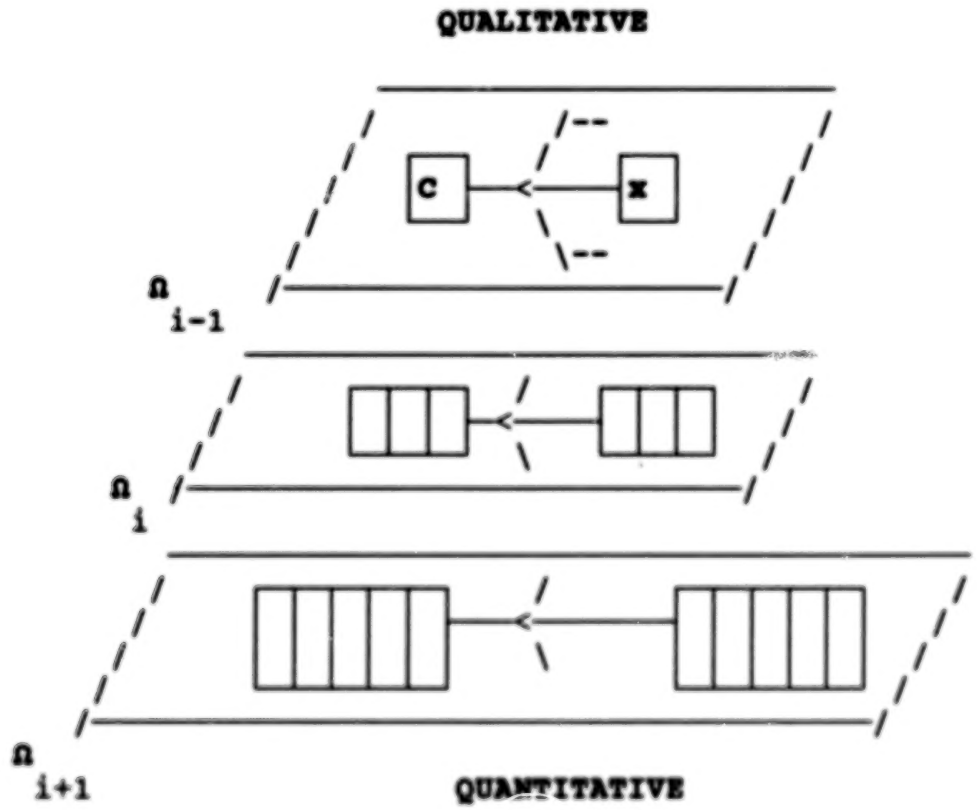

Figure 4

MULTI-DISCIPLINARY ASPECTS OF THE DOMAIN OF KNOWLEDGE

Most design problems require a combination of knowledge from different domains. For example, in the design of wood structures [7], wood science, wood engineering, and structural engineering are combined. In building design [8], it is architectural, structural, mechanical, and electrical engineering; in aerospace structures [9], aerodynamics, structural engineering, and mechanical engineering. In some design problems, the interaction among the various knowledge domains may be mostly sequential for the larger components of the process, whereas some sub-problems could be solved in parallel [10]. In all cases, a strong interaction exists among the different sources of knowledge, a fact which calls for new approaches such as simultaneous engineering and integrated activities.

The complex structure being designed, e.g., a building, may be decomposed differently in each one of the knowledge domains and may have different function hierarchies in these domains. These various views of the same complex structure can be represented with corresponding hierarchies in the levels of the MLSN. The hierarchies of the different domains are interconnected by the appropriate semantic links, which account for the particular aspects of the context in which the complex structure is used within each discipline. An example is the relationship between the structural decomposition provided by an architect, which becomes the functional decomposition serving as the starting point for design by a structural engineer.

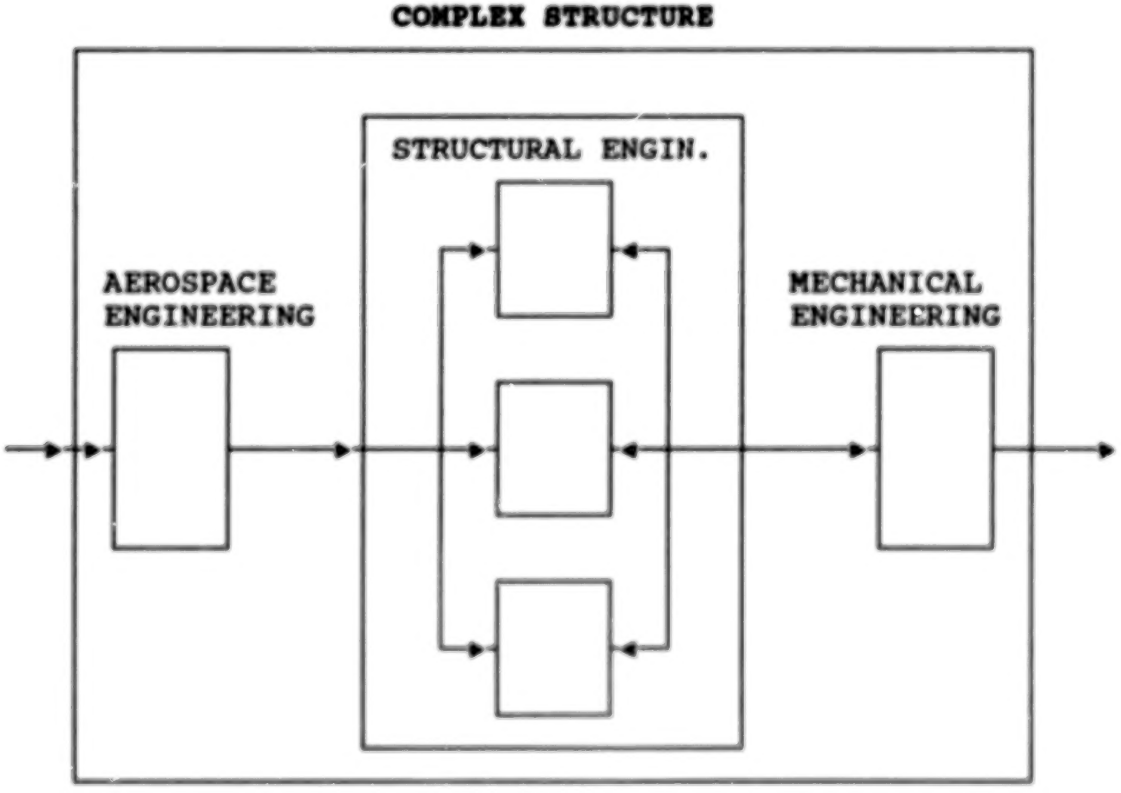

Figure 5

DECLARATIVE AND PROCEDURAL DEFINITIONS

Two different kinds of knowledge are used to perform a cognitive activity: Declarative knowledge and the procedural knowledge. Declarative knowledge consists of what we know about events, objects, and the relationships between them. Declarative knowledge is also referred to as propositional knowledge and can easily be represented by semantic networks [2, 11]. Procedural knowledge describes how to perform various activities and the dynamic process of how and why operations are performed upon the declarative knowledge.

At a higher conceptual level, declarative and procedural descriptions are part of different knowledge processing skills. According to [12], we first form some declarative knowledge while learning a task; we then correct the declarative knowledge in the associative stage to form some procedural knowledge; in the autonomous stage, these procedures become highly automated. In familiar problems, experts use procedural knowledge in a relatively rapid and automatic fashion [13, 14] and in a new and unusual situation they still have to rely on their declarative knowledge.

Hence we propose that procedural knowledge is used for routine designs [15], declarative knowledge is used for creative and innovative designs, and a combination of both is used for design by redesign [16].

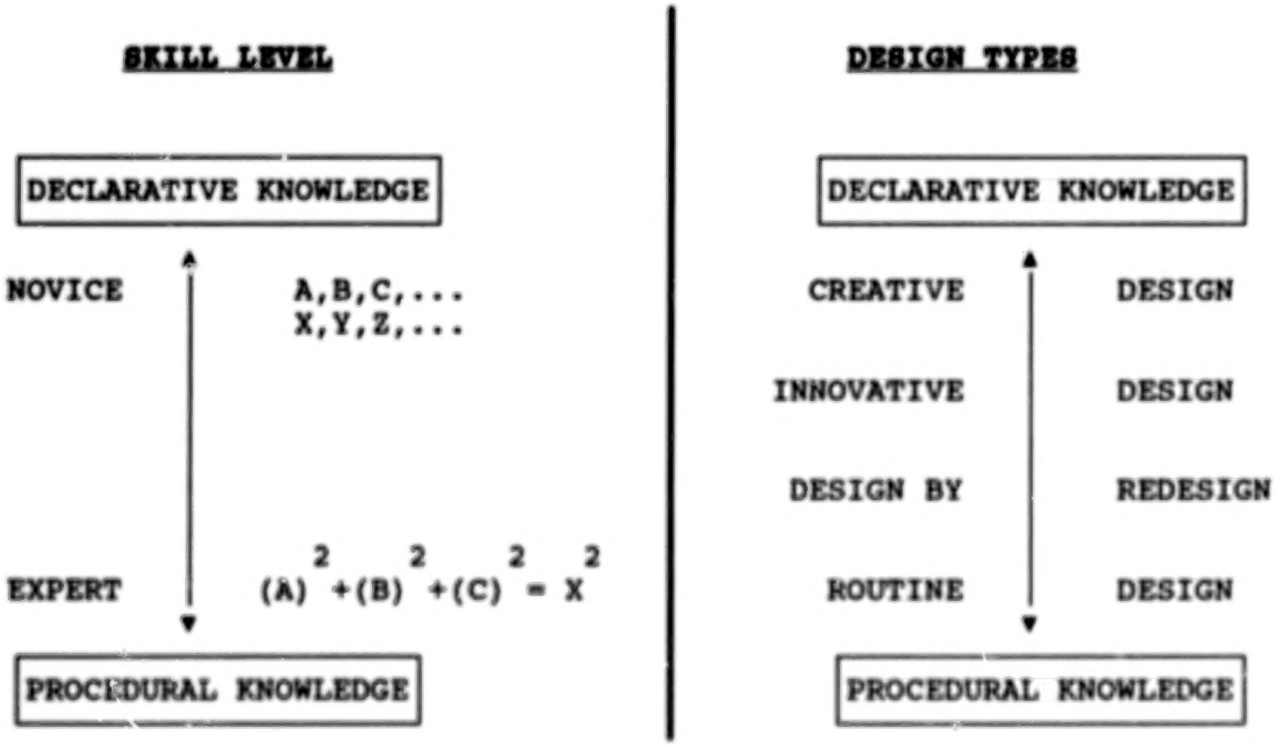

Figure 6

FROM QUALITATIVE TO QUANTITATIVE, COMPLETE OR PARTIAL ENVISIONMENT

The human mind can envision a complex system in its entirety or zero-in on one part of it. In doing so, it switches from higher levels of abstraction where the information tends to be more qualitative to lower levels of abstraction where it is more quantitative [6]. This is exemplified in the decompositional stage of design in which one critical component or sub-system is designed in more detail with the assumption that it will later fit with the rest.

Just as the human mind shifts from qualitative to quantitative descriptions, so does the design process. A design at a deeper level of description defines one at a higher level by providing more detail about the components. This characterization corresponds to the cognitive process of definition (the reverse of abstraction). It can also describe the reasons for having to define more precisely the concepts parametric in nature and includes the procedures to do so.

Modeling the design knowledge in multiple layers is especially appropriate in routine design [15]: The structures being designed and their components stay fundamentally the same from one application to the next. Only the numerical values of the parameters change from one specialization to another. It is therefore not necessary to abstract toward the generalized conceptual structure, design after design. This process corresponds to moving from one level upward, then back down in the MLSN in a fundamentally qualitative-then-quantitative process.

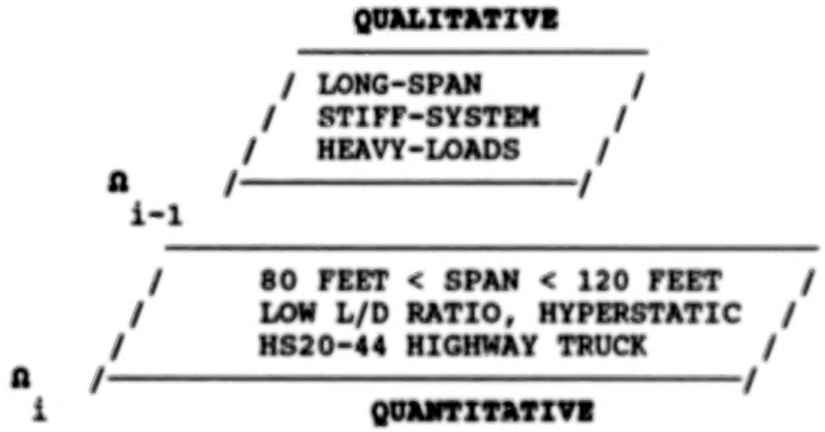

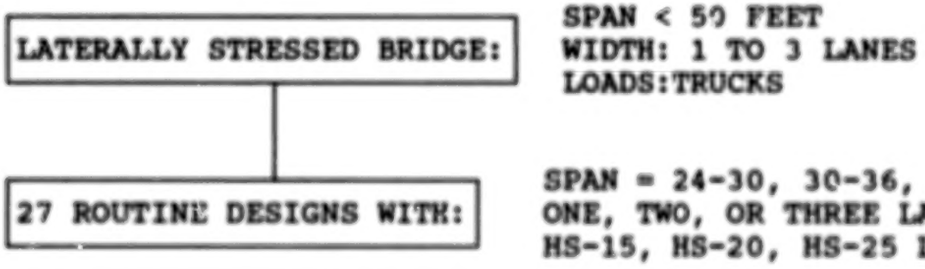
LATERALLY STRESSED BRIDGE:
SPAN < 50 FEET
WIDTH: 1 TO 3 LANES
LOADS:TRUCKS
27 ROUTINE DESIGNS WITH:
SPAN = 24-30, 30-36, 36-42 FEET.
ONE, TWO, OR THREE LANE-BRIDGE
HS-15, HS-20, HS-25 LOADINGS

Figure 7

SIMULATION: DESIGN AND EVALUATION

The procedures of design and evaluation are dual of one another in the following sense: Design consists of creating the structure of a device that exhibits a specific and desired behavior or that is meant to serve an intended purpose. Evaluation, on the other hand, consists of analyzing the behavior of a device in an effort to understand what its structure must be for it to exhibit that behavior. Both design and evaluation processes use the same knowledge base of facts and relations; only the manipulations of the components vary between the processes, as will be shown later.

Design and evaluation can be viewed as two refinements of the concept of simulation. Simulation is the attempt to make the composition of a system exhibit a certain behavior, and depends on the ability to create the system in the first place, whether it is a preliminary design alternative or a model of an existing system.

Because of their duality and generalization to the same concept, it is logical to integrate a design and a risk assessment into the same program: The structure of a complex system is established to some degree of completeness during a preliminary design. That structure can then be investigated to evaluate the risk associated with a potential failure of some of the components of the structure. The decision to accept or reject the preliminary design alternative is then made based on the results of the risk analysis.

DESIGN: BEHAVIOR OR FUNCTION → STRUCTURE

EVALUATION: STRUCTURE → BEHAVIOR AND/OR FUNCTION

∴ **DESIGN AND EVALUATION ARE DUAL ON A SEMIOTIC BASIS**

CONSEQUENCES: . GENERALIZATION OF BOTH TO SIMULATION

. INTEGRATION OF PRELIMINARY DESIGN AND RISK ASSESSMENT

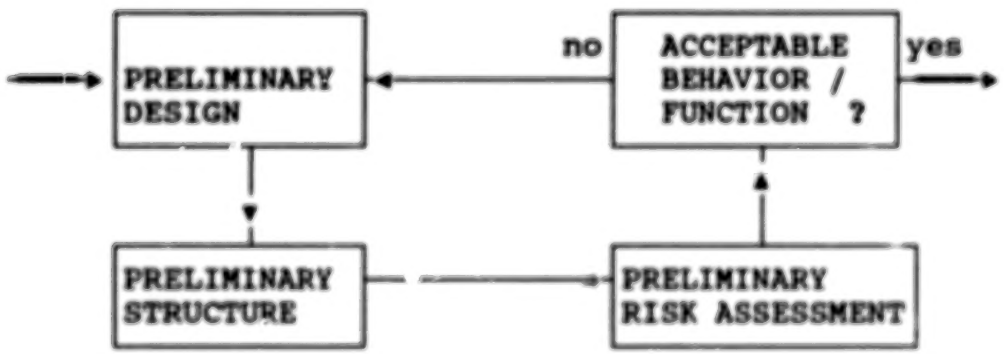

Figure 8

FUNDAMENTAL DESIGN STRATEGIES AND THEIR COGNITIVE EQUIVALENTS

Every design involves four steps: Problem formulation, conceptual design, embodiment design, and final design. The first step of the conceptual design establishes the functional decomposition of a complex system and its components. This decomposition corresponds to the cognitive processes of 1) specialization of a concept into an instance, and 2) individuation of the concept into sub-components.

The second step of the conceptual design is the design synthesis. This assembles some components into a more complex structural hierarchy which corresponds to the earlier functional decomposition. The corresponding cognitive process is the aggregation of concepts.

Some basic design strategies applicable during the conceptual design are the routine design, design by redesign, innovative design, and creative design. Any combination of these can lead to even more complex strategies.

Design by redesign first generalizes a concept to a higher-order class-concept and then specializes to another instance. Routine design first abstracts to a more qualitative model of the same structure and redefines it into another more quantitative model. Both processes are sketched on the MLSN below. As already mentioned, procedural knowledge is used in routine design, declarative knowledge in creative design, and a combination of both in innovative design and design by redesign.

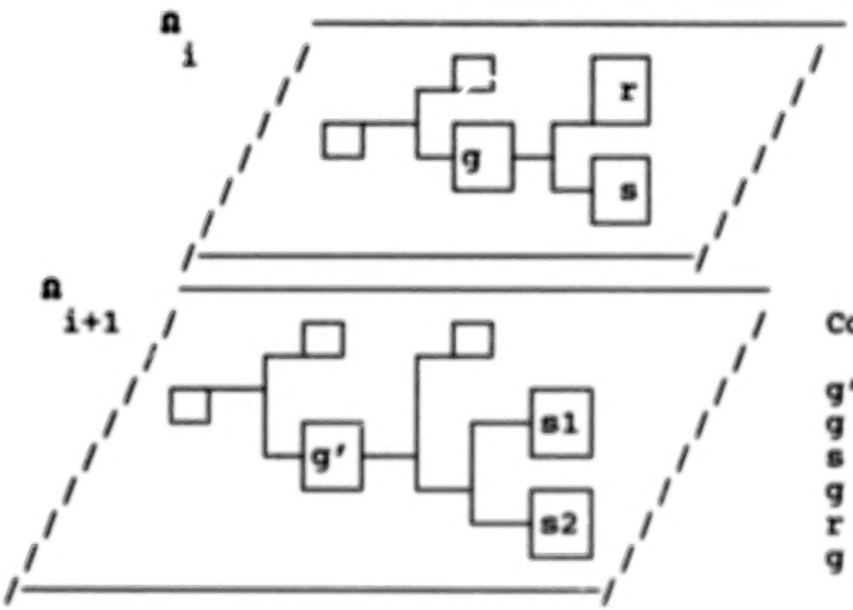

Cognitive processes:

g' to g: abstraction
g to g': definition
s to g: generalization
g to s: specialization
r & s into g: aggregation
g in r & s: individuation

Design strategies and the MLSN:

- Routine design: path from s1 up to s, then down to s2
- Design by redesign: path s1 to g', then to s2

Figure 9

DESIGN PROCEDURES AND THE SEMIOTIC RELATIONSHIPS

The reasoning procedures of the design problem solving process the knowledge among the components of a semiotic device, either by deriving one semiotic component from another inside one device, or by comparing similar components between two devices. There are six possible relationships among the three semiotic components of a device, all used either in design or analysis.

The FUNCTION-to-STRUCTURE mapping (i.e., deriving the structure from the function) and the BEHAVIOR-to-STRUCTURE mapping take place in the design synthesis. They use teleological reasoning. The STRUCTURE-to-FUNCTION and the STRUCTURE-to-BEHAVIOR mappings are analysis processes. They use causal reasoning.

Except for the mapping from structure to behavior, all mappings are of the type one to many. For example, several functions can be met by one structure, just as multiple structures could serve one function. A given structure can only generate one behavior at a time, with a fixed context.

The FUNCTION-to-BEHAVIOR mapping can be part of the innovative design which consists of finding new applications to an existing device. This mapping can be one to many. Finally, the BEHAVIOR-to-FUNCTION mapping corresponds to a qualitative analysis process and is a one to one mapping if considered in one context.

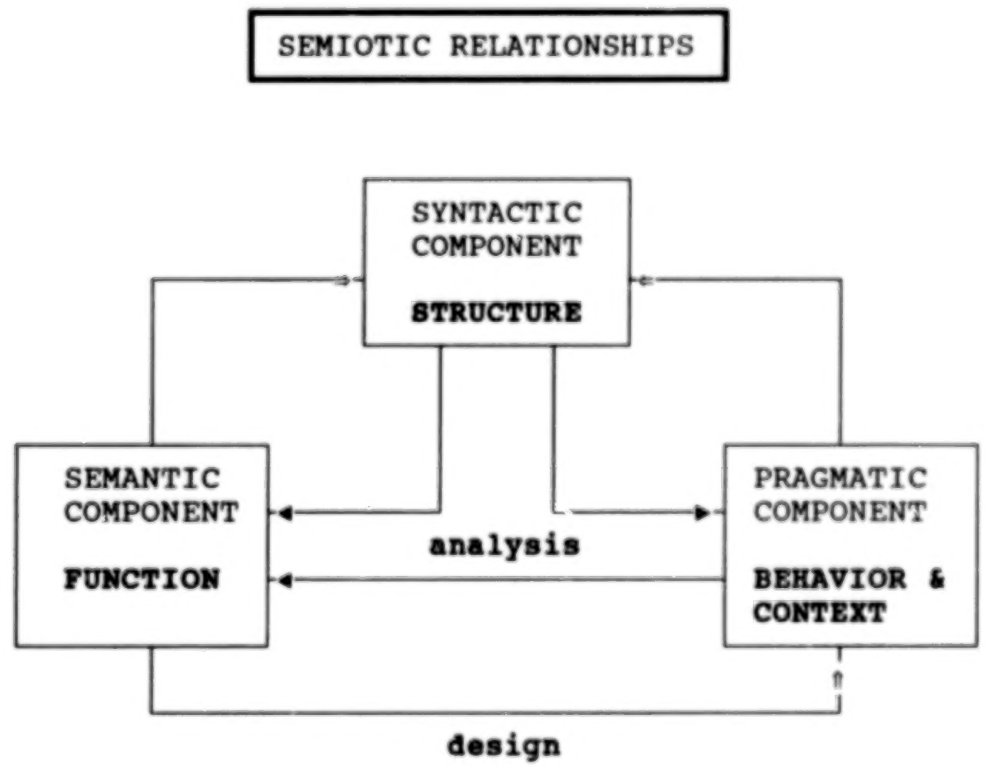

Figure 10

DESIGN STRATEGIES AND THE SEMIOTIC RELATIONSHIPS

The design process is based at the fundamental level on causal and teleological reasoning. Causal reasoning processes "what it is" in order to derive "what it does". It is applied, for example, in a backward chaining manner in the FUNCTION-TO-BEHAVIOR mapping of an innovative design where a new usage is identified for a device. Teleological reasoning, by contrast, processes "what it is for" to derive "what it should be". It is applied, for example, in the traditional derivation of the STRUCTURE from the FUNCTION.

At a higher level, some design strategies are Design by analogy, which compares corresponding components of different devices; design by constraint satisfaction, which builds up information requirements from the context for the function and structure of a device; and design by analysis, as in the innovative design process mentioned above. In case-based designs as in design by analogy, all transformations could be used [17].

Even higher order design strategies still manipulate the semiotic components. Routine design involves transformations of a structure from one instance into another one. Design by redesign involves iterations on the transformations between the function and/or the behavior and the structure. In all multidisciplinary designs, structures of one domain are functions for another. Through the design process, the structures of the second domain finish completing the description of the initial structures.

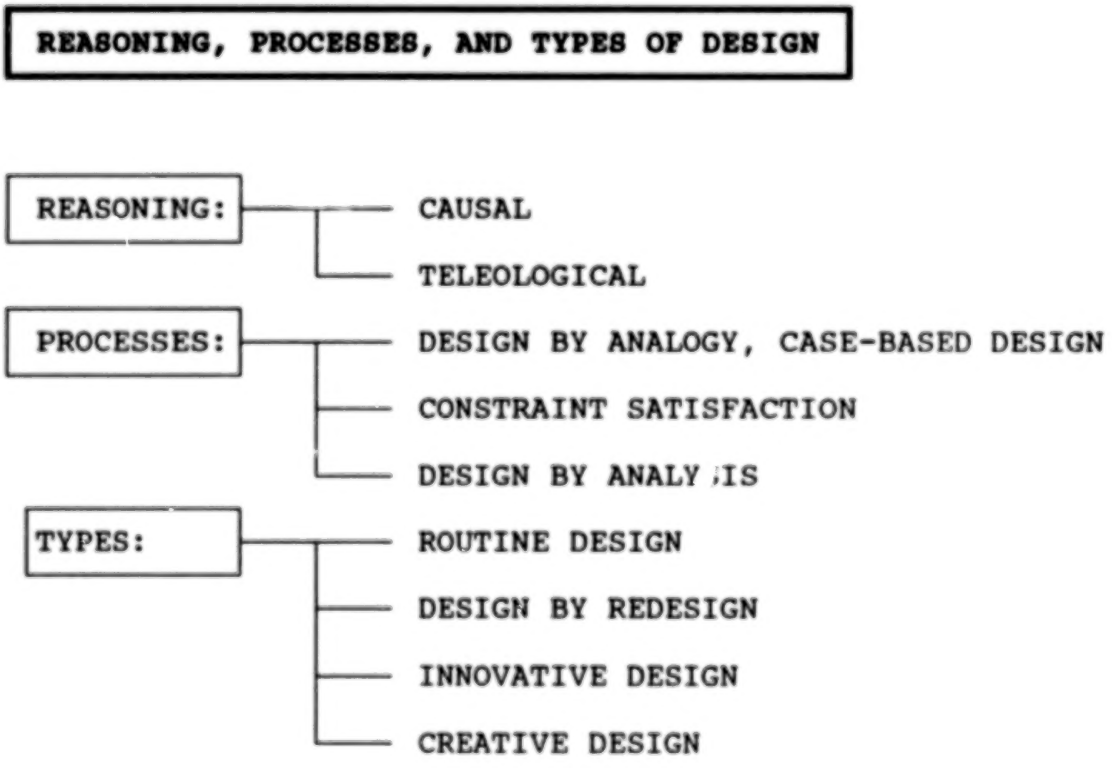

Figure 11

SUMMARY

The research in automating the design and evaluation of complex systems led to the formulation of a cognitive knowledge structure developed to facilitate the acquisition and representation of knowledge at multiple levels of abstraction.

The knowledge structure, the multiple layer semantic nets (MLSN), consists of isomorphous semantic nets describing the relationships among concepts viewed as semiotic paradigms. The components of the semiotic paradigms (structure, function, behavior and context) are described from qualitative levels to quantitative levels by both declarative and procedural descriptions.

The MLSN was described here in the perpective of the design process and the design strategies it should handle. It is also applied in another component of the research to investigate and develop techniques, based on qualitative reasoning, to evaluate complex systems.

The MLSN is now used to guide the development of a computer program which will perform both the design and the risk assessment for complex structural systems.

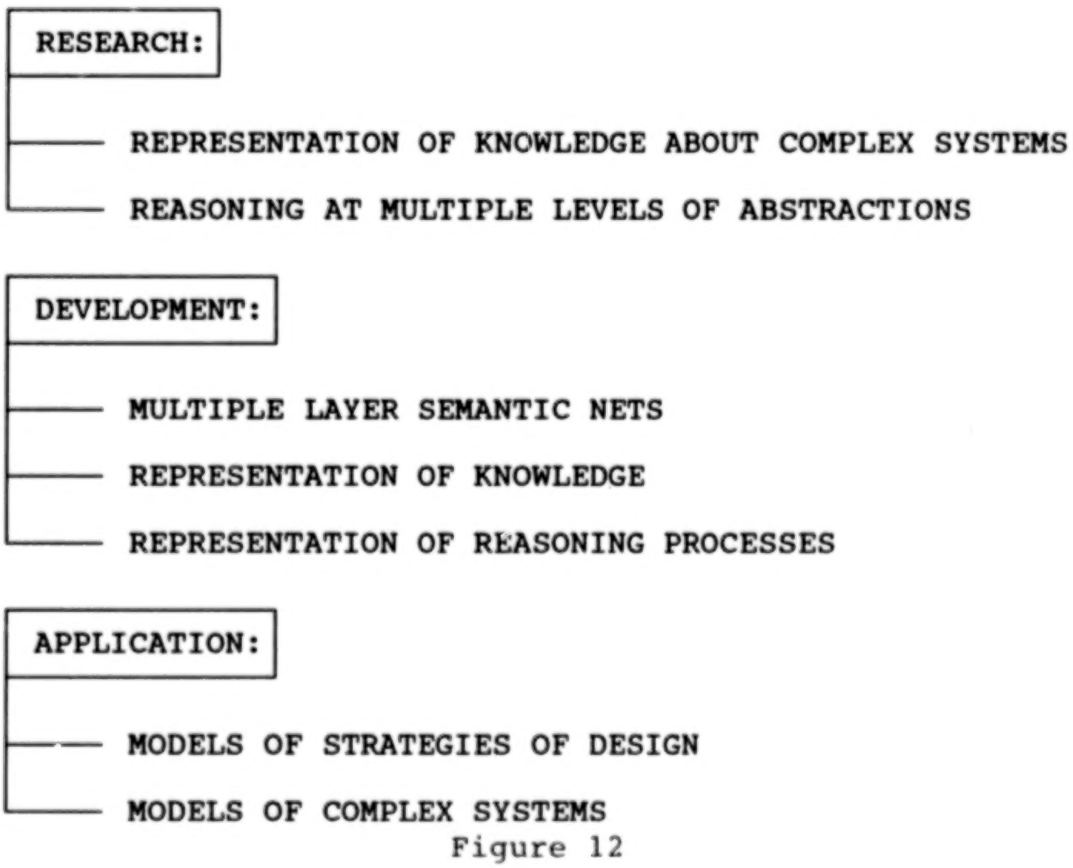

Figure 12

REFERENCES

1. Goel, V. & P. Pirolli; 1989; Motivating the Notion of Generic Design within Information Processing Theory: The Design Problem Space; AI Magazine, Spring 1989, 18-36.
2. Sowa, J.F. 1984; Conceptual Structures; Addison-Wesley.
3. Pearson, C. 1982; The Cognitive Sciences: A Semiotic Paradigm; in Languages, Minds, and Brains; Ed. by T.W. Thomas & R.J. Scholes; Erlbaum, Pub.
4. Newell, A. 1980; Physical Symbol System; Cognitive Science, Vol 4.
5. Rumelhart, D.E, J.L. McClelland, and the PDP Research Group; 1986; Parallel-Distributed Processing - Explorations in the Micro-Structure of Cognition; Vol. 1 & 2; The MIT Press.
6. Franck, B.M. 1989a; Qualitative Engineering at Various Levels of Conception for Design and Evaluation of Structures; 2nd Conference on Industrial and Engineering Applications of Artificial Intelligence and Expert Systems; ACM Press; Vol 1, 441-448.
7. Franck, B.M. 1989b; Qualitative Engineering of Wood Structures; 6th Conference on Computing in Civil Engineering; ASCE, 875-882.
8. Sriram, D. 1986; DESTINY: A Model for Integrated Structural Design; International Journal of AI in Engineering; Computational Mechanics Publications; Vol.1, No. 2.
9. Rogers, J.L. 1989a; A Knowledge-Based Tool for Multilevel Decomposition of a Complex Design Problem; NASA Technical Paper 2903; NASA Langley Research Center.
10. Rogers, J.L. 1989b; The Potential Application of the Blackboard Model of Problem Solving to Multi-Disciplinary Design; NASA Technical Memorandum No. 101633; NASA Langley Research Center.
11. Gordon, S.E. 1989; Theory and Methods for Knowledge Acquisition; AI Applications in Natural Resource Management; Vol. 3, No. 3.
12. Anderson, J. 1987; Skill Acquisition: Compilation of Weak- Method Problem Solutions; Psychological Review 92(2):192-210.
13. Anderson, J. 1985; Cognitive Psychology and Its Implications (2nd Edition); W.H. Freeman and Company; New York.
14. Newell, A. & H. Simon; 1972; Human Problem Solving; Prentice-Hall.
15. Brown, D.C., & B. Chandrasekaran; 1985; Knowledge and Control for Design Problem Solving; Technical Report, Laboratory of Artificial Intelligence Research; Department of Computer and Information Science; The Ohio State University.
16. Dixon, J.R., & M.K. Simmons. 1984; Expert Systems for Engineering Design: Standard V-Belt Design as an Example of the Design-Evaluation-Redesign Architecture; 1984 ASME Computers in Engineering Conference.
17. Holyoak, K.J., & P Thagard. 1989; Analogical Mapping by Constraint Satisfaction; Cognitive Science 13, 295-355.

NASA
National Aeronautics and Space Administration

Report Documentation Page

1. Report No.	2. Government Accession No.	3. Recipient's Catalog No.
NASA CP-3064		

4. Title and Subtitle	5. Report Date
Research in Structures, Structural Dynamics and Materials - 1990	March 1990
	6. Performing Organization Code

7. Author(s)	8. Performing Organization Report No.
Jean-François M. Barthelemy and Ahmed K. Noor, Compilers	L-16735
	10. Work Unit No. 505-63-01-07

9. Performing Organization Name and Address	11. Contract or Grant No.
NASA Langley Research Center Hampton, Virginia 23665-5225	

12. Sponsoring Agency Name and Address	13. Type of Report and Period Covered
National Aeronautics and Space Administration Washington, DC 20546-0001	Conference Publication
	14. Sponsoring Agency Code

15. Supplementary Notes

Jean-François M. Barthelemy - NASA Langley Research Center, Hampton, Virginia

Ahmed K. Noor - George Washington University - Joint Institute for the Advancement of Flight Sciences - NASA Langley Research Center, Hampton, Virginia

16. Abstract

The AIAA/ASME/ASCE/AHS/ASC 31st Structures, Structural Dynamics and Materials (SDM) Conference was held on April 2-4, 1990 in Long Beach, California. This publication is a compilation of presentations of the work-in-progress sessions and does not contain papers from the regular sessions since those papers are published by AIAA in the conference proceedings.

17. Key Words (Suggested by Author(s))	18. Distribution Statement
SDM Conference, Work-in-Progress Structures Structural Dynamics Materials	Unclassified - Unlimited Subject Category 39

19. Security Classif. (of this report)	20. Security Classif. (of this page)	21. No. of pages	22. Price
Unclassified	Unclassified	292	A13

NASA FORM 1626 OCT 86 For sale by the National Information Service, Springfield, Virginia 22161-2171 NASA Langley, 1990